Salt tectonic imaging at crustal and experimental scales by seismic migration and adjoint method : offshore application context

Javier Abreu-Torres

THÈSE

En vue de l'obtention du

DOCTORAT DE L'UNIVERSITÉ DE TOULOUSE

Délivré par : *l'Université Toulouse 3 Paul Sabatier (UT3 Paul Sabatier)*

Présentée et soutenue le *15/06/2022* **par :**

Javier ABREU-TORRES

Imagerie de milieux salifères aux échelles crustales et expérimentales par méthodes de migration sismique et méthode de l'adjoint: applications marines.

Salt tectonic imaging at crustal and experimental scales by seismic migration and adjoint method: offshore application context.

JURY

Yann CAPDEVILLE	Directeur de Recherche LPG Nantes	Rapporteur
Hervé CHAURIS	Professeur, Paris-Tech	Rapporteur
Jose DARROZES	Maître de Conférences/HDR, GET-Toulouse	Directeur de Thèse
Julien DIAZ	Directeur de Recherche, INRIA-Bordeaux	Examinateur
Nathalie FAVRETTO-CRISTINI	Chargée de recherche/HDR, LMA-Marseille	Invitée
Roland MARTIN	Ingénieur de recherche/HDR, GET-Toulouse	Directeur de Thèse
Myriam Schmutz	Professeure, IPB-Bordeaux	Examinatrice
Olivier VANDERHAEGHE	Professeur, GET-Toulouse	Examinateur

École doctorale et spécialité :
SDU2E : Astrophysique, Sciences de l'Espace, Planétologie

Unité de Recherche :
Géosciences Environnement Toulouse (UMR 5563)

Directeur(s) de Thèse :
Roland MARTIN et *Jose DARROZES*

Rapporteurs :
Yann CAPDEVILLE et *Hervé CHAURIS*

Abstract

Finding salt geological structures is an important economic reason for exploration in the world because they constitute a natural trap for various resources such as oil, natural gas, water, and also the salt itself can be exploitable. However, the imaging of these structures is a great challenge. Due to the properties of salt, with propagation velocities much higher than the adjacent strata, seismic waves are trapped within these structures, producing a large number of spurious numerical artifacts, such as multiples. This interferes with the primary seismic signal, making it impossible to see clearly what is underneath the salt structures (salt domes for instance).

Among all the geophysical exploration methods, the Reverse Time Migration method (RTM), which is part of the methods that solve the complete seismic waveform, is a very powerful imaging tool, even in regions of complex geology. In this work we use the adjoint-based RTM method, which basically consists of three stages: the solution of the wave equation (forward problem), the solution of the adjoint wave equation (adjoint problem), and the imaging condition, which consists in the correlation of the forward and adjoint wavefields.

This work can be divided in two cases of study: the first case consists in a two-dimensional synthetic model of a salt dome, taken from the final migration of a real survey in the Gulf of Mexico. The second case consists in an experimental three-dimensional model (WAVES), elaborated by the LMA laboratory in Marseille (France), which simulates a salt structure (with surrounding sedimentary structures), and a basement. The model was immersed in water to recreate a reallistic marine survey. Two different data types were obtained in this experiment: zero-offset and multi-offset data.

To compute the adjoint-based RTM method we use fourth-order finite differences in both cases. Furthermore, in the second case we used the UniSolver code, which solves the adjoint-based RTM method using fourth-order finite differences and MPI-based parallelism. It was also necessary to implement the viscoelastic equations to simulate the effect of attenuation. Because of this, the Checkpointing scheme is introduced to calculate the imaging condition and ensures physical and numerical stability in the migration procedure.

In the first case study we analyze the recovery of the salt dome image that different sensitivity kernels produce. We calculate these kernels using different parametrizations (density - P velocity), (density - Lamé constants), or (density - P impedance) for an acoustic rheology. We also study how the use of different a priori models affects the final image depending on the kind of kernel computed. Using the results obtained previously in 2D, we calculate synthetic three-dimensional kernels using an elastic rheology. In the second case (the realistic/experimental case), we first perform a calibration of the model properties for zero-offset data, and once the synthetic and real data fit well, we calculate the three-dimensional kernels. We then compute the forward problem of the multi-offset data with and without attenuation effects (nearly constant factor Q). We compare the synthetic data computed with elastic or viscoelastic rheologies with the real data. This will allow to see the impact of attenuation in the signals. This will pave the way to viscoelastic full waveform in salt tectonic context. Finally, we implemented the Least Squares Reverse Time Migration (LSRTM) algorithm for the two-dimensional acoustic synthetic data and for the 3-dimensional viscoelastic real data, which is an iterative inversion process, we have followed the Conjugated Gradient (CG) approach, checking that Wolfe conditions (convergence and curvature of the misfit functions are satisfied). We applied the LSRTM method to reduce the cross-talks caused by interference of the reflected waves, in this way it would be possible to enhance the interfaces in the reflectivity images.

Keywords: Salt domes, wave equation, seismic imaging, RTM method, kernel.

Abstract

La découverte de structures géologiques salines est une raison économique importante pour l'exploration dans le monde car elles constituent un piège naturel pour diverses ressources telles que le pétrole, le gaz naturel, l'eau, et le sel lui-même peut être exploitable. Cependant, l'imagerie de ces structures est un grand défi. En raison des propriétés du sel, dont les vitesses de propagation sont beaucoup plus élevées que celles des strates adjacentes, les ondes sismiques sont piégées dans ces structures, produisant un grand nombre d'artefacts numériques parasites, tels que des multiples. Cela interfère avec le signal sismique primaire, ce qui empêche de voir clairement ce qui se trouve sous les structures salifères (dmes de sel par exemple).

Parmi toutes les méthodes d'exploration géophysique, la méthode de migration par renversement temporel (RTM), qui fait partie des méthodes qui utilisent la résolution de la forme d'onde sismique complète, est un outil d'imagerie très puissant, même dans les régions à géologie complexe. Dans ce travail, nous utilisons la méthode RTM basée sur l'adjoint, qui consiste essentiellement en trois étapes : la solution de l'équation des ondes (problème direct), la solution de l'équation des ondes adjointe (problème adjoint) et la condition d'imagerie, qui consiste en la corrélation des champs d'ondes directs et adjoints.

Ce travail peut être divisé en deux cas d'étude: le premier cas consiste en un modèle synthétique bidimensionnel d'un dôme de sel, issu de la migration finale d'une étude réelle dans le Golfe du Mexique. Le second cas consiste en un modèle tridimensionnel expérimental (WAVES), élaboré par le laboratoire LMA de Marseille (France), qui simule une structure saline (avec les structures sédimentaires environnantes), et un socle. Le modèle a été immergé dans l'eau pour recréer un sondage marin réaliste. Deux types de données différents ont été obtenus dans cette expérience : des données à décalage nul ("zero-offset") et des données à décalage multiple ("multi-offset").

Pour résoudre l'équation des ondes impliquée dans la méthode RTM basée sur l'adjoint, nous utilisons des différences finies d'ordre 4 dans les deux cas. De plus, dans le second cas, nous avons utilisé le code UniSolver, qui résout la méthode RTM basée sur l'adjoint en utilisant des différences finies d'ordre 4 et un parallélisme basé sur MPI. Il a également été nécessaire d'implémenter les équations viscoélastiques pour simuler l'effet de l'atténuation. Pour cette raison, le schéma de type "Checkpointing" est introduit pour calculer la condition d'imagerie et assurer la stabilité physique et numérique dans la procédure de migration.

Dans le premier cas d'étude, nous analysons la reconstruction de l'image du dôme de sel que produisent différents noyaux de sensibilité. Nous calculons ces noyaux en utilisant différentes paramétrisations (densité - vitesse P), ou (densité - constantes de Lamé) pour une rhéologie acoustique. Nous étudions également comment l'utilisation de différents modèles a priori affecte l'image finale en fonction du type de noyau calculé. En utilisant les résultats obtenus précédemment en 2D, nous calculons des noyaux synthétiques tridimensionnels en utilisant une rhéologie élastique. Dans le second cas (le cas réaliste/expérimental), nous effectuons d'abord une calibration des propriétés du modèle pour des données à décalage nul, et une fois que les données synthétiques et réelles s'ajustent bien, nous calculons les noyaux tridimensionnels. Nous résolvons ensuite le problème direct pour le cas à décalage multiple avec et sans effets d'atténuation (facteur Q presque constant). Nous comparons les données synthétiques calculées avec des rhéologies élastiques ou viscoélastiques avec les données réelles. Cela permet ainsi de voir l'impact de l'atténuation dans les signaux. Cela ouvrira la voie à de la RTM et des simulations de la forme d'onde complète viscoélastique dans des contextes tectoniques salifères.

Mots clés : Dômes de sel, équation des ondes, imagerie sismique, méthode RTM, noyaux.

Acknowledgments

O the depth of the riches both of the wisdom and knowledge of God! how unsearchable are his judgments, and his ways past finding out! Romans 11:33

To my parents Javier Abreu-Gonzalez and Silvia Torres for instilling in me the path of faith. Thanks to this knowledge I was able to finish this work.

Furthermore, I thank my thesis directors Roland Martin and José Darrozes for their patience during this long process. I also thank Bastien Plazzoles for all his technical support during the whole process of my thesis.

I thank my jury, especially Hervé Chauris and Yann Capdeville for all their valuable suggestions before and after the defense of my thesis. I also thank Nathalie Favretto for sharing with me the WAVES model data and for her suggestions on chapter 4 of this work.

I thank all the people I met during my stay in Toulouse, it would be impossible to name them all, but they all contributed to make my stay in Toulouse very pleasant and that contributed to the completion of my thesis.

Finally, I thank the SENER-CONACYT project 128376, IMP H.61006 for funding this work and also the GET laboratory for funding in the last months of the project.

Contents

Chapter 1

General introduction

In the context of salt tectonics, using advanced reflectivity techniques like the *Reverse Time Migration* (RTM) or *Full Waveform Inversion* (FWI) techniques, geologist and geophysicist community aims at reconstructing salt tectonic structures and the geological structures beneath the salt domes that could trap resources like hydrocarbons, natural gas, or the salt itself. Here we aim at retrieving the salt dome structure (top and bottom) and the interfaces surrounding it by validating and using similar seismic imaging tools that we developed to study the following two specific cases:

- Recovering the top and bottom of a non-diapiric dome and the geological interfaces around it from a synthetic model in the Gulf of Mexico.
- Recovering the top and bottom of a diapiric salt dome and the interfaces around it from the experimental model WAVES at the laboratory scale (thanks to the data and previous analysis provided by our colleagues of the LMA/Laboratoire de Mécanique et d'Acoustique de Marseille).

We have also studied three important issues in seismic imaging (the parameterization, the preconditioning and the a priori model) in order to recover the dome structure and the interfaces under the dome. We analyzed these issues in a synthetic model and applied them to the experimental model (WAVES).

We will discuss with more detail these objectives in section 1.2. We will now proceed to discuss the geological context of this work.

1.1 Geological context

1.1.1 Salt tectonics context: Importance of its study.

In the context of Earth Sciences, rock salt is a crystalline aggregate of the mineral halite (NaCl) [Hudec and Jackson, 2007]. However, in the literature it is common to use "salt" to refer to all rocks composed mostly of halite. The study of salt deposit basins and structures has

become very important since the middle of the 20th century in the petroleum industry because according to Warren [1989] "about 70% of the world's giant oil fields in carbonate rocks bear a relationship to evaporites (Zhang Vi-gang 1981) and all of the giant gas fields in thrust belts have an evaporite seal (Downey 1984)". The petrol systems consist essentially of:

- Source rock: Presence of organic matter at a determined temperature and pressure to "mature" the rock and generate hydrocarbons.
- Reservoir rock: It has adequate porosity to store fluids (commonly sedimentary rocks). The hydrocarbons are transmitted to the reservoir rocks from the source rock through the migration process.
- Seal rock: It is an impermeable rock, which prevents the hydrocarbons from migrating (salt rocks).

To find the existence of a petroleum system, the existence and interaction of the aforementioned rock types is crucial. Focusing on the seal rocks, saline structures due to their impermeability are the most common seal rock. For relevant economic reasons many studies have been carried out to know the location and delimitation of these bodies. Furthermore, in Escalona and Mann [2006] the formation of the petroleum systems of the Maracaibo basin is described, which was controlled by tectonic events, influencing the generation, migration and accumulation of hydrocarbons. In Pilcher et al. [2011], the primary basins of the northern Gulf of Mexico, which form stratigraphic successions in allochthonous salt, are described. These geological environments present all the characteristics of a petroleum system (source rock, seal rock and storage rock).

However, it is worth asking whether the study of salt domes will continue to be relevant given the decrease in oil production worldwide and environmental issues due to oil extraction. Thanks to the development of CO_2 injection techniques that have been gaining relevance in recent years (Yu et al. [2015], Jia et al. [2019], and Janna et al. [2020]) studies on salt domes continue to generate interest. According to Jia et al. [2019] CO_2 injection is a promising method to rejuvenate the shale oil reservoirs after the primary production. This study was applied in the northern part of the Gulf of Mexico (a region with strong salt tectonics). One of the advantages of CO_2 injection is the reduction of greenhouse gases through CO_2 sequestration (Janna et al. [2020]). In addition, salt domes are considered as potential sites for hydrogen storage (Karnkowski and Czapowski [2007], Tarkowski and Czapowski [2018]), which is a less polluting alternative to fossil fuels.

1.1.2 Salt structures and their formation.

The formation of large salt deposits begins in the hot and dry subtropical regions of the world (where evaporation of water exceeds rainfall). This occurs mainly in closed sedimentary basins or in inland seas protected by natural barriers. In these regions seawater evaporates leaving a saturated brine.

Subsequently, the minerals contained are precipitated according to their solubility in water, and the rocks formed are called evaporites (carbonates, gypsum, halite). In fact the most common evaporite is halite (rock salt). Salt accumulations can exceed several kilometers if the basin is regularly refilled with seawater.

One of the characteristics of salt is that it is incompressible, so the density remains constant. This characteristic is important because over a geologic period of millions of years, large areas of salt are buried by sedimentation processes. The adjacent sediments that bury the salt tend to increase in density with depth. As a result, a density inversion occurs (heavy rocks over lighter rocks). Then, these sediments begin to sink through the salt, displacing it upward. This floating salt forms intrusions called diapirs. We can see in Figure 1.1 five schemes representing the formation of salt domes and some salt structures associated to different tectonic styles and other phenomena (erosion, density differences, compression, etc). For more information about the generation of salt structures, we refer to Talbot and Jackson [1987], Hudec and Jackson [2007], and Belenitskaya [2016].

In Figure 1.2 we can see the principal salt basins around the world. In Europe, we can find the Zechstein basin in Poland, which is mostly explored for their salt mines and by hydrogen deposition in rock caverns [Krzywiec, 2004; Tarkowski and Czapowski, 2018]. In the Middle East region we find the Zagros mountain chain, which is made up of salt domes, with the characteristic of saline surface outcrops, this basin is also studied for the reservoirs of hydrocarbons [Jahani et al., 2007, 2017; Talbot and Alavi, 1996]. In Africa we find the West Africa salt basin (from north Namibia to south Cameroon). This basin is primarily studied for the reservoirs of hydrocarbons (Marton et al. [2000] and Tari et al. [2003]). In America, we find the Gulf of Mexico Basin, which is very important in the exploration of hydrocarbons. In this salt basin there are two main types of salt structures: diapiric and non-diapiric (Wu et al. [1990], Liro [1992], Reed [1994]). This is one of the main reasons why, here in our present work, we will focus our attention on imaging and modelling these two types of salt domes.

It is important to mention that the economic importance of the study of salt domes is not only restricted to oil exploration, but also to the exploitation of the salt itself and the search for other resources that are also trapped by the salt, such as water, hydrogen and natural gas. For this reason it is very important to estimate the location and volume of these bodies. Seismic imaging is the most used method to this purpose which, thanks to its depth of investigation and resolution in complex regions, gives a good idea of what we could find in the subsurface.

1.1.3 Scientific problems

However, when imaging regions with salt tectonism using the seismic method, there are some issues to be considered. According to Ratcliff et al. [1992] and Jones and Davison [2014a] some of these issues are the following:

- Ability to correctly describe the geology from a priori information of the studied region. By this we mean having good a priori models from which we will start to recover the

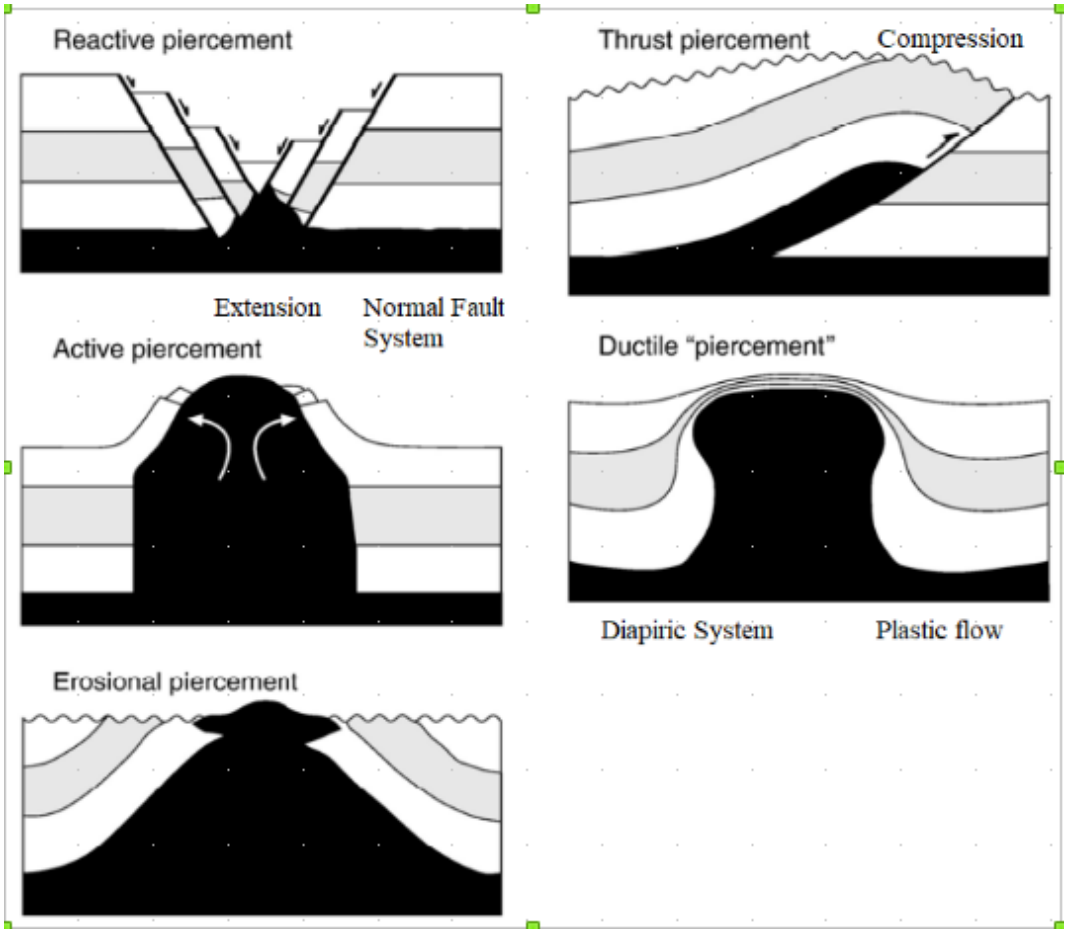

Figure 1.1. Types of salt piercement depending on the tectonic styles or other phenomena: Extension, Compression with the associated brittle deformation, erosional activity (non-tectonic) and diapiric flow (non-tectonic), modified from Hudec and Jackson [2007].

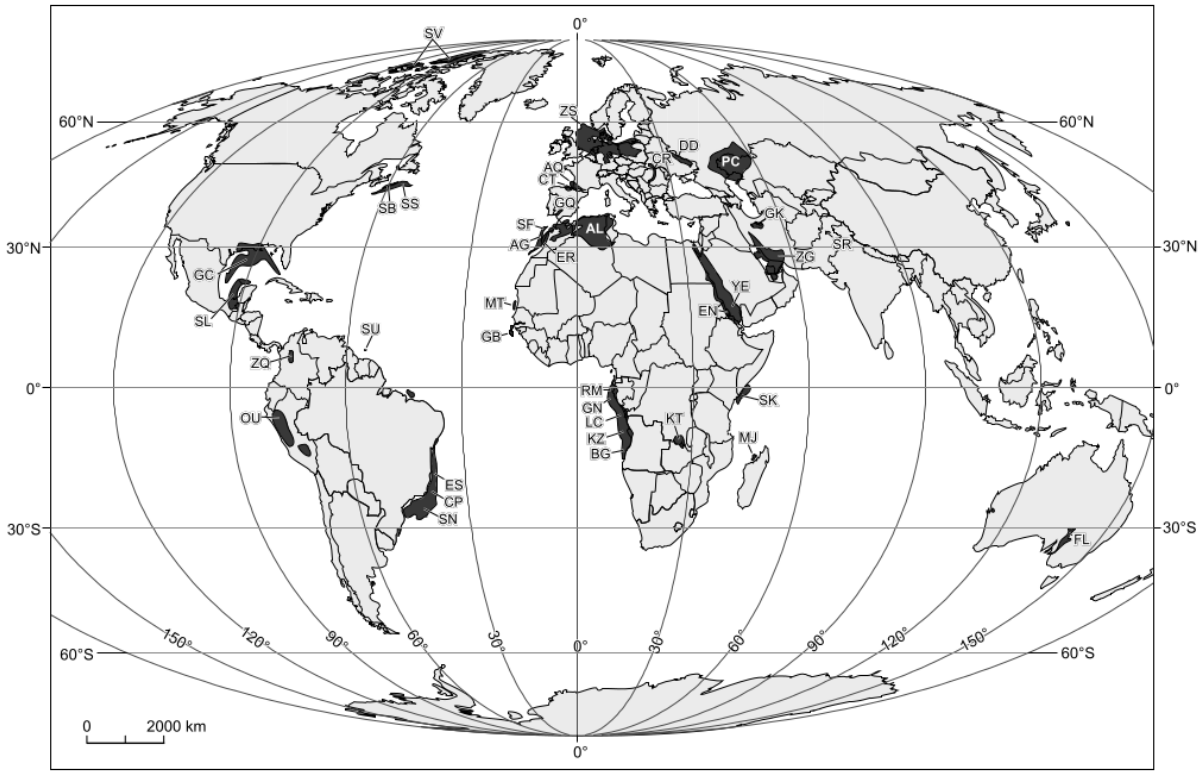

Figure 1.2. Principal salt basins in the world. Basin abbreviations: AG=Agadir, AL=Atlas, AQ=Aquitaine, BG=Benguela-Namibe, CP=Campos, CR=Carpathian, CT=Cantabtian-West Pyrenees, DD=Dnepr-Donetz, EN=Eritrean, ER=Essaouira, ES=Espirito Santo, FL=Flinders, GB=Guinea-Bissau, GC=Gulf Coast-Gulf of Mexico, GK=Great Kavir-Garmsar-Qom, GN=Gabon, GQ=Guadalquivir, KT=Katanga, KZ=Kwanza, LC=Lower Congo, MJ=Majunga, MT=Mauritania, OU=Oriente-Ucayali, PC=Precaspian, RM=Rio Muni, SB=Sable, SF=Safi, SK=Somali-Kenya, SL=Salina-Sigsbee, SN=Santos, SR=Salt Range, SS=Scotian Slope, SU=Suriname, SV=Sverdrup, YE=Yemeni, ZG=Zagros, ZQ=Zipaquira, ZS=Zechstein. Taken from Hudec and Jackson [2006].

interfaces of the medium.

- Steeply inclined flanks: The very inclined flanks are difficult to map because the incidence angles of the waves are close to zero degrees with respect to the flanks of the dome. This causes that there are regions in which the seismic waves have a grazing incidence, making difficult to delimit the flanks well. As an example of this phenomenon see figure 1.3. For this reason it is important to have a good illumination, and this could be achieved by increasing the offsets (distance source-receiver).

- High impedance contrast: Due to the fact that the impedance contrast between the salt and the adjacent sediments is very high, the seismic waves are "trapped" inside salt structures generating a high amount of multiple events. This causes interferences between primary events from sub-saline events and internal multiples of the salt structure. Consequently, the sub-saline sediments are hardly seen in seismic images. In Figure 1.3 we can also observe this phenomenon.

- Complex travel paths: In many cases the travel paths that the waves follow in the vicinity of salt dome is very complicated. This produces a weak correlation between the real and predicted data which will lower the image quality in those regions. The prism waves can be generated by these complex paths. These waves are reflected at two interfaces along the travel path from the source to the receiver generating spurious artifacts. They are very common in regions with steeply sloping flanks such as canyons (Deeks and Lumley [2015]) and salt domes (Malcolm et al. [2011], Kudin et al. [2018]). In Malcolm et al. [2011] they found that data recorded on receivers that are far away from the inclined structures allow to deal with prism waves. In Dai and Schuster [2013a] and Kudin et al. [2018] they use Born sources to generate prism wave images that could image in a correct way the salt dome flanks. In Figure 1.4 we show the travel path that follows a prism wave in a salt-tectonic context.

However, technological advances in the field of seismic tomography have made it possible to develop methods to improve the imaging of complex geological regions such as salt domes. Some of these methods are the Reverse Time Migration (RTM) [Chang and McMechan, 1986; Whitmore, 1983], and also more modern versions such as the Least Squares RTM (LS-RTM) [Dai et al., 2010; Feng and Schuster, 2017], and Full Waveform Inversion (FWI) (Virieux and Operto [2009], Xu et al. [2012]) that have the advantage of involving the last advances of full waveform inversion techniques. We will see these methods in more detail later.

In the next section we will provide the scope of this work.

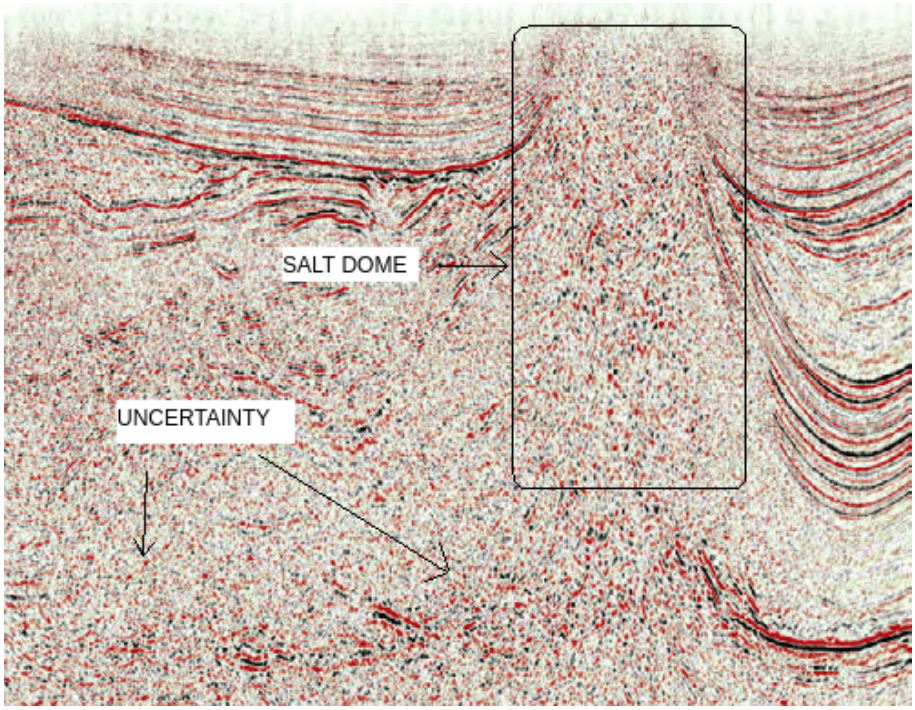

Figure 1.3. Example of a seismic image of a salt dome. We can see how the flanks of the salt dome are not well defined. In addition, the structures underneath the dome are practically impossible to see. Modified from Buehnemann et al. [2002].

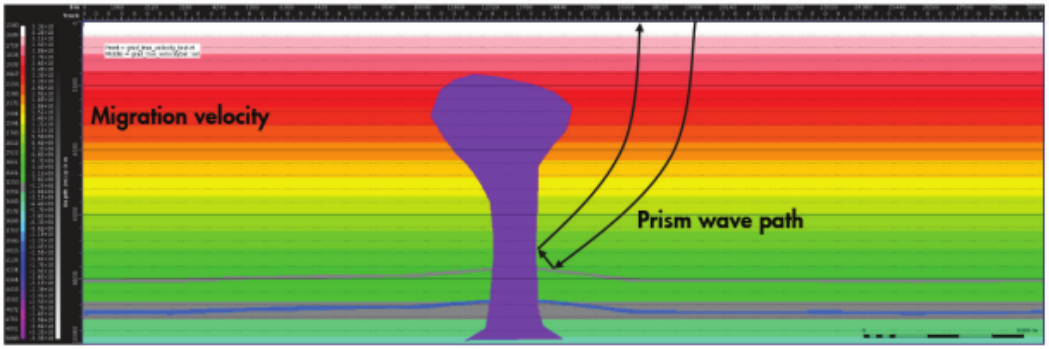

Figure 1.4. Example of the travel path followed by a prism wave in a salt tectonic context. Taken from Kudin et al. [2018]

1.2 Scope of the study.

In this work we will deal with the seismic imaging of two types of structures that we could commonly find over the world as in the Gulf of Mexico (Wu et al. [1990], Liro [1992], Reed [1994]): diapiric and non-diapiric salt bodies, in which we seek to recover the base of the dome and the interfaces under the dome. This is interesting because as mentioned in the section 1.1.1 generally hydrocarbons are trapped under salt dome structures. We choose these objectives to start first with 2D seismic imaging of simple non-diapiric structures (considered less complicated because the adjacent sediments don't present curvature close to the boundaries of the dome). After this we will work on the diapiric salt structure of the experimental case WAVES. We describe hereafter our two objectives:

- **First case (non-diapiric salt dome).** The first structure corresponds to a salt dome, which was adapted from an actual interpretation of seismic data in the Gulf of Mexico. By fit, we mean here that we focused on a single salt body among all the original bodies. The "real" data are generated from the two-dimensional Vp density and velocity models, so this is a study of synthetic and acoustic data. In Figure 1.5, we present the complete synthetic Vp model and our selected salt structure. Initially, our challenge here is to define the right parameterization to compute the RTM images, as well as a good way to normalize them to reduce artifacts in the images and recover the background and interfaces under the dome.

- **Second case (diapiric salt structure).** The second case consists in processing real experimental data obtained in the laboratory LMA in Marseille (Solymosi et al. [2020]) to validate our inversion code UniSolver for diapiric salt structure imaging and characterization. This experimental model, called WAVES, consists in a 3D crystal glass volume very similar to a salt dome, surrounded by several types of clays and resins to mimic the adjacent sediments generally found around a salt dome. Furthermore, aluminium was used to simulate the basement. The model was immersed in water to simulate realistic marine data acquisition. In this particular context, our study is complementary to the Solymosi et al. [2020]'s work. We apply the FWI techniques to iteratively reconstruct the model and the interfaces from the smoothed background WAVES model, and improve the reflectivity images. Moreover, in this real case, attenuation effects are present and we aim now at applying our reconstruction method to a 3D viscoelastic medium, while 2D viscoelastic reconstruction has been done previously for those WAVES data by Solymosi et al. [2020]. As Solymosi did in 3D, we perform also a calibration of viscoelastic parameters but on different profiles than those chosen by Solymosi et al. [2020]. Indeed, in our study we want not only to recover the base of the dome and the interfaces under the dome, but also to characterize the model by FWI. To perform those reconstructions we consider a different seismic line to take 3D effects into account during the imaging process.

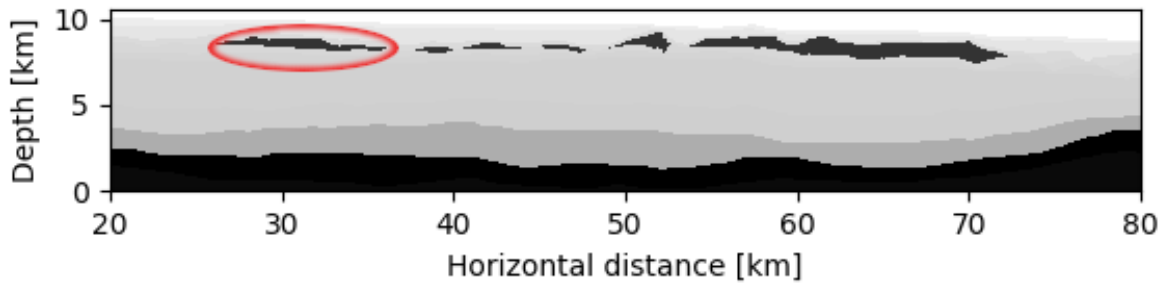

Figure 1.5. Synthetic V_P model that corresponds to the final migration image of a region in the Gulf of Mexico. Different types of non-diapiric structures are present. The red-selected structure corresponds to the structure we choose to perform the 2D seismic imaging.

Hereafter, we thus provide a brief and non-exhaustive review of different seismic imaging techniques and we also mention some technical challenges and scientific problems to be solved in seismic imaging for the specific case of salt dome modelling.

1.3 Upper crust and near surface imaging.

The main objective of geophysical exploration methods is to estimate the values of parameters describing the subsurface. In general, in all geophysical methods, the processes to estimate these subsoil parameters are represented in the next flowchart of the Figure 1.6, where we can distinguish three steps: Data acquisition, data processing and data interpretation. As the data processing is the stage in which we work, we mark it in red to differentiate it from the other stages. We will do so in the rest of the manuscript.

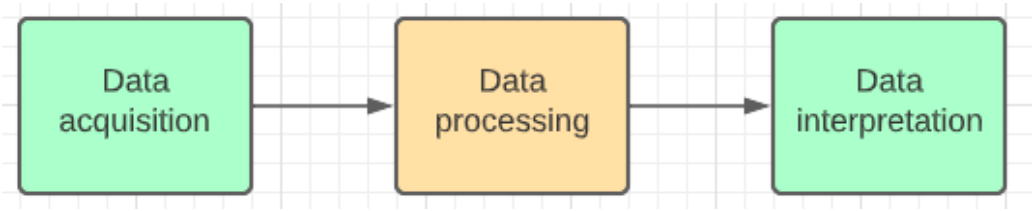

Figure 1.6. General process of a geophysical method to estimate the subsoil parameters.

Among all the geophysical exploration methods, the seismic method is the most used in the exploration of regions with complex geology because of its penetration capacity (great depth of exploration), and also because the ability to reduce the wavelength scales is increased, which in turn increases the imaging resolution and the possibility of observing the interfaces better. According to Schuster [2011], seismic tomography is a procedure for estimating earth's rock parameters from seismic data. These parameters are normally expressed as the P and S velocity and the density, and represented by 2D or 3D graphics.

In the next paragraphs we will discuss the three stages of Figure 1.6 in the context of the seismic method:

- **Acquisition**: Seismic data acquisitions or seismic surveys involve large-scale projects carried out on the land or sea surface. Broadly speaking, they consist of an array of sources and receivers whose location depends on the type of survey being performed. In active seismic acquisition, the source is artificially injected, generating a seismic wave that propagates through the subsurface, traveling through the various interfaces. After several events of refraction and reflection, the receivers record the energy of the seismic waves, obtaining the raw seismic data consisting in the variation of the amplitude with respect to time. We can see in Figure 1.7 a representation of how a multioffset acquisition is performed.

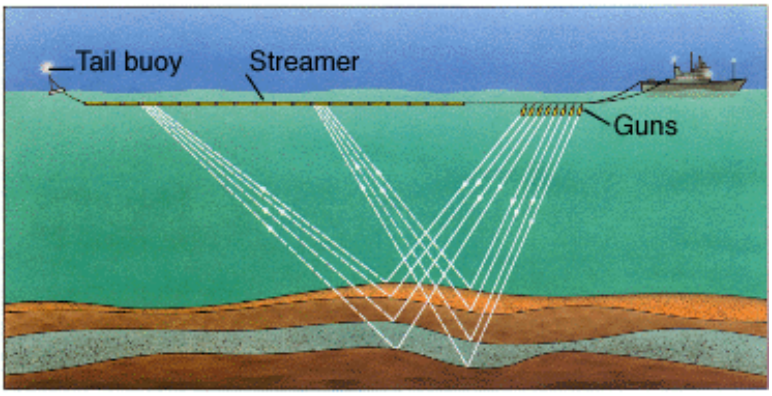

Figure 1.7. Representation of real seismic marine data acquisition. The seismic sources are generated by the airguns (on the right of the image). These sources propagate through the water, and they arrive to the ocean bottom sediments where they are refracted or reflected. The reflected energy travel back to the surface to arrive to the streamer, which is the cable that contains the receivers, in which the temporal signal is recorded. Taken from https://glossary.oilfield.slb.com

There are two types of seismic methods according to the type of data to be studied (refracted and reflected data, see Figure 1.8):

- **Seismic refraction:** Studies the refracted waves and more specifically the first arrivals of the refracted waves. This method could be applied to estimate the velocity of compression (V_P) of the layers. It is normally used in civil engineering to estimate the basement depth and for the determination of the conditions (weathering, fracturing) of the rock where the structures will be located.
- **Seismic reflection:** Focuses on the reflected waves, which are generated when the seismic wave travels through two regions with different impedances ($Z = \rho V$). The seismic reflection method has certain advantages over the seismic refraction method. For example, we can also estimate the shear wave velocity (V_S), we can explore complex geological areas (salt domes or steeply inclined interfaces), and we can increase the exploration depth. However, the processing of these data is more complicated than for refraction data.

The Figure 1.8 shows the differences between the acquisition of reflected and refracted data.

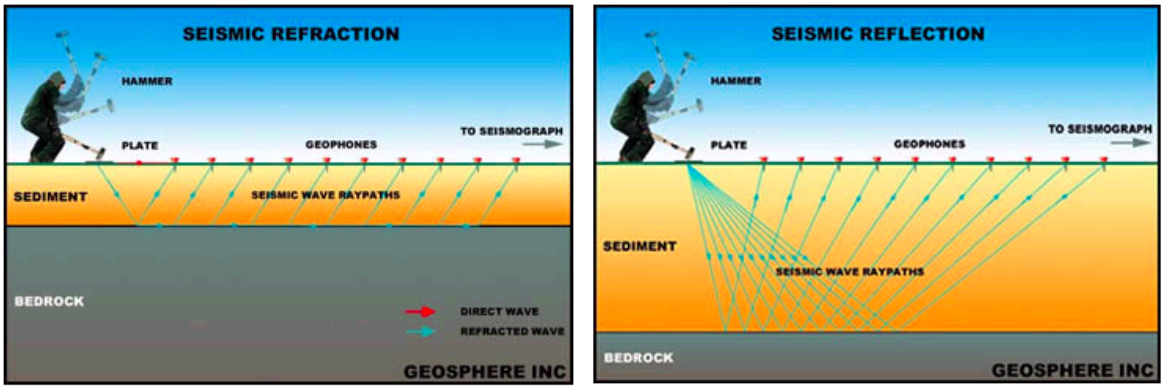

(a) (b)

Figure 1.8. Different types of seismic methods depending on the waves analyzed. In Figure (a), we analyze the refracted wave. In case the angle of incidence of the wave is the critical angle, the wave will propagate through the surface of the bedrock and then will return to the surface. In figure (b), we analyze the reflected wave. Seismic waves propagate through the sediment, and when they arrive to an interface marking a boundary between two different impedances, the waves will reflect and return to the surface. The seismic source is generated here by hammer but it can also be generated by other sources (explosive charges, vibrators, airguns, waterguns, etc). Taken from https://earthquake.usgs.gov.

Different survey designs are available depending on the goals and costs of the study. They could be divided in land and marine surveys.

In land surveys, the sources could be:

- Explosive sources: in most cases dynamite is preferred. They must be buried to increase the signal transmitted to the subsoil. They are generally considered as isotropic.
- Vibratory sources: Generally consisting in vibroseis trucks, which contain a heavy mass that vibrates vertically on a base plate to transfer energy into the subsurface.
- Weight drops: An example of these sources is a sledge-hammer hitting a metal plate on the ground. These types of sources are used in shallow subsurface studies due to their low energy generated (generally considered as isotropic sources).

In marine surveys the sources could be (they are generally considered as compressional isotropic sources):

- Airguns: they are metal cylinders through which high pressure air is forced through and into the water column where it creates a pressure pulse. They are the most used sources among the marine sources.
- Sparkers: they generate a pressure pulse in the form of a bubble by discharging an electrical current into the water.
- Boomers: they generate the pressure differential mechanically. They are used for shallow surveys.

There exist 2-D and 3-D surveys. In 2-D surveys, the array of sources and receivers follows a line in which sources and receivers are placed. While in 3-D surveys sources and receivers are placed in a “rectangular area", generally along parallel lines. In case of marine surveys, sources and receivers could be placed at both the surface or at the bathymetry, in which case it is called Ocean Bottom Survey (OBC).

There also exist the Vertical Seismic Profiles (VSPs), in which receivers are located along a vertical line into a well. A source is placed near the wellhead. The advantages of the VSPs are that the full wavefields (both up and down going waves) are recorded and give more information on the seismic properties at depth.

- **Processing**: Seismic data processing involves all the processing performed on the raw data to elaborate the seismic images of the subsurface. This stage consists of several individual steps. The number of steps and the order in which they are performed vary according to the method used. However, some references in the literature (Yilmaz [2001]) usually follow the order shown in the flow diagram shown in Figure 1.9. We describe these steps in the next paragraphs.

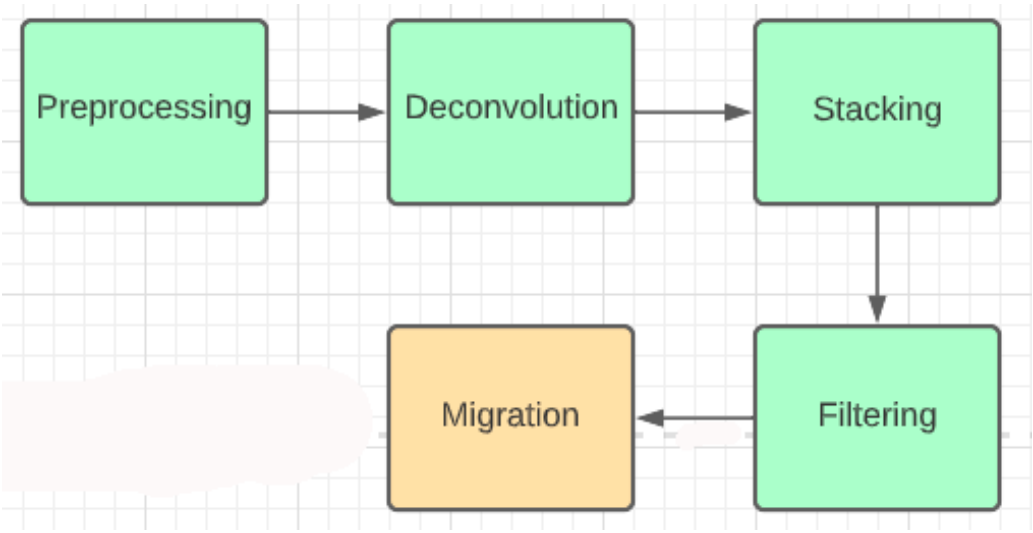

Figure 1.9. Principal processing steps.

  - **Preprocessing**:The data are converted to a convenient format for the next processing steps. Preprocessing also involves trace editing, where noisy traces could be eliminated. Gaining also could be performed at this stage, which involves amplitude compensation due to geometric dispersion (the amplitude of the signal decreases as the distance between sources and receivers (offset) increases) [Yilmaz, 2001].
  - **Deconvolution**: To better understand the principal idea behind the deconvolution process, we should present the convolutional model of the Earth:

$$x(t) = w(t) * e(t) + n(t), \tag{1.1}$$

where $x(t)$ is the recorded seismogram, $w(t)$ represents the basic seismic wavelet (the amplitude of the seismic source in time), $e(t)$ is the earth's impulse response, $n(t)$ is the random ambient noise, and the symbol * denotes the convolution. The equation 1.1, expresses what happens in a real seismic survey to obtain the recorded seismogram $x(t)$. We should notice that with the exception of the recorded seismograms $x(t)$ we don't know exactly the earth's impulse response, the seismic wavelet nor the ambient noise. However, if we assume that the noise component $n(t)$ is zero, and that the wavelet source $w(t)$ is known, the equation 1.1 reduces to: $x(t) = w(t) * e(t)$, which in the frequency domain is expressed as: $X(\omega) = W(\omega)E(\omega)$. Therefore:

$$E(\omega) = \frac{X(\omega)}{W(\omega)}, \tag{1.2}$$

where the equation 1.2 could be seen as an inverse filter. We can therefore say that the deconvolution process consists in removing the source effects from the recorded seismograms by using inverse filtering technique. In other words, we are reducing the source to an impulse to avoid that the shape of the original source has an effect on the data. The deconvolution process could be resumed by the next flowchart:

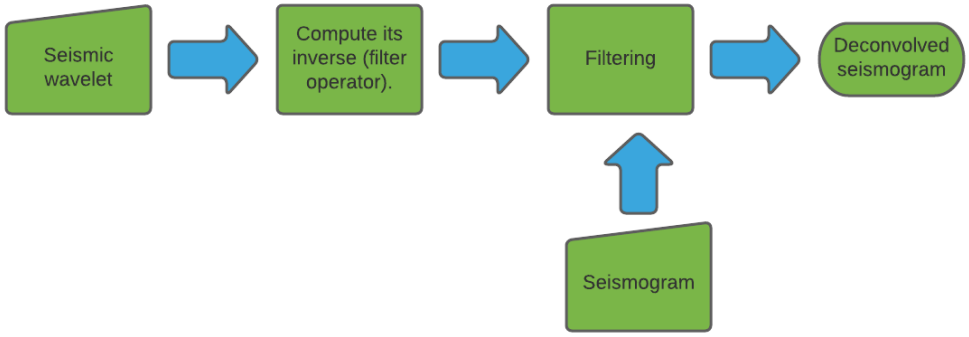

Figure 1.10. Flowchart of the deconvolution process.

– **Stacking**: As in the case of the deconvolution process, stacking involves many stages. The objective of these stages is to correct the data from the offset influence (distance between source and receiver). To better understand the idea of the stacking process, we first should know the Common Midpoint data format. Generally the stacking process starts from a Common Midpoint gather. We can see an example of this configuration in Figure 1.11(a). It is called Common Midpoint gather because in case of an idealized horizontal layer, all the reflections points coincide at the same point for all source-receiver pairs.

  In Figure 1.11(b) we can see the recorded seismic traces, where arrival times along the offset direction denote an hyperbolic trajectory as follows: $t(x)^2 = x^2/v^2 + t(0)^2$, where $t(x)$ is the arrival time in function of the offset x, v is the velocity of the

layer above the reflector, and $t(0)$ is twice the time recorded between the common midpoint and the common depth point (Figure 1.11(a)).

The Normal Moveout correction (NMO) consists in correcting the influence of the offset in the arrival times as follows: $t(0) = \sqrt{t(x)^2 - x^2/v_{NMO}^2}$, where v_{NMO} is the NMO velocity, which should be obtained by either a priori model or by estimations. In more complicated geologies (in presence of dip reflectors) the NMO correction changes. We refer to Yilmaz [2001] for more detail.

After the NMO correction the seismic traces look as in Figure 1.11(c), where the arrival times look as an horizontal line. Finally all the traces that correspond to the same common depth point are stacked to obtain a single trace (Figure 1.11(d)). We can say that the main benefit of the stacking process is to highlight the SNR due to the sum of the traces. In Figure 1.12 we present a summary of the stacking stages.

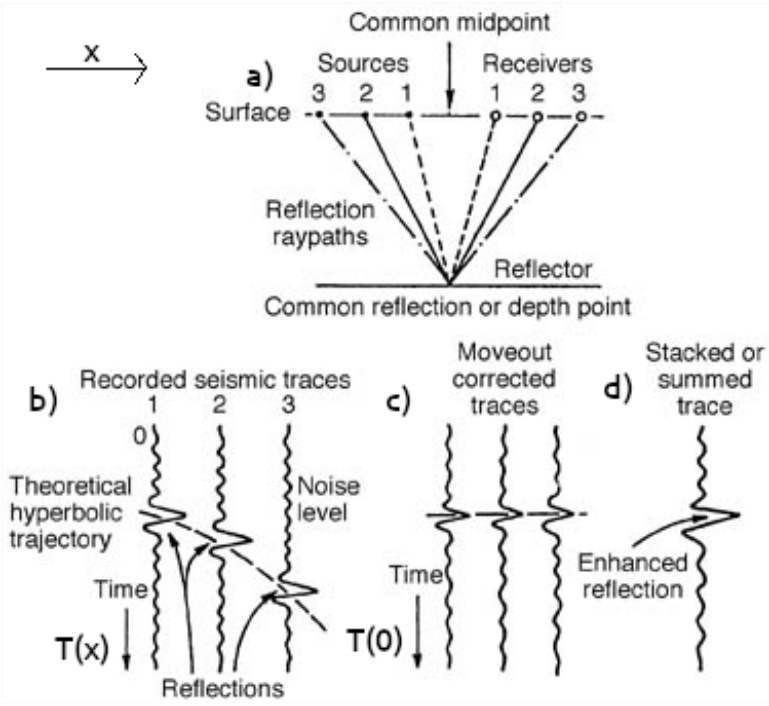

Figure 1.11. Example of a CMP gather (a). With the raw recorded seismic traces (b). After moveout correction the seismogram traces look as in Figure (c). Finally we obtain a single trace (Figure (d)) after stacking all the moveout corrected traces. In all the Figures the horizontal axis is represented by the offset (x). In Figure (b) the time depends on the offset T(x). However in Figures (c) and (d) the vertical axis represents the zero offset time (T(0)). Modified from https://glossary.oilfield.slb.com

– **Migration**: It is a reflectivity-based technique and is an essential process because in the stacked section, the position of the geological structures and interfaces (faults, anticline, sincline, oil reservoir) are not located at their true position. Migration process also increases spatial resolution and collapses diffractions. Earlier migrated images were presented in time domain (to be compared with the stacked section [Yilmaz, 2001]. We can see in Figure 1.13 the original idea behind the migration. For example in Figure 1.13(a), we can see an explosive inclined reflector. This is

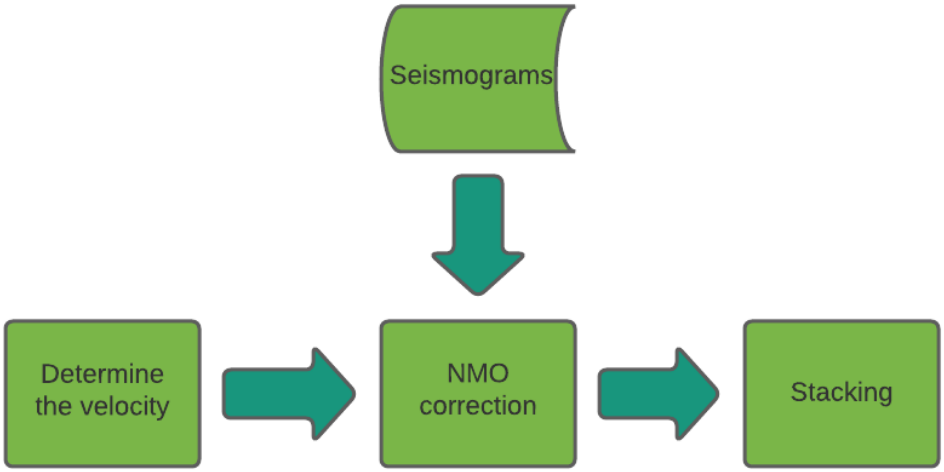

Figure 1.12. Stacking stages.

an idealized concept in which we imagine that we have sources along the reflector (blue circles) that travel to the surface receivers (red circles). In Figure 1.13(b) we have a zero offset section. This means that sources and receivers are located at the same position (red circles) (we can approximately arrive to this configuration after stacking). In Figure 1.13(c) we can see that the real angle of inclination of the reflector (blue line) is different from the angle obtained by the zero offset section (green line). The objective of the migration is to collapse the structures to their real position. We will discuss deeper the migration process and the different approaches related to it in the next subsection .

- **Interpretation**: Finally when we were able to obtain a good seismic image of the subsurface, we arrive to the interpretation of seismic images. This step consists in the application of geological knowledge of the principal features of seismic images.

In this project we focus on the migration process of seismic raw data. As we will see later, there are several types of migration processing methods. Among them, the Reverse Time Migration (RTM) is the mostly used technique nowadays for complex geological areas and has been improved in the last decades to attenuate multiples.

1.3.1 State of the art of the seismic imaging techniques.

Seismic imaging, which involves the location of geologic interfaces from exploration seismic data, has historically been related to the migration process. The migration process is the last step in seismic data processing before interpretation. Because of this, it is a process that has received significant attention in the context of seismic exploration methods. In addition, due to its complexity, it requires more computing power than other seismic data processing steps.

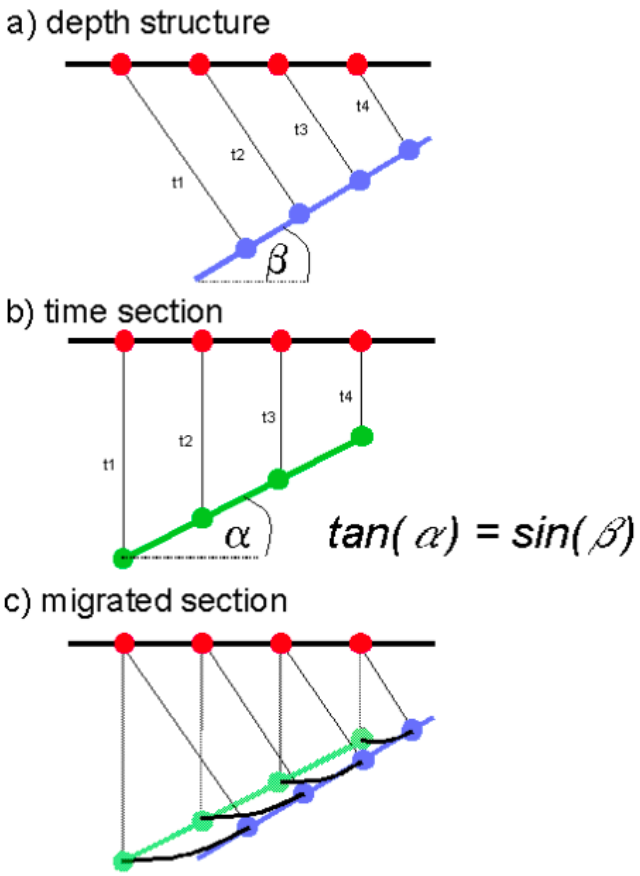

Figure 1.13. In Figure (a), we see a real dip reflector represented by the blue line with "imaginary" sources (blue circles) along it. These sources are propagated to the real receivers (red circles located at the surface). The angle between the dip reflector and the horizontal is β. In Figure (b) we see the zero offset section of the dip reflector of Figure (a), where the inclination angle is α. In Figure (c) we see the migration process that sets the location of the dip reflector at its true position. Taken from http://www.xsgeo.com/course/mig.htm vers. 1, released 29/01/1999

Indeed, in Robinson and Enders [1983] and Telford et al. [1990], seismic migration and seismic imaging are treated as the same process.

According to Sheriff [2002], the migration is a reflectivity technique defined as an inversion operation involving rearrangement of seismic information elements so that reflections and diffractions are plotted at their true locations. We have shown in Figures 1.13 the original idea of the migration. In other words migration could be seen as a transformation from the time domain to the depth domain in which interfaces "migrate" to their original position.

To talk about the first works of migration, we can go back to Claerbout's works, where he talks about finding a reflector map, whose purpose is to indicate the location of the reflectors. In [Claerbout, 1971], is discussed a comparison between real data and synthetic data obtained through a prior model, and even it is mentioned the possibility of improving the prior model in an iterative process. These ideas can be considered as precedents to the RTM and LSRTM. These two last techniques have been developed in more detail in later years.

In the literature we can refer to two different image reconstruction approaches: classical and modern approaches. The classical approaches refer mainly to methods based on ray tracing

(Eikonal equation), among which we find:

- **Zero offset migration.** The Figure 1.13 shows its principle. As we have explained earlier, in a constant velocity medium as shown in (Figure 1.13(a)), we can see the direct path in which the seismic energy travels from the dip reflector with an angle β. In this figure the vertical axis represents depth. In Figure 1.13(b) which represents a zero offset section (vertical axis represents time), the angle α is different from β ($\beta > \alpha$).

  Generally it is performed after stacking process (Poststack migration). However if the stacking process does not produce good zero offset data, this migration process is performed before the stacking process (Prestack migration), which involves a higher computational cost than the poststack migration.

- **Time and depth migration.** Time migration is performed if the horizontal gradient of the velocity model is not too strong. However, if the horizontal gradient of the velocity is high, the time migration can't correct the positions of the reflectors and for this reason the depth migration must be calculated [Yilmaz, 2001]. For the migration process to be correct (that is to say equal to Figure 1.13(a)), the vertical axis of Figure 1.13(b) must be transformed in depth and it requires a knowledge of the velocity field (in order to convert from the recorded time section to the migrated depth section).

- **Kirchoff migration.** One of the most widely used methods in earlier years is the Kirchoff migration, which solves the wave integral equation along diffraction curves (Schneider [1978], Bevc [1997], and Hokstad [2000]). The main idea of this method is that hyperbolas in the offset-time domain become semicircles in the spatial domain. Basically Kirchoff migration consists of the sum of amplitudes along the hyperbolic diffraction curves in the offset-time domain and their corresponding mapping in the spatial domain. In Figure 1.14, where red points represent sources and receivers, the green points and lines represent the offset-time domain (non-migrated) events, and the blue points and lines represent the migrated events. We present some examples of what is performed in the Kirchoff migration. For example in Figure 1.14(a) we can see how the green point (before migration) has migrated to a semi-circle in the migrated section. In Figure 1.14(b) we can see that a diffraction (green hyperbola) of the non-migrated section, is collapsed to a blue point in the migrated section by summation of amplitudes along the hyperbola. The blue point is located at the intersection of all the black circles. Finally in Figure 1.14(c) we see a dipping green event that is migrated to its correct location at the blue line. We can conclude that the zero offset section is considered to be constructed by a superposition of diffractors that form a coherent event in the offset-time domain. When there exists a discontinuity in the spatial domain, this effect would be reflected as an hyperbolic diffraction in the time domain as in Figure 1.14(b). However, when there is a continuous structure in the spatial domain, it would be reflected as a coherent event in time domain as in Figure 1.14(c).

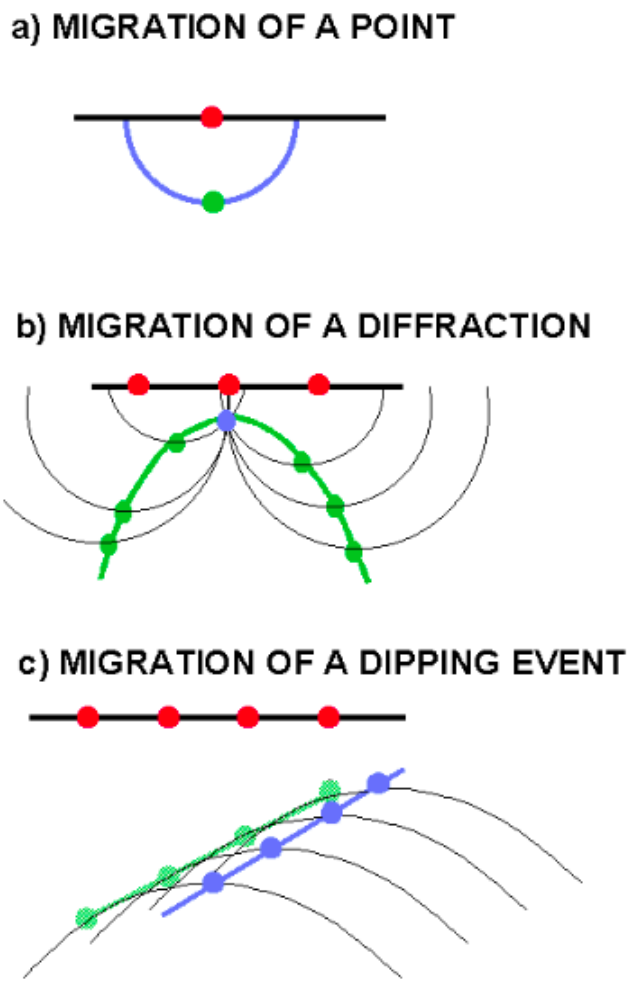

Figure 1.14. Red points represent the position of sources and receivers, the green points and lines represent the non-migrated offset time domain events, and the blue points and lines represent the migrated events. Migration of a point (Figure (a)), migration of a diffraction (Figure (b)), and migration of a dipping event (Figure (c)). Taken from http://www.xsgeo.com/course/mig.htm vers. 1, released 29/01/1999

Thanks to the work done by Tarantola and Valette [1982] and Lailly and Bednar [1983] there has been an important transition to modern approaches which are based on the solution of the full waveform and the adjoint methods. Among these modern approaches we could find the Reverse Time Migration (RTM), the Least Square Reverse Time Migration (LSRTM) and the Full Waveform Inversion (FWI), these two last methods being data inversion-based methods:

- **Reverse Time Migration (RTM).** Thanks to the advancement of computer technology, it has been possible to implement imaging methods that involve the full wave equation resolution on large volumes of data, such as the Reverse Time Migration (RTM) method. Among the first works of this method we can find Baysal et al. [1983] and McMechan [1983]. The original concept of the RTM relates to the transformation of seismic information from the time domain to the depth domain. The RTM is based on computing reflectivity images that aim at detecting the main interfaces of the model that reflect and scatter a maximum of energy (this is strongly related to impedance, because

the energy increases as the difference between the impedance of two adjacent layers increases). Depending on the radiation patterns of P and S waves, their interactions and phase conversions at the interfaces, reflectivity images corresponding to high wave number "model perturbation" of a smoothed background model can be recovered. Depending on the parametrization chosen we might recover much better the interfaces. According to Feng and Schuster [2017] the P and S waves impedance reflectivity images reduce crosstalks due to scattering radiation patterns are more dissimilar than those related to Lamé parameters λ and μ. In other words, the P and S impedance reflectivity images allow to separate much better the phases and wavelengths compared to V_p and V_s (or λ and μ). We can see in Figure 1.15 the flowchart of the RTM process to obtain the reflectivity images. We start from a background model and calculate the forward problem using this model to obtain the predicted data. Then we compute the adjoint problem by using a source that is the difference between the real and predicted data. Finally we compute the imaging condition by correlating the back-propagated field with the adjoint field to generate the reflectitivy images. We refer to Chattopadhyay and McMechan [2008] and Zhang and Shi [2019] for a more extensive study on the imaging condition.

In recent years, improvements have been made to the RTM method. For example it is well known that in visco-elastic media when calculating the image condition with the classical approach, instability in the solution occurs. That is why in Wang et al. [2018] an adaptivity stabilization method for Q-compensated RTM is proposed.

In addition, the Reverse Time Migration of multiples method has been developed, which exploits the fact that the multiples travel through regions of difficult access that the primary signal cannot reach. Because of this, this method has been successfully applied in regions of complex salt tectonics. For more information on these methods we refer to Liu et al. [2011], Wang et al. [2017].

- **Full Waveform Inversion (FWI).** The FWI method is an iterative non-linear full waveform inversion method that consists in finding the model parameters $\mathbf{m}$ that minimizes the misfit function χ defined as:

$$\chi = \frac{1}{2}||\boldsymbol{Lm} - \boldsymbol{D}||^2, \tag{1.3}$$

where $\boldsymbol{Lm}$ means in simple words that the elastodynamic wave equations are applied to the parameters $\boldsymbol{m}$ (forward problem), and $\boldsymbol{D}$ represents the real data (Lailly and Santosa [1984], Tarantola [1984], Mora [1987], Pratt et al. [1996], Virieux and Operto [2009]). We look at this function with more detail later.

Among the methods to minimize the misfit function in the context of FWI, we find: the steepest descent method (Yang [2021], Ren [2022]), the pre-conditioned conjugate gradient method (Yang et al. [2015a], Pan et al. [2017]), or the truncated Newton method (Métivier et al. [2013], Métivier et al. [2017]).

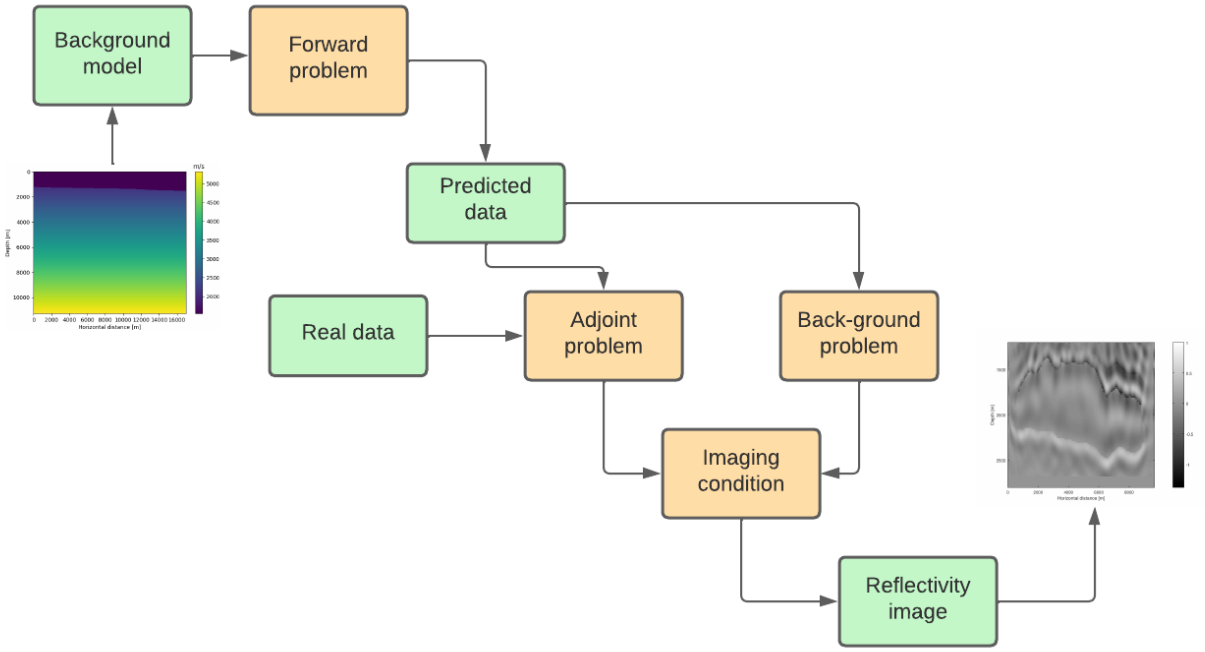

Figure 1.15. Flowchart of the RTM process. Starting with an a priori model with low frequencies and ending with a reflectivity image where high frequencies are highlighted.

In salt domes seismic imaging context, the FWI has been applied to real data with success in recent years. In Shen et al. [2017] FWI was applied in wide-offset ocean-bottom-node data over Atlantic Field in deep water Gulf of Mexico, where they demonstrated that with a low-frequency long offset data, FWI can correct major error in the salt dome definition. In Wang et al. [2019] FWI is applied to wide and full azimuth streamer data and ocean-bottom-node (OBN) data from the Keathly canyon, where they demonstrated that FWI is able to build complex salt velocity models with different types of input data including wide and full azimuth streamer and (OBN) data.

The FWI continues to be a technique widely used recently. However, it has a high computational cost in 3D problems and depends heavily on the initial model. This is why in the context of FWI inversion of salt dome models, deep-learning based inversion methods have been also proposed. In Sun et al. [2020] a recurrent neural network (RNN) has been developed and compared to the Conjugate Gradiend and l-BFGS methods, in which RNN is more stable. In Ren et al. [2020] they proposed a seismic waveform inversion network (SWIN) resulting in good velocity inversion and fast convergence. In Liu et al. [2021] they proposed a P-wave velocity model building method in the common-shot gather and common-receiver gather.

- **Least Squares Reverse Time Migration (LSRTM).** The LSRTM method is a linearized inversion method that consists in finding the reflectivity model $\boldsymbol{r}$ that minimizes

the misfit function χ defined as:

$$\chi = \frac{1}{2}||\boldsymbol{Lr} - \boldsymbol{D}||^2, \tag{1.4}$$

where $\boldsymbol{L}$ is here a demigration operator, $\boldsymbol{r}$ is the reflectivity image, and $\boldsymbol{D}$ represents the observed data. The conventional RTM is the first approximation of the LSRTM reflectivity model $\boldsymbol{r}$, which is used to generate the synthetic data $\boldsymbol{Lr}$ (Wong et al. [2011], Dai et al. [2012], Dong et al. [2012], Stanton and Sacchi [2014] Zhang et al. [2015]).

LSRTM is not a characterization method like FWI because it aims to invert the reflectivity model, but due to its linear nature LSRTM converges faster than FWI. However, in 3D media the computational cost remains quite high. That is why in Dai et al. [2012], Dai and Schuster [2013b] linear phase shift encoding is applied to inject simultaneous sources with cross-talk reduction as well as reduction of computational time.

In Zhang and Schuster [2014] the LSRTM of multiples (LSRTMM) are applied to the 2D synthetic model Sigsbee 2B, in which by using free-surface multiples they suppress the cross-talks in the final image and correct for source statics. This correction is related to the near surface velocity anomalies beneath the source or receiver. However, with strong cross-talk noise and imperfectly separated data, synthetic tests have demonstrated that LSRTMM does not have significant advantages compared to RTM.

Up to that time the LSRTM had worked mainly with acoustic rheology. Then, in Dutta and Schuster [2014] and Dai et al. [2015], the LSRTM is applied in a visco-acoustic rheology context, where some improvements over the reflectivity images have been reached due to attenuation implementation. In Ren et al. [2017], Feng and Schuster [2017] an elastic-rheology LSRTM is implemented, generating reflectivity images with fewer artifacts, better amplitude balancing and higher resolution compared to acoustic LSRTM. Finally in Guo and McMechan [2018] a visco-elastic rheology is applied using the generalized Zener standard linear solid model, in which they found that visco-elastic LSRTM has stronger and more continuous amplitudes for the structures in and beneath low-Q zones.

A deep learning approach has been proposed by Zhang et al. [2022] in the context of the LSRTM method. They introduce the convolutional neural network (CNN) for the pre-stack LSRTM. They tested this method in the complex synthetic Marmousi-2 model obtaining high quality subsurface images at a low computational cost.

1.3.2 Techniques used in this work.

For the first objective of this work we implemented the RTM over a synthetic model in an acoustic rheology. We test two types of a priori information: a gradient-based model, where the properties of the medium increase with depth, and a smoothed-model, where a Gaussian filter

is applied to the true model. We also test different ways to preconditionate the migrated image in order to see better the deep interfaces: Preconditioning by the forward or adjoint energy, pseudo-hessian, or depth weighting (i.e a depth dependent weighting function is applied to the model perturbations or the model regularization terms to increase the model resolution at depth). In our study, the best way to preconditionate the migrated image is by using the forward energy. We also test different ways to parameterize the migrated image: (ρ, λ, μ), (ρ', V_P, V_S), or (ρ'', Z_P, Z_S), where λ and μ are the Lamé coefficients, V_P and V_S represent the P and S velocities and Z_P and Z_S represent the P and S impedances, while ρ, ρ' and ρ'' represent the density associated to the parametrizations of Lamé coefficients, velocities or impedances respectively. In our studies all the different parametrizations behave in a similar way.

In Figure 1.16, we describe the whole process that we have implemented in this project for the second objective (WAVES model). After having filtered the real data, we perform an iterative process to minimize the misfit function (equation 1.6). This iterative process is composed by two successive steps:

- First we improve the background model by applying the steepest descent method in which we test several step lengths to see if they satisfy the first Wolfe condition. We choose the step length that minimizes the misfit function. The search direction is obtained by computing the gradient of the misfit function (RTM) associated to the background model and we precondition it by the forward energy. We use the step length and the search direction to obtain the model 1.

- Then we improve the model 1 by applying the non-linear conjugate gradient method in which we test several step lengths to see if they satisfy the two Wolfe conditions, and we choose the step length that minimizes the misfit function. To compute the search direction we calculate the gradient of the misfit function (RTM) associated to the model 1 and we precondition it by the forward energy. We use the step length and the search direction to obtain the model 2.

After several iterations of this whole iterative inversion process, the model images are getting better from the low to the high wavenumber model perturbations. In this way FWI (and also the RTM) is also a process based on separation of scales.

1.3.3 Thesis structure.

Apart this current chapter which consists of the general introduction, this thesis is organized in 4 chapters.

The chapter 2 contains the description of the equations governing the wave equation for elastic and viscoelastic rheologies. We also describe the classical and adjoint-based RTM method with the computation of the sensitivity kernels. We continue by describing the iterative LSRTM and FWI methods. We also describe the numerical methods used to solve the equations

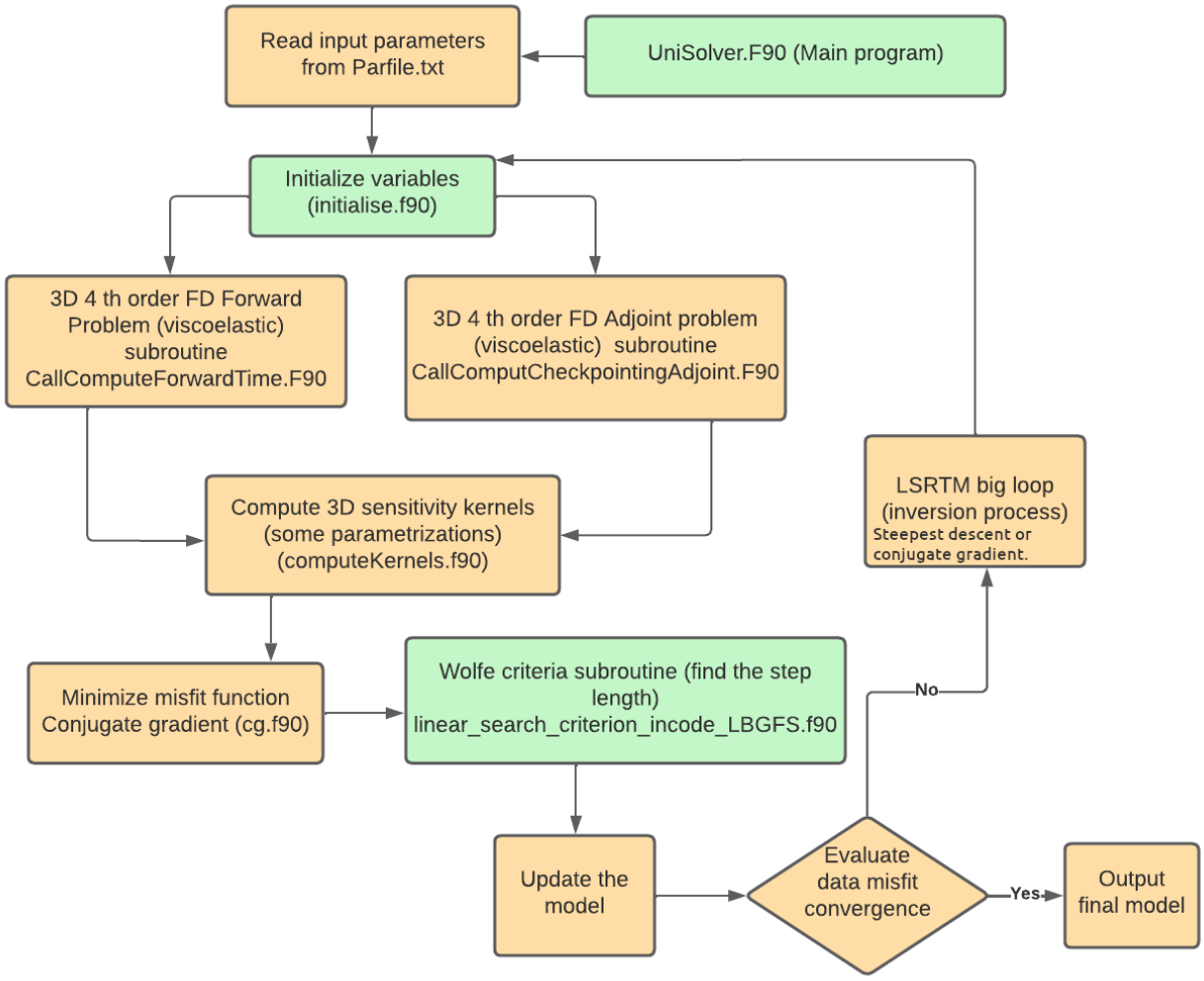

Figure 1.16. Flowchart of the whole process that we use in this work, including the LSRTM process. The flowchart of the Figure 1.15 is repeated many times as needed in the calculation of the sensitivity kernels until reduction of the data residual misfit function.

described previously. We focus principally on the finite differences method (implemented at 4-th in space in this work) but we also present a brief description of the finite element method in the appendix D. After that, we present the spatial and time discretization we used, including the dispersion and stability conditions that must be satisfied. We also present the CPML absorbing boundary conditions we used to avoid numerical artifacts at the computational domain outer boundaries. Then we show the computational checkpointing scheme, which is necessary to solve the time reversal viscoelastic wave equations without numerical instabilities and thus to enable the calculation of the sensitivity kernels in presence of attenuation. Finally we briefly describe the origin of the multiple contamination in the image conditions and sensitivity kernels.

The chapter 3 contains all the process to obtain the seismic images from the 2D synthetic data built on the interpretation of seismic data recorded in the Gulf of Mexico. We present in this chapter the 2D elastic wave equations, we follow a similar approach as in the chapter 2. However in this chapter we include the different parametrizations that could be implemented to construct the reflectivity images. Moreover, we present an analysis of the physical implications of the imaging condition (correlation between the back-propagated and adjoint wavefields). We show our results by using 4 background models (a priori models), and we discuss the contribution of the density (K_ρ) or compressional (K_{Vp}, K_λ or K_{Zp}) kernels for different model parametrizations to the different (low to high) wavenumbers recovery. We also add in this chapter images obtained from 3D synthetic data using the same 2D model lengthened in the transverse direction to obtain a 3D model. The 2D results of this chapter were computed by using a parallelized FORTRAN-90/2008 code while the 3D results are obtained with the fourth-order finite difference UNISOLVER parallelized code. Both 2D and great part of the 3D codes have been developped by Javier Abreu-Torres.

The chapter 4 contains the results obtained from the zero offset and multioffset data taken from the real data set of the 3D WAVES experiment provided by our colleagues of the LMA in Marseille (B. Solymosi, Nathalie Favretto-Cristini, Vadim Monteiller and Paul Cristini). First of all, we describe the dimensions and the measured properties of the materials used to construct the WAVES model. Then we show the sources and receivers that were implemented in this experiment. After that, we show the spatial and time discretization, the adaptation of the data (interpolation and filtering), and the calibration of the properties of the materials we apply. Then we present the RTM kernels obtained by using the zero-offset data with and without attenuation, as well as the model properties and reflectivities obtained after FWI around a low frequency background a priori model. To obtain the results of this chapter we use the 3D parallel UNISOLVER code (mainly written in Fortran2013 and parallelized using MPI/Message Passing Interface libraries), in which I participated by implementing and parallelizing the fourth-order finite difference scheme in parallel (the code was previously at 2nd order in space), the viscoelastic wave equations and some other subroutines like those related to the sensitivity kernels computation, the preconditioning calculations and the FWI process : we could find some examples of these routines in the appendices A, B, and C.

Finally in the chapter 5 we present the general conclusions and perspectives.

1.4 Introduction (en français)

Dans le contexte de la tectonique du sel, en utilisant des techniques de réflectivité avancées comme les techniques de *Reverse Time Migration* (RTM) ou de *Full Waveform Inversion* (FWI), la communauté des géologues et des géophysiciens vise à reconstruire les structures tectoniques du sel et les structures géologiques sous les dômes de sel qui pourraient piéger des ressources comme les hydrocarbures, le gaz naturel ou le sel lui-même. Ici, nous visons à retrouver la structure des dômes de sel (haut et bas) et les interfaces qui les entourent en validant et en utilisant des outils d'imagerie sismique similaires que nous avons développés pour étudier les deux cas spécifiques suivants:

- Récupération du sommet et du fond d'un dôme non diapirique et des interfaces géologiques qui l'entourent à partir d'un modèle synthétique dans le Golfe du Mexique.
- Récupération du haut et du bas d'un dôme de sel diapirique et des interfaces qui l'entourent à partir du modèle expérimental WAVES à l'échelle du laboratoire (grâce aux données et aux analyses précédentes fournies par nos collègues du LMA/Laboratoire de Mécanique et d'Acoustique de Marseille).

Nous avons également étudié trois questions importantes en imagerie sismique (la paramétrisation, le préconditionnement et le modèle a priori) afin de récupérer la structure du dôme et les interfaces sous le dôme. Nous avons analysé ces questions dans un modèle synthétique et les avons appliquées au modèle expérimental (WAVES).

Nous discuterons plus en détail de ces objectifs dans la section 1.2. Nous allons maintenant aborder le contexte géologique de ce travail.

1.4.1 Contexte géologique

a) Contexte de la tectonique saline : Importance de son étude.

Dans le contexte des sciences de la Terre, le sel gemme est un agrégat cristallin du minéral halite (NaCl) [Hudec and Jackson, 2007]; il s'agit d'un agrégat d'halite. Toutefois, dans la littérature, il est courant d'utiliser le terme "sel" pour désigner toutes les roches composées principalement d'halite. L'étude des bassins et des structures des dépôts de sel est devenue très importante depuis le milieu du 20ème siècle dans l'industrie pétrolière car selon Warren [1989] "environ 70% des champs pétroliers géants du monde dans les roches carbonatées ont un rapport avec les évaporites (Zhang Vi-gang 1981) et tous les champs de gaz géants dans les ceintures de chevauchement ont un joint d'évaporite (Downey 1984)". Les systèmes pétroliers sont essentiellement constitués de:.

- Roche mère: Présence de matière organique à une température et une pression déterminées pour "mûrir" la roche et générer des hydrocarbures.

- Roche réservoir: Elle présente une porosité suffisante pour stocker les fluides (généralement des roches sédimentaires). Les hydrocarbures sont transmis aux roches réservoirs depuis la roche mère par le processus de migration.

- Roche de couverture: Il s'agit d'une roche imperméable, qui empêche les hydrocarbures de migrer (roches salines).

Pour trouver l'existence d'un système pétrolier, l'existence et l'interaction des types de roches susmentionnés sont cruciales. Si l'on se concentre sur les roches étanches, les structures salines, en raison de leur imperméabilité, sont les roches étanches les plus courantes. Pour des raisons économiques pertinentes, de nombreuses études ont été menées pour connaître l'emplacement et la délimitation de ces corps.

En outre, dans Escalona and Mann [2006] décrit la formation des systèmes pétroliers du bassin de Maracaibo, qui a été contrôlée par des événements tectoniques, influençant la génération, la migration et l'accumulation des hydrocarbures. Dans Pilcher et al. [2011], les bassins primaires du nord du Golfe du Mexique, qui forment des successions stratigraphiques dans le sel allochtone, sont décrits. Ces environnements géologiques présentent toutes les caractéristiques d'un système pétrolier (roche mère, roche d'étanchéité et roche de stockage).

Cependant, il convient de se demander si l'étude des dômes de sel restera pertinente compte tenu de la diminution de la production de pétrole dans le monde et des problèmes environnementaux dus à l'extraction du pétrole. Grâce au développement des techniques d'injection de CO_2 qui ont gagné en pertinence ces dernières années (Yu et al. [2015], Jia et al. [2019], et Janna et al. [2020]), les études sur les dômes de sel continuent de susciter de l'intérêt. Selon Jia et al. [2019] l'injection de CO_2 est une méthode prometteuse pour rajeunir les réservoirs de pétrole de schiste après la production primaire. Cette étude a été appliquée dans la partie nord du Golfe du Mexique (une région à forte tectonique saline). L'un des avantages de l'injection de CO_2 est la réduction des gaz à effet de serre par la séquestration du CO_2 (Janna et al. [2020]). En outre, les dômes de sel sont considérés comme des sites potentiels pour le stockage de l'hydrogène (Karnkowski and Czapowski [2007], Tarkowski and Czapowski [2018]), qui constitue une alternative moins polluante aux combustibles fossiles.

1.4.2 Les structures des sels et leur formation

La formation de grands dépôts de sel commence dans les régions subtropicales chaudes et sèches du monde (où l'évaporation de l'eau dépasse les précipitations). Cela se produit principalement dans les bassins sédimentaires fermés ou dans les mers intérieures protégées par des barrières naturelles. Dans ces régions, l'eau de mer s'évapore en laissant une saumure saturée.

Par la suite, les minéraux contenus sont précipités en fonction de leur solubilité dans l'eau, et les roches formées sont généralement appelées évaporites (carbonates, gypse, halite). En fait, l'évaporite la plus courante est l'halite (sel gemme). Les accumulations de sel peuvent dépasser

plusieurs kilomètres si le bassin est régulièrement rechargé en eau de mer.

L'une des caractéristiques du sel est qu'il est incompressible, de sorte que sa densité reste constante. Cette caractéristique est importante car, sur une période géologique de plusieurs millions d'années, de vastes zones de sel sont enfouies par les processus de sédimentation. Les sédiments adjacents qui enfouissent le sel ont tendance à augmenter en densité avec la profondeur. En conséquence, une inversion de densité se produit (des roches lourdes sur des roches plus légères). Ensuite, ces sédiments commencent à s'enfoncer dans le sel, le déplaçant vers le haut. Nous pouvons voir dans la Figure 1.1 cinq schémas représentant la formation des dômes de sel et de certaines structures salines associées à différents styles tectoniques et à d'autres phénomènes (érosion, différences de densité, compression, etc.). Pour plus d'informations sur la génération de structures salines, nous renvoyons le lecteur à Talbot and Jackson [1987], Hudec and Jackson [2007], et Belenitskaya [2016].

Dans la figure 1.2, nous pouvons voir les principaux bassins salins dans le monde. En Europe, nous trouvons le bassin de Zechstein en Pologne, qui est principalement exploré pour ses mines de sel et par dépôt d'hydrogène dans des cavernes rocheuses [Krzywiec, 2004; Tarkowski and Czapowski, 2018]. Dans la région du Moyen-Orient, nous trouvons la chaîne de montagnes de Zagros, qui est constituée de dômes de sel, avec la caractéristique d'affleurements salins en surface, ce bassin est également étudié pour les réservoirs d'hydrocarbures [Jahani et al., 2007, 2017; Talbot and Alavi, 1996]. En Afrique, on trouve le bassin salin d'Afrique de l'Ouest (du nord de la Namibie au sud du Cameroun). Ce bassin est principalement étudié pour les réservoirs d'hydrocarbures (Marton et al. [2000] et Tari et al. [2003]). En Amérique, on trouve le bassin du Golfe du Mexique, qui est très important dans l'exploration des hydrocarbures. Dans ce bassin salin, il existe deux grands types de structures salines : diapiriques et non diapiriques (Wu et al. [1990], Liro [1992], Reed [1994]). Here in our present work we will focus our attention on imaging and modelling these two types of salt domes.

Il est important de mentionner que l'importance économique de l'étude des dômes de sel ne se limite pas seulement à l'exploration pétrolière, mais aussi à l'exploitation du sel lui-même et à la recherche d'autres ressources qui sont également piégées par le sel, comme l'eau, l'hydrogène et le gaz naturel. C'est pourquoi il est très important d'estimer l'emplacement et le volume de ces corps. L'imagerie sismique est la méthode la plus utilisée à cette fin qui, grâce à sa profondeur d'investigation et à sa résolution dans les régions complexes, donne une bonne idée de ce que l'on pourrait trouver dans le sous-sol. Nous présentons donc ci-après une revue brève et non exhaustive des différentes techniques d'imagerie sismique et nous mentionnons également certains défis techniques et problèmes scientifiques à résoudre en imagerie sismique pour le cas spécifique de la modélisation des dômes de sel.

1.4.3 Problèmes scientifiques

Cependant, lorsque l'on veut représenter des régions présentant un tectonisme salin en utilisant la méthode sismique, il faut tenir compte de certains problèmes. D'après Ratcliff et al.

[1992] et Jones and Davison [2014a], certains de ces problèmes sont les suivants:.

- Capacité à décrire correctement la géologie à partir d'informations a priori de la région étudiée. Il s'agit d'avoir de bons modèles a priori à partir desquels on va commencer à récupérer les interfaces du milieu.

- Flancs fortement inclinés: Les flancs très inclinés sont difficiles à cartographier car les angles d'incidence des ondes sont proches de zéro degré par rapport aux flancs du dôme. Ceci fait qu'il y a des régions dans lesquelles les ondes sismiques arrivent à incidence rasante. Il est donc difficile de bien délimiter les flancs. Comme exemple de ce phénomène, voir la figure 1.3. C'est pourquoi il est important d'avoir un bon éclairage, ce qui peut être obtenu en augmentant les offsets (distance source-récepteur).

- Contraste d'impédance élevé: En raison du fait que le contraste d'impédance entre le sel et les sédiments adjacents est très élevé, les ondes sismiques sont "piégées" à l'intérieur des structures de sel, générant ainsi un nombre élevé d'événements multiples. Cela provoque des interférences entre les événements primaires provenant des événements sub-salins et les multiples internes de la structure saline. Par conséquent, les sédiments sub-salins sont difficiles à voir sur les images sismiques. Dans la figure 1.3 nous pouvons observer ce phénomène.

- Trajets complexes : Dans de nombreux cas, les trajectoires que suivent les vagues à proximité du dôme de sel sont très complexes. Cela produit une faible corrélation entre les données réelles et prédites, ce qui réduit la qualité de l'image dans ces régions. Les ondes prismatiques peuvent être générées par ces trajectoires complexes. Ces ondes sont réfléchies à deux interfaces le long du trajet de la source au récepteur, ce qui génère des artefacts parasites. Elles sont très courantes dans les régions dont les flancs sont fortement inclinés, comme les canyons (Deeks and Lumley [2015]) et les dômes de sel (Malcolm et al. [2011], Kudin et al. [2018]). Dans Malcolm et al. [2011], les auteurs ont constaté que les données enregistrées sur des récepteurs éloignés des structures inclinées permettent de traiter les ondes prismatiques. Dans les figures Dai and Schuster [2013a] et Kudin et al. [2018], ils utilisent des sources de Born pour générer des images d'ondes prismatiques permettant d'imager correctement les flancs des dômes de sel. Dans la figure 1.4, nous montrons le chemin de déplacement qui suit une onde prismatique dans un contexte salin-tectonique.

Cependant, les progrès technologiques dans le domaine de la tomographie sismique ont permis de développer des méthodes pour améliorer l'imagerie de régions géologiques complexes telles que les dômes de sel. Certaines de ces méthodes sont la Reverse Time Migration (RTM) [Chang and McMechan, 1986; Whitmore, 1983], et aussi des versions plus modernes comme la Least Squares RTM (LS-RTM) [Dai et al., 2010; Feng and Schuster, 2017] , qui a l'avantage d'impliquer les dernières avancées des techniques d'inversion de forme d'onde complète. Nous

avons résumé ces méthodes dans les sections précédentes et nous les aborderons plus en détail par la suite.

Dans la section suivante, nous présenterons les champs d'application de ce projet.

1.4.4 Scopus de l'étude

Dans ce travail, nous traiterons de l'imagerie sismique de deux types de structures que nous pourrions trouver couramment dans le monde comme dans le Golfe du Mexique (Wu et al. [1990], Liro [1992], Reed [1994]) : les corps salins diapiriques et non-diapiriques, dans lesquels nous cherchons à récupérer la base du dôme et les interfaces sous le dôme. Ceci est intéressant car comme mentionné dans la section 1.1.1 généralement les hydrocarbures sont piégés sous les structures de dômes de sel. Nous choisissons ces objectifs pour commencer par l'imagerie sismique 2D de structures simples non diapiriques (considérées comme moins compliquées car les sédiments adjacents ne présentent pas de courbure près des limites du dôme). Ensuite, nous travaillerons sur la structure saline diapirique du cas expérimental WAVES. Nous décrivons ci-après nos deux objectifs :

- **Premier cas (dôme de sel non diapirique).** La première structure correspond à un dôme de sel, qui a été adapté à partir d'une interprétation réelle de données sismiques dans le Golfe du Mexique. Par adapté, nous voulons dire ici que nous nous sommes concentrés sur un seul corps salin parmi tous les corps originaux. Les données "réelles" sont générées à partir des modèles de densité et de vitesse Vp en deux dimensions, il s'agit donc ici d'une étude des données synthétiques et acoustiques. Dans la figure 1.5, nous présentons le modèle Vp synthétique complet et la structure de sel que nous avons sélectionnée. Dans un premier temps, notre défi ici consiste à définir la bonne paramétrisation pour calculer les images RTM, ainsi qu'une bonne façon de les normaliser pour réduire les artefacts dans les images et retrouver le fond et les interfaces sous le dôme.

- **Deuxième cas (structures de sel diapirique)** Le deuxième cas consiste à traiter des données expérimentales réelles obtenues au laboratoire LMA à Marseille (Solymosi et al. [2020]) afin de valider notre code d'inversion UniSolver pour l'imagerie et la caractérisation des structures salines diapiriques. Ce modèle expérimental, appelé WAVES, consiste en un volume 3D de verre cristallin très similaire à un dôme de sel, entouré de plusieurs types d'argiles et de résines pour imiter les sédiments adjacents que l'on trouve généralement autour d'un dôme de sel. De plus, de l'aluminium a été utilisé pour simuler le sous-sol. Le modèle a été immergé dans l'eau pour simuler une acquisition réaliste de données marines. Notre étude est complémentaire au travail de Solymosi et al. [2020]. Nous appliquons les techniques FWI pour reconstruire itérativement le modèle et les interfaces à partir du modèle WAVES de fond lissé, et améliorer les images de réflectivité. De plus, dans ce cas réel, des effets d'atténuation sont présents et nous visons maintenant à appliquer notre méthode de reconstruction à un milieu viscoélastique 3D, alors que la reconstruction

viscoélastique 2D a été faite précédemment pour ces données WAVES par Solymosi et al. [2020]. Comme Solymosi l'a fait en 3D, nous effectuons également une calibration des paramètres viscoélastiques mais sur des profils différents de ceux choisis par Solymosi et al. [2020]. En effet, dans notre étude nous voulons non seulement récupérer la base du dôme et les interfaces sous le dôme, mais aussi caractériser le modèle par FWI. Pour réaliser ces reconstructions nous considérons une ligne sismique différente afin de prendre en compte les effets 3D lors du processus d'imagerie.

Nous présentons donc ci-après une revue brève et non exhaustive des différentes techniques d'imagerie sismique et nous mentionnons également certains défis techniques et problèmes scientifiques à résoudre en imagerie sismique pour le cas spécifique de la modélisation des dômes de sel.

1.5 Imagerie de la croûte supérieure et de la proche surface.

L'objectif principal des méthodes d'exploration géophysique est d'estimer les valeurs des paramètres décrivant le sous-sol. En général, dans toutes les méthodes géophysiques, les processus d'estimation de ces paramètres du sous-sol sont représentés dans l'organigramme suivant de la Figure 1.6, où l'on peut distinguer trois étapes: l'acquisition des données, leur traitement et leur interprétation. Le traitement des données étant l'étape dans laquelle nous travaillons, nous le marquons en rouge pour le différencier des autres étapes. Nous ferons de même dans le reste du manuscrit.

Parmi toutes les méthodes d'exploration géophysique, la méthode sismique est la plus utilisée dans l'exploration des régions à géologie complexe en raison de sa capacité de pénétration (grande profondeur d'exploration), et parce que la capacité de réduire les échelles de longueur d'onde est accrue, ce qui augmente la résolution et la possibilité de mieux observer les interfaces. Selon Schuster [2011], la tomographie sismique est une procédure d'estimation des paramètres de la roche terrestre à partir de données sismiques. Ces paramètres sont normalement exprimés par la vitesse P et S et la densité, et représentés par des graphiques 2D ou 3D.

Dans les prochains paragraphes, nous aborderons les trois étapes de la Figure 1.6 dans le cadre de la méthode sismique:

- **Acquisition**: Les campagnes d'acquisition de données sismiques sont des projets de grande envergure réalisés à la surface de la terre ou en mer. De manière générale, elles consistent en un réseau de sources et de récepteurs dont l'emplacement dépend du type d'étude réalisée. La source est injectée artificiellement, générant une onde sismique qui se propage dans le sous-sol en traversant les différentes interfaces du milieu. Après plusieurs événements de réfraction et de réflexion des ondes, les récepteurs enregistrent l'énergie

des ondes sismiques, obtenant ainsi les données sismiques brutes constituées de la variation de l'amplitude en fonction du temps. Nous pouvons voir dans la figure 1.7 une représentation de la manière dont est effectuée une acquisition multi-offset.

Il existe deux types de méthodes sismiques en fonction du type de données à étudier (données réfractées et réfléchies, voir la figure 1.8):

- **La réfraction sismique**: Étudie les ondes réfractées et plus particulièrement les premières arrivées des ondes réfractées. Cette méthode peut être appliquée pour estimer la vitesse de compression (V_P) des couches. Elle est normalement utilisée en génie civil pour estimer la profondeur du sous-sol et pour déterminer les conditions (altération, fracturation) de la roche où seront localisées les structures.
- **La réflexion sismique:** Se concentre sur les ondes réfléchies, qui sont générées lorsque l'onde sismique traverse deux régions d'impédances différentes ($Z = \rho V$). La méthode de sismique réflexion présente certains avantages par rapport à la méthode de sismique réfraction. Par exemple, nous pouvons également estimer la vitesse de l'onde de cisaillement (V_S), explorer des zones géologiques complexes (dômes de sel ou interfaces fortement inclinées), ou encore augmenter la profondeur d'exploration. Cependant, le traitement de ces données est plus compliqué que pour les données de réfraction.

La Figure 1.8 montre les différences entre l'acquisition de données réfléchies et réfractées.

Différentes configurations de campagnes sismiques sont disponibles en fonction des objectifs et des coûts de l'étude. Ils peuvent être divisés en campagnes terrestres et marines.

Dans le cas des campagnes terrestres, les sources peuvent être:

- Sources explosives: dans la plupart des cas, des charges explosives telles que la dynamite sont utilisées. Elles doivent être enterrées pour augmenter le signal transmis dans le sous-sol.
- Sources vibratoires: il s'agit généralement de camions vibrants, qui contiennent une masse lourde qui vibre verticalement sur une base constituée d'une plaque métallique plane pour transférer l'énergie dans le sous-sol.
- Chute de poids: un exemple de ces sources est une masse (ou un marteau) frappant une plaque métallique sur le sol. Ces types de sources sont utilisés dans les études du sous-sol à faible profondeur en raison de la faible énergie qu'elles génèrent.

Pour les campagnes marines les sources peuvent être:

- Pistolets à air comprimé: ce sont des cylindres métalliques à travers lesquels de l'air à haute pression est forcé de passer et de pénétrer dans la colonne d'eau où il crée une impulsion de pression. Ce sont les sources les plus utilisées parmi les sources marines.

- "Sparkers": ils génèrent une impulsion de pression sous forme de bulle en déchargeant un courant électrique dans l'eau.
- "Boomers": ils génèrent mécaniquement la différence de pression. Ils sont utilisés pour les sondages à faible profondeur.

Il existe des configurations de sources et récepteurs en 2-D et 3-D. Dans les configurations 2-D, le réseau de sources et de récepteurs suit une ligne dans laquelle sont placés les sources et les récepteurs. Alors que dans les configurations 3-D, les sources et les récepteurs sont placés dans une "zone rectangulaire", généralement le long de lignes parallèles. Dans le cas des campagnes marines, les sources et les récepteurs peuvent être placés à la fois en surface ou au niveau de la bathymétrie, auquel cas on parle de Ocean Bottom Survey (OBC).

Il existe également les profils sismiques verticaux (VSP), dans lesquels les récepteurs sont placés le long d'une ligne verticale dans un puits. Une source est placée près de la tête du puits. Les avantages des VSP sont que les champs d'ondes complets (ondes ascendantes et descendantes) sont enregistrés et donnent plus d'informations des propriétés sismiques en profondeur.

- **Traitement des données**: Le traitement des données sismiques comprend tous les traitements effectués sur les données brutes pour élaborer les images sismiques du sous-sol. Cette étape se compose de plusieurs étapes individuelles. Le nombre d'étapes et l'ordre dans lequel elles sont réalisées varient en fonction de la méthode utilisée. Cependant, certaines références dans la littérature (Yilmaz [2001]) suivent généralement l'ordre indiqué dans le diagramme de flux présenté dans la Figure 1.9. Nous décrivons ces étapes dans les paragraphes suivants.

  - **Pré-traitement**: Les données sont converties dans un format pratique pour les étapes de traitement suivantes. Le prétraitement comprend également l'édition des traces, où les traces bruitées peuvent être éliminées. Un gain peut également être effectué à ce stade, ce qui implique une compensation d'amplitude due à la dispersion géométrique (l'amplitude du signal diminue lorsque la distance entre les sources et les récepteurs (offset) augmente) [Yilmaz, 2001].
  - **Déconvolution**: Pour mieux comprendre l'idée principale derrière le processus de déconvolution, nous devons présenter le modèle convolutif de la Terre (équation 1.1). Cette équation exprime ce qui se passe lors d'une étude sismique réelle pour obtenir le sismogramme enregistré $x(t)$. Nous devons remarquer qu'à l'exception des sismogrammes enregistrés $x(t)$, nous ne connaissons pas exactement la réponse impulsionnelle de la terre, l'ondelette sismique ou le bruit ambiant. Cependant, si nous supposons que la composante du bruit est nulle $n(t)$, et que la source d'ondelettes est connue, l'équation 1.1 se réduit à : $x(t) = w(t) * e(t)$ qui, en termes de fréquence,

s'exprime comme suit: $X(\omega) = W(\omega)E(\omega)$. Par conséquent nous obtenons l'équation 1.2 qui pourrait être considérée comme un filtre inverse. Nous pouvons donc dire que le processus de déconvolution consiste à supprimer les effets de source des sismogrammes enregistrés en utilisant une technique de filtrage inverse. En d'autres termes, nous réduisons la source à une impulsion pour éviter que la forme de la source ait un effet sur les données. Le processus de déconvolution peut être repris par l'organigramme suivant de figure 1.10.

– **Sommation/"Stacking"**: Comme dans le cas du processus de déconvolution, la sommation ("stacking") comporte de nombreuses étapes. L'objectif de ces étapes est de corriger les données de l'influence du décalage (distance entre la source et le récepteur). Pour mieux comprendre l'idée du processus de sommation, nous devons d'abord connaître le format de données du point médian commun ("Common Midpoint gather"). En général, le processus de sommation commence à partir d'un "Common Midpoint gather". Nous pouvons voir un exemple de cette configuration dans la Figure 1.11(a). Il est appelé "Common Midpoint gather" car dans le cas d'une couche horizontale idéalisée, tous les points de réflexion coïncident au même endroit pour toutes les paires source-récepteur.

  Sur la Figure 1.11(b) nous pouvons voir les traces sismiques enregistrées, où les temps d'arrivée le long de la direction de décalage ("offset") dénotent une trajectoire hyperbolique comme suit : $t(x)^2 = x^2/v^2 + t(0)^2$, où $t(x)$ est le temps d'arrivée en fonction de l'offset x, v est la vitesse de la couche au-dessus du réflecteur, et $t(0)$ est deux fois le temps enregistré entre le "common midpont" et le "common depth point" (Figure 1.11(a)).

  La correction "Normal Moveout" (NMO) consiste à corriger l'influence du décalage ("offset") dans les temps d'arrivée comme suit : $t(0) = \sqrt{t(x)^2 - x^2/v_{NMO}^2}$ où v_{NMO} est la vitesse NMO, qui doit être obtenue soit par un modèle a priori, soit par des estimations. Dans les géologies plus compliquées (en présence de réflecteurs avec pendage), la correction NMO change. Nous nous référons à Yilmaz [2001] pour plus de détails.

  Après la correction NMO, les traces sismiques se présentent comme dans la figure 1.11(c), où les temps d'arrivée se présentent sous la forme d'une ligne horizontale. Enfin, toutes les traces qui correspondent au même point de profondeur commun "Common Depth point") sont empilées pour obtenir une seule trace (Figure 1.11(d.)). Nous pouvons dire que le principal avantage du processus de sommation est de mettre en évidence le rapport signal sur bruit dû à la somme des traces. Dans la figure 1.12, nous présentons un résumé des étapes de la sommation.

– **Migration**: Il s'agit d'une technique basée sur la réflectivité et d'un processus essentiel car dans la section empilée /"stacked" (i.e après le processus de sommation), la position des structures géologiques et des interfaces (failles, anticlinal, sincli-

nal, réservoir de pétrole) n'est pas localisée à sa position réelle. Le processus de migration augmente également la résolution spatiale et réduit les diffractions. Les images migrées précédemment ont été présentées dans le domaine temporel (pour être comparées à la section empilée [Yilmaz, 2001]). We can see in Figure 1.13 the original idea behind the migration. For example in Figure 1.13(a), we can see an explosive inclined reflector. Il s'agit d'un concept idéalisé dans lequel nous imaginons que nous avons des sources le long du réflecteur (cercles bleus) qui se déplacent vers les récepteurs en surface (cercles rouges). Dans la figure 1.13(b), nous avons une section à décalage nul. Cela signifie que les sources et les récepteurs sont situés à la même position (cercles rouges) (nous pouvons approximativement arriver à cette configuration après sommation/"stacking"). Sur la figure 1.13(c), nous pouvons voir que l'angle réel d'inclinaison du réflecteur (ligne bleue) est différent de l'angle obtenu par la section à décalage nul (ligne verte). L'objectif de la migration est de ramener les structures à leur position réelle. Nous discuterons plus en profondeur du processus de migration et des différentes approches qui y sont liées dans la prochaine sous-section.

- **Interprétation**: Enfin, lorsque nous avons pu obtenir une bonne image sismique du sous-sol, nous arrivons à l'interprétation des images sismiques. Cette étape consiste en l'application des connaissances géologiques à la définition des principales caractéristiques des images sismiques.

Dans ce projet, nous nous concentrons sur le traitement de la migration des données sismiques brutes. Comme nous le verrons plus tard, il existe plusieurs types de méthodes de traitement par migration, la plus utilisée de nos jours étant la Reverse Time Migration (RTM) pour les zones géologiques complexes, améliorée au cours des dernières décennies pour atténuer les multiples.

1.5.1 Etat de l'art des techniques d'imagerie sismique.

L'imagerie sismique, qui implique la localisation d'interfaces géologiques à partir de données sismiques d'exploration, a historiquement été liée au processus de migration. Le processus de migration est la dernière étape du traitement des données sismiques avant l'interprétation. Pour cette raison, c'est un processus qui a fait l'objet d'une attention particulière dans le contexte des méthodes d'exploration sismique. En outre, en raison de sa complexité, il requiert une plus grande puissance de calcul que les autres étapes du traitement des données sismiques. En effet, dans Robinson and Enders [1983] et Telford et al. [1990], la migration sismique et l'imagerie sismique sont traitées comme le même processus.

Selon Sheriff [2002], la migration est une technique de réflectivité définie comme une opération d'inversion impliquant un réarrangement des éléments d'information sismique de façon à ce que les réflexions et les diffractions soient représentées à leur emplacement réel. Nous avons montré dans les figures 1.13 l'idée originelle et générale de la migration. Cependant,

les méthodes de migration ont évolué au cours des dernières années. En d'autres termes, la migration pourrait être considérée comme une transformation du domaine temporel au domaine de la profondeur, dans laquelle les interfaces "migrent" vers leur position d'origine.

Pour parler des premiers travaux de migration, nous pouvons remonter aux travaux de Claerbout, où il parle de trouver une carte de réflecteurs, dont le but est d'indiquer l'emplacement des réflecteurs. Dans [Claerbout, 1971], une comparaison entre des données réelles et des données synthétiques obtenues par un modèle préalable (a priori) y est discutée, et même il y est mentionné la possibilité d'améliorer le modèle préalable dans un processus itératif. Ces idées peuvent être considérées comme des précédents au RTM et au LSRTM. Ces techniques sont développées plus en détail dans les années suivantes. Dans la littérature, nous pouvons faire référence à deux approches différentes de la reconstruction d'images : Les approches classiques et les approches modernes. Les approches classiques font principalement référence aux méthodes basées sur le traçage de rayons (équation d'Eikonal). Parmi lesquelles on trouve :

- **Migration "zero offset"**. La figure 1.13 en montre le principe. Comme nous l'avons expliqué précédemment, dans un milieu à vitesse constante, comme le montre la figure 1.13(a), nous pouvons voir la trajectoire directe dans laquelle l'énergie sismique se déplace depuis le réflecteur d'immersion avec un angle β. Dans cette figure, l'axe vertical représente la profondeur. Sur la figure 1.13(b) qui représente une section à décalage nul (l'axe vertical représente le temps), l'angle α est différent de β ($\beta > \alpha$).

  En général, elle est effectuée après le processus de sommation (migration post-sommation). Cependant, si le processus d'empilement ne produit pas de bonnes données à décalage nul ('zero offset'), ce processus de migration est effectué avant le processus de sommation (migration pre-sommation), ce qui implique un coût de calcul plus élevé que la migration post-sommation.

- **Migration en temps et en profondeur.** La migration en temps est effectuée si le gradient horizontal du modèle de vitesse n'est pas trop fort. Cependant, si le gradient horizontal de la vitesse est élevé, la migration en temps ne peut pas corriger les positions des réflecteurs et pour cette raison, la migration en profondeur doit être calculée : [Yilmaz, 2001]. Pour que le processus de migration soit correct (c'est-à-dire égal à la figure 1.13(a)), l'axe vertical de la figure 1.13(b) doit être transformé en profondeur et cela nécessite une connaissance du champ de vitesse (afin de convertir la section temporelle enregistrée en section migrée en profondeur).

- **Migration de Kirchoff.** L'une des méthodes les plus utilisées les vingt dernières années est la migration de Kirchoff, qui résout l'équation intégrale des ondes le long des courbes de diffraction (Schneider [1978], Bevc [1997], et Hokstad [2000]). L'idée principale de cette méthode est que les hyperboles dans le domaine temporel deviennent des demi-cercles dans le domaine spatial. Fondamentalement, la migration de Kirchoff consiste en la sommation des amplitudes le long des courbes de diffraction hyperboliques dans

le domaine temporel et leur mise en correspondance dans le domaine spatial. Dans la figure 1.14, où les points rouges représentent les sources et les récepteurs, les points et lignes verts représentent les événements du domaine temporel (non migrés), et les points et lignes bleus représentent les événements migrés. Nous présentons quelques exemples de ce qui est réalisé dans la migration de Kirchoff. Par exemple, dans la figure 1.14(a), nous pouvons voir comment le point vert (avant la migration) a migré vers un demi-cercle dans la section migrée. Dans la figure 1.14(b), nous pouvons voir qu'une diffraction (hyperbole verte) de la section non migrée, est réduite à un point bleu dans la section migrée par la sommation des amplitudes le long de l'hyperbole. Le point bleu est situé à l'intersection de tous les cercles noirs. Enfin, dans la figure 1.14(c), nous voyons un événement vert plongeant qui est déplacé vers son emplacement correct au niveau de la ligne bleue. Nous pouvons conclure que la section "zero-offset" est considérée comme construite par une superposition de diffracteurs qui forment un événement cohérent dans le domaine du décalage temporel. Lorsqu'il existe une discontinuité dans le domaine spatial, cet effet se traduit par des diffractions hyperboliques dans le domaine temporel, comme sur la figure 1.14(b). Cependant, lorsqu'il existe une structure continue dans le domaine spatial, elle est reflétée comme un événement cohérent dans le domaine temporel, comme dans la figure 1.14(c).

Grâce au travail effectué par Tarantola and Valette [1982] et Lailly and Bednar [1983], il y a eu une transition importante vers des approches modernes qui sont basées sur la solution de la forme d'onde complète et les méthodes adjointes. Parmi ces approches modernes, on trouve la migration temporelle inverse (RTM), la migration temporelle inverse au moindre carré (LSRTM) et l'inversion de la forme d'onde complète (FWI), ces deux dernières méthodes étant des méthodes basées sur l'inversion de données :

- **"Reverse Time Migration" (RTM).** Grâce aux progrès de l'informatique, il a été possible de mettre en œuvre des méthodes d'imagerie impliquant la résolution complète de l'équation d'onde sur de grands volumes de données, comme la méthode RTM. Parmi les premiers travaux de cette méthode, on trouve Baysal et al. [1983] et McMechan [1983]. Le concept original de la RTM concerne la transformation des informations sismiques du domaine temporel au domaine de la profondeur. La RTM est basée sur le calcul d'images de réflectivité qui visent à détecter les principales interfaces du modèle qui réfléchissent et diffusent un maximum d'énergie (ceci est fortement lié à l'impédance, car l'énergie augmente avec la différence entre l'impédance de deux couches adjacentes). En fonction des "patterns" de radiation des ondes P et S, de leurs interactions et des conversions de phase aux interfaces, on peut reconstruire des images de réflectivité correspondant à une "perturbation du modèle" à nombre d'ondes élevé et ce pour pour un modèle de fond "a priori" de type lisse. En fonction de la paramétrisation choisie, nous pouvons récupérer beaucoup mieux les interfaces. D'après Feng and Schuster [2017] les images de réflectivité d'impédance des ondes P et S réduisent les crosstalks grâce aux "patterns" de

radiation diffusifs qui sont plus dissemblables que ceux liés aux paramètres de Lamé λ et μ. En d'autres termes, les images de réflectivité d'impédance P et S permettent de bien mieux séparer les phases et les longueurs d'onde par rapport à V_p et V_s (ou λ et μ). On peut voir dans la figure 1.15 l'organigramme du processus RTM pour obtenir les images de réflectivité. Nous partons d'un modèle de base "a priori" et calculons le problème direct en utilisant ce modèle pour obtenir les données prédites. Ensuite, nous calculons le problème adjoint en utilisant une source qui est la différence entre les données réelles et prédites. Enfin, nous calculons la condition d'imagerie en corrélant le champ rétro-propagé avec le champ adjoint pour générer les images de réflectivité. Nous renvoyons à Chattopadhyay and McMechan [2008] et Zhang and Shi [2019] pour une étude plus approfondie sur les conditions d'imagerie. Ces dernières années, des améliorations ont été apportées à la méthode RTM. Par exemple, il est bien connu que dans les milieux visco-élastiques, lors du calcul de la condition d'image avec l'approche classique, une instabilité de la solution se produit. C'est pourquoi, dans Wang et al. [2018], une méthode de stabilisation de l'adaptabilité pour la RTM compensée par Q est proposée. En outre, la méthode de migration temporelle inverse des multiples a été développée, qui exploite le fait que les multiples traversent des régions d'accès difficile que le signal primaire ne peut pas atteindre. De ce fait, cette méthode a été appliquée avec succès dans des régions à tectonique saline complexe. Pour plus d'informations sur ces méthodes, nous renvoyons à Liu et al. [2011], Wang et al. [2017].

- **"Full Waveform Inversion" (FWI)** La méthode FWI est une méthode itérative non linéaire d'inversion de forme d'onde complète qui consiste à trouver les paramètres du modèle $\mathbf{m}$ qui minimisent la fonction de "misfit" χ définie comme suit:

$$\chi = \frac{1}{2}||\boldsymbol{Lm} - \boldsymbol{D}||^2, \tag{1.5}$$

où $\boldsymbol{Lm}$ signifie en termes simples que les équations d'onde élastodynamiques sont appliquées aux paramètres $\boldsymbol{m}$ (problème direct), et $\boldsymbol{D}$ représente les données réelles (Lailly and Santosa [1984], Tarantola [1984], Mora [1987], Pratt et al. [1996], Virieux and Operto [2009]).

Parmi les méthodes permettant de minimiser la fonction de "misfit" dans le contexte de la FWI, on trouve : la méthode de plus grande pente (SD/Steepest descnet) (Yang [2021], Ren [2022]), la méthode du gradient conjugué préconditionné (Yang et al. [2015a], Pan et al. [2017]), ou la méthode de Newton tronquée (Métivier et al. [2013], Métivier et al. [2017]).

Dans le contexte de l'imagerie sismique des dômes de sel, la FWI a été appliquée à des données réelles avec succès ces dernières années. En Shen et al. [2017] La FWI a été appliquée à des données du type "ocean-bottom-node" (OBN) à large décalage sur le champ Atlantic dans les eaux profondes du golfe du Mexique, où ils ont démontré qu'avec

des données à basse fréquence à long offset, la FWI peut corriger une erreur majeure dans la définition du dôme de sel. Dans Wang et al. [2019] la FWI est appliquée à des données de "streamer" à ouverture large et complète et à des données OBN du canyon de Keathly, où ils ont démontré que la FWI est capable de construire des modèles complexes de vitesse du sel avec différents types de données d'entrée, y compris des données de streamer à ouverture large et complète et (OBN).

La FWI reste une technique largement utilisée ces derniers temps. Cependant, elle a un coût de calcul élevé dans les problèmes 3D et dépend fortement du modèle initial. C'est pourquoi, dans le contexte de l'inversion FWI des modèles de dômes de sel, des méthodes d'inversion basées sur l'apprentissage profond ont également été proposées. Dans Sun et al. [2020], un réseau neuronal récurrent (RNN) a été développé et comparé aux méthodes de type Gradient Conjugué et l-BFGS, dans lesquelles le RNN est plus stable. Dans Ren et al. [2020], ils ont proposé un réseau d'inversion de formes d'ondes sismiques (SWIN) permettant une bonne inversion de la vitesse et une convergence rapide. Dans le document Liu et al. [2021], ils ont proposé une méthode de construction d'un modèle de vitesse d'ondes P dans le cadre d'une collecte commune de données et d'une collecte commune de données de réception.

- **"Least Squares Reverse Time Migration" (LSRTM)** La méthode LSRTM est une méthode d'inversion linéarisée qui consiste à trouver le modèle de réflectivité $\boldsymbol{r}$ qui minimise la fonction de "misfit" χ définie comme suit:

$$\chi = \frac{1}{2}||\boldsymbol{L}\boldsymbol{r} - \boldsymbol{D}||^2, \tag{1.6}$$

où $\boldsymbol{L}$ est ici un opérateur de démigration, $\boldsymbol{r}$ est l'image de réflectivité, et $\boldsymbol{D}$ représente les données observées. Le RTM conventionnel est la première approximation du modèle de réflectivité LSRTM $\boldsymbol{r}$, qui est utilisé pour générer les données synthétiques $\boldsymbol{L}\boldsymbol{r}$ (Wong et al. [2011], Dai et al. [2012], Dong et al. [2012], Stanton and Sacchi [2014] Zhang et al. [2015]).

La LSRTM n'est pas une méthode de caractérisation comme FWI car elle vise à inverser le modèle de réflectivité, mais en raison de sa nature linéaire, LSRTM converge plus rapidement que FWI. Cependant, dans les milieux 3D, le coût de calcul reste assez élevé. C'est pourquoi dans Dai et al. [2012], Dai and Schuster [2013b] le codage par déplacement de phase linéaire est appliqué pour injecter des sources simultanées avec une réduction du "cross-talks" ainsi qu'une réduction du temps de calcul.

Dans Zhang and Schuster [2014], le LSRTM de multiples (LSRTMM) est appliqué au modèle synthétique 2D Sigsbee 2B. En utilisant des multiples de surface libre, ils suppriment les croisements dans l'image finale et corrigent la statique de la source. Cette correction est liée aux anomalies de vitesse à proximité de la surface, sous la source ou le récepteur. Cependant, avec un fort bruit du "cross-talks" et des données imparfaitement séparées, les

tests synthétiques ont démontré que le LSRTMM ne présente pas d'avantages significatifs par rapport au RTM.

Up to that time the LSRTM had worked mainly with acoustic rheology. Then, in Dutta and Schuster [2014] and Dai et al. [2015], the LSRTM is applied in a visco-acoustic rheology context, where some improvements over the reflectivity images have been reached due to attenuation implementation. In Ren et al. [2017], Feng and Schuster [2017] an elastic-rheology LSRTM is implemented, generating reflectivity images with fewer artifacts, better amplitude balancing and higher resolution compared to acoustic LSRTM. Finally in Guo and McMechan [2018] a visco-elastic rheology is applied using the generalized Zener standard linear solid model, in which they found that visco-elastic LSRTM has stronger and more continuous amplitudes for the structures in and beneath low-Q zones.

Une approche d'apprentissage profond a été proposée par Zhang et al. [2022] dans le contexte de la méthode LSRTM. Ils introduisent le réseau neuronal convolutionnel (CNN) pour le LSRTM pré-empilé. Ils ont testé cette méthode dans le modèle synthétique complexe de Marmousi-2 en obtenant des images de subsurface de haute qualité à un faible coût de calcul.

1.5.2 Techniques utilisées dans ce travail.

Pour le premier objectif de ce travail, nous avons implémenté la RTM sur un modèle synthétique dans une rhéologie acoustique. Nous testons deux types d'information a priori : un modèle basé sur le gradient, où les propriétés du milieu augmentent avec la profondeur, et un modèle lissé, où un filtre gaussien est appliqué au modèle réel. Nous testons également différentes manières de préconditionner l'image migrée afin de mieux voir les interfaces profondes: préconditionnement par l'énergie directe ou adjointe, pseudo-hessienne, ou pondération en fonction de la profondeur (c'est-à-dire qu'une fonction de pondération dépendant de la profondeur est appliquée aux perturbations du modèle ou aux termes de régularisation du modèle afin d'augmenter la résolution du modèle en profondeur). Dans notre étude, la meilleure façon de préconditionner l'image migrée est d'utiliser l'énergie directe. Nous testons également différentes façons de paramétrer l'image migrée : (ρ, λ, μ), (ρ', V_P, V_S), ou (ρ'', Z_P, Z_S), où λ et μ sont les coefficients de Lamé, V_P et V_S représentent les vitesses P et S et Z_P et Z_S représentent les impédances P et S, tandis que ρ, ρ' et ρ'' représentent la densité associée aux paramétrisations des coefficients de Lamé, des vitesses ou des impédances respectivement. Dans nos études, toutes les différentes paramétrisations se comportent de manière similaire.

Dans la figure 1.16, nous décrivons l'ensemble du processus que nous avons mis en œuvre dans ce projet pour le deuxième objectif (modèle WAVES). Après avoir filtré les données réelles, nous effectuons un processus itératif pour minimiser la fonction misfit (équation 1.6). Ce processus itératif est composé de deux étapes successives:

- Tout d'abord, nous améliorons le modèle a priori en appliquant la méthode de descente la plus abrupte dans laquelle nous testons plusieurs longueurs de pas pour voir si elles satisfont la première condition de Wolfe. Nous choisissons la longueur de pas qui minimise la fonction de "misfit". La direction de recherche est obtenue en calculant le gradient de la fonction de "misfit" (RTM) associée au modèle de base et nous la préconditionnons par l'énergie directe. Nous utilisons la longueur de pas et la direction de recherche pour obtenir le modèle 1.

- Ensuite, nous améliorons le modèle 1 en appliquant la méthode du gradient conjugué non linéaire dans laquelle nous testons plusieurs longueurs de pas pour voir si elles satisfont les deux conditions de Wolfe, et nous choisissons la longueur de pas qui minimise la fonction de "misfit". Pour calculer la direction de recherche, nous calculons le gradient de la fonction de "misfit" (RTM) associée au modèle 1 et nous le préconditionnons par l'énergie directe. Nous utilisons la longueur de pas et la direction de recherche pour obtenir le modèle 2.

1.5.3 Structure de la thèse

A part ce chapitre qui constitue l'introduction générale, cette thèse est organisée en 4 chapitres.

Le chapitre 2 contient la description des équations régissant l'équation d'onde pour les rhéologies élastique et viscoélastique. Nous décrivons la méthode RTM classique basée sur la théorie de l'adjoint avec le calcul des noyaux de sensibilité. Nous poursuivons en décrivant les méthodes d'inversion itérative LSRTM et FWI. Nous décrivons également les méthodes numériques utilisées pour résoudre les équations décrites précédemment. Nous nous concentrons principalement sur la méthode des différences finies (c'est la méthode que nous avons implémentée au 4ème ordre en espace dans ce travail) mais nous présentons également une brève description de la méthode des éléments finis dans l'annexe D. Ensuite, nous présentons la discrétisation spatiale et temporelle que nous avons utilisée, y compris les conditions de dispersion et de stabilité qui doivent être satisfaites. Nous présentons également les conditions aux limites absorbantes CPML que nous avons utilisées pour éviter les artefacts numériques aux frontières du domaine de calcul. Nous montrons ensuite le schéma de la technique de "Checkpointing" qui est nécessaire pour résoudre l'équation d'onde viscoélastique dans le processus de renversement temporel sans introduire d'instabilités numériques et donc pour calculer les noyaux de sensibilité en présence d'atténuation. Enfin, nous décrivons brièvement l'origine de la contamination des images par les multiples.

Le chapitre 3 contient tout le processus pour obtenir les images sismiques à partir des données synthétiques 2D construites à partir de l'interprétation des données sismiques enregistrées dans le Golfe du Mexique. Nous présentons dans ce chapitre les équations des ondes élastiques 2D, nous suivons une approche similaire à celle du chapitre 2. Cependant, dans ce chapitre, nous incluons les différentes paramétrisations qui pourraient être mises en œuvre

pour construire les images de réflectivité. De plus, nous présentons une analyse des implications physiques de la condition d'imagerie (corrélation entre les champs d'ondes rétro-propagés et adjoints). Nous montrons nos résultats en utilisant 4 modèles de "background" (modèles a priori), et nous discutons de la contribution des noyaux de densité (K_ρ) ou de compression (K_{Vp}, K_λ ou K_{Zp}) pour différentes paramétrisations des modèles dans la reconstruction des différents images pour différents nombres d'onde (bas à élevés). Nous ajoutons également dans ce chapitre des images obtenues à partir de données synthétiques 3D en utilisant le même modèle 2D mais allongé dans la direction transversale pour obtenir un modèle 3D. Les résultats 2D de ce chapitre ont été calculés en utilisant un code FORTRAN-90/2008 parallélisé développé par Javier Abreu-Torres.

Le chapitre 4 contient les résultats obtenus à partir des données à décalage nul ('zero-offset') et à décalage multiple tirées de l'ensemble des données réelles de l'expérience WAVES 3D. Tout d'abord, nous décrivons les dimensions et les propriétés mesurées des matériaux utilisés pour construire le modèle WAVES. Ensuite, nous montrons les sources et les récepteurs qui ont été implémentés dans cette expérience. Après cela, nous montrons la discrétisation spatiale et temporelle, l'adaptation des données (interpolation et filtrage), et la calibration des propriétés des matériaux que nous appliquons. Nous présentons ensuite les noyaux de sensibilité obtenus par RTM en utilisant les données à décalage nul avec et sans atténuation. Pour obtenir les résultats 3D de ce chapitre, nous utilisons le code parallèle UNISOLVER (parallélisé avec les librairies MPI/Message Passing Interface et écrit en grande partie en Fortran2013), auquel j'ai participé en implémentant le schéma de différences finies d'ordre 4 en parallèle (code précédemment implémenté à l'ordre 2 en espace), les équations d'ondes viscoélastiques et quelques autres sous-programmes: le lecteur pourra trouver quelques exemples de ces codes dans les annexes A, B, et C.

Enfin, dans le chapitre 5, nous présentons les conclusions générales, les discussions et les perspectives.

Chapter 2

Seismic wave equation resolution and seismic imaging methods.

In geophysics there are several exploration methods, such as seismic, gravimetric, magnetic, electromagnetic, electrical and electromagnetic methods among the best known. Each one gives us information about the distribution of different rocks and fluids of the subsurface. Seismic methods have a wider range of applications, ranging from the exploration of fossil fuels and groundwater, to applications for geotectonics studies, due to its high level of penetration and resolution. It makes it very appropriate to explore complex geological regions, such as salt domes (e.g.) Eby and Clark [1935], Ratcliff et al. [1992], Cao et al. [2021].

In this chapter, we develop the 3D elastodynamic wave equations in elastic and acoustic media. We also consider the different types of sources we can inject, as well as the initial and boundary conditions that must be satisfied. Then, we discuss the physical principle of the classical imaging conditions, and develop the equations of the adjoint-based imaging conditions that will allow us to reconstruct better the main interfaces of the media under study. We summarize also how the sensitivity kernels are computed in practice. After that, we describe the classical RTM method and the iterative LSRTM for seismic imaging in one hand, and FWI methods for both seismic imaging and seismic properties characterization in another hand, all these methods being based on the adjoint theory. We then mention the main numerical methods to solve the wave equation, focusing our attention on the finite-differences method and the spatial and temporal discretizations. After that we comment the dispersion and stability conditions that must be satisfied to avoid spurious noise in the solutions and maintain bounded results. Finally, we explain the absorbing boundary conditions (here the Perfectly matched Layers) that must be implemented to mimick an infinite or semi-infinite medium.

2.1 Forward problem equations.

The observed seismic data are obtained by recording the variations of pressure or displacement over time through a specifically designed seismic array. The arrival times of the

seismic signals, as well as their amplitude, depend on the density and elastic properties of the subsoil. This set of properties is associated to parameters $\boldsymbol{m}$.

In seismic data acquisition g represents the operator which relates the subsoil parameters $\boldsymbol{m}$ to the recorded data $\boldsymbol{d}$. This is called the Forward problem, and the data set $\boldsymbol{d}$ is related to parameters $\boldsymbol{m}$ through a linear or non-linear mapping function g as follows:

$$\boldsymbol{d} = g(\boldsymbol{m}), \tag{2.1}$$

Therefore, we can also say that it exists an “inverse" relation expressed in equation

$$\boldsymbol{m} = g^{-1}(\boldsymbol{d}), \tag{2.2}$$

which is called the inverse problem. The goal of all geophysical exploration is to be able to calculate the distribution of the subsoil parameters from observed data. However in practice, the inverse mapping of g^{-1} is never computed and therefore the resolution of a matrix system is proposed.

2.1.1 Elastic rheology of the medium.

Because the propagation of seismic waves depends on the elastic properties of rocks, it is important to briefly discuss the most important aspects of elasticity in solid media.

Elastic bodies have the property of recovering their original shape and volume after being subjected to external forces. The Cauchy stress tensor contains the information of the stress distribution. Considering an orthogonal reference system, the stress tensor $\boldsymbol{\tau}$ is defined as follows:

$$\begin{bmatrix} \tau_{xx} & \tau_{xy} & \tau_{xz} \\ \tau_{yx} & \tau_{yy} & \tau_{yz} \\ \tau_{zx} & \tau_{zy} & \tau_{zz} \end{bmatrix} \tag{2.3}$$

This is a symmetric matrix in the isotropic case, where the elements represent the force per unit area. The elements of the principal diagonal τ_{xx}, τ_{yy}, and τ_{zz} represent the compressional stresses, while the other elements (the deviatoric matrix) denote the shear stresses.

In general, the stress tensor $\boldsymbol{\tau}$ is related to the strain tensor $\boldsymbol{\epsilon}$ by applying the Hooke's law as:

$$\boldsymbol{\tau} = \boldsymbol{C} : \boldsymbol{\epsilon}, \tag{2.4}$$

where $\boldsymbol{C}$ is the fourth-order elastic tensor, and the strain tensor is defined as:

$$\boldsymbol{\epsilon} = \frac{1}{2}(\nabla \boldsymbol{u} + \nabla \boldsymbol{u}^T), \tag{2.5}$$

where $\boldsymbol{u}$ is the displacement vector.

Considering a linear, isotropic medium, the tensor $\boldsymbol{C}$ could be expressed as:

$$C_{ijkl} = \lambda\delta_{ij}\delta_{kl} + \mu(\delta_{ik}\delta_{jl} + \delta_{il}\delta_{jk}), \tag{2.6}$$

where δ is the Kronecker delta, and λ and μ are the elastic Lamé parameters (λ is related to the compressional movements, while μ is related to the shear movements). Therefore, the Hooke's law (equation 2.4) can be written as:

$$\tau_{ij} = \lambda\delta_{ij}\epsilon kk + 2\mu\epsilon_{ij}. \tag{2.7}$$

The tensor $\boldsymbol{C}$ has the following symmetries:

$$\begin{aligned} C_{ijkl} &= C_{klij}, \\ C_{ijkl} &= C_{jikl} = C_{jilk}. \end{aligned} \tag{2.8}$$

Considering that the physical medium is composed of infinitesimal particles, the normal strains, that are applied to each particle, are expressed as:

$$\epsilon_{xx} = \frac{\partial u_x}{\partial x}, \epsilon_{yy} = \frac{\partial u_y}{\partial y}, \epsilon_{zz} = \frac{\partial u_z}{\partial z}, \tag{2.9}$$

where u_x, u_y, and u_z are the components of the displacement $\boldsymbol{u}$ in the x, y, and z directions respectively. These strains involve a change in volume, but not in shape.

The shear strains, which involve a change in shape but not in volume, are expresed as:

$$\begin{aligned} \epsilon_{xy} = \epsilon_{yx} &= \frac{\partial u_y}{\partial x} + \frac{\partial u_x}{\partial y}, \\ \epsilon_{xz} = \epsilon_{zx} &= \frac{\partial u_z}{\partial x} + \frac{\partial u_x}{\partial z}, \\ \epsilon_{yz} = \epsilon_{zy} &= \frac{\partial u_z}{\partial y} + \frac{\partial u_y}{\partial z}. \end{aligned} \tag{2.10}$$

2.1.2 Elastodynamic equations.

Considering the stress tensor $\boldsymbol{\tau}$, we can say that the variation of the stress in the x-direction is equal to:

$$\left(\frac{\partial \tau_{xx}}{\partial x} + \frac{\partial \tau_{xy}}{\partial x} + \frac{\partial \tau_{xz}}{\partial x}\right) dx, \tag{2.11}$$

where dx is an infinitesimal distance. Therefore, we can say that the internal force acting in the direction of the x-axis is:

$$\left(\frac{\partial \tau_{xx}}{\partial x} + \frac{\partial \tau_{xy}}{\partial x} + \frac{\partial \tau_{xz}}{\partial x}\right) dx\, dy\, dz, \tag{2.12}$$

where $dy\, dz$ is the infinitesimal area normal to the direction x.

From the Newton's second law, which says that:

$$m\boldsymbol{a} = \boldsymbol{F}, \tag{2.13}$$

where $\boldsymbol{F}$ is the total force (internal $\boldsymbol{F^{int}}$ and external $\boldsymbol{F^{ext}}$) applied to a particle of mass m, and $\boldsymbol{a}$ is the acceleration to which the particle is subjected due to the effects of the force $\boldsymbol{F}$, we can write for each elementary volume $dx\,dy\,dz$ using equation 2.12:

$$\rho\frac{\partial^2 u_i}{\partial t^2} = F_i^{int} + F_i^{ext}, \tag{2.14}$$

where ρ represents the density of the particle, $F_i^{int} = \partial_j \tau_{ij}$ are the internal forces per unit volume and $F_i^{ext} = f_i$ the external sources per unit volume (source of excitation of the medium, etc...) for $i = 1$ to D (D being the space dimension: $2D$ or $3D$). Considering the Hooke's law (equation 2.4), and using equations 2.9 and 2.10, we can write for the x-axis that:

$$\begin{aligned}
\tau_{xx} &= (\lambda + 2\mu)\frac{\partial u_x}{\partial x} + \lambda\left(\frac{\partial u_y}{\partial y} + \frac{\partial u_z}{\partial z}\right), \\
\tau_{xy} &= \mu\left(\frac{\partial u_y}{\partial x} + \frac{\partial u_x}{\partial y}\right), \\
\tau_{xz} &= \mu\left(\frac{\partial u_z}{\partial x} + \frac{\partial u_x}{\partial z}\right).
\end{aligned} \tag{2.15}$$

By deriving with respect to time we have:

$$\begin{aligned}
\frac{\partial \tau_{xx}}{\partial t} &= (\lambda + 2\mu)\frac{\partial v_x}{\partial x} + \lambda\left(\frac{\partial v_y}{\partial y} + \frac{\partial v_z}{\partial z}\right), \\
\frac{\partial \tau_{xy}}{\partial t} &= \mu\left(\frac{\partial v_y}{\partial x} + \frac{\partial v_x}{\partial y}\right), \\
\frac{\partial \tau_{xz}}{\partial t} &= \mu\left(\frac{\partial v_z}{\partial x} + \frac{\partial v_x}{\partial z}\right),
\end{aligned} \tag{2.16}$$

where (v_x, v_y, v_z) are the components of the velocity vector $\boldsymbol{v}$. Taking equations 2.14 and 2.16,

and making an analogy for directions y and z, we obtain the 3D elastic wave equations:

$$\begin{aligned}
\rho\frac{\partial v_x}{\partial t} &= \frac{\partial \tau_{xx}}{\partial x}+\frac{\partial \tau_{xy}}{\partial x}+\frac{\partial \tau_{xz}}{\partial x}+f_x,\\
\rho\frac{\partial v_y}{\partial t} &= \frac{\partial \tau_{xy}}{\partial y}+\frac{\partial \tau_{yy}}{\partial y}+\frac{\partial \tau_{yz}}{\partial y}+f_y,\\
\rho\frac{\partial v_z}{\partial t} &= \frac{\partial \tau_{xz}}{\partial z}+\frac{\partial \tau_{yz}}{\partial z}+\frac{\partial \tau_{zz}}{\partial z}+f_z,\\
\frac{\partial \tau_{xx}}{\partial t} &= (\lambda+2\mu)\frac{\partial v_x}{\partial x}+\lambda\left(\frac{\partial v_y}{\partial y}+\frac{\partial v_z}{\partial z}\right),\\
\frac{\partial \tau_{yy}}{\partial t} &= (\lambda+2\mu)\frac{\partial v_y}{\partial y}+\lambda\left(\frac{\partial v_x}{\partial x}+\frac{\partial v_z}{\partial z}\right),\\
\frac{\partial \tau_{zz}}{\partial t} &= (\lambda+2\mu)\frac{\partial v_z}{\partial z}+\lambda\left(\frac{\partial v_x}{\partial x}+\frac{\partial v_y}{\partial y}\right),\\
\frac{\partial \tau_{xy}}{\partial t} &= \mu\left(\frac{\partial v_y}{\partial x}+\frac{\partial v_x}{\partial y}\right),\\
\frac{\partial \tau_{xz}}{\partial t} &= \mu\left(\frac{\partial v_z}{\partial x}+\frac{\partial v_x}{\partial z}\right),\\
\frac{\partial \tau_{yz}}{\partial t} &= \mu\left(\frac{\partial v_y}{\partial z}+\frac{\partial v_z}{\partial y}\right),
\end{aligned} \tag{2.17}$$

where (f_x, f_y, f_z) is the vector of external sources. Therefore, in the absence of shear stresses ($\mu = 0$), the 3D acoustic wave equations can be derived and expressed as:

$$\begin{aligned}
\rho\frac{\partial v_x}{\partial t} &= \frac{\partial p}{\partial x},\\
\rho\frac{\partial v_y}{\partial t} &= \frac{\partial p}{\partial y},\\
\rho\frac{\partial v_z}{\partial t} &= \frac{\partial p}{\partial z},\\
\frac{\partial p}{\partial t} &= \kappa\left(\frac{\partial v_x}{\partial x}+\frac{\partial v_y}{\partial y}+\frac{\partial v_z}{\partial z}\right)+f
\end{aligned} \tag{2.18}$$

where p represents the pressure perturbation of the medium, κ is the bulk modulus, and f is a scalar. We must take care of the source in the fluid, where it must be isotropic. We will talk more about this in the next subsection.

2.1.3 Source type in the medium.

The external sources are attributed to natural (earthquakes) or artificial causes (explosions). The external sources can be injected into the medium as point forces (at one point of the computational domain) or as moment tensors where:

$$\boldsymbol{f} = -\nabla \cdot \boldsymbol{M}(\boldsymbol{x}, t). \tag{2.19}$$

The time function of the source can be any signal having a limited frequency band. For example the time wavelet function can be introduced as:

1. a Gaussian function: $g(t) = \exp[-a(t-t_0)^2]$,
2. a first derivative of the Gaussian function: $g'(t) = -2a(t-t_0)\exp[-a(t-t_0)^2]$,
3. a Ricker function: $r(t) = 2a[-1+2a(t-t_0)^2]\exp[-a(t-t_0)^2])$,

where $a = 4\pi^2 f_0^2$, f_0 is the dominant frequency of the source spectrum, $t_0 = c/f_0$ is a delay time, and c could be a chosen coefficient (generally $c \approx 1$).

Special attention should be paid to the numerical injection of the source. If the source is injected into the fluid, i.e., an acoustic medium, the sources must be injected as in equations 2.18, where f is isotropic. However if the sources are injected in an elastic medium, they must be injected as in equations 2.17, where the point source force (f_x, f_y, f_z) has different components depending on the direction. If the source is an explosion, then the source is injected as in equation 2.19, with an anisotropic moment tensor $\boldsymbol{M}$ $(M_{ij} = 0,\ i \neq j)$, and $M_{11} = M_{22} = M_{33}$.

2.1.4 Initial and boundary conditions.

The initial conditions for $u_i(\boldsymbol{x}, t)$, $v_i(\boldsymbol{x}, t)$ and $\tau_{ij}(\boldsymbol{x}, t)$, imply equilibrium at the beginning of the simulation $(t = 0)$, and could be written as:

$$\begin{aligned} u_i(\boldsymbol{x}, 0) = v_i(\boldsymbol{x}, 0) = 0 \ \forall\ i \in [1, D], \\ \tau_{ij}(\boldsymbol{x}, 0) = 0 \ \forall\ i, j \in [1, D], \end{aligned} \tag{2.20}$$

where D is the space dimension of the simulation.

Different boundary conditions can be applied:

- Rigid boundaries (Dirichlet conditions),
- Free surface conditions,
- Absorbing boundary conditions.

For the Dirichlet condition: $u_i = 0\ \forall\ i \in 1, D$ on Γ^d, where Γ^d represents the rigid surface of the physical domain.

For the free surface conditions: $\tau \cdot \overrightarrow{n} = 0$ $(\tau_{ij} n_j = 0)$ on Γ^s, where Γ^s is the free surface.

For the absorbing boundary conditions, we can use the following types: Paraxial conditions or Perfectly Matched Layer (PML) conditions. We will discuss this topic further.

The outer boundary $\delta\Omega$ is the union of all possible boundary conditions considered in each one of our studies.

2.1.5 Viscoelasticity in the wave equation.

In the previous equations we assumed that the Earth is perfectly elastic, which implies that elastic moduli and seismic waves velocities are independent of frequency. However, in reality we observe that the wave's amplitude decays with time, due to the effects of dispersion and attenuation, which significantly affects the amplitude and arrival time of the waves [Carcione, 1993; Liu et al., 1976]. In order to reflect the effects of the attenuation, the Hooke's law (equation 2.4) needs to be modified in the next way:

$$\boldsymbol{\tau}(t) = \int_{-\infty}^{\infty} \partial_t \boldsymbol{C}(t-\eta) : \nabla \boldsymbol{u}(\eta) \mathrm{d}\eta, \tag{2.21}$$

where $\boldsymbol{\tau}$ is the stress tensor, $\boldsymbol{C}$ is the elastic tensor, and $\boldsymbol{u}$ is the vector of displacement.

The viscoelasticity of a medium could be modeled by using a series of SLS mechanisms, and applying some of the rheological models: Zener, Maxwell, or Kelvin-Voigt body Standard Linear Solid (SLS) models. In this work we assumed a Zener SLS model.

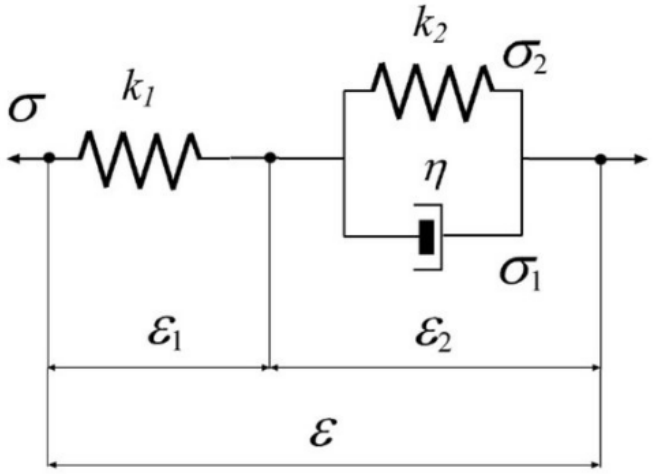

Figure 2.1. Mechanical model for a Zener material. σ represents the stresses (in the manuscript represented by τ), ϵ represents the strains, k represents a spring (elastic behaviour), and η represents a dashpot (viscous behaviour). Taken from Carcione [2007].

In a viscoelastic material its instantaneous response is given by the unrelaxed modulus C^U_{ijkl}, this means that it behaves as an elastic material [Moczo and Kristek, 2005]. However, the longterm equilibrium response is given by the relaxed modulus C^R_{ijkl}. The relation between these two modulus is given by:

$$C^U_{ijkl} = C^R_{ijkl}\left[1 - \sum_{l=1}^{L}(\eta^{\epsilon\ell}_{ijkl}/\eta^{\tau\ell})\right], \tag{2.22}$$

where $\eta^{\tau\ell}$ and $\eta^{\epsilon\ell}_{ijkl}$ are the stress relaxation time and the strain relaxation time respectively, and L represents the number of SLS mechanisms. To compute the relaxation times we use the code SolvOpt developed by Lombard and Matignon [2016]. The quality factor is defined as

(according to Moczo and Kristek [2005]):

$$Q(\epsilon) = \frac{\mathrm{Re}M(\epsilon)}{\mathrm{Im}M(\epsilon)}, \tag{2.23}$$

where $\boldsymbol{M}(t) = \partial_t \boldsymbol{C}$. The quality factor, which can be considered constant in a wide range of frequencies, can be modeled as a series of L SLS mechanisms, with $L = 3$, commonly used to mimic the quality factor Q [Martin and Komatitsch, 2009].

The modulus defect $\delta \boldsymbol{C}^\ell$ associated with each standard linear solid (SLS) mechanism is defined as :

$$\delta C^\ell_{ijkl} = -C^R_{ijkl}(1 - \eta^{\epsilon\ell}_{ijkl}/\eta^{\tau\ell}) \tag{2.24}$$

According to Komatitsch and Tromp [1999] equation 2.21 can be written in the form:

$$\boldsymbol{\tau} = \boldsymbol{C}^U : \nabla \boldsymbol{u} - \sum_{\ell=1}^{L} \boldsymbol{R}^\ell, \tag{2.25}$$

where for each standard linear solid

$$\partial_t \boldsymbol{R}^\ell = -\boldsymbol{R}^\ell/\eta^{\tau\ell} + \delta \boldsymbol{C}^\ell : \nabla \boldsymbol{u}/\eta^{\tau\ell}. \tag{2.26}$$

Therefore the elastodynamic equations in a viscoelastic medium could be written as:

$$\begin{aligned} \rho \partial_t \boldsymbol{v} &= \nabla \cdot \boldsymbol{\tau} \\ \partial \boldsymbol{\tau} &= \boldsymbol{C}^U : \nabla \boldsymbol{v} - \sum_{\ell=1}^{L} \boldsymbol{R}^\ell \\ \partial_t \boldsymbol{R}^\ell &= -\boldsymbol{R}^\ell/\eta^{\tau\ell} + \delta \boldsymbol{C}^\ell : \nabla \boldsymbol{u}/\eta^{\tau\ell}, \end{aligned} \tag{2.27}$$

where $\boldsymbol{v}$ represents the velocity vector.

To represent equations 2.27 in an isotropic medium, we can express the strain tensor $\boldsymbol{\epsilon}$ as:

$$\epsilon_{ij} = \frac{1}{2}\left(\frac{\partial v_i}{\partial x_j} + \frac{\partial v_j}{\partial x_i}\right), \tag{2.28}$$

and the trace of the strain tensor is represented as: $Tr(\epsilon) = \sum_{i=1}^{D} \epsilon_{ii}$, where D is the spatial dimension. The indices i and j can take values of 1, 2, or 3. Therefore, equations 2.27 could be expressed as:

$$\begin{aligned} \rho \partial_t v_i &= \partial_j \tau_{ij} \\ \partial_t \tau_{ij} &= \lambda^U \delta_{ij} Tr(\boldsymbol{\epsilon}) + 2\mu^U \epsilon_{ij} - \sum_{\ell=1}^{L} R^\ell_{ij} \\ \partial_t R^\ell_{ij} &= -R^\ell_{ij}/\eta^{\tau\ell} + \delta C^\ell_{ik} \epsilon_{kj}/\eta^{\tau\ell}, \end{aligned} \tag{2.29}$$

In a practical view, to simulate the viscoelasticity of the medium using the Zener model, one needs to adapt the quality factor Q to the frequency range of the signal's spectrum by using relaxation mechanisms. The relaxation times are represented by points in the frequency interval, and their associated weights. To ensure the positivity of the weights, we follow the non-linear optimization approach proposed by Blanc et al. [2016]. This approach gives a better fit between the quality factor Q and the interval of frequencies desired.

2.2 Reverse Time Migration method.

The *Reverse Time Migration* method (RTM) is a reflectivity imaging method based on the reflection and pattern radiation of seismic waves. It highlights the small wavelengths of a model around a large wavelength background model and gives the position of the interfaces. In other words, this method detects the impedance changes of the subsoil materials. The image intensity (amplitude) is related to the impedance contrast between two materials. If this contrast is very large, it will show up very well in the image, but if the impedance contrast is very low, it will not show up well in the image obtained.

Formally, among the first works that talk about RTM, we can find: Baysal et al. [1983], McMechan [1983], and Whitmore [1983], where the classical RTM is presented. After having recorded and filtered the real data (vertical component for acoustic RTM and all components for elastic RTM), we can define 3 stages in RTM:

- Calculation of the forward problem: In this stage we solve the elastodynamic equations to obtain the predicted data (equation 2.17 in case of an elastic rheology) for the background model. This model represents the values of the subsoil predicted parameters.

- Calculation of the classical back-propagated and adjoint problems: In this stage we simultaneously solve two wave equations (one for the forward "back-propagated" field and one for the adjoint field). For more detail we refer to the subsection 2.6.

- Calculation of the imaging condition: In this stage we construct the subsoil image based on correlations of back-propagated and adjoint fields. There are two principal approaches: The classical and the adjoint imaging condition. We will discuss these two approaches in the next subsections.

Imaging condition is a crucial step in the RTM process, because in this stage we construct the subsoil image. As mentioned in the first paragraph, the RTM highlights the subsurface interfaces. In the case of the adjoint imaging condition, the resulting image is also the gradient of the misfit function with respect to the parameters, with the parametrizations (ρ, λ, μ), (ρ, V_p, V_s), and (ρ, Z_p, Z_s). This fact is related to the detection of interfaces, because the gradient represents the change with respect to a parameter (which occurs where there is an interface).

In practice, as we have shown in the flowchart of (Figure 1.15 in section 1.3.1), we start by computing the forward problem by solving the elastodynamic equations. We use the background

model, that could be obtained by smoothing the true model (in our case we applied a Gaussian filter), saving the predicted data at the receiver's position. Then we compute the adjoint problem injecting the difference of the observed and the predicted data as the adjoint source. We also compute the back-propagated problem using the predicted data. Finally, we correlate the adjoint and back-propagated problems to obtain the image of the subsoil.

To conclude this subsection, it is important to emphasize that the RTM method highlights the small wavelengths involved in interface detection. It is not an inversion method in the sense that we will not find an approximation of the real parameters. The final result represents the change of the misfit function with respect to the subsurface parameters.

2.2.1 Classical imaging condition.

The calculation of the forward problem consists in solving the elastodynamic equations (2.17 or 2.18). This step is similar to the classical and adjoint-based imaging conditions.

The classical imaging condition could be obtained according to Claerbout [1971] and Chattopadhyay and McMechan [2008] as follows:

$$I(\boldsymbol{x}) = \sum_t S(\boldsymbol{x}, t) R(\boldsymbol{x}, t), \tag{2.30}$$

where I represents the image in the $\boldsymbol{x}$ domain, S is the source wavefield propagated in time from the source coordinates, and R is the receiver wavefield propagated backward in time from the receiver coordinates.

The equation 2.30, can also be seen as a correlation between the source and receiver wavefields. When the amplitude of this correlation increases, this indicates a coincidence between the two wavefields, which in an ideal case only occurs at reflectors (interface locations). However it is well known that the multiples which correspond to boundaries in the layer produce spurious interfaces associated with real interfaces.

Indeed, for example in the scheme shown in figure 2.2 we summarize how direct waves and multiples interact and can generate true or spurious interfaces: interferences can occur between direct (or forward multiples) and back-propagated multiples. More particularly we can see how the direct wave $\mathcal{D}_{\mathcal{F}}$ interacting with the primary $\mathcal{P}_{\mathcal{B}}$ generates an interface at the correct depth at point G_1. However, when interacting with the multiple $\mathcal{M}^1_{\mathcal{B}}$, an incorrect interface H is produced. We can also see other phenomena that could occur, such as the interference of the multiples with the primaries that occurs at the correct interface J. We will see how we could treat this problem in the following chapters. The reader is referred to chapter 3 for more details (section 3.1.3).

The RTM (*Reverse Time Migration*) method uses this imaging condition and, as its name indicates, a "reverse time propagation" is performed. It is important to clarify that RTM is not an inversion process, because the main objective is to highlight the subsurface interfaces at their correct position, without estimating the subsurface parameters.

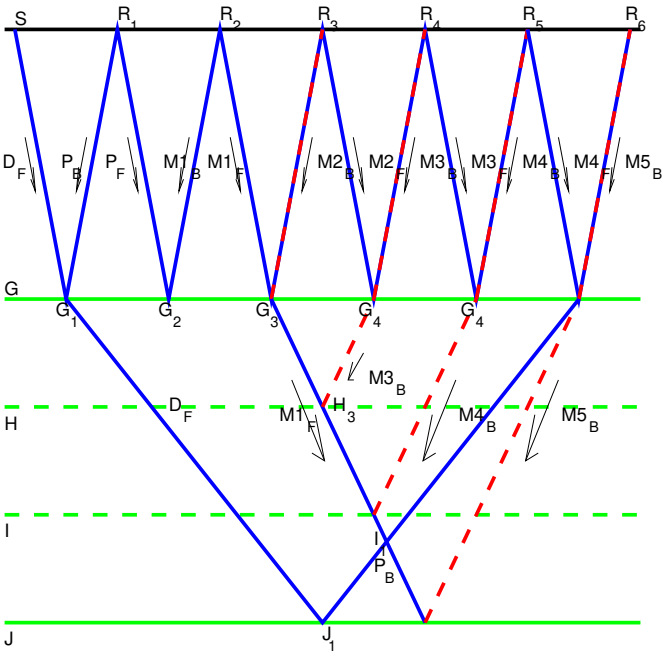

Figure 2.2. Correlation between the direct wavefield $\mathcal{D}_{\mathcal{F}}$ of the forward wavefield $\mathcal{F}$ and the primaries and multiples ($\mathcal{P}_{\mathcal{B}}$ and $\mathcal{M}_{\mathcal{B}}$) of the back-propagated wavefield $\mathcal{B}$. We can see that the direct wave $\mathcal{D}_{\mathcal{F}}$ interacts with the primary $\mathcal{P}_{\mathcal{B}}$ from receiver R_1 at the interface G represented with a solid green line (the exact interaction is at the point G_1), and it interacts with the primary coming from receiver R_6 at the interface J represented with a solid green line (the exact interaction is at the point J_1) . However we can also see that the multiple $M1_F$ interacts with different "back-propagated" multiples ($M3_B$ and $M4_B$) from receivers R_4, R_5 at spurious interfaces H and I respectively (represented with dashed green lines). We can also see another phenomenon called interference: the multiple $M1_F$ interacts with the multiples $M5_B$ from receiver R_6 at the true interface J.

2.2.2 Adjoint-based RTM imaging condition.

The objective of seismic imaging is to highlight the high frequencies of the structures of the model to appreciate the subsurface interfaces. The adjoint theory-based methods reach this objective because they calculate the gradient of a misfit function with respect to the subsurface parameters. This gradient highlights the perturbation of the data misfit function with respect to a perturbation of the low frequency model, which makes high frequencies (like the model interfaces) to appear more clearly.

In order to formulate the adjoint-based imaging condition we focus our attention to the adjoint theory formulation. In the adjoint theory method we aim at computing the gradient of the misfit function $\chi(\boldsymbol{m})$, which depends on the parameter $\boldsymbol{m}$. This function is defined as :

$$\chi(\boldsymbol{m}) = \frac{1}{2}\sum_{r=1}^{N}\int_0^T ||\boldsymbol{u}(\boldsymbol{x_r}, t, \boldsymbol{m}) - \boldsymbol{d}(\boldsymbol{x_r}, t)||^2 dt, \tag{2.31}$$

where $\boldsymbol{u}$ represents the synthetic data that depend on the current parameters $\boldsymbol{m}$, which is the initial background model, $\boldsymbol{d}$ represents the recorded (observed) data, $\boldsymbol{x_r}$ are the coordinates of the receivers, N is the total number of receivers, and T is the total time of the simulation. More important we aim at computing a perturbation of the initial model that is a function of the perturbation of χ.

This misfit χ function is perturbed under the constraint that the synthetic data $\boldsymbol{u}$ must satisfy the wave equations (2.17), which in a more compacted way are expressed as:

$$\begin{aligned} \rho\frac{\partial^2 \boldsymbol{u}}{\partial t^2} &= \nabla\cdot\boldsymbol{\tau} + \boldsymbol{f}, \\ \boldsymbol{\tau} &= \boldsymbol{C} : \nabla\boldsymbol{u}. \end{aligned} \tag{2.32}$$

Simultaneously, the adjoint-wave equations must be solved. In the general case, these equations are expressed as:

$$\begin{aligned} \rho\frac{\partial^2 \boldsymbol{u}^\dagger}{\partial t^2} &= \nabla\cdot\boldsymbol{\tau}^\dagger + \boldsymbol{f}^\dagger, \\ \boldsymbol{\tau}^\dagger &= \boldsymbol{C}^\dagger : \nabla\boldsymbol{u}^\dagger, \end{aligned} \tag{2.33}$$

where the variables with superscript † indicate the adjoint variables associated to the adjoint problem. Hereafter we describe how these adjoint equations are derived.

Following the Lagrange multiplier method, we introduce this new misfit function to optimize the minimization problem:

$$\begin{aligned} \chi'(\boldsymbol{m}) = &\frac{1}{2}\sum_{r=1}^{N}\int_0^T ||\boldsymbol{u}(\boldsymbol{x_r}, t, \boldsymbol{m}) - \boldsymbol{d}(\boldsymbol{x_r}, t)||^2 \mathrm{d}t \\ &- \int_0^T\int_\Omega \boldsymbol{\gamma}\cdot\left[\rho\frac{\partial^2\boldsymbol{u}}{\partial t^2} - \nabla\cdot\boldsymbol{\tau} - \boldsymbol{f}\right]\mathrm{d}\Omega\mathrm{d}t, \end{aligned} \tag{2.34}$$

where Ω represents the physical domain, and $\boldsymbol{\gamma} = \boldsymbol{u}^\dagger$ denotes the adjoint (Lagrange multiplier) vector that must satisfy equations 2.33. This new misfit function is the same as the original one because $\rho\frac{\partial^2 \boldsymbol{u}}{\partial t^2} - \nabla \cdot \boldsymbol{\tau} - \boldsymbol{f} = 0$. This implies that by minimizing the misfit function χ', the original misfit function χ is also minimized under the constraint that the elastic wave equations 2.32 are satisfied.

To find the minimum of χ', we must perturb χ' with respect to the physical parameters using the chain rule in the following way:

$$\begin{aligned}\delta\chi' = \int_O^T \int_\Omega \sum_{r=1}^{N} \left[\boldsymbol{u}(\boldsymbol{x_r}, t, \boldsymbol{m}) - d(\boldsymbol{x_r}, t)\right] \delta(\boldsymbol{x} - \boldsymbol{x_r}) \cdot \delta\boldsymbol{u}(\boldsymbol{x}, t) d\Omega dt \\ - \int_0^T \int_\Omega \boldsymbol{\gamma} \cdot \left[\delta\rho \frac{\partial^2 \boldsymbol{u}}{\partial t^2} - \nabla \cdot (\delta\boldsymbol{C} : \nabla\boldsymbol{u} - \delta\boldsymbol{f})\right] d\Omega dt \\ - \int_0^T \int_\Omega \boldsymbol{\gamma} \cdot \left[\rho \frac{\partial^2 \delta\boldsymbol{u}}{\partial t^2} - \nabla \cdot (\boldsymbol{C} : \nabla\delta\boldsymbol{u})\right] d\Omega dt, \end{aligned} \tag{2.35}$$

where $\delta(\boldsymbol{x} - \boldsymbol{x_r}) = 1$ if $\boldsymbol{x} = \boldsymbol{x_r}$ (receiver position), and $\delta(\boldsymbol{x} - \boldsymbol{x_r}) = 0$ if $\boldsymbol{x} \neq \boldsymbol{x_r}$.

By integrating by parts with respect to time and space both $\boldsymbol{u}$ and $\delta\boldsymbol{u}$, we obtain that:

$$\begin{aligned}\delta\chi &= \int_0^T \int_\Omega \sum_{r=1}^{N} [\boldsymbol{u}(\boldsymbol{x_r}, t) - \boldsymbol{d}(\boldsymbol{x_r}, t)] \delta(\boldsymbol{x} - \boldsymbol{x_r}) \cdot \delta\boldsymbol{u}(\boldsymbol{x}, t) d\Omega dt \\ &- \int_0^T \int_\Omega \left(\delta\rho\boldsymbol{\gamma} \cdot \frac{\partial^2 \boldsymbol{u}}{\partial t^2} + \nabla\boldsymbol{\gamma} : \delta\boldsymbol{C} : \nabla\boldsymbol{u} - \boldsymbol{\gamma} \cdot \delta\boldsymbol{f}\right) d\Omega dt \\ &- \int_0^T \int_\Omega \left[\rho \frac{\partial^2 \boldsymbol{\gamma}}{\partial t^2} - \nabla \cdot \boldsymbol{C} : \nabla\boldsymbol{\gamma}\right] \cdot \delta\boldsymbol{u} \; d\Omega dt \\ &- \int_\Omega \left[\rho \left(\boldsymbol{\gamma} \cdot \frac{\partial \delta\boldsymbol{u}}{\partial t} - \frac{\partial \boldsymbol{\gamma}}{\partial t} \cdot \delta\boldsymbol{u}\right)\right]_0^T d\Omega dt \\ &+ \int_0^T \int_{\partial\Omega} \boldsymbol{\gamma} \cdot [\hat{n} \cdot (\delta\boldsymbol{C} : \nabla\boldsymbol{u} + \boldsymbol{C} : \nabla\delta\boldsymbol{u})] - \hat{n} \cdot (\boldsymbol{C} : \nabla\boldsymbol{\gamma}) \cdot \delta\boldsymbol{u} \; d\Omega dt, \end{aligned} \tag{2.36}$$

where $[f]_0^T$ indicates $f(T) - f(0)$.

Applying free surface conditions as well as initial conditions we have:

$$\begin{aligned}\hat{n} \cdot (\delta\boldsymbol{C} : \nabla\boldsymbol{u} + \boldsymbol{C} : \nabla\delta\boldsymbol{u}) = 0 \text{ on } \Gamma^s \\ \delta\boldsymbol{u}(\boldsymbol{x}, 0) = \frac{\partial \delta\boldsymbol{u}(\boldsymbol{x}, 0)}{\partial t} = 0. \end{aligned} \tag{2.37}$$

Therefore, we can write that:

$$\begin{aligned}
\delta\chi &= \int_0^T \int_\Omega \sum_{r=1}^{N} [\boldsymbol{u}(\boldsymbol{x_r},t) - \boldsymbol{d}(\boldsymbol{x_r},t)]\delta(\boldsymbol{x}-\boldsymbol{x_r}) \cdot \delta\boldsymbol{u}(\boldsymbol{x},t) d\Omega dt \\
&- \int_0^T \int_\Omega \left(\delta\rho\boldsymbol{\gamma} \cdot \frac{\partial^2 \boldsymbol{u}}{\partial t^2} + \nabla\boldsymbol{\gamma} : \delta\boldsymbol{C} : \nabla\boldsymbol{u} - \boldsymbol{\gamma} \cdot \delta\boldsymbol{f} \right) d\Omega dt \\
&- \int_0^T \int_\Omega \left[\rho \frac{\partial^2 \boldsymbol{\gamma}}{\partial t^2} - \nabla \cdot \boldsymbol{C} : \nabla\boldsymbol{\gamma} \right] \cdot \delta\boldsymbol{u} \; d\Omega dt \\
&- \int_\Omega \left[\rho \left(\boldsymbol{\gamma} \cdot \frac{\partial \delta\boldsymbol{u}}{\partial t} - \frac{\partial \boldsymbol{\gamma}}{\partial t} \cdot \delta\boldsymbol{u} \right) \right]^T d\Omega dt \\
&- \int_0^T \int_{\partial\Omega} \hat{n} \cdot (\boldsymbol{C} : \nabla\boldsymbol{\gamma}) \cdot \delta\boldsymbol{u} \; d^2x dt. \qquad (2.38)
\end{aligned}$$

It is important to note that the Lagrange multiplier is equal to the adjoint wavefield ($\boldsymbol{\gamma}(\boldsymbol{x}, T-t) \equiv \boldsymbol{u}^\dagger(\boldsymbol{x},t)$). Therefore the Lagrange multiplier must satisfy the wave equations (2.33), and we can write that :

$$\rho \frac{\partial^2 \boldsymbol{\gamma}}{\partial t^2} - \nabla \cdot \boldsymbol{C} : \nabla\boldsymbol{\gamma} = \sum_{r=1}^{N} [\boldsymbol{u}(\boldsymbol{x_r},t) - \boldsymbol{d}(\boldsymbol{x_r},t)]\delta(\boldsymbol{x}-\boldsymbol{x_r})], \qquad (2.39)$$

with the following ending and free surface conditions:

$$\begin{aligned}
\boldsymbol{u}^\dagger(\boldsymbol{x},0) = \frac{\partial \boldsymbol{u}^\dagger(\boldsymbol{x},0)}{\partial t} = \boldsymbol{\gamma}(\boldsymbol{x},T) = \frac{\partial \boldsymbol{\gamma}(\boldsymbol{x},T)}{\partial t} = 0 \\
\hat{n} \cdot (\boldsymbol{C} : \nabla\boldsymbol{\gamma}) = 0 \text{ on } \Gamma^s. \qquad (2.40)
\end{aligned}$$

We can then see from equation 2.39 that the adjoint source is the difference between the synthetic and real data at the receiver locations as follows:

$$f^\dagger = \sum_{r=1}^{N} [\boldsymbol{u}(\boldsymbol{x_r},t) - \boldsymbol{d}(\boldsymbol{x_r},t)]\delta(\boldsymbol{x}-\boldsymbol{x_r}). \qquad (2.41)$$

Taking into account the equations 2.39 and 2.40, the perturbation of the misfit function with respect to the parameters is reduced to:

$$\delta\chi = -\int_0^T \int_\Omega \left(\delta\rho\boldsymbol{\gamma} \cdot \frac{\partial^2 \boldsymbol{u}}{\partial t^2} + \nabla\boldsymbol{\gamma} : \delta\boldsymbol{C} : \nabla\boldsymbol{u} - \boldsymbol{\gamma} \cdot \delta\boldsymbol{f} \right) d\Omega dt. \qquad (2.42)$$

For a well known source (i.e $\delta\boldsymbol{f} = 0$) we can write:

$$\delta\chi = \int_\Omega (\delta\rho K_\rho + \delta\boldsymbol{C} :: K_{\boldsymbol{C}}) \, \mathrm{d}\Omega, \qquad (2.43)$$

where $\delta \boldsymbol{C} :: K_{\boldsymbol{C}} = \delta C_{ijkl} K_{C_ijkl}$, and the sensitivity kernels can be expressed as:

$$\begin{aligned} K_\rho(\boldsymbol{x}) &= -\int_0^T \boldsymbol{u}^\dagger(\boldsymbol{x}, T-t)\ \frac{\partial^2 \boldsymbol{u}(\boldsymbol{x},t)}{\partial t^2}\ \mathrm{d}t, \\ K_{\boldsymbol{C}}(\boldsymbol{x}) &= -\int_0^T \nabla \boldsymbol{u}^\dagger(\boldsymbol{x}, T-t) : \nabla \boldsymbol{u}(\boldsymbol{x},t)\ \mathrm{d}t. \end{aligned} \tag{2.44}$$

Following an isotropic approach, $C_{ijkl} = (\kappa - \frac{2}{3}\mu)\delta_{jk}\delta_{lm} + \mu(\delta_{jm}\delta_{kl} + \delta_{kl})$. This is the same as equation 2.6, where we now introduce the bulk modulus $\kappa = \lambda + \frac{2}{3}\mu$. Integrating by parts the kernel K_ρ and considering an isotropic model, we could express the kernels in the following way for the parametrization (ρ, κ, μ):

$$\begin{aligned} K_\rho(\boldsymbol{x}) &= -\int_0^T \boldsymbol{v}^\dagger(\boldsymbol{x}, T-t)\boldsymbol{v}(\boldsymbol{x},t)\mathrm{d}t, \\ K_\kappa(\boldsymbol{x}) &= -\int_0^T \nabla \cdot \boldsymbol{u}^\dagger(\boldsymbol{x}, T-t)\nabla \cdot \boldsymbol{u}(\boldsymbol{x},t)\mathrm{d}t, \\ K_\mu &= -2\int_0^T \boldsymbol{D}^\dagger(\boldsymbol{x}, T-t) : \boldsymbol{D}(\boldsymbol{x},t)\mathrm{d}t, \end{aligned} \tag{2.45}$$

where $\boldsymbol{v}^\dagger$ and $\boldsymbol{v}$ represent the adjoint and forward time derivatives of the displacements, and

$$\begin{aligned} \boldsymbol{D} &= \frac{1}{2}[\nabla \boldsymbol{u} + \nabla \boldsymbol{u}^T] - \frac{1}{3}(\nabla \cdot \boldsymbol{u})\mathrm{I} \\ \boldsymbol{D}^\dagger &= \frac{1}{2}[\nabla \boldsymbol{u}^\dagger + \nabla \boldsymbol{u}^{\dagger^T}] - \frac{1}{3}(\nabla \cdot \boldsymbol{u}^\dagger)\mathrm{I}, \end{aligned} \tag{2.46}$$

indicate the forward and adjoint traceless strain deviator.

For the parametrization (ρ, α, β), where α and β denote the compression and shear wave velocities respectively, we can write the sensitivity kernels as follows :

$$\begin{aligned} K'_\rho &= K_\rho + K_\kappa + K_\mu, \\ K_\alpha &= 2\left(\frac{\kappa + \frac{4}{3}\mu}{\kappa}\right) K_\kappa, \\ K_\beta &= 2\left(K_\mu - \frac{4\mu}{3\kappa} K_\kappa\right). \end{aligned} \tag{2.47}$$

It is important to say that the development we have presented previously, is part of a process of inversion of the parameters (*Full Waveform Inversion*), where the adjoint source must be calculated as in equation 2.41. However, in the context of the RTM, the adjoint source could be injected through observed data only such as: $f^\dagger = \sum_{r=1}^{N} \boldsymbol{d}(\boldsymbol{x_r}, t)\delta(\boldsymbol{x} - \boldsymbol{x_r})$, as we discuss in subsection 2.2.1.

An interesting point about the adjoint imaging condition, is that the sensitivity kernels are the gradient of the misfit function (equation 3.3). This fact is exploited by the LSRTM method, which we will discuss in the next section.

2.3 Principles of the LSRTM method.

The *Least Squares Reverse Time Migration* (LSRTM) is an improvement of the RTM method, in which the reflectivity images are iteratively computed and improved by minimizing the seismic data residual misfit function. Among the improvements of LSRTM with respect to RTM, we can mention the following: images with fewer artifacts, better amplitude balancing and higher resolution [Feng and Schuster, 2017]. We can also refer to Dong et al. [2012], Dutta and Schuster [2014] and Wang et al. [2016].

In the first paragraph of the section 2.2, we said that RTM highlights the small wavelengths. This effect is better appreciated in LSRTM method. We can say that LSRTM method acts as a low wavelength filter. Indeed, at each iteration, the background reflectivity r_0, which contains large wavelengths initially, progressively loses these large wavelengths to finish with a reflectivity with a small wavelength (high wave number) content in which we can appreciate the interfaces. And now we detail the LSRTM algorithm.

We define here the recorded data as: $\boldsymbol{D} = \boldsymbol{Lm}$, where $\boldsymbol{L}$ is the forward modeling operator (using the Born approximation or a linearization of the elastodynamic equations) that is related to the solution of equations 2.17 or 2.29 in case of an elastic or visco-elastic rheology respectively, and therefore $\boldsymbol{Lm}$ is the forward problem applied to the real-parameter model of the subsoil $\boldsymbol{m}$. According to Dong et al. [2012] and Zhang et al. [2015] the first approximation to the reflectivity image is given by:

$$\boldsymbol{r_0} = \boldsymbol{L^T}[\boldsymbol{Lm_0} - \boldsymbol{D}], \tag{2.48}$$

where $\boldsymbol{L^T}$ is the migration operator, which is the adjoint of the forward operator, and $\boldsymbol{m_0}$ is the background model. The equation 2.48 also represents the RTM process.

We detail now the LSRTM algorithm. The LSRTM is a linearisation of the inverse problem that consists in computing the reflectivity model around an initial low frequency background model $\boldsymbol{m_0}$.

The misfit function for the LSRTM method is defined as:

$$\chi = \frac{1}{2}||\boldsymbol{Lr} - \boldsymbol{D}||^2, \tag{2.49}$$

in this equation, $\boldsymbol{Lr}$ represents a demigration process applied to the current reflectivity image $\boldsymbol{r}$. This process reconstructs the seismic reflection data from reflectivity images that were constructed with the RTM method (Weibull and Arntsen [2014], Zhang et al. [2015]).

Given the observed data $\boldsymbol{D}$, the initial reflectivity model $\boldsymbol{r_0}$ and the initial predicted data $\boldsymbol{d_0} = \boldsymbol{Lr_0}$, we iteratively update the reflectivity model at each i-th iteration of a linear conjugate gradient process as follows:

1. Compute the gradient of the misfit function as:

$$\mathbf{g}^{i+1} = \mathbf{L}^T(\mathbf{L}\mathbf{r}^{i+1} - \mathbf{d}) \tag{2.50}$$

2. Update the preconditioned gradient as follows:

$$\begin{aligned} \mathbf{dk}^{i+1} &= -\mathbf{C}\mathbf{g}^{i+1} + \beta \mathbf{dk}^{i}, \\ \beta &= \frac{(\mathbf{g}^{i+1})^T \mathbf{C}\mathbf{g}^{i+1}}{(\mathbf{g}^{i})^T \mathbf{C}\mathbf{g}^{i}}, \end{aligned} \tag{2.51}$$

where $\boldsymbol{C}$ can be defined as the approximation of the inverse of the Hessian B (taken commonly as the diagonal of the Hessian) or the forward energy as follows:

$$\begin{aligned} \boldsymbol{C} &= \left(\boldsymbol{diag}(\boldsymbol{B})^{-1}\right)^{i+1} = \frac{\boldsymbol{r^{i+1} - r^{i}}}{\boldsymbol{g^{i+1} - g^{i}}}, \\ \boldsymbol{C} &= 1/\int_0^T (\boldsymbol{u_x}^2 + \boldsymbol{u_y}^2 + \boldsymbol{u_z}^2) dt. \end{aligned} \tag{2.52}$$

The tensor **dk** represents the new search direction to find the parameters that minimize the misfit function; and the parameter β is computed using the Fletcher-Reeves formula [Nocedal and Wright, 2006].

3. Compute the step length as is defined in Nocedal and Wright [2006] for the Line Search Newton-CG algorithm as follows:

$$\alpha = \frac{(\mathbf{dk}^{i+1})^T \mathbf{g}^{i+1}}{(\mathbf{L}\mathbf{dk}^{i+1})^T \mathbf{L}\mathbf{dk}^{i+1}}, \tag{2.53}$$

where **Ldk** is the demigration process applied to **dk**.

4. Update the new reflectivity model as:

$$\boldsymbol{r}^{i+2} = \boldsymbol{r}^{i+1} + \alpha \mathbf{dk}^{i+1} \tag{2.54}$$

In the first iteration we set $\beta = 0$, therefore the first search direction is defined as: $\mathbf{dk}^0 = -\mathbf{g}^0$. Moreover, to compute the approximated Hessian used in equation 2.53, we applied a finite differences approach as follows: $\mathbf{B}\mathbf{k}^{i+1} = (\mathbf{g}^{i+1} - \mathbf{g}^{i})/\Delta \boldsymbol{r}$ (with $\Delta \boldsymbol{r} = \mathbf{r}^{i+1} - \mathbf{r}^{i}$). This implies that for the first iteration we can not compute the Hessian following this approach, and instead the forward energy is thus rather used in this case as a preconditionner.

2.4 Principles of the FWI method

Unlike the LSRTM method, the FWI is a non-linear inversion method whose objective is to invert the model parameter m instead of reflectivity r, and therefore the operator L and L^T are different from those of the LSRTM method as we will see below. We must minimize the misfit function defined as:

$$\chi = \frac{1}{2}||\boldsymbol{L}\boldsymbol{m} - \boldsymbol{D}||^2 + \frac{\eta}{2}||\sqrt{\boldsymbol{W}}(\boldsymbol{m} - \boldsymbol{m_0})||^2, \tag{2.55}$$

where $\boldsymbol{D}$ are the observed data, $\boldsymbol{Lm}$ are the predicted data calculated by the forward problem applied to the current model parameters $\boldsymbol{m}$ as in equations 2.17 or 2.29 for elastic or viscoelastic rheology. The second term $\frac{\eta}{2}||\sqrt{\boldsymbol{W}}(\mathbf{m}-\boldsymbol{m_0})||^2$ is related to a regularization process. It seeks to penalize those parameter values that diverge from the a priori model $\boldsymbol{m_0}$. The matrix $\boldsymbol{W}$ is a depth weighting operator to reduce the non-uniqueness of the solution. In this work we choose to increase this weight from the bathymetry with a factor of z^2, where z represents depth. Indeed, we follow the same idea as in the next chapter where the model should be better taken into account at depth. Due to the geometrical divergence of the wave fields with distance to the source, the gradients tend to decrease with the distance to the source. It is thus important to increase the perturbations at depth by increasing this weight with depth and consequently to obtain model changes at depth. The parameter η scales the values of the regularization term and the misfit in the same range. For more information about the regularization term, we refer to Asnaashari et al. [2013]; Hermans et al. [2012]; Martin et al. [2017, 2013, 2018]; Monteiller et al. [2015].

In order to minimize the misfit function χ, iterative techniques such as the steepest-descent or the non-linear *Conjugate Gradient* method (CG) are implemented. We iteratively update the subsoil parameters at each i-th iteration of the CG inversion process as follows:

1. Compute the gradient of the misfit function:

$$\mathbf{g}^{i+1} = \mathbf{L}^T(\mathbf{L}\mathbf{m}^{i+1} - \mathbf{d}) + \eta\boldsymbol{W}(\mathbf{m} - \boldsymbol{m_0}). \tag{2.56}$$

The gradient of the misfit function is equivalent to the sensitivity kernels we defined in RTM method when the adjoint source is defined as the difference between predicted and real data. In this step it is possible to pre-condition the gradient as in Tang and Lee [2010], Métivier et al. [2015], Feng and Schuster [2017].

2. Update the preconditioned gradient as follows:

$$\begin{aligned} \mathbf{dk}^{i+1} &= -\mathbf{C}\mathbf{g}^{i+1} + \beta\mathbf{dk}^i, \\ \beta &= \frac{(\mathbf{g}^{i+1})^T\mathbf{C}\mathbf{g}^{i+1}}{(\mathbf{g}^i)^T\mathbf{C}\mathbf{g}^i}, \end{aligned} \tag{2.57}$$

where $\boldsymbol{C}$ can be defined as the approximation of the inverse of the Hessian B (taken commonly as the diagonal of the Hessian) or the forward energy as follows:

$$\begin{aligned} \boldsymbol{C} &= \left(\boldsymbol{diag(B)^{-1}}\right)^{i+1} = \frac{\boldsymbol{m^{i+1}} - \boldsymbol{m^i}}{\boldsymbol{g^{i+1}} - \boldsymbol{g^i}} \\ \boldsymbol{C} &= 1/\int_0^T (\boldsymbol{u_x}^2 + \boldsymbol{u_y}^2 + \boldsymbol{u_z}^2)dt \end{aligned} \tag{2.58}$$

The tensor **dk** represents the new search direction to find the parameters that minimize the misfit function; and the parameter β is computed using the Fletcher-Reeves formula [Nocedal and Wright, 2006].

3. In contrast to the LSRTM method, in the FWI we don't apply the equation 2.53 because FWI is a non-linear method. We must therefore propose a step α that satisfies Wolfe's conditions to ensure convergence, which is more suitable to non-linear inversions. Wolfe conditions are defined according to Nocedal and Wright [2006] as:

$$\begin{aligned} \chi(\boldsymbol{m_i} + \alpha_i \boldsymbol{dk_i}) &\leq \chi(\boldsymbol{m_i}) + c_1 \alpha_k \nabla \chi_i^T \boldsymbol{dk_i}, \\ |\nabla \chi(\boldsymbol{m_i} + \alpha_i \boldsymbol{dk_i})^T \boldsymbol{dk_i}| &\leq c_2 |\nabla \chi_i^T \boldsymbol{dk_i}|, \end{aligned} \tag{2.59}$$

where i denotes the iteration step, $\nabla\chi$ represents the gradient of the misfit function ($\boldsymbol{g}$=$\nabla\chi$), and $0 < c_1 < c_2 < 1$ (in this work we use $c_1 = 0.1$, $c_2 = 0.4$). The first condition, also known as the Armijo condition, is related to the convergence of the misfit function (the misfit function must decay at each iteration). The second condition (curvature condition) is related to the slope of the misfit function : this condition means that the absolute value of the new slope smaller that c_2 times the absolute value of the initial slope.

In this work we define the first step length as: $\alpha = max(abs(0.1\mathbf{m}/\mathbf{dk}))$. In this way we ensure to have : $max(abs(\alpha\mathbf{dk}/\mathbf{m})) = 0.1$. If this step length does not satisfy Wolfe's conditions, we try half of this step length until some step length satisfies these conditions. Another option is testing a given number of step lengths and take among those that satisfy Wolfe's conditions the one that produces the minimum misfit.

4. Update the new model as:

$$\boldsymbol{m}^{i+2} = \boldsymbol{m}^{i+1} + \alpha \mathbf{dk}^{i+1} \tag{2.60}$$

We should notice that for the first iteration of the FWI process (which is the first iteration of the steepest descent) it is not possible to compute equations 2.57 because we do not have access to the first perturbation $\mathbf{dk}^i$. For this reason in the first iteration we should set $\beta = 0$, therefore the first search direction is defined as: $\mathbf{dk}^0 = -\mathbf{g}^0$ which is the gradient computed for the background (i.e initial) model. Moreover, to compute the Hessian used in equation 2.53, we applied a finite differences approach as follows: $\mathbf{Bk}^{i+1} = (\mathbf{g}^{i+1} - \mathbf{g}^i)/\Delta\mathbf{m}$ (with $\Delta\mathbf{m} = \mathbf{m}^{i+1} - \mathbf{m}^i$). This implies that for the first iteration we can not compute the pseudo-Hessian following this approach. However, in this work we prefer to normalize the kernels in all the iterations by the forward energy because no numerical instabilities are appearing with this normalization unlike normalizing by the pseudo-Hessian which introduces numerical instabilities. Therefore we must find a first step length using other approaches. In Nocedal and Wright [2006], it is recommended to take α equal to 1.

In Figure 2.3, we present a comparison between the flowcharts of the LSRTM and FWI methods. One difference is that in order to obtain the first reflectivity model for LSRTM, the RTM is applied to the background model. In the FWI we can also obtain the reflectivity by calculating the gradient of the current model, this calculation (kernels calculated by RTM) is implicitly performed in the FWI to find the search direction of the new model, unlike the

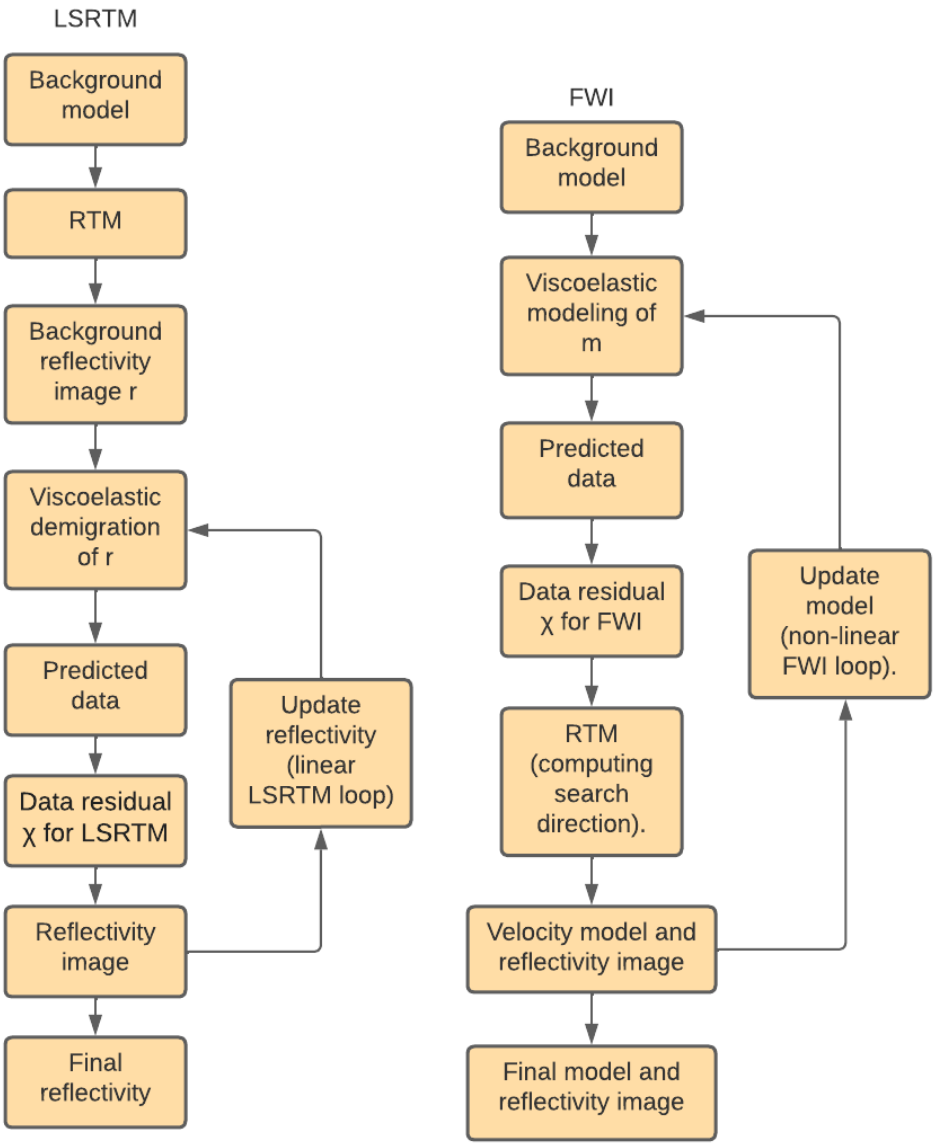

Figure 2.3. Comparison between the flowcharts of the LSRTM and FWI methods.

LSRTM technique where the reflectivity is optimized by always using the background model.

2.5 Numerical solution of the wave equation.

The study of seismic wave propagation in homogeneous continuous media is possible for simple geometries by means of the analytical solution. However, in realistic (heterogeneous) media, it is necessary to discretize the elastodynamic equations in space and time through specific numerical methods.

Numerical methods can be classified into two main categories:

- Weak formulation methods based on integral techniques such as the integral form of the wave equation. Among these methods we can cite: Finite elements, spectral elements,

Discontinuous Galerkin, and the boundary element method. We refer to the appendix D for more details.

- Strong formulation methods based on differential discretizations such as the finite differences and pseudo-spectral methods.

In the next subsection we will talk in more detail about the finite difference method that is implemented in UNISOLVER. We used it for our different imaging studies.

2.5.1 Finite differences method.

The finite differences method has been first applied for wave equations context by Yee [1966], Alford et al. [1974], Kelly et al. [1976],Madariaga [1976], Virieux [1986]. This method consists in approximating the spatial domain through finite cells in which the solution is calculated.

Finite differences are based on Taylor series, which are defined as follows:

$$f(x) = \sum_{n=0}^{\infty} \frac{f(x_i)^n}{n!}(x - x_i)^n + O(h^{n+1}), \tag{2.61}$$

where f is a continuously differentiable function of x, x_i denotes a sample where the function is known, $f(x_i)^n$ represents the n-th derivative of f at the sample x_i, n is the approximation order, and $O(h^{n+1})$ is the truncation error.

Leting $n = 1$, and $x - x_i = \Delta x$ denoting the spatial sampling, we can write:

$$f(x_{i+1}) = f(x_i) + \frac{\partial f}{\partial x}(x_i)\Delta x + O(h^2). \tag{2.62}$$

Then we can express different spatially discretized derivatives at first and the second order:

$$\begin{aligned} \frac{\partial f}{\partial x}(x_i) &= \frac{f(x_{i+1}) - f(x_i)}{\Delta x} + O(h) \\ \frac{\partial f}{\partial x}(x_i) &= \frac{f(x_i) - f(x_{i-1})}{\Delta x} + O(h) \\ \frac{\partial f}{\partial x}(x_i) &= \frac{f(x_{i+1}) - f(x_{i-1})}{2\Delta x} + O(h^2), \end{aligned} \tag{2.63}$$

which represent the backward, forward and central derivatives respectively.

In this work we prefer to use fourth-order staggered grid discretization as described in the next subsection.

2.5.2 Spatial and temporal discretization.

We use staggered grids [Graves, 1996; Virieux, 1986] as shown in 2D to visualize it better in the figure 2.4.

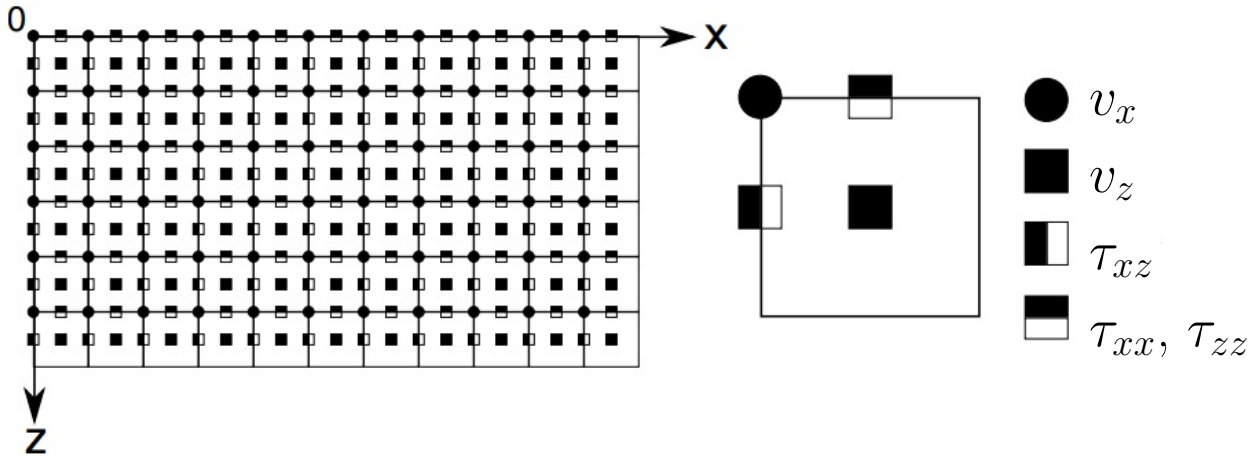

Figure 2.4. Discretization of the spatial domain in a 2D section following the staggered grids proposed by Virieux [1986] at the second-order or Graves [1996] at the fourth-order.

In this particular mesh, the spacing between two adjacent elements is $\frac{\Delta x}{2}$. For each variable f (that can take the values of particle velocity components v_i or stresses τ_{ij}), we can write the spatial derivatives at the 4-th order in space as follows:

$$\begin{aligned}\frac{\partial f}{\partial x} \mid x_{i+1/2} &= \frac{-f(x_{i+2}) + 27f(x_{i+1}) - 27f(x_i) + f(x_{i-1})}{24\Delta x} + O(h^4),\\ \frac{\partial f}{\partial x} \mid x_{i-1/2} &= \frac{-f(x_{i+1}) + 27f(x_i) - 27f(x_{i-1}) + f(x_{i-2})}{24\Delta x} + O(h^4).\end{aligned} \tag{2.64}$$

Similar calculations are applied along y and z directions.

The discretization in time is performed by using the second-order leap-frog time-stepping algorithm [Virieux, 1986]. This algorithm is expressed in a compact form as follows :

$$\begin{aligned}\boldsymbol{v}^{n+1} &= \boldsymbol{v}^n + \Delta t(div(\boldsymbol{\tau}^{n+1/2}) + \boldsymbol{f}^{n+1/2}),\\ \boldsymbol{\tau}^{n+1/2} &= \boldsymbol{\tau}^{n-1/2} + \Delta t \boldsymbol{C} : \dot{\boldsymbol{\epsilon}}(\boldsymbol{v}^n),\end{aligned} \tag{2.65}$$

where n represents the n-th sample in time and Δt denotes the time sampling.

2.5.3 Dispersion and stability conditions.

To determine the resolution of the grid (spatial sampling interval), it is necessary to avoid numerical dispersion, which is a phenomenon produced by an inadequate spatial sampling of the simulated signal in the frequency range of the source. According to Moczo et al. [2000], in practice it must be fulfilled that the minimum wavelength is discretized by at least 6 grid points for a 4th order approximation and at least 10 points for the 2nd order approximation as follows:

$$\begin{aligned}N_\lambda &= \frac{\beta_{min}}{\Delta x f_{max}} \geq 10 \text{ for } 2nd \text{ order},\\ N_\lambda &= \frac{\beta_{min}}{\Delta x f_{max}} \geq 6 \text{ for } 4th \text{ order},\end{aligned} \tag{2.66}$$

where N_λ is the minimum number of points per minimum wavelength, β_{min} is the minimum value of the seismic velocities associated to the shear wave velocity, and f_{max} is the maximum source frequency (Nyquist frequency).

To determine the sampling interval in time, the stability condition must be satisfied as follows [Moczo et al., 2000]:

$$\Delta t \frac{\alpha_{max}}{h_{min}} \leq \frac{6}{7\sqrt{3}}, \tag{2.67}$$

considering that $h = \Delta x = \Delta y = \Delta z$ and α_{max} is the maximum value of the compressional seismic velocity. It is very important to satisfy the stability condition to ensure that the amplitudes of the wavefields remain bounded.

2.5.4 Absorbing boundary conditions.

In addition, it is also essential to take into account the absorbing boundaries. It happens that, because the computational domain is bounded, spurious reflections are generated at the edges of the domain, as if the medium were isolated. This happens because the outer boundaries are not properly treated to mimic an infinite or semi-infinite medium. It is for this reason that in order to simulate an unbounded medium, absorbing boundary conditions must be implemented.

In this work we chose "*Perfectly Matched Layer*" (PML) absorbing boundary conditions. The principle of the PML consists in defining an outer "*absorbing layer*" with fictitious attenuation properties, in which the impedance between the physical domain and the absorbing layer is very low. The "*Convolutional Perfectly Matched Layer*" (C-PML) is an improvement of the PML, in which the attenuation of grazing-incidence waves are included. The C-PML were first applied to electromagnetic waves [Roden and Gedney, 2000]. In the context of seismic waves, they were implemented by Komatitsch and Martin [2007]. The main idea is to rewrite the elastodynamic equations by replacing the ∂_x derivatives in the x direction by new derivatives $\partial_{\tilde{x}}$. According to the x direction we can write the derivatives in the direction x as:

$$\partial_{\tilde{x}} = \bar{S}(x,t) * \partial_x, \tag{2.68}$$

where $\tilde{x}$ is a new complex coordinate. $\bar{S}(x,t)$ is the inverse Fourier transform of $1/S_x$, S_x being the stretching function defined as:

$$S_x = \kappa_x + \frac{d_x}{\alpha_x + i\omega}, \tag{2.69}$$

where d_x is a "*damping profile*" in the x direction, κ_x and α_x two real variables ($\alpha_x \geq 0, \kappa_x \geq 0$)
.

After some algebraic transformations (see Komatitsch and Martin [2007]), we have:

$$\partial_{\tilde{x}} = \frac{1}{\kappa_x}\partial_x + \psi_x, \tag{2.70}$$

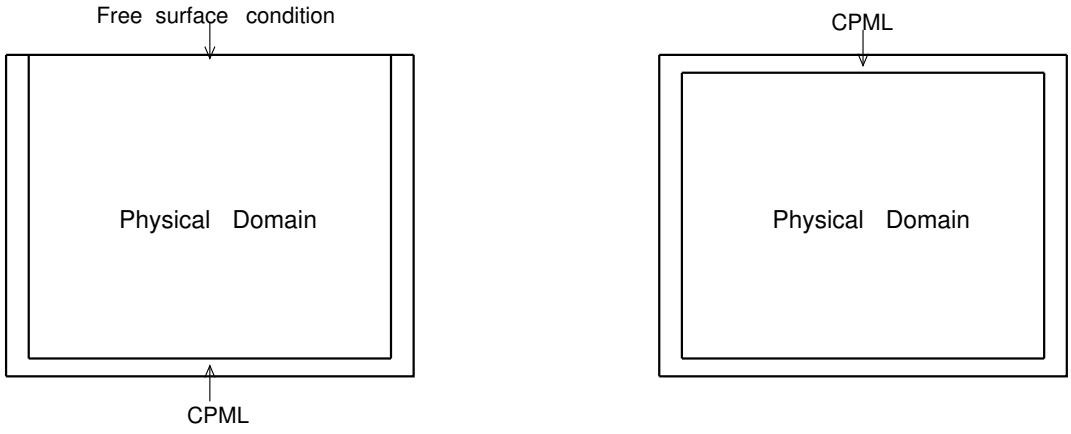

(a) (b)

Figure 2.5. Different computational domains used to solve the proposed RTM algorithm applying free-surface conditions (a) or absorbing-boundary conditions (b) on the top in order to attenuate free-surface artifacts.

where ψ_x is a memory variable in the direction x, and $\kappa_x = 1+(\kappa_{max}-1)^m$. ψ_x can be advanced in time at the second order with the following time-stepping using:

$$\psi_x^n = b_x \psi_x^{n-1} + a_x(\partial_x)^{n+1/2}, \tag{2.71}$$

and

$$\begin{aligned} b_x &= \exp\left[-(d_x/\kappa_x + \alpha_x)\Delta t\right], \\ a_x &= \frac{d_x}{\kappa_x(d_x + \kappa_x\alpha_x)}(b_x - 1), \\ \alpha_x &= \alpha_{max}[1 - (x/L)^p], \end{aligned} \tag{2.72}$$

with

The damping profile could be defined according to Gedney [1998] as:

$$\begin{aligned} d_x(x) &= d_0\left(\frac{x}{L}\right)^N, \\ d_0 &= -(N+1)Vp_{max}\log\frac{R_c}{2L} \end{aligned} \tag{2.73}$$

where L is the thickness of the C-PML, $N = 2$, Vp_{max} is the maximum value of the compression velocity model, and $R_c = 0.1\%$ is a theoretical reflection coefficient. The C-PML formulation for directions y and z is similar as in the x direction.

We can see in the 2D figures (3.6), the distribution of the conventional computational domain (a), and a computational domain surrounded by C-PMLs to attenuate spurious multiple artifacts (as we are going to explain in the next chapter).

2.6 Generalization of the Checkpointing-based sensitivity kernel calculations.

In order to calculate the imaging condition in the context of the RTM algorithm, it is necessary to calculate the correlation between the forward and adjoint wavefields (equations 2.45). The natural process of RTM, consists of first calculating the forward problem. However it is necessary to have access to the all the history of the forward problem when computing the imaging condition. There exists three approaches to handle this issue:

The first approach to compute the sensitivity kernels consists in storing the forward field at all the time steps. Then we correlate the adjoint field with the backward field, which is previously stored in the disk. However, the amount of memory required in this approach is prohibitive in most cases.

The second approach consists in a first step in storing only the solutions obtained at the last time step of the forward problem and also the solution at the boundaries of the model at each time step. In a second second step the sensitivity kernels are obtained by correlating the adjoint and backward fields. The backward field is computed by taking the last time step solution of the forward model as the initial backward solution and by reinjecting the forward solutions at the outer boundaries (previously stored in the boundaries of the model) from the last time step to the first time step of the forward problem. This is called also the reverse time process. In contrast to the previous approach, it is saved a lot of computer memory. However two fields are computed simultaneously (the adjoint and the backward field). This approach is stable in the acoustic and the elastic rheology. But when we want to implement a viscoelastic rheology, where attenuation is required, it is necessary to apply the checkpointing approach.

In general words, the checkpointing strategy consists in storing the system state only at distinct checkpoints (corresponding to different time frames) to save memory. To recompute the system states that have not been stored, we calculate the forward model by chunks from each checkpoints, i.e from the last checkpoint frame in time to the first checkpoint frame. In each chunk, the simulation is computed in the forward direction, this way we ensure that the effects of attenuation are maintained. According to Griewank and Walther [2000], the optimal number of checkpoints C could be obtained as: $C = \log_2(N)$, where N is the total number of time steps.

Figures 2.6, show the behaviour of each approach to the calculation of the sensitivity kernels. We define the checkpointing algorithm as shown in Algorithm 1 (see Yang et al. [2016]).

Having described the equations of elastodynamics governing the direct and adjoint problem, as well as how we discretized the model in this project, it is necessary to present the flowchart in Figure 2.7, a schematic of the UniSolver.F90 code, which we used to obtain the three-dimensional results of this project. In this diagram the pink blocks indicate the processes in which J. Abreu Torres participated. We can see some examples of these subroutines in the

appendices A, B, and C.

Algorithm 1 Checkpointing.

Distribute checkpoints $s_0, \cdots, s_{c-1}$ in time.
for $n = 0, N-1$ **do**
  Compute the wavefield forward state in time: $F^n : w^n \to w^{n+1}$.
  if $n \in s_0, \cdots, s_{c-1}$ **then**
    Store the state wavefield at w^{n+1}.
  end if
end for
for $n = N-1, 0$ **do**
  Find the closest checkpoint s_i immediately before to the current time level n $(s_i \leq n < s_{i+1})$,
  Read the wavefield state $w^{s_{i+1}}$ at the checkpoint s_i,
  for $k = s_{i+1}, n$ **do**
    do forward modeling $F^k : w^k \to w^{k+1}$
    if $k \in s_{i+1}, \cdots, s_{c-1}$ **then**
      Store the wavefield state k at these checkpoint positions.
    end if
  end for
end for

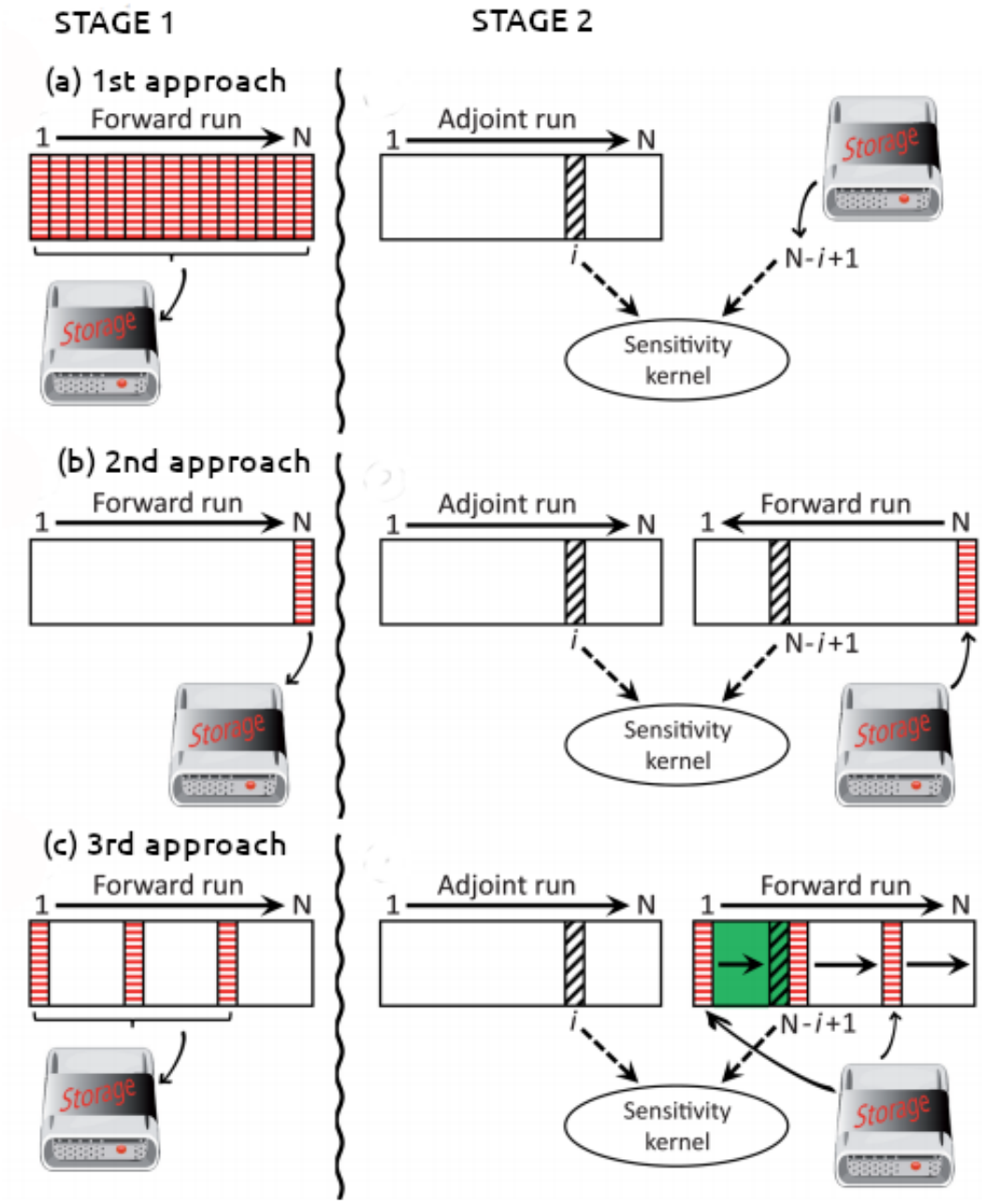

Figure 2.6. Three different approaches (a,b,c) to compute the sensitivity kernels divided in stages 1 and 2. In the first approach (figure a) all the time steps of the forward run are stored in memory and used later to correlate with the adjoint run to obtain the sensitivity kernels. In the second approach (figure b) we store in memory the forward solution at the outer boundaries at each time step and also the forward solution in the entire computational domain but only at the last time step. Then the backward field is computed by solving the wave equation in reverse time from the last time step to the first time step, by taking the last time step forward solution as the initial backward field, and by re-injecting the forward solution (previously stored at the boundaries) as the backward field. At each time step, the backward field is correlated with the adjoint field. Two simulations are computed simultaneously. Finally, in the checkpointing approach (figure c), the forward run is stored at different checkpoint frames in time. Then two simulations are computed simultaneously, but instead of computing the forward field backwards from the last time step to the first, one computes the forward field in chunks in reverse order, but each chunk is computed in the *forward* direction. Modified from Komatitsch et al. [2016].

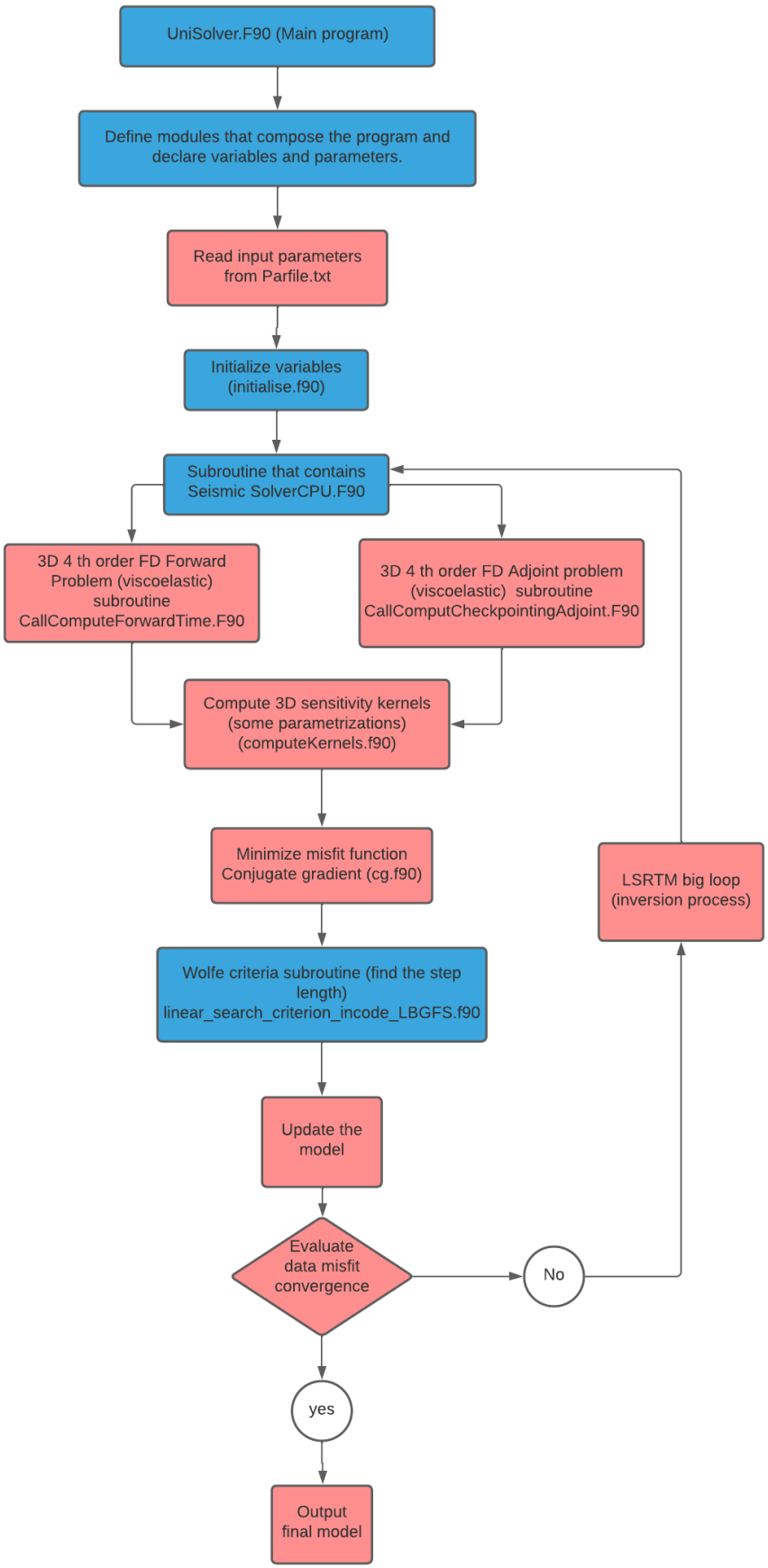

Figure 2.7. Process that the code UniSolver.F90 follows to obtain the kernels we obtained in this project. The pink rectangles mean that the subroutine was coded by J. Abreu-Torres. Note: For the Wolfe criteria we must try several step lengths until the criteria are satisfied. For this reason we must update the model and compute the gradient of the misfit function (kernels).

2.7 Multiple contamination of seismic data.

We believe it is important to speak in general terms about multiple contamination, which is a very recurrent problem in seismic imaging of complex regions.

According to Sheriff [2002], a multiple is seismic energy that has been reflected more than once. Unlike primary events that is the seismic energy that has been reflected just once. In figure 2.8 we see a primary event (red line) that has been reflected just once. However the multiples have been reflected more tan once. We can see that multiples could be reflected at different interfaces.

One of the main ways to classify multiple events is by its order. The order of a multiple is the number of times that the energy has reflected "downward". In Figure 2.9 we can see multiple events of 1st to 3rd order. We can see how the number of times that they have reflected downward matches the order of each multiple.

We can also classify the multiples by their place of reflection. According this classification multiples are divided into internal and free-surface multiple. Free-surface multiples are those which have had at least one downward reflection at the free-surface (in Figure 2.9 all the events are free-surface multiples). While internal multiples have had all their downward reflections at the internal layers as shown in Figure 2.10. It is important to distinguish between these two types of multiples because free-surface multiples have a much higher amplitude than internal multiples. Therefore, they are the most studied, and most of the methods used to attenuate multiples are focused on these type of multiples.

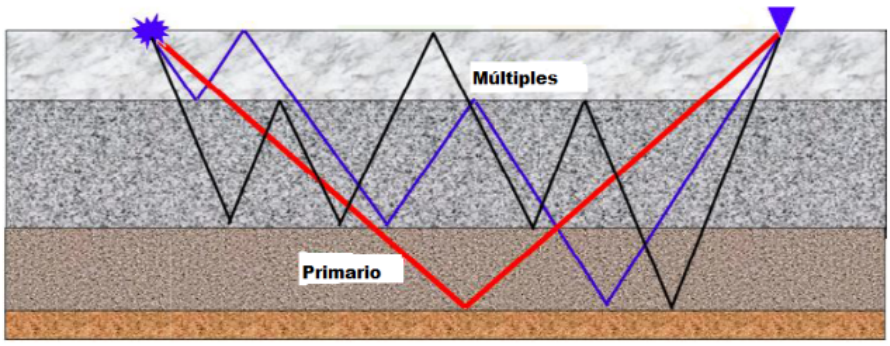

Figure 2.8. Comparison between a primary event (red line), and multiple events (black and blue lines). Taken from CGG presentation (2013).

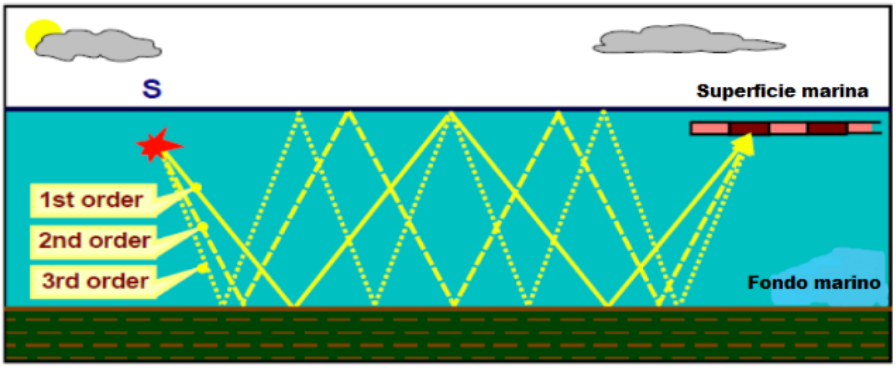

Figure 2.9. Different types of multiples according to their order (1-3). The 1st order multiple has reflected downward one time at the marine surface, the 2nd order multiple has reflected downward two times and the 3red order multiple has reflected downward 3 times. Taken from CGG presentation (2013).

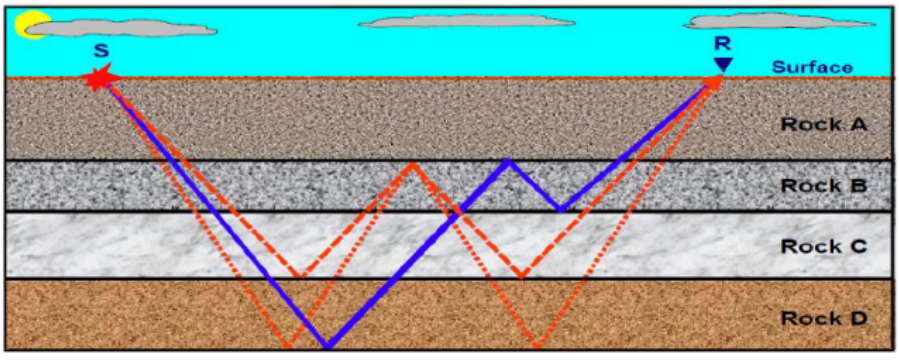

Figure 2.10. Example of internal multiples. Taken from CGG presentation (2013).

2.8 Conclusions

I have presented the methodology used to perform the calculations in this work. For which I relied on a code called UniSolver, which is implemented in parallel and uses second order finite differences with an elastic rheology to solve the direct problem. For my part I added some improvements to that code:

- Upgrade of finite differences from the second to the fourth order in space.
- Implementation of visco-elastic rheology.
- Implementation of different parameterizations for both the migration and FWI processes: (ρ, λ, μ), (ρ', V_P, V_S), and (ρ'', Z_P, Z_S) and their respective logarithms. The parameterizations without logarithm produced the best results in terms of seismic images in our different case studies.
- Implementation of different kernel preconditioning: Forward and adjoint energy, pseudo-hessian. The forward energy preconditioning produces the best results.
- Algorithm for FWI with steepest descent and non-linear conjugate gradient method.
- Implementation of a source encoding approach for the inversion of chapter 4 (see the details summarized in that chapter) .

Chapter 3

2D and 3D synthetic sensitivity analysis

The objective of this chapter is to present the results of RTM migration applied to 2D and 3D synthetic models that are representative models of real regions of the Gulf of Mexico with strong saline tectonism, using different a priori models. We also present a SNR analysis to determine the influence of the different a priori models on the final image.

The first section of this chapter, which corresponds to the 2D models, was submitted to the Survey in Geophysics journal, the second part corresponds to the 3D models. Below is a brief summary of the article and the article as published.

3.1 2D synthetic RTM and sensitivity analysis of the kernels.

Seismic imaging of geological regions with strong salt tectonics represents a great challenge for the scientific community. This is due to the complex structure of the salt bodies and the strong impedance contrast between the salt and the adjacent strata.

The seismic images of these zones present a high physical 'noise' contamination, which generally interferes with the seismic signal, generating images difficult to interpret. In most cases physical 'noise' attributed to multiples or diffractions is so strong that it is impossible to see the structures below the base of the dome. Generally this physical noise is attributed to the multiple reflections that are generated on the free surface, although there are also internal multiples, but these tend to have a lower amplitude than the free surface ones.

There are many techniques to attenuate physical 'noise' due to multiple contamination such as $\tau - p$ domain filtering techniques (used when there is a considerable time difference between primaries and multiples), or prediction techniques (SRME) (when there is not enough time delay between primaries and multiples). Even nowadays, techniques are being developed to elaborate seismic images using multiples, taking advantage of the wide coverage in their trajectory that these events present in comparison with the primaries. We implement a technique

that consists of a replacement of the free surface conditions by absorbing boundary conditions within the computational domain in both the direct problem and the adjoint problem to filter and attenuate free-surface related multiples and their impact in the seismic images. In this work we performed seismic imaging using the RTM technique on 2D synthetic, acoustic data related to salt domes. We also performed a sensitivity analysis by obtaining the SNR at different interfaces of our model to determine the type of information provided by the different parameterizations to calculate the kernels.

Surveys in Geophysics (2022) 43:703–736
https://doi.org/10.1007/s10712-021-09689-7

Salt Tectonic Modeling Using Reverse Time Migration Imaging and Sensitivity Kernel Wavelength Analysis

J. Abreu-Torres[1] · Roland Martin[1] · J. C. Ortiz-Alemán[1,2] · José Darrozes[1] · J. Urrutia-Fucugauchi[3,4]

Received: 23 June 2021 / Accepted: 9 December 2021 / Published online: 27 January 2022

3.1.1 SUMMARY

It is of particular importance for structural geology, geophysical exploration and also obvious economical purposes to retrieve structures possibly hidden below salt domes. And these domes could trap hydrocarbon or gas. We thus propose a sensitivity analysis of seismic data in salt tectonic areas to identify different wavelengths associated to the geological structures under study involving salt domes. The wavelengths associated to the density or seismic velocities of the medium can give us information about the localization of shallow or deep geological structures surrounding salt domes in off-shore context. Seismic data can be more sensitive to density at depth below the salt dome or to seismic velocities close to or around it. Depending on the wavelengths associated to those two different properties, the dome shape and the different interfaces can be located and recovered at different depths.

In a first approach, using velocity and density models from a salt tectonic region in the Gulf of Mexico we simulate a two-dimensional seismic data acquisition. Using these synthetic data, we aim at retrieving the salt dome shape as well as the surrounding and deepest geological layers. In this purpose we propose to compute better imaging conditions by attenuating free surface multiples and introducing an adjoint theory-based *Reverse Time Migration* RTM method, enhancing the limits of salt bodies and also the layers under salt structures. To obtain these imaging conditions, we compute the compressional and density sensitivity kernels K_λ and K_ρ using seismic sources activated separately. In this particular synthetic context we are focusing here our attention to attenuate the free surface multiples. To do this, the synthetic 'observed' data computed with the free surface are introduced as adjoint sources and we replace the free surface condition by PML absorbing conditions in both the forward, backward and adjoint simulations needed to compute the kernels (subsections 3.2.2-3.2.4). Mathematically, this is equivalent to applying the image condition of the equations 3.30. We compare the quality of the kernels applying different strategies related to the normalization of kernels by the

forward or adjoint energy to retrieve the interfaces in depth more clearly with more intensity, and different property parametrizations were tested to improve the imaging conditions. The specific wavelengths associated to the different (shallow to deep) interfaces are obtained using Signal-to-Noise-Ratios (SNRs) applied to both density and seismic velocity kernels. In some cases density or seismic velocity kernels are more suited to retrieve the interfaces at different depths.

3.1.2 INTRODUCTION

In 1900, Spindletop discovery (the first Salt dome oil at a depth of 300 m) started the exploration of the Golf Coast, one of the most important oil areas in the world. In the Gulf of Mexico over five hundred salt domes were discovered. This type of structure is an important attraction for geologists around the world. Indeed, in addition to the possibility of sheltering oil or gas reservoirs, they fascinate by the saliferous geological structures [Jones, 2012; McCann et al., 2012] that they develop. They are also a real challenge for geophysicists because if the seismic imaging gives a suitable image of the top of these domes, the lower limits as well as the underlying layers are masked by numerous interferences generated by the salt structures. Salt displacements generate steeply dipping complex-shaped structures that pose significant challenges for seismic velocity model building and migration (see Jones and Davison [2014b]). In the last three decades, recent advances in seismic imaging algorithms have permitted imaging of steep structures using Reverse Time Migration (RTM) [Hale et al., 1992] among other techniques.

Historically, the term 'seismic imaging' has been used to describe a technique that uses the energy generated by active or passive seismic sources to generate images of the geological features of the subsoil [Robertsson et al., 2011].

In terms of seismic imaging, the forward problem (equation 3.1) expresses what happens in a seismic survey to obtain the real data. In this equation, $\boldsymbol{d}$ represents the data set recorded in seismograms, $\boldsymbol{m}$ expresses the subsoil parameters, and g is an operator which relates the parameters to the data, such as:

$$\boldsymbol{d} = g(\boldsymbol{m}), \tag{3.1}$$

The forward problem consists in recording the amplitude of seismic waves that propagate through the media with different properties before being recorded by the seismic receivers. This dataset contains the information of all the geological bodies through which the seismic waves have travelled.

Using this dataset we can obtain subsoil images. Actually, there exist two main approaches to generate seismic images, which are:

- **The migration approach**: It is based on the image principle [Claerbout, 1971]: "a reflector exists where the source and receivers coincide in time and space". It allows to define the main interfaces of the model rather than the real values of the model parameters.

- **The inverse problem theory approach**: It consists in minimizing some functional defined over the data set for a given model space. Using this approach we also determine the approximate values of the subsoil parameters.

In this paper we focus on the migration approach. Seismic migration is "an inversion operation involving rearrangements of seismic information elements so that reflections and diffractions are plotted at their true locations" [Sheriff, 2002].

The first works related to seismic migration solved partially the wave equation, they are based in the ray theory, in which the wavefronts are approximated to rays, and the wave equation is not solved completely (the Eikonal equation is defined instead). Among the ray-based migration techniques, Kirchhoff migration is the most known method, in which the integral form of the wave equation is solved. We can cite Hagedoorn [1954], Postma [1955], Dix [1955] as some of the pioneering works in the field of the ray-based seismic migration methods.

Thanks to the evolution of computational technology, some methods were proposed applying the complete solution of the wave equation. In the context of full-waveform methods, we refer to Claerbout [1971], Claerbout et al. [1985], Loewenthal et al. [1976], Tarantola [1984].

In recent years, some improvements to the RTM have been proposed, one of the most important is the *Least Squares Reverse Time Migration* (LSTRM), which consists in applying a least-squares misfit function between the observed and predicted data. This approach is related to the Full Waveform Inversion (FWI) based in the adjoint theory, in the sense that the misfit function (the difference between observed and predicted data) is minimized. While the FWI is a non-linear method, the LSRTM is a linearization of the FWI around a smooth medium/large wavelength background model. In LSRTM method, the RTM must be calculated in each iteration to obtain the search direction to upgrade the reflectivity model. For further information see Zhu and Tromp [2013], Zhang et al. [2015], and Feng and Schuster [2017].

One of the main challenges of seismic imaging geological structures involving salt domes is to see the structures at the base of the dome and especially the interfaces that exist underneath the salt body. Many authors have demonstrated that multiples are primarily responsible for this drawback (the reader is referred to some authors like Dellmour et al. [2016]; Soleimani et al. [2018], for the more recent ones, about this issue). In fact, the signals produced by multiple events decrease the quality of seismic processing by interfering with signals from primary events. This fact hinders a proper interpretation of migrated seismic images. By attenuating the multiples, we could obtain a cleaner image that would allow better interpretations of the geologic structures.

Traditionally, multiple events have been considered as spurious signal. Several attenuation approaches have been developed and some are based on exploiting moveout differences between primary and multiple events [Berkhout and Verschuur, 2006]. For instance, Radon transform converts seismic data from offset-time domain to speed-intercept time domain, in which multiple and primary events are clearly distinguishable by their moveouts, allowing attenuation of multiples without affecting primaries [Durrani and Bisset, 1984; Foster and Mosher, 1992;

Gholami, 2017; Ortiz-Alemán et al., 2019; Sacchi and Ulrych, 1995].

However, when primary and multiple moveouts are similar, it is more convenient to apply methods based on the predictability approach, where primary and multiple paths of seismic events are computed by solving the wave equation. These techniques were initially applied for multiple's removal related to the seabed and are commonly referred as *Surface Related Multiple Elimination* (SRME) [Behura and Forghani, 2012; Jakubowicz, 1998; Verschuur and Berkhout, 1992]. In the context of complex geological areas (salt tectonics), we could refer to Weglein et al. [1997].

In the field of seismic data migration and attenuation of multiples, the method *Reverse Time Migration of Multiples* (RTMM) has been developed [Jones and Davison, 2014b; Liu et al., 2011, 2015; Wang et al., 2013; Yang et al., 2015b; Zhang and Schuster, 2013], which consists of a modification to the image condition. In these methods, the observed data contain only multiples, and they are back-propagated and correlated with an impulsive source following the RTM algorithm, the multiples are then extracted by predictability techniques such as SRME. It is considered that multiple events provide extra information to the images due to their different paths and access to regions where primaries can't reach. Therefore, the multiples are not attenuated.

Marchenko imaging is a technique used to image the subsurface of the Earth using primary and multiples events. The studies of this method have produced some notable advances in the treatment of seismic multiples. Following a practical point of view, Marchenko imaging [Jia et al., 2017; Wapenaar et al., 2014] consists in redatuming receivers and sources at each depth of interest (generally at the location of a reflector).

Finally, in Vdovina et al. [2015], RTM is used for multiple attenuation, in which multiples must be predicted and eliminated before calculating the RTM algorithm. In addition, free surface conditions are replaced by absorbing boundary conditions. Therefore, the imaging condition is the correlation between two wave fields without multiples. However, it is required to attenuate the multiples before the migration process.

We thus apply here a similar idea as in Vdovina et al. [2015] to the particular context of synthetic data, i.e an idea in which we replace the free surface conditions by PML absorbing layer conditions to filter the first free surface multiples and build this way attenuated seismic images with less artifacts due to those multiples. In subsection 3.2.5 ad 3.2.6 we thus present results with observed data containing free-surface multiples (obtained by computing the direct problem using the true model and the computational domain indicated in the figure 3.6(a)). The adjoint source is here the residual between observed and synthetic data, the synthetic data being computed for different large wavelength a priori/background models. These subsections are not part of the original publication. We also present in appendix F the results with observed data with attenuation of multiples (obtained by computing the direct problem using the true model and the computational domain of the figure 3.6(b)).

In this paper we consider a migration approach, in which the imaging condition is calculated following the adjoint-theory approach. The correlation between the observed and pre-

dicted wavefields is computed using the Fréchet derivatives of the misfit function [Douma et al., 2010; Plessix, 2006; Tromp et al., 2005; Zhu et al., 2013]: see section a). In the offshore context, we focus our present work on the analysis of the retrieved wavelengths of the medium that are obtained via the calculation of the sensitivity kernels (derivatives of Fréchet) with respect to the different parameters of the subsoil (density and seismic velocities). We study the behaviour of these kernels when information on the prior models increase using Signal-to-Noise ratios (SNRs). The wavelengths recovered thanks to those SNRs give us information on the geological interfaces at different depths depending on the choice of the physical parameters (density or seismic velocity). We have found that the relation between the depth of some selected interfaces and the SNR behaves differently depending on the seismic parameter associated to the kernels. In order to improve the imaging conditions obtained by the sensitivity kernels, we aim to attenuate free-surface multiples by using a computational artifice that consists in the use of optimized Convolutional Perfectly Matched Layers (CPML) absorbing-boundary conditions instead of free-surface conditions at the top of the computational domain. It is important to note that the use of absorbing boundaries to attenuate free surface multiples has not been studied with deep enough insight in the context of RTM method in previous works. However this approach helps to better visualize not only the layers around the salt structures but also deeper sub-salt layers located below these salt structures by attenuating the free surface multiples.

This work is divided in four sections. The first section introduces the purpose of this study, followed by the section that includes the adjoint based theory of the RTM method. The third section presents some examples of the results obtained. Finally, the last section contains the discussions where we discussed the analysis of the different kernels and their respective wavelengths that can be recovered) and the conclusions.

3.1.3 ADJOINT THEORY

We first summarize the theory of conventional RTM algorithm, to understand their imaging condition differences compared with the method proposed in this work.

a) Adjoint theory based Reverse Time Migration

RTM is an algorithm that generates an image of the subsoil interfaces from the observed data. It is based in the imaging principle proposed by Claerbout et al. [1985], which says that a reflector exists where the source and receivers wavefields coincide in time and space.

Since RTM is a complete waveform algorithm, it is mandatory to solve the elastodynamic

equations, expressed as follows:

$$\begin{aligned}
\rho\frac{\partial v_x}{\partial t} &= \frac{\partial \tau_{xx}}{\partial x} + \frac{\partial \tau_{xz}}{\partial z} + f_x, \\
\rho\frac{\partial v_z}{\partial t} &= \frac{\partial \tau_{xz}}{\partial x} + \frac{\partial \tau_{zz}}{\partial z} + f_z, \\
\frac{\partial \tau_{xx}}{\partial t} &= (\lambda + 2\mu)\frac{\partial v_x}{\partial x} + \lambda\frac{\partial v_z}{\partial z}, \\
\frac{\partial \tau_{zz}}{\partial t} &= (\lambda + 2\mu)\frac{\partial v_z}{\partial z} + \lambda\frac{\partial v_x}{\partial x}, \\
\frac{\partial \tau_{xz}}{\partial t} &= \mu(\frac{\partial v_x}{\partial z} + \frac{\partial v_z}{\partial x}),
\end{aligned} \tag{3.2}$$

where ρ, λ, and μ are the density and Lamé coefficients which describe the medium, (v_x, v_z) and (f_x, f_z) are the velocity and force vectors respectively, and $(\tau_{xx}, \tau_{zz}, \tau_{xz})$ the stress tensor.

Following the adjoint theory [Lailly and Santosa, 1984; Monteiller et al., 2015; Plessix, 2006; Tarantola, 1984; Tromp et al., 2005], the misfit function between synthetic data $\mathcal{S}$ from the forward problem and the observed data $\mathcal{R}$ recorded at the receivers is described as:

$$\chi(\boldsymbol{m}) = \frac{1}{2}\sum_{r=1}^{N}\int_0^T ||\mathcal{S}(\overline{x_r}, t, \boldsymbol{m}) - \mathcal{R}(\overline{x_r}, t)||^2 dt, \tag{3.3}$$

where $\boldsymbol{m}$ represents the subsoil parameters, N is the number of receivers r, $\overline{x_r}$ is the position of the receivers, and T is the total time of propagation.

According to Chang and McMechan [1986], Liu et al. [2011], it exists three steps in the RTM algorithm described as follows:

1. **Forward modeling**. It consists in calculating the numerical solution of the elastodynamic equations 3.2 for the subsoil parameters of the current models, and for explosive sources $f(\overline{x}_s, t)$ that are introduced at the position $\overline{x}_s$ as follows:

$$f_i(\overline{x}_s, t) = C\delta(\overline{x} - \overline{x}_s)\delta(t - t')\delta_{ij}, \tag{3.4}$$

   where C is the source amplitude and δ_{ij} is the Kronecker delta distribution indicating the source direction. The solution of the direct model is the source wavefield $\mathcal{S}$.

2. **Adjoint modeling**. It consists in solving the elastodynamic equations in reverse time in the subsoil model. The adjoint source $f^\dagger$ is introduced as the retropropagated residuals between the data computed for the current model and the retropropagated observed data [Tromp et al., 2005]:

$$f_i^\dagger(\overline{x}, t) = \sum_{r=1}^{N}(\mathcal{F}_i(\overline{x_r}, (T - t)) - \mathcal{R}_i(\overline{x_r}, (T - t)))\delta(\overline{x} - \overline{x_r}), \tag{3.5}$$

   where $\mathcal{F}_i$ and $\mathcal{R}_i$ are the i-th component of the data computed for the current model and the observed data respectively. These residuals are injected at the receiver locations

$\overline{x_r}$, and T is the total time of the experiment. The way in which the adjoint source is calculated is a consequence of the misfit function (equation 3.3). The solution of the adjoint modeling is also the adjoint retro-propagated wavefield response $\mathcal{B}$ for the adjoint source $f^{\dagger}$, obtained as follows according to Tromp et al. [2005].

$$\mathcal{B}_j(\overline{x}, T-t') = \int_0^{T-t'} \int_V \sum_{i=1}^{M} G_{ji}(\overline{x_r}, \overline{x}; T-t-t') f_i^{\dagger}(\overline{x_r}, t) dV(\overline{x}) dt, \tag{3.6}$$

where M is the number of adjoint wavefield components, G_{ji} is the Green tensor, (i, j) are the components of the tensor, and V is the volume of the medium. To develop the adjoint method with the purpose of showing the adjoint kernels, we presented the adjoint source as shown in equation 3.5. However, for the RTM method we can implement the adjoint source by only injecting the observed data as explained in Virieux and Operto [2009]

3. **Imaging condition**. The subsoil imaging condition I is obtained by a correlation between the forward and adjoint retropropagated wavefields. We show here in a general way its calculation:

$$I(\overline{x}) = \sum_{t=1}^{T} \mathcal{F}(\overline{x}, t) * \mathcal{B}(\overline{x}, T-t), \tag{3.7}$$

where $\mathcal{F}$ represents the forward wavefield and $\mathcal{B}$ the adjoint retro-propagated wavefield, and n representing the time step. The regions with greater amplitude indicate coincidence between the two wave fields, which is a sign of reflector presence. Furthermore, according to Chattopadhyay and McMechan [2008], we can normalize the imaging condition I by the square of the forward or adjoint energy as shown in equations 3.8:

$$\begin{aligned} I(\overline{x}) &= \frac{\sum_{t=1}^{T} \mathcal{F}(\overline{x}, t) * \mathcal{B}(\overline{x}, T-t)}{\sum_{t=1}^{T} \mathcal{F}(\overline{x}, t)^2}, \\ I(\overline{x}) &= \frac{\sum_{t=1}^{T} \mathcal{F}(\overline{x}, t) * \mathcal{B}(\overline{x}, T-t)}{\sum_{t=1}^{T} \mathcal{B}(\overline{x}, t)^2}. \end{aligned} \tag{3.8}$$

Those normalizations allow to increase the illumination of the deeper interfaces. In terms of imaging these results are similar compared to the imaging condition of equation 3.7, because they only focus on the interfaces and not on the true amplitudes.

b) Sensitivity kernels based on adjoint theory.

Now that we have described briefly the general stages of the RTM method, we now develop the equations describing the RTM in the context of the adjoint theory applied to the elastic seismic full wave equation.

Using the adjoint theory, we compute the RTM seismic image as the high frequency perturbations of the model under study (i.e the main interfaces of the model), perturbations that can be computed as the gradient of the misfit function. This gradient of the misfit function

represents the variations of the computed synthetic seismic data respect to the real (measured/observed) data for a given background a priori model: the prior model is generally chosen as smooth to make the high frequencies of the real model to appear as well as the high impedance contrasts of the real model at the interfaces. This model perturbation, which is also the the data misfit gradient, is computed for a given low frequency (smoothed) a priori background model and provides the high frequency perturbations of this a priori model. We aim by this mean to retrieve the main interfaces of the model. By using a Lagrangian approach in the context of the adjoint theory, this perturbation of the misfit function of equation 3.3 is thus computed under the constraint that the synthetic data from the forward problem ($\mathcal{S}$) satisfy the wave equations 3.2. Besides, to compute this misfit gradient, the following adjoint elastodynamic equations must also be solved at the same time:

$$\begin{aligned}
\rho\frac{\partial v_x^\dagger}{\partial t} &= \frac{\partial \tau_{xx}^\dagger}{\partial x} + \frac{\partial \tau_{xz}^\dagger}{\partial z} + f_x^\dagger,\\
\rho\frac{\partial v_z^\dagger}{\partial t} &= \frac{\partial \tau_{xz}^\dagger}{\partial x} + \frac{\partial \tau_{zz}^\dagger}{\partial z} + f_z^\dagger,\\
\frac{\partial \tau_{xx}^\dagger}{\partial t} &= (\lambda+2\mu)\frac{\partial v_x^\dagger}{\partial x} + \lambda\frac{\partial v_z^\dagger}{\partial z},\\
\frac{\partial \tau_{zz}^\dagger}{\partial t} &= (\lambda+2\mu)\frac{\partial v_z^\dagger}{\partial z} + \lambda\frac{\partial v_x^\dagger}{\partial x},\\
\frac{\partial \tau_{xz}^\dagger}{\partial t} &= \mu(\frac{\partial v_x^\dagger}{\partial z} + \frac{\partial v_z^\dagger}{\partial x}),
\end{aligned} \tag{3.9}$$

where $(v_x^\dagger, v_z^\dagger)$ is the adjoint velocity vector, $(\tau_{xx}^\dagger, \tau_{zz}^\dagger, \tau_{xz}^\dagger)$ is the adjoint stress tensor, and $(f_x^\dagger, f_z^\dagger)$ is the force vector corresponding to the adjoint source of equation 3.5. We now introduce a new misfit function using the Lagrange multiplier method according to Liu and Tromp [2006]:

$$\chi'(\boldsymbol{m}) = \chi(\boldsymbol{m}) + \int_0^T \int_\Omega \gamma \cdot \left(\rho\frac{\partial^2 u}{\partial t^2} - \nabla\cdot\tau - f\right) d\Omega dt, \tag{3.10}$$

where $\gamma(\overline{x}, t)$ represents the Lagrange multiplier, Ω represents the computational domain of the model, and $u = \mathcal{S}$ is the synthetic displacement vector. Furthermore $u^\dagger(\overline{x}, t) = \gamma(\overline{x}, T-t)$, implying that the Lagrangian multiplier satisfies the adjoint wave equations 3.9.

c) Different parametrizations of the sensitivity kernels.

The variation of the misfit function with respect to the subsoil parameters could be written in a general way as:

$$\delta\chi = \frac{\delta\chi}{\delta\rho}\delta\rho + \frac{\delta\chi}{\delta\lambda}\delta\lambda + \frac{\delta\chi}{\delta\mu}\delta\mu, \tag{3.11}$$

where $\frac{\delta\chi}{\delta\rho}$, $\frac{\delta\chi}{\delta\lambda}$, $\frac{\delta\chi}{\delta\mu}$, represent the Fréchet derivatives of the misfit function (equation 3.3) with respect to density and Lamé parameters respectively. They also express the correlation between the forward and adjoint wavefields. At the first iteration of the FWI method, these Fréchet derivatives are the RTM imaging conditions for the a priori model. Here, we thus compute the

RTM imaging conditions only for the low frequency a priori model.

For the (ρ, λ, μ) parametrization, the adjoint kernels K_ρ, K_λ, and K_μ are calculated according to Tromp et al. [2005] as:

$$\begin{aligned} K_\rho(\overline{x}) &= \frac{\delta\chi}{\delta\rho} = \int_0^T u^\dagger(\overline{x}, T-t) \cdot \partial_t^2 u(\overline{x}, t) dt, \\ K_\lambda(\overline{x}) &= \frac{\delta\chi}{\delta\lambda} = \int_0^T \nabla \cdot u^\dagger(\overline{x}, T-t) \nabla \cdot u(\overline{x}, t) dt, \\ K_\mu(\overline{x}) &= \frac{\delta\chi}{\delta\mu} = 2\int_0^T \nabla u^\dagger(\overline{x}, T-t) \colon \nabla u(\overline{x}, t) dt, \end{aligned} \tag{3.12}$$

where u and $u^\dagger$ are the displacements of the forward and adjoint wavefields.

By introducing integration by parts K_ρ could be expressed as:

$$K_\rho(\overline{x}) = \int_0^T v^\dagger(\overline{x}, T-t) \cdot v(\overline{x}, t) dt, \tag{3.13}$$

where v and $v^\dagger$ are the particle velocities for the forward and adjoint wavefields respectively. Different parametrizations have been tested: (ρ, λ, μ), (ρ, V_p, V_s), and (ρ, Z_p, Z_s) as well as their logarithms, where V_p and V_s are the velocities P and S respectively, and $Z_p = \rho * V_p$, $Z_s = \rho * V_s$ are the impedances.

For the parametrization (ρ, V_p, V_s) the kernels are expresed as:

$$\begin{aligned} K'_\rho &= K_\rho + (V_p^2 - 2V_s^2)K_\lambda + V_s^2 K_\mu, \\ K_{V_p} &= 2\rho V_p K_\lambda \\ K_{V_s} &= -4\rho V_s K_\lambda + 2\rho K_\mu, \end{aligned} \tag{3.14}$$

For the parametrization (ρ, Z_p, Z_s), the kernels are expressed as:

$$\begin{aligned} K''_\rho &= K_\rho - (V_p^2 - 2V_s^2)K_\lambda - V_s^2 K_\mu, \\ K_{Zp} &= 2V_p K_\lambda \\ K_{Zs} &= -4V_s K_\lambda + 2V_s K_\mu. \end{aligned} \tag{3.15}$$

The variation of the misfit function with respect to the logarithm of different subsoil parameters could be expressed from equation 3.11 as :

$$\delta\chi = \rho K_\rho \frac{\delta\rho}{\rho} + \lambda K_\lambda \frac{\delta\lambda}{\lambda} + \mu K_\mu \frac{\delta\mu}{\mu}, \tag{3.16}$$

where $\frac{\delta\rho}{\rho} = \delta \ln \rho$, $\frac{\delta\lambda}{\lambda} = \delta \ln \lambda$, $\frac{\delta\mu}{\mu} = \delta \ln \mu$. Therefore, for the parametrization $(\ln\rho, \ln\lambda, \ln\mu)$

the sensitivity kernels with respect to the logarithm of the subsoil parameters are expressed as:

$$\begin{aligned} K_{\ln\rho} &= \rho K_\rho, \\ K_{\ln\lambda} &= \lambda K_\lambda, \\ K_{\ln\mu} &= \mu K_\mu. \end{aligned} \tag{3.17}$$

For the parametrization $(\ln\rho, \ln V_p, \ln V_s)$:

$$\begin{aligned} K'_{\ln\rho} &= \rho K'_\rho, \\ K_{\ln V_p} &= V_p K_{V_p}, \\ K_{\ln V_s} &= V_s K_{V_s}. \end{aligned} \tag{3.18}$$

Finally, for the parametrization $(\ln\rho, \ln Z_p, \ln Z_s)$:

$$\begin{aligned} K''_{\ln\rho} &= \rho K''_\rho, \\ K_{\ln Z_p} &= Z_p K_{Zp}, \\ K_{\ln Z_s} &= Z_s K_{Zs}. \end{aligned} \tag{3.19}$$

d) Normalization of the sensitivity kernels.

As indicated previously in the subsection a), we can normalize the kernels by the forward or adjoint energy. For the specific case of the acoustic problem, the forward normalized kernels could be expressed as:

$$\begin{aligned} K_\rho^N &= \frac{\int_0^T v^\dagger(\overline{x}, T-t)\cdot v(\overline{x},t)}{\int_0^T v(\overline{x},t)^2} \\ K_\lambda^N &= \frac{\int_0^T \nabla\cdot u^\dagger(\overline{x}, T-t)\cdot \nabla\cdot u(\overline{x},t)}{\int_0^T \nabla\cdot u(\overline{x},t)^2}. \end{aligned} \tag{3.20}$$

We can show that the kernels $K_{\ln\rho}^N$ and $K_{\ln\lambda}^N$ are the same as the kernels K_ρ^N and K_λ^N because:

$$\begin{aligned} K_{\ln\rho}^N &= \frac{\cancel{\rho(\overline{x})}\int_0^T v^\dagger(\overline{x}, T-t)\cdot v(\overline{x},t)}{\cancel{\rho(\overline{x})}\int_0^T v(\overline{x},t)^2} \\ K_{\ln\lambda}^N &= \frac{\cancel{\lambda(\overline{x})}\int_0^T \nabla\cdot u^\dagger(\overline{x}, T-t)\cdot \nabla\cdot u(\overline{x},t)}{\cancel{\lambda(\overline{x})}\int_0^T \nabla\cdot u(\overline{x},t)^2}. \end{aligned} \tag{3.21}$$

e) Typical imaging condition.

Returning to the subject of the imaging condition (equation 3.7) and according to [Liu et al., 2011], when the observed data are injected as the back-propagated source, the wavefields $\mathcal{F}$ and $\mathcal{B}$ of equation 3.7, could be expressed as a decomposition of primaries and multiples as follows:

$$\begin{aligned}\mathcal{F}(\overline{x},n) &= \mathcal{D}_{\mathcal{F}}(\overline{x},n) + \mathcal{P}_{\mathcal{F}}(\overline{x},n) + \mathcal{M}_{\mathcal{F}}(\overline{x},n),\\ \mathcal{B}(\overline{x},n) &= \mathcal{P}_{\mathcal{B}}(\overline{x},n) + \mathcal{M}_{\mathcal{B}}(\overline{x},n),\end{aligned} \tag{3.22}$$

where $\mathcal{P}_{\mathcal{F}}$, $\mathcal{P}_{\mathcal{B}}$, $\mathcal{M}_{\mathcal{F}}$, and $\mathcal{M}_{\mathcal{B}}$ are respectively the primaries $\mathcal{P}$ and multiples $\mathcal{M}$ of the forward and adjoint retro-propagated wavefields respectively. The term $\mathcal{D}_{\mathcal{F}}$ represents the down-going impulsive source before its first reflection. The multiple terms are considered as the sum of all multiples of different order:

$$\begin{aligned}\mathcal{M}_{\mathcal{F}} &= \mathcal{M}^1_{\mathcal{F}} + \mathcal{M}^2_{\mathcal{F}} + \mathcal{M}^3_{\mathcal{F}} + \dots\\ \mathcal{M}_{\mathcal{B}} &= \mathcal{M}^1_{\mathcal{B}} + \mathcal{M}^2_{\mathcal{B}} + \mathcal{M}^3_{\mathcal{B}} + \dots\end{aligned} \tag{3.23}$$

Deriving from equation 3.22 and considering that there was no prior attenuation of multiples, the imaging condition (equation 3.7) for each source could be written as:

$$I(\overline{x}) = \sum_{n=1}^{N} \left[\mathcal{D}_{\mathcal{F}}(\overline{x},n) + \mathcal{P}_{\mathcal{F}}(\overline{x},n) + \mathcal{M}_{\mathcal{F}}(\overline{x},n)\right] * \left[\mathcal{P}_{\mathcal{B}}(\overline{x},n) + \mathcal{M}_{\mathcal{B}}(\overline{x},n)\right]. \tag{3.24}$$

After applying the distributive property of correlation, we obtain:

$$\begin{aligned}I(\overline{x},n) = &\sum_{n=1}^{N} \mathcal{D}_{\mathcal{F}}(\overline{x},n) * \mathcal{P}_{\mathcal{B}}(\overline{x},n) + \sum_{n=1}^{N} \mathcal{D}_{\mathcal{F}}(\overline{x},n) * \mathcal{M}_{\mathcal{B}}(\overline{x},n)\\ &+ \sum_{n=1}^{N} \mathcal{P}_{\mathcal{F}}(\overline{x},n) * \mathcal{P}_{\mathcal{B}}(\overline{x},n) + \sum_{n=1}^{N} \mathcal{P}_{\mathcal{F}}(\overline{x},n) * \mathcal{M}_{\mathcal{B}}(\overline{x},n)\\ &+ \sum_{n=1}^{N} \mathcal{M}_{\mathcal{F}}(\overline{x},n) * \mathcal{P}_{\mathcal{B}}(\overline{x},n) + \sum_{n=1}^{N} \mathcal{M}_{\mathcal{F}}(\overline{x},n) * \mathcal{M}_{\mathcal{B}}(\overline{x},n).\end{aligned} \tag{3.25}$$

Therefore, the image is obtained by the the sum of different correlations, where the different terms of equation 3.25 produce different effects to the image. We are going to name each of the terms as follows to facilitate the explanation:

$$\begin{aligned} A &= \sum_{n=1}^{N} \mathcal{D}_{\mathcal{F}}(\overline{x},n) * \mathcal{P}_{\mathcal{B}}(\overline{x},n), & B &= \sum_{n=1}^{N} \mathcal{D}_{\mathcal{F}}(\overline{x},n) * \mathcal{M}_{\mathcal{B}}(\overline{x},n),\\ C &= \sum_{n=1}^{N} \mathcal{P}_{\mathcal{F}}(\overline{x},n) * \mathcal{P}_{\mathcal{B}}(\overline{x},n), & D &= \sum_{n=1}^{N} \mathcal{P}_{\mathcal{F}}(\overline{x},n) * \mathcal{M}_{\mathcal{B}}(\overline{x},n)\\ E &= \sum_{n=1}^{N} \mathcal{M}_{\mathcal{F}}(\overline{x},n) * \mathcal{P}_{\mathcal{B}}(\overline{x},n), & F &= \sum_{n=1}^{N} \mathcal{M}_{\mathcal{F}}(\overline{x},n) * \mathcal{M}_{\mathcal{B}}(\overline{x},n).\end{aligned}$$

In the next Figures (3.1-3.3) the solid black and green lines represent the surface and an interface respectively, the dashed green lines represent the depth of some incorrect artifact. Finaly the green lines are identified as G, H, I to distinguish the different depths in which wavefields

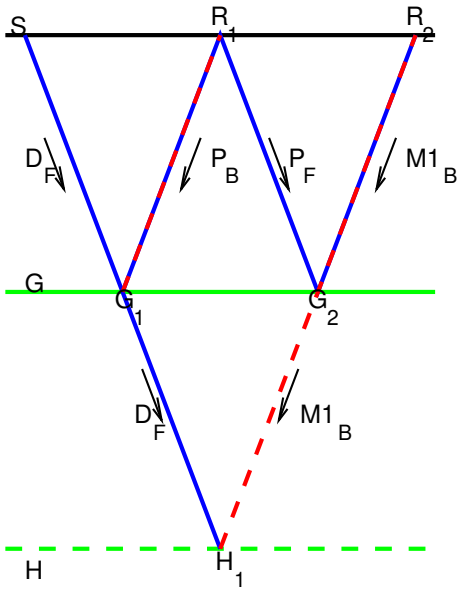

Figure 3.1. Physical meaning of the correlation between the direct wave $\mathcal{D}_{\mathcal{F}}$ of the forward wavefield $\mathcal{F}$ and the primaries and multiples ($\mathcal{P}_{\mathcal{B}}$ and $\mathcal{M}_{\mathcal{B}}$) of the retro-propagated adjoint wavefield $\mathcal{B}$.

correlate in the different points G_1-G_5, H_1-H_3 and I_1. The points S, R_1, R_2, R_3, R_4, and R_5 represent the location of the source and the receivers. These figures show the physical effect of the different correlations of the imaging condition of equation 3.25, considering the wavefields as rays.

The first term A of equation 3.25 represents the correlation between the forward wavefield $\mathcal{D}_{\mathcal{F}}$ and the primary $\mathcal{P}_{\mathcal{B}}$ of the retro-propagated adjoint wavefield $\mathcal{B}$.

The second term B represents the correlation of the same forward wave $\mathcal{D}_{\mathcal{F}}$ with the multiples $\mathcal{M}_{\mathcal{B}}$ of the adjoint retro-propagated wavefield (including all the orders).

The Figure 3.1 shows that $\mathcal{D}_{\mathcal{F}}$ interacts with $\mathcal{P}_{\mathcal{B}}$ at the point G_1, which gives the correct depth of the interface. However, $\mathcal{D}_{\mathcal{F}}$ interacts with $\mathcal{M}^1_{\mathcal{B}}$ (the first-order multiple of the adjoint retropropagated wavefield) at an incorrect depth (point H_1). We can also say that when the forward wavefield $\mathcal{D}_{\mathcal{F}}$ interacts with a higher order multiple they will do it at an incorrect depth that increases as the order of the multiple increases.

The term C expresses the correlation between primaries $\mathcal{P}_{\mathcal{F}}$ of the forward wavefield $\mathcal{F}$ with the primaries $\mathcal{P}_{\mathcal{B}}$ of the adjoint retro-propagated wavefield $\mathcal{B}$. We can see in Figure 3.1 that both wavefields never coincide in any point, therefore the correlation between $\mathcal{P}_{\mathcal{F}}$ and $\mathcal{P}_{\mathcal{B}}$ is null.

The term D expresses the correlation between the primaries $\mathcal{P}_{\mathcal{F}}$ of the forward wavefield $\mathcal{F}$ with the backward multiples $\mathcal{M}_{\mathcal{B}}$ of the adjoint retropropagated wavefield (all multiples are included). In Figure 3.2 we can see that the interaction between $\mathcal{P}_{\mathcal{F}}$ with the first order multiple $\mathcal{M}^1_{\mathcal{B}}$ of the retropropagated wavefield occurs at the correct depth of the interface at

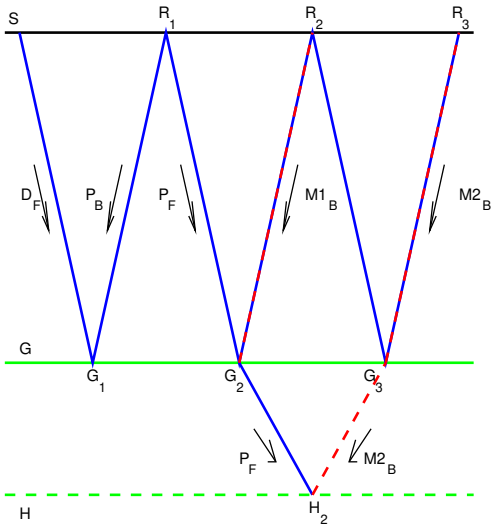

Figure 3.2. Physical meaning of the correlation between primaries $\mathcal{P}_{\mathcal{F}}$ of the forward wavefield $\mathcal{F}$ and multiples ($\mathcal{M}^1_{\mathcal{B}}$ and $\mathcal{M}^2_{\mathcal{B}}$) of the adjoint retropropagated wavefield $\mathcal{B}$.

point G_2. However, when $\mathcal{P}_{\mathcal{F}}$ interacts with the second order multiple $\mathcal{M}^2_{\mathcal{B}}$ of the adjoint retropropagated wavefield, they do it at an incorrect depth at point H_2. We can extrapolate this fact to higher orders where as the order of the multiple increases the depth of correlation increases. A summary of the correlation terms C and D are present in the following equations 3.26:

$$\begin{aligned}
&\sum_{n=1}^{N} \mathcal{P}_{\mathcal{F}} * \mathcal{P}_{\mathcal{B}} = 0 \\
&\sum_{n=1}^{N} \mathcal{P}_{\mathcal{F}} * \mathcal{M}^m_{\mathcal{B}} = image, m = 1 \\
&\sum_{n=1}^{N} \mathcal{P}_{\mathcal{F}} * \mathcal{M}^m_{\mathcal{B}} = artifact, m > 1,
\end{aligned} \tag{3.26}$$

where m is the order of the multiples.

The term E, which represents the correlation between the multiples $\mathcal{M}_{\mathcal{F}}$ of the forward multiple wavefield $\mathcal{F}$ and the primaries $\mathcal{P}_{\mathcal{B}}$ of the retropropagated adjoint wavefield $\mathcal{B}$, does not produce neither an image nor an artifact because they will never coincide in any point. Therefore, the contribution of the term E to the equation 3.25 is null.

Considering Figure 3.3, the term F represents the interaction between the multiples $\mathcal{M}_{\mathcal{F}}$ of the forward wavefield $\mathcal{F}$ and the multiples $\mathcal{M}_{\mathcal{B}}$ of the adjoint retropropagated wavefield $\mathcal{B}$, we can see that the first order multiple $\mathbf{M}^1_{\mathcal{F}}$ of the wavefield $\mathcal{F}$ interacts with the second order multiple $\mathcal{M}^2_{\mathcal{B}}$ of the adjoint wavefield $\mathcal{B}$ in the correct depth at point G_3. Nevertheless, when this first order multiple $\mathbf{M}^1_{\mathcal{F}}$ interacts with third and fourth order multiples ($\mathbf{M}^3_{\mathcal{B}}$ and $\mathbf{M}^4_{\mathcal{B}}$) coming from receivers R_2 and R_3 respectively, artifacts are produced at wrong depths (points H_3 and I_1). These depths increase as the difference between the orders of the multiples of the forward and adjoint wavefields increase.

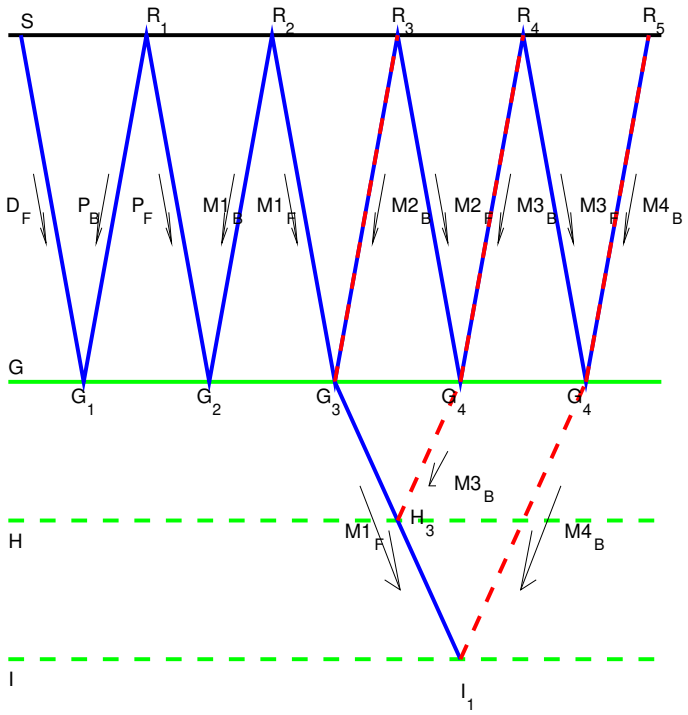

Figure 3.3. Physical effect of the correlation between the first order multiple $\mathcal{M}^1_{\mathcal{F}}$ of the forward wavefield $\mathcal{F}$ and the second, third and fourth order multiples ($\mathcal{M}^2_{\mathcal{B}}$, $\mathcal{M}^3_{\mathcal{B}}$, $\mathcal{M}^4_{\mathcal{B}}$) of the adjoint retro-propagated wavefield $\mathcal{B}$.

Summarizing the effects of terms E and F, and extending what was said in equations 3.26, we can write that:

$$\begin{aligned}
&\sum_{n=1}^{N} \mathcal{M}_{\mathcal{F}}^{m} * \mathcal{M}_{\mathcal{B}}^{m+1} = image \\
&\sum_{n=1}^{N} \mathcal{M}_{\mathcal{F}wave}^{m} * \mathcal{M}_{\mathcal{B}}^{m+p} = artifact; \quad p > 1 \\
&\sum_{n=1}^{N} \mathcal{M}_{\mathcal{F}}^{r} * \mathcal{M}_{\mathcal{B}}^{q} = 0; \quad q < r,
\end{aligned} \tag{3.27}$$

where the superscripts refer to the order of the multiples.

Finally, we can write equation 3.25 as:

$$\begin{aligned}
&\sum_{n=1}^{N} [\mathcal{D}(\overline{x}, n) * \mathcal{P}_{\mathcal{B}}(\overline{x}, n) + \mathcal{P}_{\mathcal{F}}(\overline{x}, n) * \mathcal{M}_{\mathcal{B}}^{1}(\overline{x}, n) + \mathcal{M}_{\mathcal{F}}^{m} * \mathcal{M}_{\mathcal{B}}^{m+1}] = image \\
&\sum_{n=1}^{N} [\mathcal{D}(\overline{x}, n) * \mathcal{M}_{\mathcal{B}}(\overline{x}, n) + \mathcal{P}_{\mathcal{F}}(\overline{x}, n) * \mathcal{M}_{\mathcal{B}}^{p}(\overline{x}, n) + \mathcal{M}_{\mathcal{F}}^{m} * \mathcal{M}_{\mathcal{B}}^{m+p}] = artifact,
\end{aligned} \tag{3.28}$$

where the superscripts represent the order of the multiples and $p > 1$ and m could take any value.

f) Imaging condition when absorbing boundary conditions at the top of the model are applied.

We propose a computational artifice that consists in replacing the free surface by absorbing boundary conditions on the top of the mesh in order to analyze the reflections absorbed at the free surface and see how to attenuate or remove them. In figures 3.6 we present a comparison between different computational domains. Figure 3.6(a) represents the classical computational domain used for solving the wave equation, while figure 3.6(b) a layer of absorbing-boundary conditions replaces the free-surface conditions layer. Although when applying this computational domain we are not solving the original physical wave equation (i.e in presence of the free surface), we applied this computational artifice to enhance the interfaces by reducing the effect of free-surface multiples.

Ignoring internal multiples, the wavefields $\mathcal{F}$ and $\mathcal{B}$ can thus be written as:

$$\begin{aligned}
\mathcal{F}(\overline{x}, t) &= \mathcal{D}(\overline{x}, n) + \mathcal{P}_{\mathcal{F}}(\overline{x}, n), \\
\mathcal{B}(\overline{x}, n) &= \mathcal{P}_{\mathcal{B}}(\overline{x}, n) + \mathcal{M}_{\mathcal{B}}(\overline{x}, n),
\end{aligned} \tag{3.29}$$

where in comparison to equation (3.22), the wavefield $\mathcal{F}(\overline{x}, t)$ is free of multiples due to the absorbing boundary that replaces the free surface. Therefore, the equations (3.28) could

be written as:

$$\sum_{n=1}^{N}[\mathcal{D}(\overline{x},n)*\mathcal{P}_{\mathcal{B}}(\overline{x},n)+\mathcal{P}_{\mathcal{F}}(\overline{x},n)*\mathcal{M}^{1}_{\mathcal{B}}(\overline{x},n)]=image$$
$$\sum_{n=1}^{N}[\mathcal{D}(\overline{x},n)*\mathcal{M}_{\mathcal{B}}(\overline{x},n)+\mathcal{P}_{\mathcal{F}}(\overline{x},n)*\mathcal{M}^{m}_{\mathcal{B}}\overline{x},n)]=artifact, \tag{3.30}$$

where $m>1$ is the order of the multiple. Compared to equations 3.28, the artifact contribution has lost one term, therefore the deeper artifacts (see figure 3.3) are drastically attenuated.

In case that we apply a multiple attenuation process before computing the RTM process, we will thus obtain an image condition given by the following equation 3.31 which is more simply expressed as a correlation between the direct forward wavefield D and the primaries $P_{\mathcal{B}}$ of the adjoint retropropagated wavefield $\mathcal{B}$) :

$$I(\overline{x})=\sum_{n=1}^{N}\mathcal{D}(\overline{x},n)*\mathcal{P}_{\mathcal{B}}(\overline{x},n). \tag{3.31}$$

We can see also that although we have reduced the artifact effect, we have also lost two terms (see equations 3.28) in the image contribution.

g) Imaging conditions when the adjoint source is the residual between observed and calculated data.

In this section we consider the development of the equations of sections (e)-f)) and only mention some of these equations considering that the adjoint source is the residual between the calculated and observed data. The equation 3.22 is replaced by

$$\mathcal{F}(\overline{x},n)=\mathcal{D}_{\mathcal{F}}(\overline{x},n)+\mathcal{P}_{\mathcal{F}}(\overline{x},n)+\mathcal{M}_{\mathcal{F}}(\overline{x},n),$$
$$\mathcal{B}(\overline{x},n)=\mathcal{P}_{\mathcal{B}cal}(\overline{x},n)+\mathcal{M}_{\mathcal{B}cal}(\overline{x},n)-\mathcal{P}_{\mathcal{B}}(\overline{x},n)-\mathcal{M}_{\mathcal{B}}(\overline{x},n), \tag{3.32}$$

where $\mathcal{P}_{\mathcal{B}cal}$ and $\mathcal{M}_{\mathcal{B}cal}$ are the primaries and multiples of the calculated data respectively. In this equation, the back-propagated source is defined as the residual between the calculated and observed data, unlike equation 3.22, where the observed data are injected as the back-propagated source.

Therefore, following the same development from equation 3.24 to 3.28 the imaging condition is defined here as:

$$\sum_{n=1}^{N}[\mathcal{D}(\overline{x},n)*\mathcal{P}_{\mathcal{B}cal}(\overline{x},n)+\mathcal{P}_{\mathcal{F}}(\overline{x},n)*\mathcal{M}^{1}_{\mathcal{B}cal}(\overline{x},n)+\mathcal{M}^{m}_{\mathcal{F}}*\mathcal{M}^{m+1}_{\mathcal{B}cal}$$
$$-\mathcal{D}(\overline{x},n)*\mathcal{P}_{\mathcal{B}}(\overline{x},n)-\mathcal{P}_{\mathcal{F}}(\overline{x},n)*\mathcal{M}^{1}_{\mathcal{B}}(\overline{x},n)-\mathcal{M}^{m}_{\mathcal{F}}*\mathcal{M}^{m+1}_{\mathcal{B}}]=image$$
$$\sum_{n=1}^{N}[\mathcal{D}(\overline{x},n)*\mathcal{M}_{\mathcal{B}cal}(\overline{x},n)+\mathcal{P}_{\mathcal{F}}(\overline{x},n)*\mathcal{M}^{p}_{\mathcal{B}cal}(\overline{x},n)+\mathcal{M}^{m}_{\mathcal{F}}*\mathcal{M}^{m+p}_{\mathcal{B}cal}$$
$$-\mathcal{D}(\overline{x},n)*\mathcal{M}_{\mathcal{B}}(\overline{x},n)-\mathcal{P}_{\mathcal{F}}(\overline{x},n)*\mathcal{M}^{p}_{\mathcal{B}}(\overline{x},n)-\mathcal{M}^{m}_{\mathcal{F}}*\mathcal{M}^{m+p}_{\mathcal{B}}]=artifact. \tag{3.33}$$

When we apply absorbing-boundary conditions at the top of the computational domain, the equation 3.33 reduces to:

$$\sum_{n=1}^{N}[\mathcal{D}(\overline{x},n)*\mathcal{P}_{\mathcal{B}cal}(\overline{x},n)+\mathcal{P}_{\mathcal{F}}(\overline{x},n)*\mathcal{M}^{1}_{\mathcal{B}cal}(\overline{x},n)]$$
$$-\mathcal{D}(\overline{x},n)*\mathcal{P}_{\mathcal{B}}(\overline{x},n)-\mathcal{P}_{\mathcal{F}}(\overline{x},n)*\mathcal{M}^{1}_{\mathcal{B}}(\overline{x},n)]=image$$
$$\sum_{n=1}^{N}[\mathcal{D}(\overline{x},n)*\mathcal{M}_{\mathcal{B}cal}(\overline{x},n)+\mathcal{P}_{\mathcal{F}}(\overline{x},n)*\mathcal{M}^{m}_{\mathcal{B}cal}\overline{x},n)] \tag{3.34}$$
$$-\mathcal{D}(\overline{x},n)*\mathcal{M}_{\mathcal{B}}(\overline{x},n)-\mathcal{P}_{\mathcal{F}}(\overline{x},n)*\mathcal{M}^{m}_{\mathcal{B}}\overline{x},n)]=artifact, \tag{3.35}$$

and finally when in the observed data the free-surface multiples are attenuated, the imaging condition reduces to:

$$\sum_{n=1}^{N}[\mathcal{D}(\overline{x},n)*\mathcal{P}_{\mathcal{B}cal}(\overline{x},n)-\mathcal{D}(\overline{x},n)*\mathcal{P}_{\mathcal{B}}(\overline{x},n)]. \tag{3.36}$$

Therefore, unlike the equations shown in points e and f, in these imaging conditions the influence of the adjoint source (residual), is observed. Where the terms associated with the observed data appear with a negative sign, this could cancel the correct signal, for example in equation 3.36.

3.2 Results in 2D

We tested our algorithm using synthetic density and velocity models (Figures 3.4(a) and 3.4(b) respectively) representing a region of the Gulf of Mexico with strong presence of salt tectonics. The figure 3.4(c) represents the impedance model. In the following we aim at comparing the sensitivity kernels using different sets of a priori models.

Different a priori models. As first a priori model, we fix the bathymetry and we set depth-increasing parameter values of the densities and velocities under the bathymetry (figures 3.5(a) and 3.5(b)). For simplicity we name it “model M1". We also smoothed the true model by applying a Gaussian filter with standard deviation of 12 m/s, and we named this smoothed model as the a priori “model M2" (Figures 3.5(c), and 3.5(d)).

3.2.1 Numerical parameters

The 2D acoustic elastodynamic equations were solved by using a second order staggered grid finite difference scheme proposed by Virieux [1986]. The time and spatial sampling are $\Delta t = 0.0025$s, $\Delta x = \Delta z = 20.0$m, and the total time of simulation is 8 seconds.

In a first approach, to reduce CPU time and to see how the different parametrizations work, we introduce a simultaneous-sources scheme. The sources and receivers are located at the surface with a separation of 20 meters between them. Furthermore, the explosive sources $f(t)$

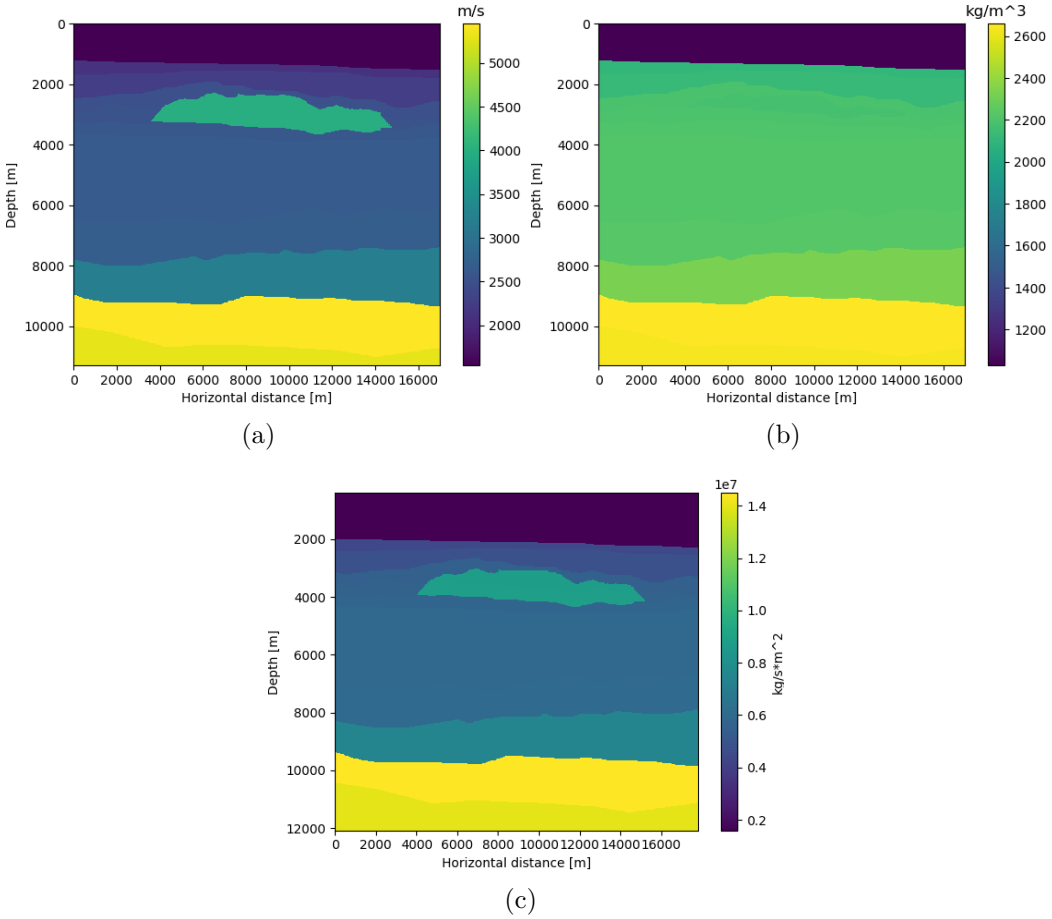

Figure 3.4. Figures a, b, and c represent the “true" P velocity, density and impedance models respectively used to obtain the observed data in figures 3.8.

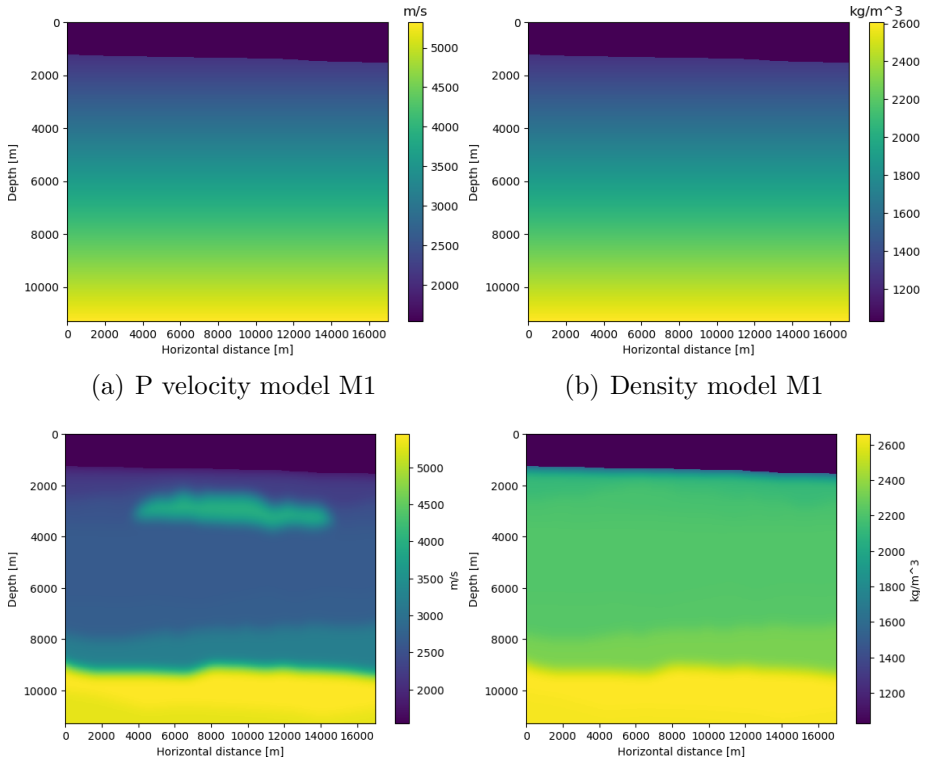

(a) P velocity model M1

(b) Density model M1

(c) P velocity model M2

(d) Density model M2

Figure 3.5. Figures a and b represent the P velocity and density a priori models "M1" respectively, considering a gradient from the minimal value (under the bathymetry) to the maximal value (bottom of the model), used to compute the RTM images. In Figures c and d, we smoothed the true model (a priori model "M2").

were simulated using the derivative of a Gaussian impulse (equation 3.37), where $\gamma = 4\pi^2 f_0^2$, f_0 and $t_0 = 1.2/f_0$ are the dominant frequency and the time delay respectively, A is the source amplitude, and n represents the time samples:

$$f(n\Delta t) = -2A\gamma(n\Delta t - t_0)e^{-\gamma(n\Delta t - t_0)^2}. \tag{3.37}$$

In addition, CPML absorbing boundary conditions were implemented as indicated in Komatitsch and Martin [2007]. In Figures 3.6, we present the two-dimensional computational domains used in this work. The Figure 3.6(a) represents the computational domain used (i.e in presence of the free surface) to compute the real observed data, while the Figure 3.6(b) represents a computational domain altered by a computational artifice (we changed the top free-surface conditions by CPML absorbing boundary conditions) to compute the forward and adjoint solutions for the current model.

In sections 3.2.2-3.2.4, we compute the forward and adjoint acoustic equations 3.2, 3.9 (with $\mu = 0$) in presence of PML absorbing boundary conditions at the top of the domain, using the back-propagated source as $f^\dagger = d_{obs}$ (this means also that $d_{calc} = 0$ as in the classical RTM imaging condition with almost no impedance contrast prior models). Here, the observed data were calculated applying free-surface conditions at the top of the computational domain. Therefore we are re-creating case 2, which we describe a little further down. When $d_{calc} = 0$, this also means that the seismic images are obtained in a first approach for a background/prior model containing no contrast at all or a prior model extremely smooth as described in Lailly and Bednar [1983], Claerbout et al. [1985], and Virieux and Operto [2009]. However, this case is not the most relevant, because generally we want to obtain the main interfaces for a given low frequency content prior model with enough information in it and highlight those interfaces by computing strong high frequency contrast impedances of the model.

By this mean we want to obtain at the same time all the interfaces even when we add a priori information. However, we want also to decrease multiple artifacts generated by the free surface, when we attenuate or not the free surface effects simultaneously in both the synthetic 'real' data and the computed data.

Then in subsections 3.2.5, 3.2.6 and in appendix F we introduce the adjoint source defined by the difference between observed and synthetic data for different background models, and we thus present the following cases:

- Case 1: The forward and adjoint problems were computed using the computational domain of Figure 3.6(a) (free surface condition at the top of the domain). The adjoint source is computed as $f^\dagger = d_{obs} - d_{calc}$, where the observed data d_{obs} were computed using free surface at the top of the computational domain (free-surface multiples are present).

- Case 2: The forward and adjoint problems were computed using the computational domain of Figure 3.6(b) (absorbing boundary conditions at the top of the computational domain). The adjoint source is computed as $f^\dagger = d_{obs} - d_{calc}$, where the observed data are

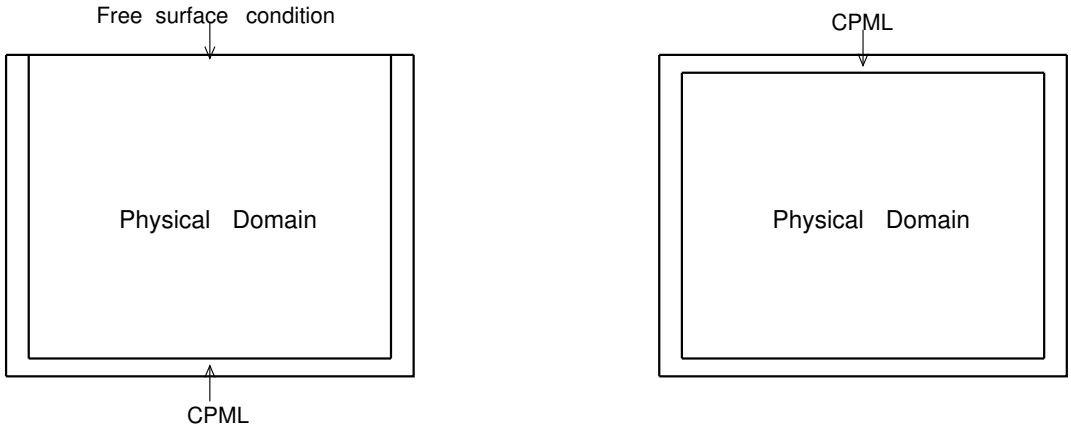

(a) (b)

Figure 3.6. Different computational domains used to solve the proposed RTM algorithm applying free-surface conditions (a) or absorbing-boundary conditions (b) on the top in order to attenuate free-surface artifacts.

the same as in case 1 (i.e with a free surface), while the synthetic data d_{calc} are computed using absorbing conditions at all four boundaries. This allows to both attenuate the first multiples and highlight the interfaces and the bathymetry with fewer artifacts due to the free surface.

- Case 3: The forward and adjoint problems were computed using absorbing boundary conditions at the top of the computational domain. The adjoint source is computed as $f^{\dagger} = d_{obs} - d_{calc}$, where the observed data were computed using absorbing boundary conditions at the top of the computational domain (free-surface multiples are attenuated).

In the next subsections we show the 2D-acoustic kernels following the parametrization (ρ, λ) and $(\ln \rho, \ln \lambda)$ (equations 3.18).

For each computational domain configuration following the equation 3.8, we applied:

- A normalization by the forward energy.
- A normalization by the adjoint energy.
- No normalization.

In Figure 3.7, we present a comparison of the snapshots during time when applying the computational domains from figure 3.6(a) (see Figures 3.7(a), 3.7(c), and 3.7(e)) and 3.6(b) (see Figures 3.7(b), 3.7(d), and 3.7(f)) respectively. In these last figures we can observe how the free-surface multiples are not generated.

The “observed" seismograms (computed using the true models from Figures 3.4(a) and 3.4(b)) are shown in Figure 3.8.

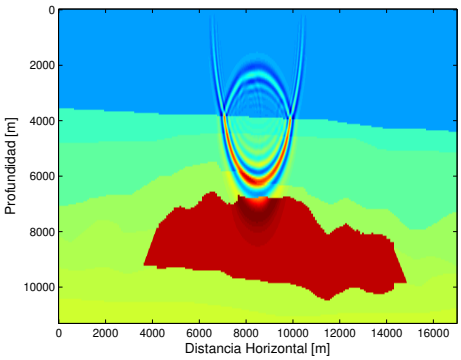

(a) $t = 1.525s$.

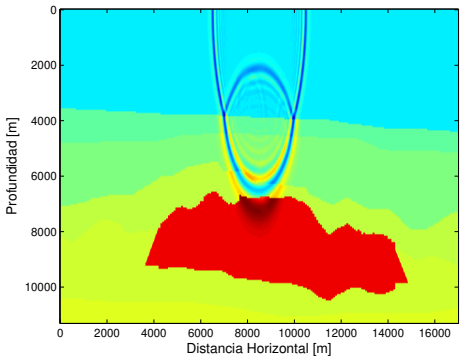

(b) $t = 1.525s$.

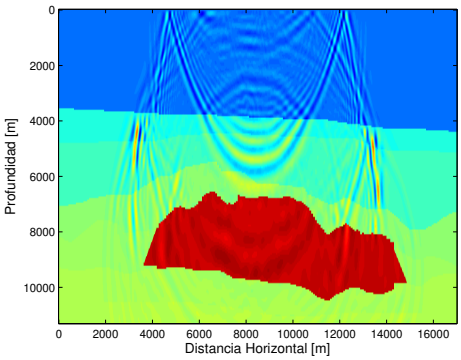

(c) $t = 3.275s$.

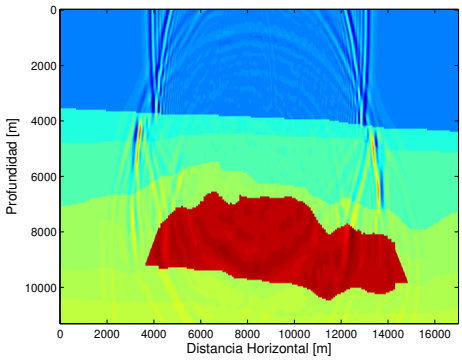

(d) $t = 3.275s$.

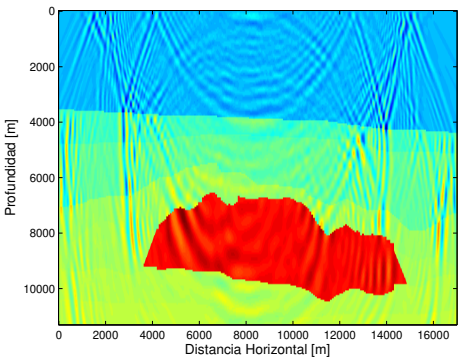

(e) $t = 4.775s$.

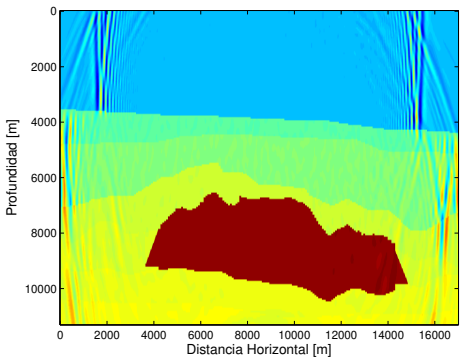

(f) $t = 4.775s$.

Figure 3.7. Zoom of the snapshots for the forward wave propagation in the “true" model, using free surface on top (Figures a, d, and e), and without free surface (PML conditions) on top (Figures b, d, and f).

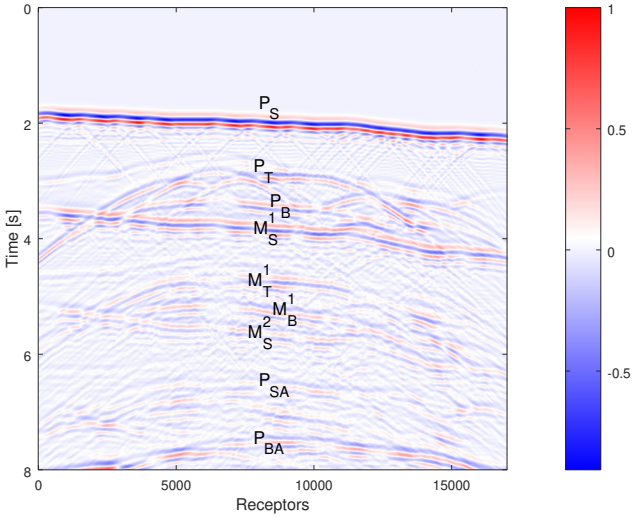

Figure 3.8. Simultaneous-sources seismogram used as the “observed" data calculated with the free surface. The principal events are marked as: P_S the sea bottom primary, P_T top of the salt primary, P_B base of the salt primary, M_S^1 order 1 multiple of the sea bottom, M_T^1 order 1 multiple of the top of salt, M_B^1 order 1 multiple of the base of salt, M_S^2 order 2 multiple of the sea bottom, P_{SA} primary sandstone, P_{BA} primary basement.

In the subsections 3.2.2 and E.1, we first show simultaneous-sources kernels using the M1 and M2 prior models to get images quickly and choose the best layouts to calculate images with separate sources (subsections 3.2.3, E.2, E.3, and 3.2.4).

To make easier the interpretation of the kernels, we assigned a number to each geological interface as shown in Figure 3.9, where the red asterisks indicate the coordinate we took to calculate the signal-to-noise ratio of Table 3.1.

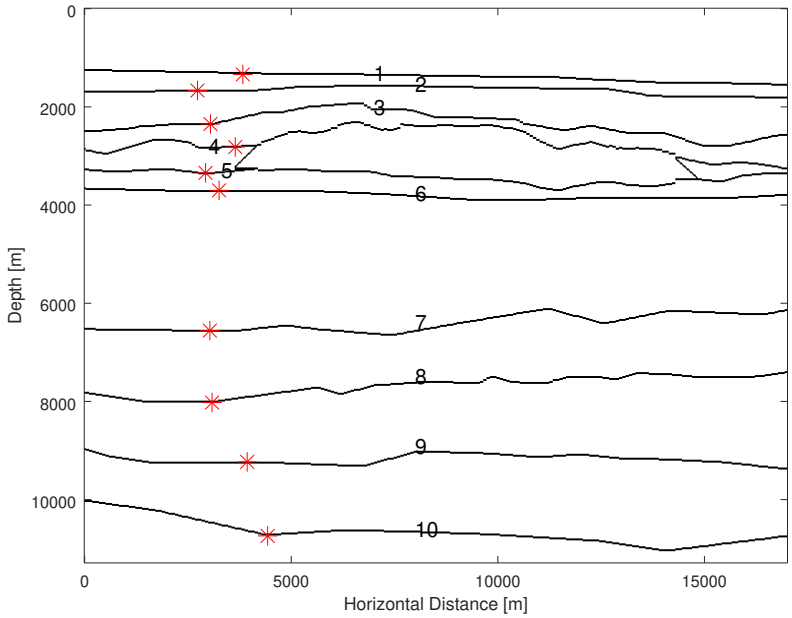

Figure 3.9. Interfaces derived from the true velocity model. The red asterisks indicate the coordinates where we took the samples of the interfaces to calculate the signal-to-noise ratio of the table 3.1.

3.2.2 Sensitivity kernels for the a priori model M1, injecting simultaneous sources.

As indicated previously, pursuing a real data processing, where we do not know the true model, we introduced the model M1 (Figures 3.5(a) and 3.5(b)) as the a priori model. We present the kernels $K_{\ln\lambda}$, $K_{\ln\rho}$, K_{lnVp}, $K''_{ln\rho}$, and K_{lnZp}, using the parametrizations ($\ln\rho$, $\ln\lambda$), ($\ln\rho$, $\ln V_p$), and ($\ln\rho$, $\ln Z_p$) (Figures 3.10). We choose not to present the kernel $K'_{ln\rho}$ due to physical high-frequency noise contamination. In this section, all the kernels were calculated applying absorbing boundary conditions at the top of the computational domain.

As we can see that the salt dome is well defined, we interpret it and set it in the next a priori model as shown in Figures E.1(a) and E.1(b) that we decide to include in the appendix F. We show the kernels obtained in the next subsection.

3.2.3 Sensitivity kernels for the a priori model M1, injecting separated sources.

In order to recreate a real survey and reduce source interferences ("cross-talks") when compared to a simultaneous sources case, we injected 50 separated sources at the surface. The kernels we obtained are shown in Figures 3.11.

To better appreciate the deeper interfaces, we applied a gain with respect to the depth: $g = z^2$, where g is the gain and z is the depth coordinate.

When we compared these kernels to kernels of Figures 3.10, we can see that artifacts close to the upper surface caused by source interferences are eliminated. We can see a better definition of the salt dome and the interface 6, although the deeper interfaces still present ambiguities.

3.2.4 Sensitivity kernels using the smoothed model M2 as the a priori model, and injecting separated sources and receivers under the bathymetry.

Following an *Ocean Bottom Cable* (OBC) approach, we simulated a separated-sources survey. We show the kernels K_λ and K_ρ in Figures 3.12 that were obtained using the smoothed model (Model M2) as the a priori model (figures 3.5(c), 3.5(d)). Figure 19 shows well defined upper interfaces especially the interface 3 and the top of the salt dome. The deeper interfaces 8 and 9 are also very well defined. We can see a slight smoothing (essentially at the upper interfaces 3-5) in kernel K_ρ with respect to kernel K_λ. This fact could be attributed to a lower frequency content in kernel K_ρ. Besides, kernel K_λ shows better the upper interfaces (2 to 6). K_ρ shows better the large wavelengths at depth, while K_λ shows better the short wavelengths close to the surface around the salt dome.

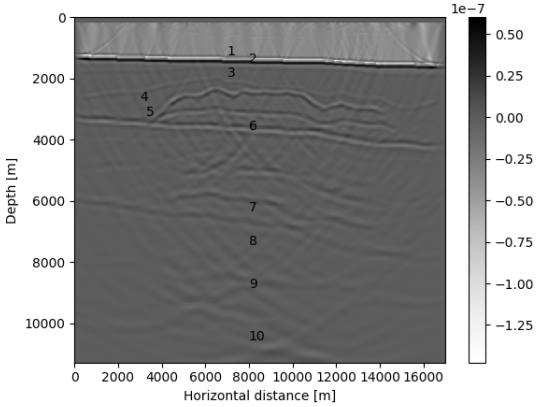

(a) Kernel $K_{\ln \lambda}$.

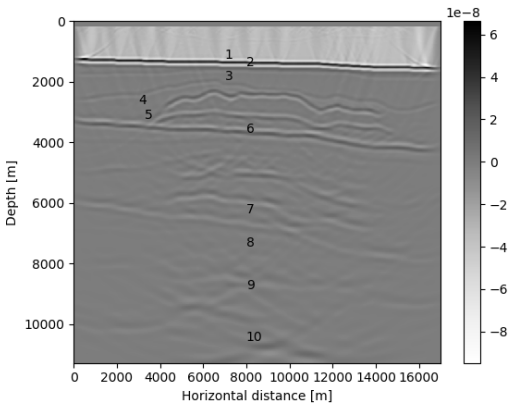

(b) Kernel $K_{\ln \rho}$.

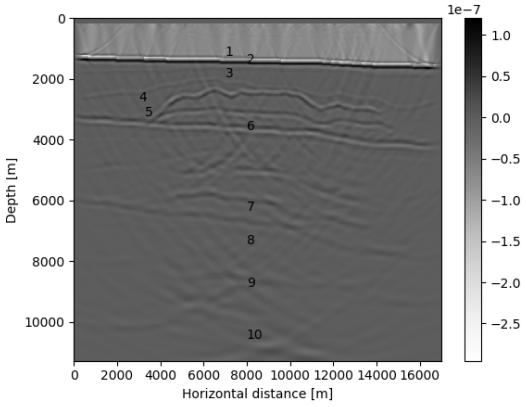

(c) Kernel $K_{\ln Vp}$.

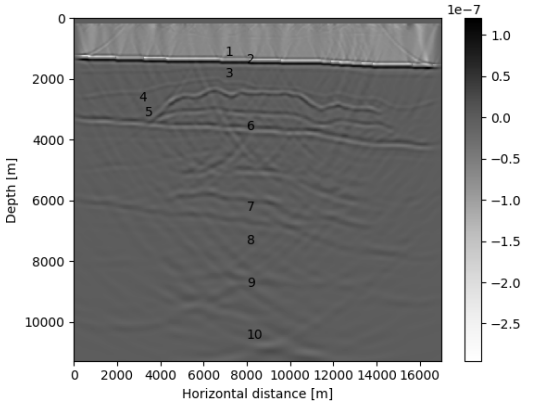

(d) Kernel $K_{\ln Zp}$.

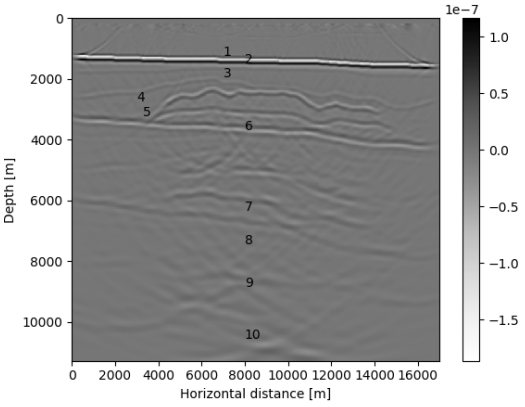

(e) Kernel $K''_{\ln \rho}$.

Figure 3.10. Kernels computed using the prior model M1, applying the case 2 with $\boldsymbol{f^{\dagger}}$=$\boldsymbol{d_{obs}}$. Figures (a,b): Kernels $K_{\ln \lambda}$ and $K_{\ln \rho}$ for the parametrization ($\ln \rho$, $\ln \lambda$). Figure (c): kernel $K_{\ln Vp}$ for the parametrization ($\ln \rho, \ln V_p$). And figures (d,e): kernels $K''_{\ln \rho}$ and $K_{\ln Zp}$ for the parametrization ($\ln \rho$, $\ln Z_p$). To compute the image we used absorbing boundary conditions at the top of the computational domain. The simultaneous sources are injected below the surface.

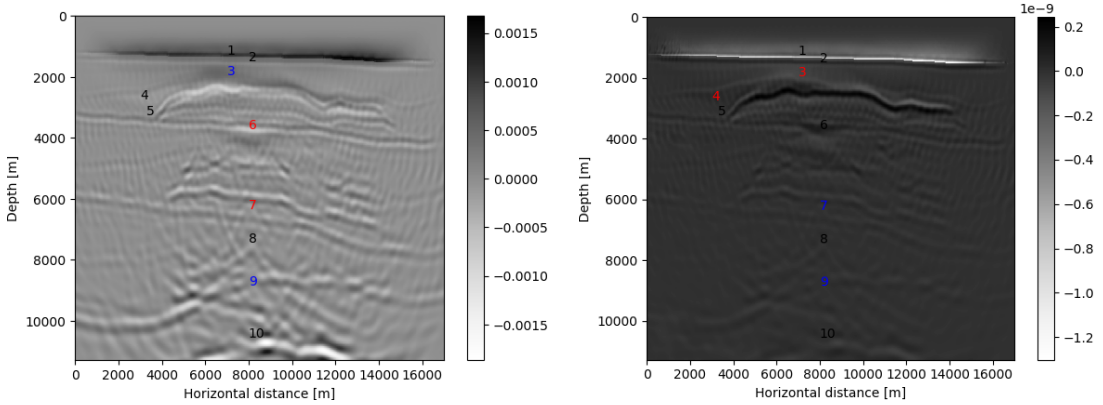

(a) Kernel K_ρ. (b) Kernel K_λ.

Figure 3.11. Kernels K_λ and K_ρ using model M1 as the a priori model (Figures 3.5(a) and 3.5(b)), applying the case 2 with $\boldsymbol{f^\dagger = d_{obs}}$. These kernels were obtained using 50 separated sources. To compute the image we used absorbing boundary conditions at the top of the computational domain. The sources and receivers are located below the surface.

This fact is interesting because the images are clearly showing that the RTM is able to separate the scales and wavelengths, and more particularly the small wavenumbers given by the density reflectivity images in one hand and the large wavenumbers provided by the V_p, λ, and Z_p kernel images in the other hand. However, there are still remaining artifacts in the image because the RTM method is not really able to reduce "cross-talks" due to interferences between correlated waves at the interfaces and their related wavelengths. This is why it would be better to apply the LS-RTM technique to reduce the artifacts more efficiently and obtain better reflectivity images by using the impedance (ρ, Z_p) parametrization.

Furthermore, as we do in the next chapter 4, we can also perform a FWI to obtain a first model in the vicinity of the a priori model and also obtain an "a posteriori" reflectivity image. During the inversion process of FWI, the attenuation of multiples is increased at the same time that the models and interfaces are recovered at the right location.

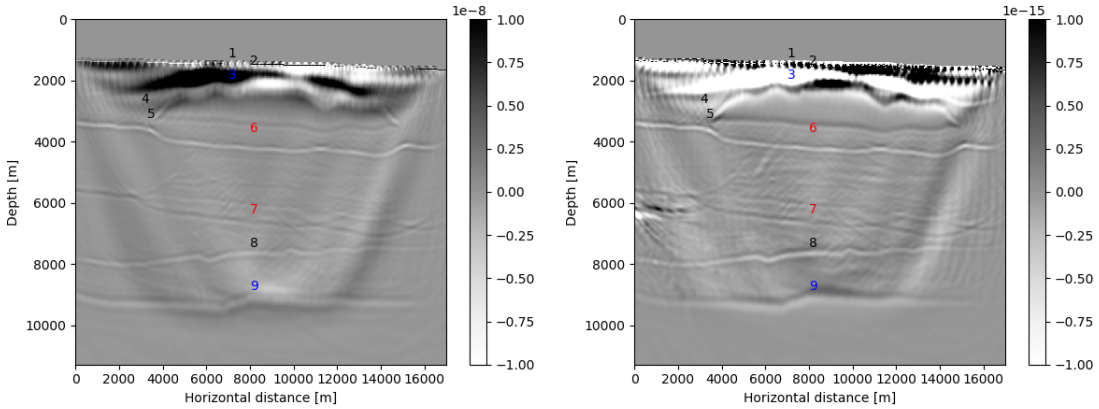

(a) Kernel K_ρ.

(b) Kernel K_λ.

Figure 3.12. Kernels K_λ and K_ρ for "OBC-like" configuration, using the smoothed M2 models (Figures a and b) as the prior models, applying the case 2, with $f^\dagger = d_{obs}$. The sources and receivers are located below the bathymetry. These kernels were obtained injecting 50 separated sources. To compute the image we used absorbing boundary conditions at the top of the computational domain.

In the subsections 3.2.5-F we present the results of the 3 cases described in the subsection 3.2.1. The main purpose of incorporating these results is to make a qualitative comparison of the different cases described and thus present arguments for or against the incorporation of absorbing boundary conditions at the top of the computational domain. For time reasons, these results were computed using simultaneous sources. The kernels are normalized by the forward energy as in equations 3.8, which in turn tends to increase these normalized kernels due to the geometrical divergence and attenuation of waves with distance to the source. The interfaces are thus better defined applying kernel normalization than without it. Furthermore, we apply to the normalized kernels a gain according to the depth z (we multiply each pixel by z), where z increases with depth. This allows also to exhibit the interfaces at depth with even more intensity.

3.2.5 Case 1: Sensitivity kernels using free-surface conditions to compute the forward and adjoint problems. The observed data were computed using free-surface conditions.

In Figures 3.13 and 3.14 we show the kernels K_ρ and K_λ calculated with the model M1 and M2 as the a priori model, using the computational domain shown in Figure 3.6(a). The observed data were calculated using the computational domain of the Figure 3.6(a) (free-surface multiples are present). The imaging condition used to compute the kernels is described by equations 3.33.

In Figures 3.13, the structure of the salt dome is retrieved, as well as the interface 6 (below the dome). However multiple contamination is present at the deepest interfaces, which prevents from correctly seeing the structures of the model.

In Figures 3.14 the structures of the dome and the interface below it are also retrieved. Furthermore the shape of the interfaces 7, 8, and 10 are better constructed than in the Figures 3.13.

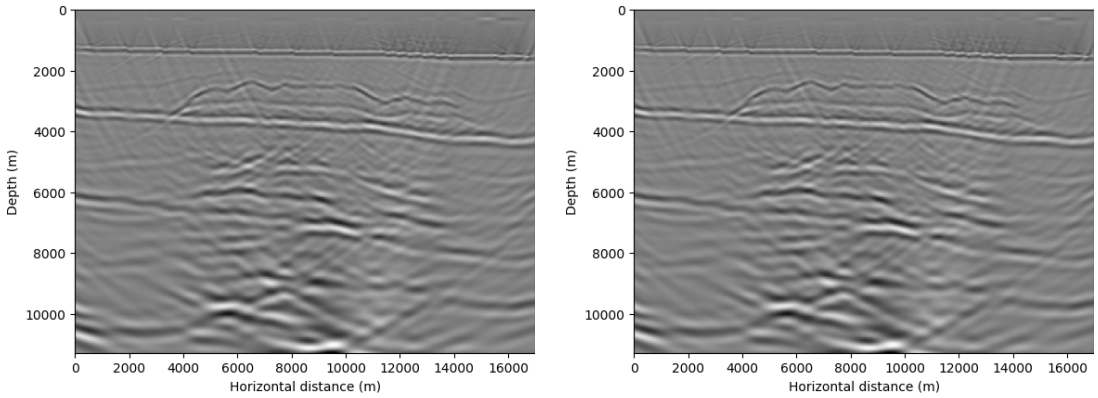

(a) Kernel K_ρ. (b) Kernel K_λ.

Figure 3.13. Kernels K_λ and K_ρ using free-surface conditions to compute the forward and adjoint problems using the model M1 as the a priori model, applying the case 1 with $\boldsymbol{f^\dagger = d_{obs} - d_{calc}}$. The observed data are computed using free surface conditions at the top of the copoutational domain (free-surface multiples are present). The kernels are normalized by the forward energy, and have a gain according to the depth by a factor of z. The sources and receivers are located at the top of the water.

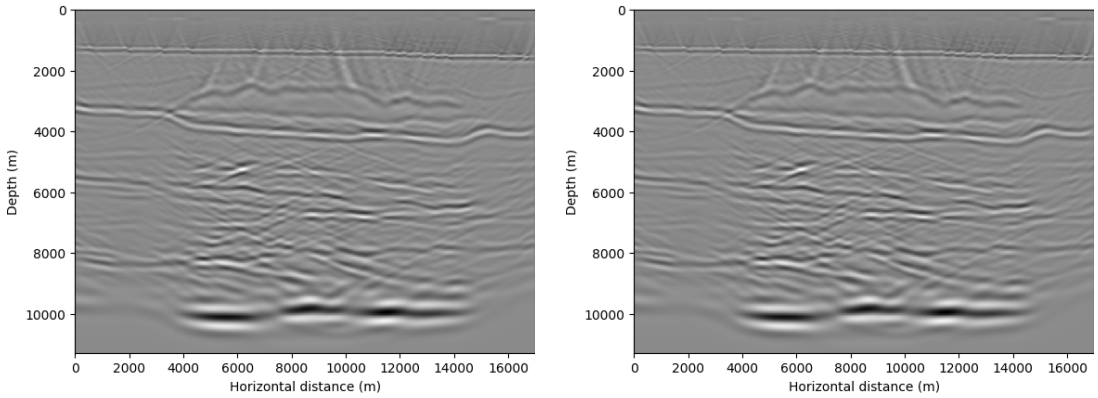

(a) Kernel K_ρ. (b) Kernel K_λ.

Figure 3.14. Kernels K_λ and K_ρ using free-surface conditions to compute the forward and adjoint problems using the model M2 as the a priori model, applying the case 1 with $\boldsymbol{f^\dagger = d_{obs} - d_{calc}}$. The observed data are computed using free surface conditions at the top of the copoutational domain (free-surface multiples are present). The sources and receivers are located at the top of the water.

3.2.6 Case 2: Sensitivity kernels using absorbing-boundary conditions to compute the forward and adjoint problems. The observed data were computed using free-surface conditions.

In Figures 3.15 and 3.16 we show the kernels K_ρ and K_λ calculated with the M1 and M2 as the a priori models, using the computational domain shown in Figure 3.6(b). The observed data were computed using free surface conditions (i.e using the computational domain of Figure 3.6(a)) and for which free-surface multiples are present. The imaging conditions used to compute the kernels are described in equations 3.34.

In kernels of Figures 3.15 the salt dome structure is correctly retrieved. At deeper distances from bathymetry we observe multiple contamination. However, this contamination is lower compared to kernels from Figures 3.13.

In figures 3.16 the salt dome structure and the interface below it are retrieved, and the multiple contamination is reduced compared to Figures 3.16.

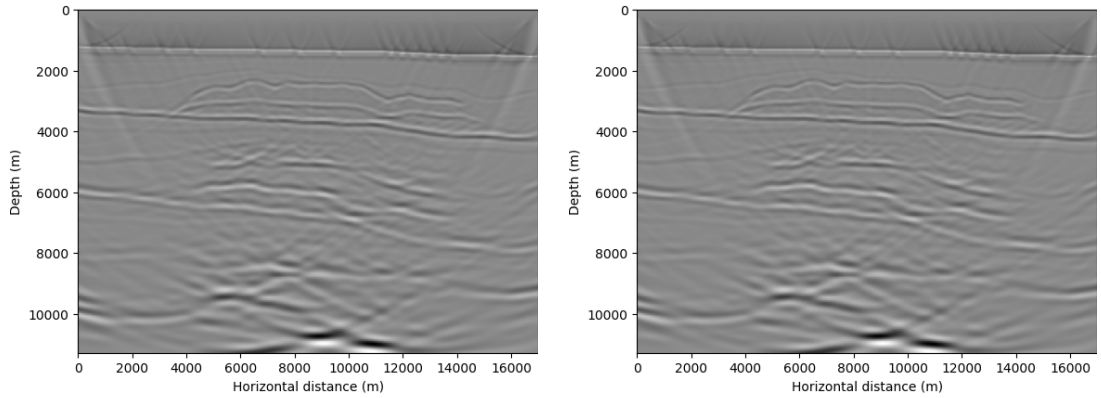

(a) Kernel K_ρ.

(b) Kernel K_λ.

Figure 3.15. Kernels K_λ and K_ρ using absorbing-boundary conditions to compute the forward and adjoint problems using the model M1 as the a priori model, applying the case 2 with $\boldsymbol{f^\dagger = d_{obs} - d_{calc}}$. The observed data are computed using free surface conditions at the top of the computational domain (free-surface multiples are present). The sources and receivers are located at the top of the water.

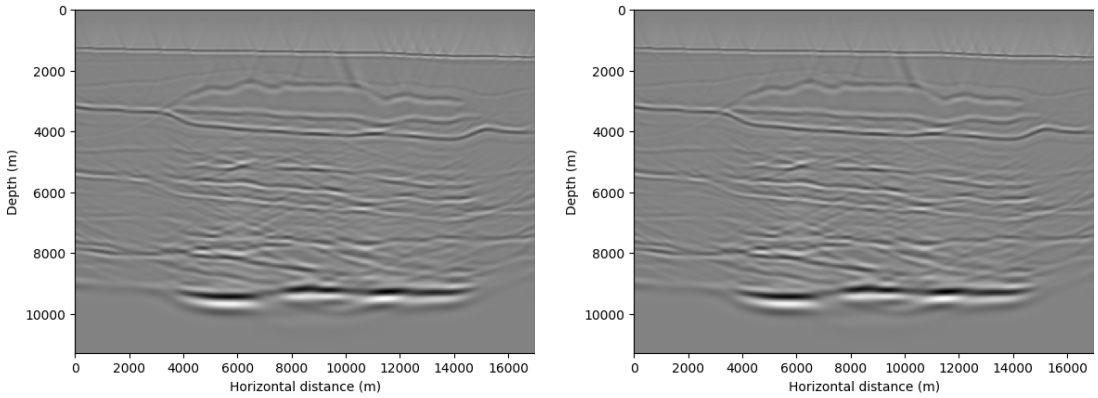

(a) Kernel K_ρ.

(b) Kernel K_λ.

Figure 3.16. Kernels K_λ and K_ρ using absorbing-boundary conditions to compute the forward and adjoint problems using the model M2 as the a priori model, applying the case 2 with $f^\dagger = d_{obs} - d_{calc}$. The observed data are computed using free surface conditions at the top of the computational domain (free-surface multiples are present). The sources and receivers are located at the top of the water.

3.3 Discussion.

In order to investigate the best strategy for determining the a priori models that provides images with less contamination by multiples and to visualise more clearly the salt dome and the interfaces underneath it, the different a priori models analyzed are:

- Model M1: A gradient in depth of the density and velocity models under the bathymetry.
- Model M2: The smoothed model.

The RTM has been applied to both M1 and M2 prior models to show the ability of RTM to better retrieve at the same time the interfaces (impedance contrast) in presence of prior model information or not.

We performed a quantitative analysis of the results by calculating the Signal-to Noise Ratio (SNR). We calculate it by choosing the value of a pixel of the interface and a value for the noise (where there is no interface) of each event (see Figure 3.9). Then we calculate the average of the signal (interface) and the noise between the 8 pixel around the pixel we have chosen (in total is an average of 9 pixels).

The ratio between the average signal (interface) and the noise represents the SNR value. In Table 3.1 we present the SNR values for the top interfaces (3 and 6), and also for the interfaces 7 and 9, that represent central and bottom interfaces respectively.

We then also calculated the SNR normalized with respect to the SNR of the deeper interface 9, that generally has the highest absolute SNR. In addition, in the Figures 3.17 and 3.18, we present graphs comparing the SNR behaviour for the 2 different a priori models to reinforce our analysis.

Based on these tables and graphs, we observe that in general the interfaces 7 and 9 have the poorest and highest details respectively. This is mainly attributed to the impedance contrast we can see in Figure 3.4(c), but also to the high amount of noise at the depth of interface 7. In general, the best interfaces (3, 9, the salt dome, and sometimes interface 6) can be better seen than the others because their impedance contrast with the surrounding layers are the highest (a factor around 2), while the contrast is much lower for the others. For instance the factor of impedance contrast is around 1 between interfaces 9 and 10, or between 6 and 7.

In general, compressional kernels (such as kernels K_λ or even K_{Vp}) are more sensitive to a decrease in wavelength in the shallowest areas of the a priori models (more information at the surface), which consequently increases the noise in depth. In other words, the kernel K_λ can then see the highest frequency details around the dome (useful for salt tectonics context studies). On the contrary, the kernel K_ρ is more sensitive to structures at depth and larger wavelengths when more information is added (useful for basin analysis).

Analizing the SNRs of the smoothed model M_2, we can see in both kernels (K_λ and K_ρ) an increase of the SNR, with a slightly SNR decay in the interface 7 due to weak impedance contrast. We can also say that at interfaces 3 and 6, the SNR related to the kernel K_λ increases.

However, in the case of kernel K_ρ, a SNR decay is observed at the same interfaces. This result agrees with that of the previous paragraph: the kernel K_λ is able to see much better the high frequencies of the images, while the kernel K_ρ highlights more the low frequencies. Besides, in general the OBC-like images show better definition of both shallow and deep interfaces when compared to images obtained with model M1 and receivers at the surface. In particular, the deep interfaces are much better retrieved.

We can compare our results with recent research studies [Guo et al., 2020; Guo and McMechan, 2020], where a smoothing of the whole true model including the salt dome model is added as an a priori model, and which is thus already accounting for the large wavelengths and the main geological structures. In our study, we can see that injecting an absorbing boundary at the top of the computational domain allows us to have a good picture by introducing a gradient of the model at depth as minimal a priori information, which allows us to identify the dome and even layers underneath it. We have been also able to study the sensitivity of density and compressional kernels to the different a priori models near the surface or at depth, to different model wavelengths even with poor information (model M1). However, internal multiples still persist, which invites us to investigate this field further by improving the RTM method thanks to the LS-RTM technique which is an iterative extension of the RTM.

Finally, focusing on the results of subsections 3.2.5 and 3.2.6, and making a qualitative analysis, we observe that in figures 3.15 and 3.16 the multiple contamination is attenuated with respect to figures 3.13 and 3.14. This means that by implementing a computational domain as shown in figure 3.6(b), the computation of the image condition allows the free surface multiples to be attenuated during this process (even though the data served has multiples). However, it is necessary to further investigate this process, such as validating it using real data, or applying it in the context of the LSRTM method, and to investigate how internal multiples can be attenuated.

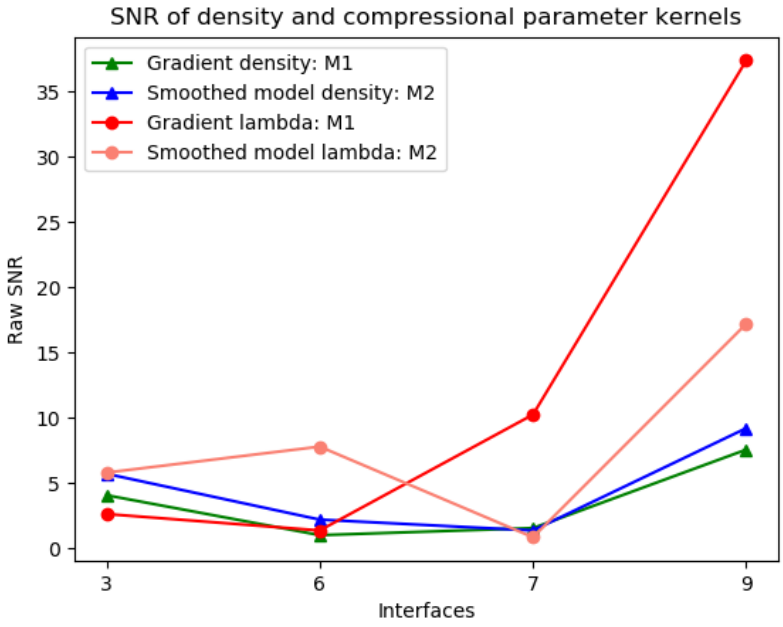

Figure 3.17. Raw SNR of interfaces 3, 6, 7, 9 for the kernels K_ρ (Figure a) and K_λ (Figure b) when applying a gain of z^2.

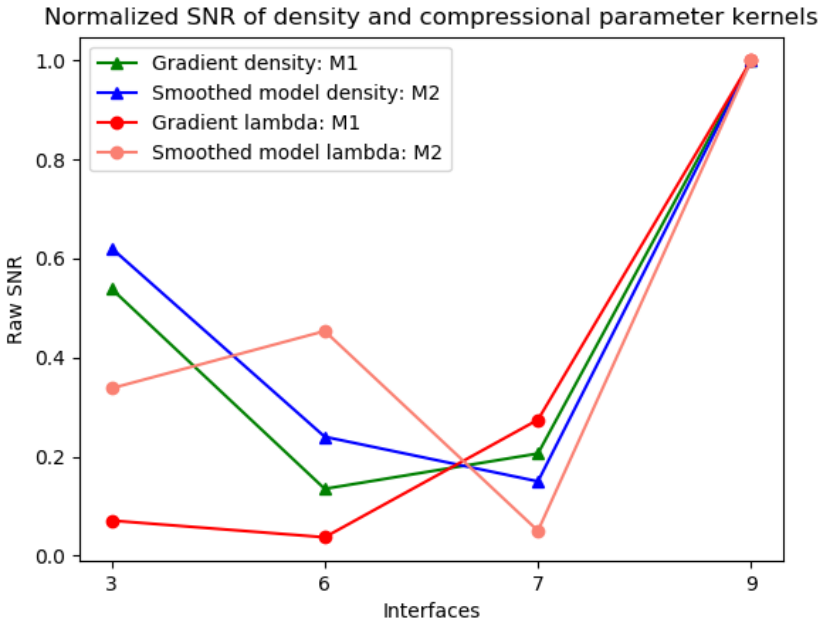

Figure 3.18. SNR of interfaces 3, 6, 7, 9 normalized by the SRN of interface 9, for the kernels K_ρ (Figure a) and K_λ (Figure b) when applying a gain of z^2.

A priori model	Kernel	Interface	Raw SNR	SNR normalized by interface 9
Model M1: gradient	K_λ	1	3.5	-
		3	2.64	0.07
		6	1.38	0.037
		7	10.25	0.27
		9	37.36	1
	K_ρ	1	1.8	-
		3	4.08	0.54
		6	1.02	0.13
		7	1.56	0.21
		9	7.57	1
Model M2: Smoothed model for OBC-like configuration	K_λ	1	77.72	-
		3	5.81	0.34
		6	7.8	0.45
		7	0.86	0.05
		9	17.2	1
	K_ρ	1	29	-
		3	5.72	0.62
		6	2.21	0.24
		7	1.38	0.15
		9	9.21	1

Table 3.1. Parametrization table of prior models indicating the SNR (absolute values or normalized values according to values at interface 9) of the sensitivity kernels related to the interfaces 1 (bathymetry), 3, 6, 7, and 9. The coordinates are indicated in Figure 3.9. For kernels K_λ and K_ρ, calculated using different a priori models, the raw SNR are normalized by z^2.

3.4 3D synthetic elastic case.

3.4.1 Experiment configuration.

In this section we present the seismic images obtained by using the 3D elastic RTM method for the synthetic data obtained by the models shown in figures 3.21. To obtain this three-dimensional model, we use the two-dimensional model of the previous chapter and replicate it along the third axis.

We interpolate the model to have a space sampling of 8 meters instead of 20 meters for the two-dimensional case. To reduce the computational time, we trimmed the model domain to concentrate on the salt dome. The dimensions of the model are 1209 (length) $\times$ 350 nodes (depth), which is equivalent to 9672 (m) $\times$ 2800 (m). To simulate a three-dimensional model, we extend the true models shown in figure 3.21 over 50 nodes (width) in the direction perpendicular to the 2D section profile that is equivalent to 400 m on the third axis.

We use the 2-nd order finite differences in time and 4-th order in space 3D wave propagation code UniSolver that we are developing in our team. The outer absorbing boundary conditions necessary for a good attenuation of the waves at the edges of the computational domains are introduced by using CPMLs (Convolutional Perfectly Matched Layers) optimized at grazing incidence.

Unisolver has been parallelized and "scaled" up to 403 processors. For strong scaling analysis we use MPI parallelization in one dimension along the horizontal axis. We divide the model into small sub-domains (1 sub-domain per processor) and spread it over 200 up to 403 processors, which means that each sub-domain has dimensions of 3 $\times$ 350 $\times$ 50 nodes for 403 processors for instance and for one single seismic migration (2 direct runs for the current problem and the adjoint problem + 1 run with "checkpointing" involving 100 intermediate memory storages of the displacement and velocity fields). We see for example in Figure 3.19 a good behavior in terms of performance for the computation of the velocity (V_P and V_S) and density sensitivity kernels for the Gulf of Mexico model on a domain of 1210 (length)$\times$450(depth) $\times$100 (width) mesh points, 8500 time steps and a dominant frequency of 4Hz.

To better understand the behaviour of the parallelism for the fourth-order finite differences method, and supposing that we are performing the parallelism along the z direction, we show in the Figure 3.20 the behaviour of the communication strategy applied between processors and performed during the fourth-order differences method, where N_{ZLOCAL} represents the number of grid points in the z direction contained in each processor ($N_{ZLOCAL} = N_Z/N_P$) (for N_P=403 processors N_{ZLOCAL}=3), with N_Z and N_P being the total number of grid points in the z direction and the total number of processors respectively. The red dashed lines indicate the extra grid points needed to compute the 4-th order finite differences method. For convenience, we only show the last nodes (grid points) of the processor P_i and the first nodes of the processor P_{i+1}. The processors P_i and P_{i+1} contain the i and $i+1$ sub-domains, which are neighbors to each other. Both processors need to communicate solutions through a buffer overlapping zone

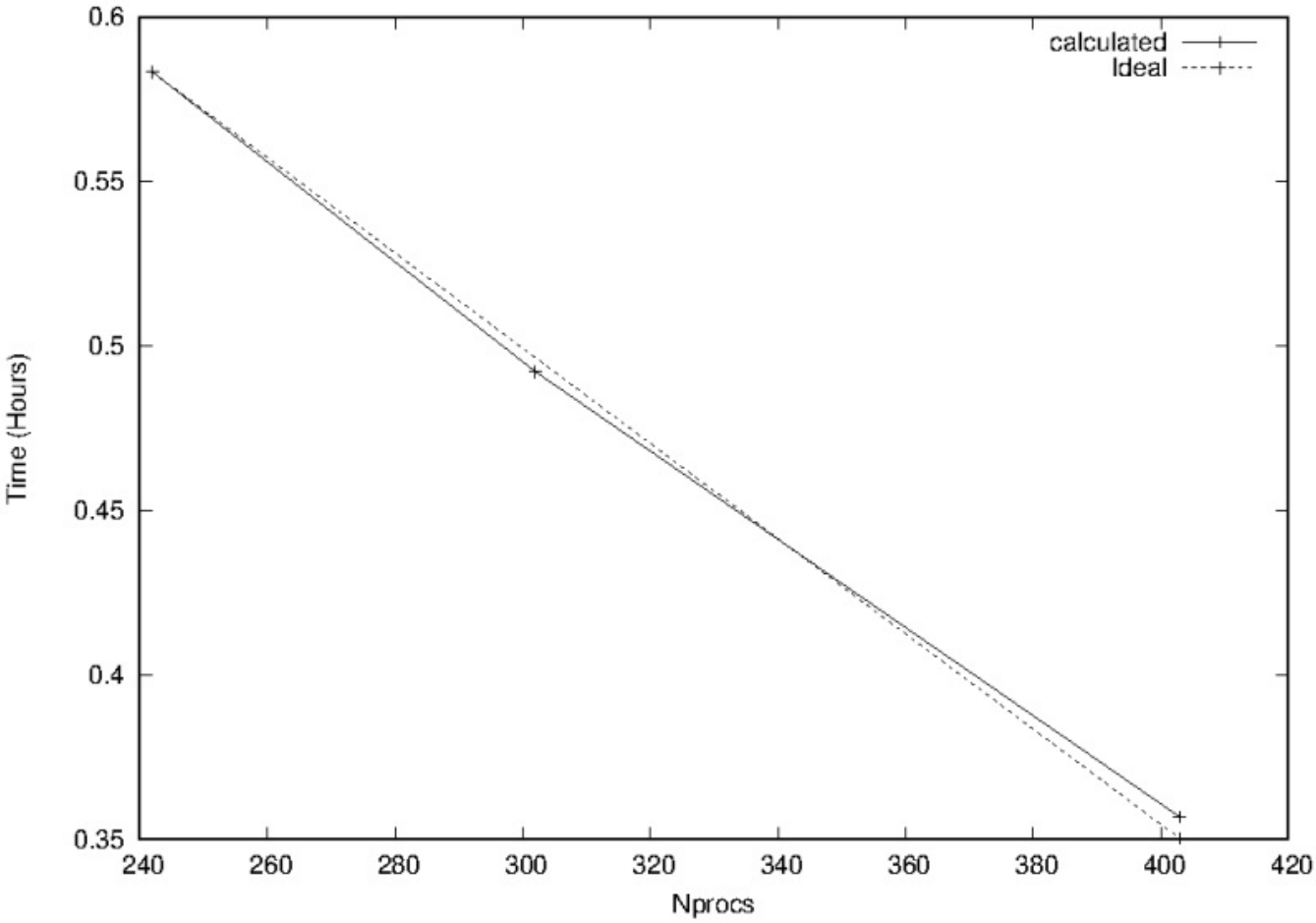

Figure 3.19. Strong scaling of UniSolver from 200 to 403 processors. Comparison of the ideal and numerically tested scaling curves.

of a few grid points. The processor P_i needs access to the information of the extra two last grid points of its sub-domain. For this reason the processor P_i receives the grid points 1 and 2 of the processor P_{i+1} and keeps them at the grid points $N_{ZLOCAL+1}$ and $N_{ZLOCAL+1}$. In the same way the processor P_{i+1} needs the two first grid points -1 and 0 of its subdomain, and it receives them from the $N_{ZLOCAL-1}$ and N_{ZLOCAL} grid points of the processor P_i and keeps them at the grid points -1 and 0 of its own subdomain.

This means that each processor sends and receives two grid points at each limit of its subdomain. With the exception of the first processor (P_1), which neither sends nor receives anything from the left, and the last processor (P_{N_p}), which neither sends nor receives anything from the right. Here, synchronous (blocking) send and receive MPI libraries are used but of course asynchronous (non-blocking) strategies could be used to reduce computing time by overlapping and hiding the time spent in communicating solutions between processors with pure computations inside each sub-domain as in Martin et al. [2008].

We now use Unisolver for RTM. We use gradient-prior models as we did in previous chapter. In other words, we fix the bathymetry and we increase the values of the parameters along the depth. We show in figure 3.22 the kernel K_{Vp} obtained by injecting separated sources in the three-dimensional model of figures 3.21. We can see that the edges of the dome are very

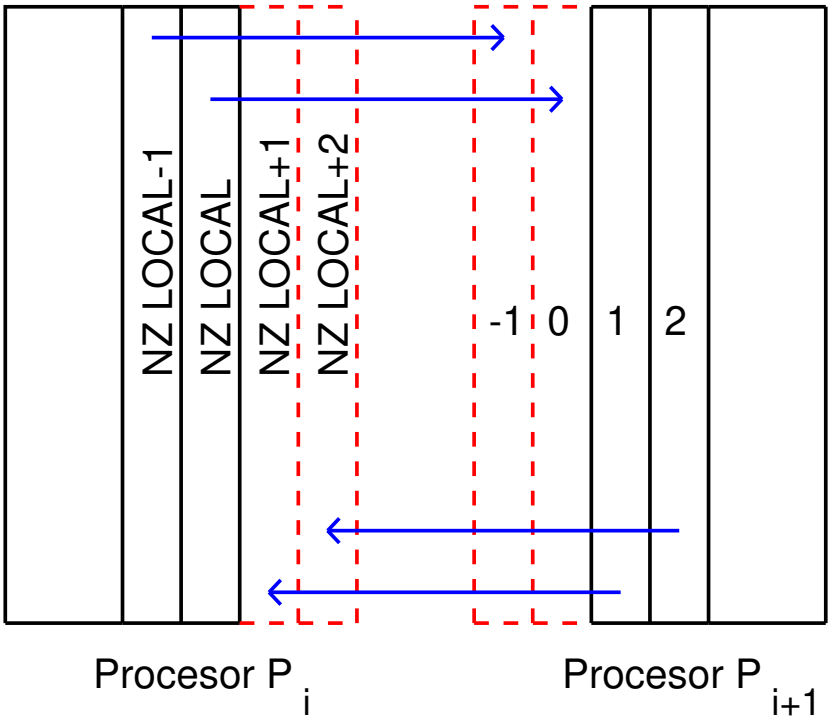

Figure 3.20. Behaviour of the parallelism for the fourth-order finite differences method. We can see two adjacent chunks of the original model. The red-dashed lines represent the additional nodes of the buffer overlapping zone used to store the information from the adjacent processors. N_{ZLOCAL} represents represents the number of nodes contained in each processor. We show here the last nodes of the processor P_i and the first nodes of the processor P_{i+1}, and how they are communicating.

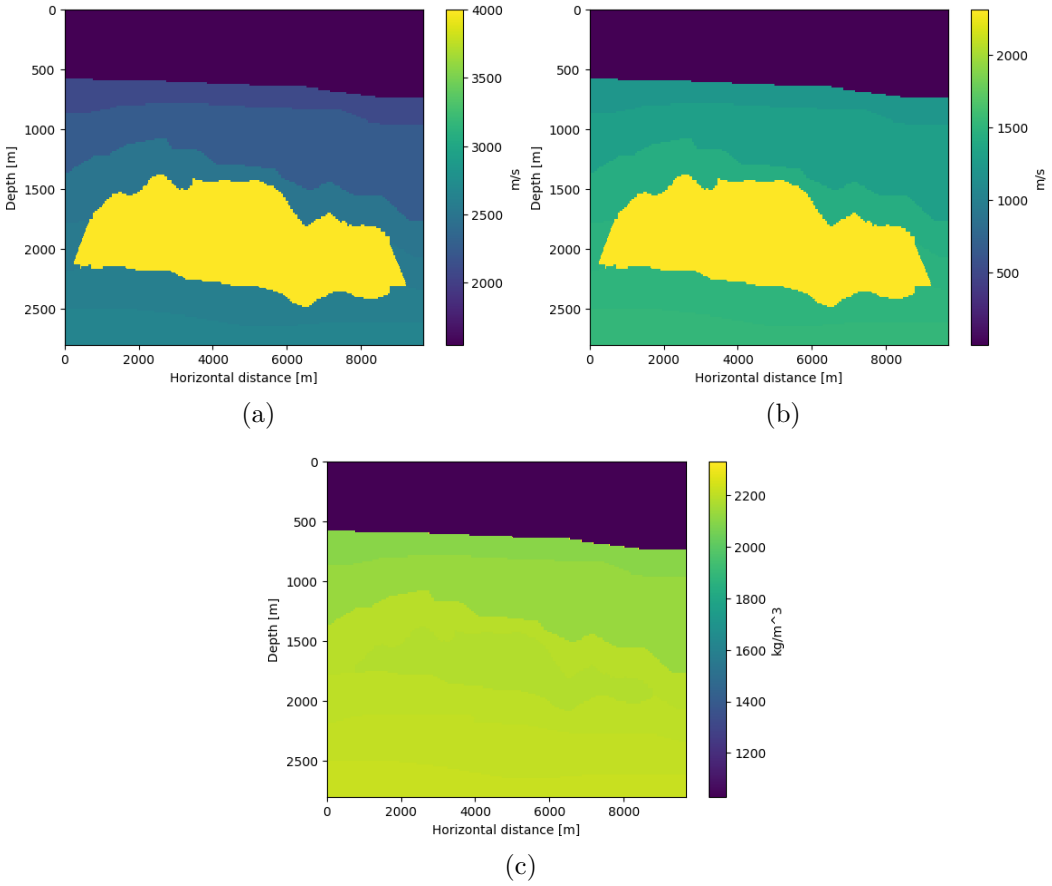

Figure 3.21. Longitudinal slice of the "true" three-dimensional compressional velocity (a), shear velocity (b) and density (c) models.

well defined despite the fact that the a priori models do not contain much information about the medium (pure depth-gradient background prior model). The interfaces are much better defined than when receivers are located at the ocean surface.

In the appendix A, I present the principal subroutine of Unisolver code that contains an external loop over the frames (for the checkpointing implementation) and an internal loop over the stages of the RTM method. Furthermore, in appendices B and C, I present the principal parts of the code where specifically I made some improvements: the computation of the separated sources kernels, the elevation to 4-th order in finite difference calculations to solve the wave equation, and the implementation of the visco-elastic wave equation.

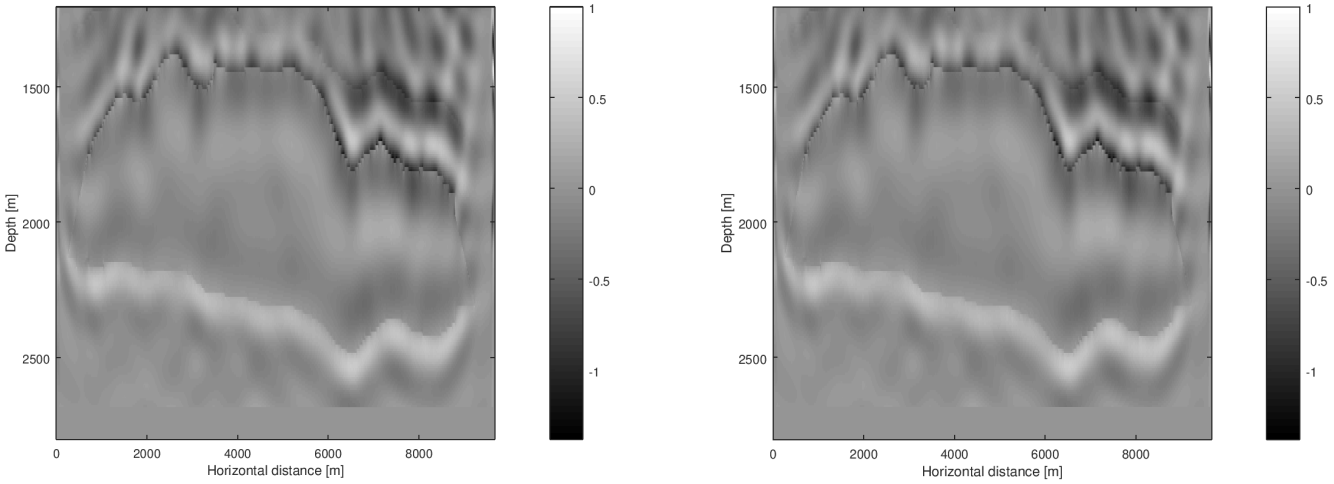

(a) (b)

Figure 3.22. Zoom of the Kernel K_ρ (Figure a) and Kernel K_{Vp} (Figure b) obtained by injecting the sources at the bathymetry. The receivers are also placed at the bathymetry. For the a priori model (pure depth-gradient background model), we fixed the bathymetry and we linearly increased the values of the parameters along depth.

3.4.2 Conclusions.

In this chapter, the main objective of our work was to demonstrate the recovery of all or at least a large part of the salt and sub-salt structures despite the interference caused by salt domes. We have shown different kernels parametrizations that were calculated using different a priori models. First we used the true parameter values, then the next a priori models were designed by fixing the bathymetry, and below it we implemented a variation of the parameter values increasing in the depth direction. The third a priori models were obtained adding the salt dome interfaces to the previous models, as an interpretation of the last kernels. Using the gradient a priori model, some artifacts are generated and possibly attributed to the lack of knowledge of the true model: these artifacts are then reduced when fixing the salt dome models.

We followed two strategies to design the configuration of the computational model. The difference lies in the top of the computational domain, where firstly we implemented free surface conditions, as is normally done, then we replaced them by absorbing boundary conditions to attenuate multiple artifacts. The results show that, indeed, the artifacts are reduced in the absorbing boundary conditions-based kernels. The main structures are more visible even if some effects of the internal multiples are still present.

We also introduced different types of parametrizations: (ρ, λ), (ρ, V_p), and (ρ, Z_p). For each of them we calculated the sensitivity kernels, and for the case of the parametrization (ρ, λ), we also calculated the kernels normalized by the forward or adjoint energy (using forward energy normalization gives better results). We observed that in general, the kernels with respect to the logarithm of the parameters and the normalized kernels (case (ρ, λ)), show a significantly better illumination at deeper interfaces.

Furthermore, our results show that the compressional kernels K_λ are more sensitive to the smallest wavelengths, while the density kernels K_ρ are more sensitive to the highest wavelengths. Besides, the SNR is another appropriate and more quantitative method to analyze the location of the cleanest and noisiest regions of the images. The SNRs are also a tool to help us in the interpretation and determination of the best illuminated interfaces (or reflectors below, around and in the dome salt structures).

Finally, the kernels of sections 3.2.5-3.2.6 obtained by applying absorbing boundary conditions on the top of the computational domain are showing in a qualitative way that the free-surface multiple contamination is attenuated compared to kernels of sections 3.15 and 3.16, when free-surface conditions are applied at the top of the computational domain.

In forthcoming works of the next chapter 4 we will solve the elastic and visco-elastic problem of the wave equation in 3D, applying checkpointing to solve the adjoint equation. We will use real data coming from a laboratory experiment, in which the geological medium represents a region with strong salt tectonics. We will also apply the LSRTM method on these real data to improve iteratively the sensitivity kernels and the reconstructed reflectivity images.

3.5 Acknowledgments

Authors acknowledge research projects SENER-CONACYT 128376, IMP H.61006. Javier Abreu Torres acknowledges scholarship grant No. 678864 from PNPC-CONACYT. We also thank the CALMIP supercomputing mesocentre of Toulouse, France, for their support through project P1135 on the Olympe supercomputer platform and the TGCC/GENCI supercomputing centre through project gen6351 on the IRENE supercomputer.

Chapter 4

3D imaging for a real case.

4.1 Introduction.

Thanks to technological advances in computing, seismic imaging methods have advanced as well, allowing to perform 3-D simulations in a short time. The seismic images of three-dimensional models present advantages with respect to the two-dimensional models because all the directions of azimuth of the spatial model are presented. In this chapter we continue with the topic of the previous chapter, but now we extend our study to 3 dimensions, and we apply a visco-elastic rheology to characterize salt domes in off-shore context at the experimental scale. We want to validate our code UniSolver using a 3D realistic seismic laboratory experiment "WAVES" containing a diapiric dome and adjacent layers. I am focusing here on the FWI method to retrieve and characterize the bottom of the dome and the interfaces below the dome.

The WAVES experiment was performed by our colleagues of the LMA team (Laboratoire de Mécanique et d'Acoustique) at Marseille/France. This experiment consists in the elaboration of a laboratory-scale seismic model representing a salt dome and some adjacent layers (Solymosi [2018], Solymosi et al. [2020], Personal Communication Favretto-Cristini [2020]). We thank the colleagues of LMA (Bence Solymosi, Nathalie Favretto-Cristini, Paul Cristini, Vadim Monteiller) by providing their WAVES data. This experiment was part of the H2020 ITN WAVES project and the article of Solymosi et al. [2020].

The objective of Solymosi is to define a robust framework for benchmarking imaging methods through small-scale laboratory experiments. This framework consists not only of the realization of the complex subsoil model, but also of "seismic" acquisitions on a reduced scale of high quality and precision. These experiments allow to provide the input data for numerical seismic models (Solymosi et al. [2018], more particularly for a salt-tectonics context Solymosi et al. [2020]). Bence Solymosi and co-authors have done all this work by using SPECFEM3D with an unstructured hexahedral mesh to honor the shape of the interfaces in a very accurate way, to retrieve the properties of the medium under study and the experimental seismic data. They performed calibration of the physical properties in 3D (density, seismic velocities and

attenuation parameters) as well as the seismic imaging using a 2D RTM method for the multi-offset data to image these types of models by using the SPECFEM method.

One of our main objectives for this section of the thesis is to perform 3D seismic imaging of the salt structure and interfaces of the experimental model, starting from a low frequency (recovering the salt structure and interfaces), i.e. starting from a low frequency model and enhancing the high frequencies using the RTM. In addition, we seek to characterize the subsurface parameters by data inversion using FWI with a steepest descent method to obtain a first new model and first related sensitivity kernels and model perturbations respect to an initial low frequency background. Then, the models are improved by using a non-linear conjugate gradient technique. Before performing any imaging or inversion process, it is important to validate first the forward problem in 3D by comparing the real data and our synthetic data. For this purpose it is necessary to correctly introduce not only the source but also the the physical properties of the medium and also the attenuation effect to reproduce the real problem. We will thus focus our attention here on property calibration with and without attenuation and on the seismic imaging of the WAVES medium using the RTM first and the characterization of the medium by FWI in a second step.

All our work is performed on the zero-offset data, which are shown in figure 4.11 where we can only see the seismic events that were generated above the dome and by the interfaces located aside the dome. In the zero-offset data we can not retrieve the main part of the interfaces below the dome, that we aim here to reconstruct.

Our work is complementary to that done by Solymosi. Indeed, different numerical methods are used (spectral elements by Solymosi and finite differences in this work), and the calibration of the properties is done on different traces. Solymosi uses a trace far away enough from the dome to avoid the curvature and scattering effects due to the salt dome and its related curved interfaces. In my case I want to reconstruct the salt dome structure derived from data including the scattering and curvature effects visible in realistic conditions. Another difference is that in Solymosi et al. [2020] the authors performed the seismic imaging using the multioffset data to study whether it is possible to retrieve the interfaces of the dome and the adjacent layers even using more complex data than zero-offset data. In our study, we decided to use in a first step the less complex data (the zero-offset data) to perform our inversions. In the future, these inversions will be completed using the multioffset data to improve the accuracy of the medium properties.

4.2 3D real viscoelastic case: The WAVES model.

Experiments at laboratory scale has become an excellent option for understanding real data at full scale and for testing imaging methods.

Data from laboratory-scale experiments have characteristics that make them more similar to real, full-scale data than synthetic data, such as: the presence of attenuation due to the loss of energy of the waves and the content of source-related noise. Therefore, laboratory-scale data

Material	**Number**	**Density** (kg/m^3)	$\boldsymbol{V_P}$ (m/s)	$\boldsymbol{V_S}$ (m/s)	Q_P	Q_S
Resin A	1,3	1172	2720	1210	25	11
Resin B	2	1680	3090	1577	26	18
Resin C	4	1800	3470	1840	53	33
Crystal glass	5	3623	4480	2845	∞	∞
Aluminium	6	2710	6441	3573	∞	∞

Table 4.1. Measured values of the different parameters of the WAVES model, according to figure 4.2. [Solymosi et al., 2020]

have reemerged in recent years [Cooper et al., 2010; Ekanem et al., 2013; Stewart et al., 2013; Xu et al., 2016]. When performing laboratory scale experiments we must assume that the waves propagate similarly as on the seismic scale. Therefore it must be fulfilled that:

- The geometry of the structures of the reduced scale is similar to that of the real-seismic scale.
- The materials of the reduced scale behave identically to real seismic scale.
- The sources must generate appropriate wave phenomena.

In this chapter, we first present the WAVES experiment setup (seismic data acquisition) of our colleagues of LMA laboratory, then we present the seismic imaging setup. After that we present results for the zero offset and multi offset cases. Finally, we discuss the results obtained.

4.2.1 Configuration of the experiment: zero offset and multi-offset setups.

a) Dimensions and parameters of the model.

The WAVES model has dimensions of 400 × 270 × 95 mm^3, and it has been scaled down by a factor of 1:20000 . This means that the WAVES model represents a 8 × 5.4 × 1.9 km^3 volume on a realistic seismic scale.

This model contains a realistic geological region with a salt body embedded in sedimentary layers. In order to simulate the physical parameters (density and propagation velocities) of the salt dome, sediments and basement, it was used crystal glass, resins, and aluminium respectively (see table 4.1). Each material is considered homogeneous and isotropic. The resins are considered visco-elastic for the source frequency range contemplated here. The crystal glass and aluminium are considered elastic. The figures 4.1 show a top view of the WAVES model and a focus on the crystal glass. The images of the orthogonal slices along x and y axes respectively are shown in figure 4.2.

The WAVES model was immersed in water to simulate an offshore seismic acquisition. No attenuation is considered in the water layer. We consider the water density as 1030 (kg/m^3). Since this density value is widely used in the literature, and seismic methods are more sensitive to velocities, it is not necessary to be very precise with the water density.

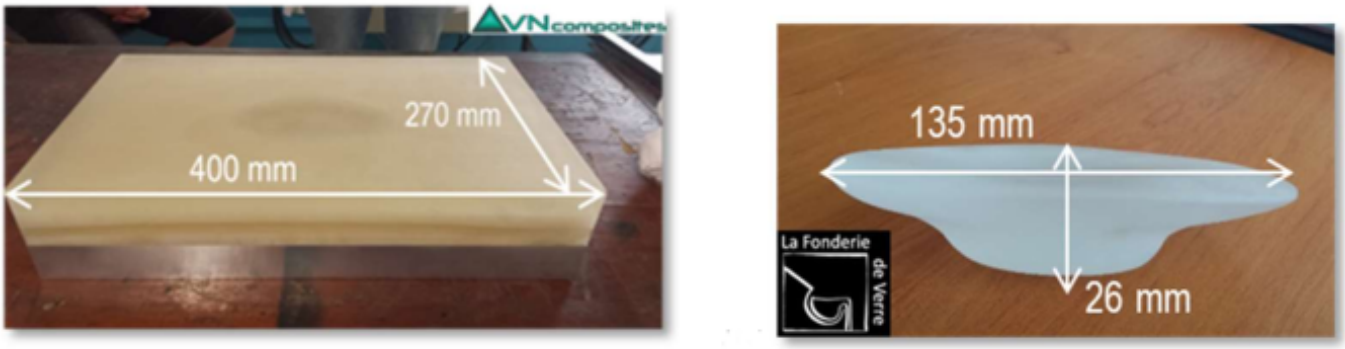

Figure 4.1. Top view of the waves model and a focus on the crystal glass. Taken from Personal Communication Favretto-Cristini [2020]

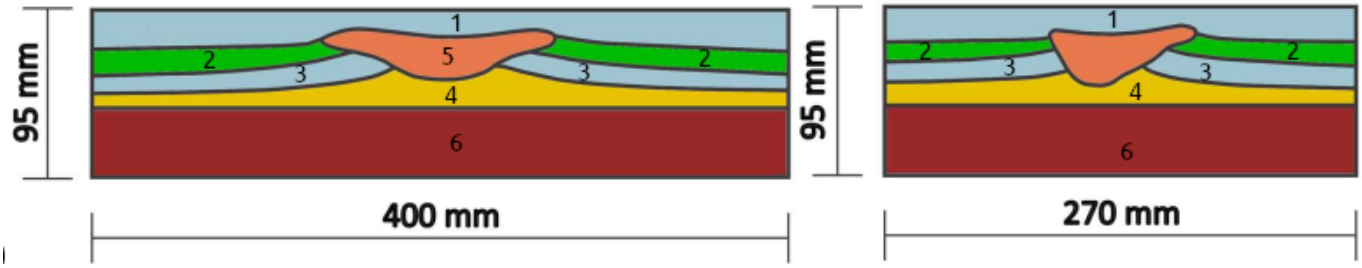

Figure 4.2. Slices of the three-dimensional WAVES model along the x (left) and y (right) directions respectively. Taken from Personal Communication Favretto-Cristini [2020]

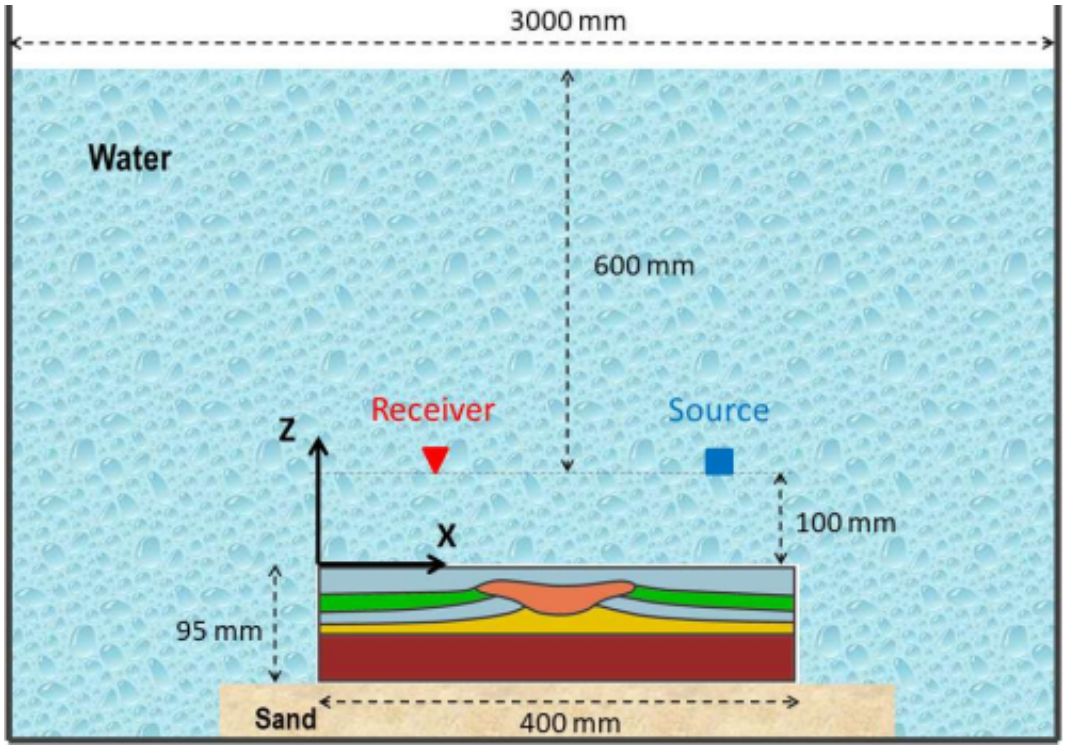

Figure 4.3. Distribution/configuration of the WAVES model inside the water. Taken from Personal Communication Favretto-Cristini [2020]

b) Sources and receivers.

The source is a custom-made piezoelectric Imasonic® transducer with an unique radiation pattern. The width of the main lobe of the beam is equal to 35° at -3 dB, generating P waves, with a dominant frequency of 500 kHz, providing a large illumination area which makes it easier to interact with the 3D properties of the WAVES model (Personal Communication Favretto-Cristini [2020]). This transducer acts as a source and also as a receiver for the zero-offset data acquisition. To numerically simulate the behaviour of the piezoelectric transducer (time signal and frequency spectrum), our colleagues of the LMA laboratory have used a disk with a radius of 6 mm, containing 253 virtual sources for the zero-offset data. For the multi-offset data the radius of the disk is 3mm (Solymosi et al. [2018], Personal Communication Favretto-Cristini [2020]). In Figure 4.4 we show the disk configuration for zero-offset data, where each virtual source contains a different time signal (they are independent). In our finite difference computational mesh each of the 253 virtual sources corresponds to a different grid node in the computational domain: we check that they do not overlap each other. Figure 4.5 represents the time signal and the amplitude spectrum of one of the sources of the transducer. The spectrum of each virtual source of the transducer was filtered at LMA and provided to us with a band-pass filter between 250-650 kHz. We can see in figure 4.5(b) that the dominant frequency is about 400 kHz.

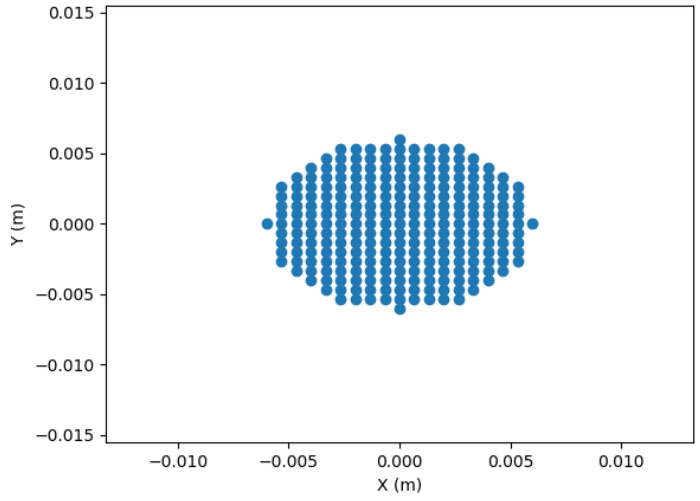

Figure 4.4. Top view of the distribution of the virtual sources in 6mm-radius the disk for the zero-offset data.

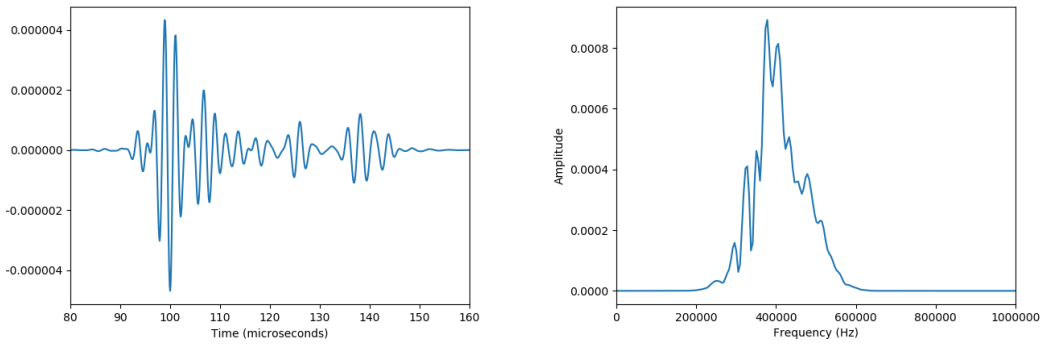

(a) (b)

Figure 4.5. Signal time and amplitude spectrum of one of the sources of the transducer. The spectrum of the source was already filtered at LMA with a band-pass filter between 250-650 kHz.

For the zero-offset configuration the piezoelectric transducer acts as both the source and the receiver. The center of the disk simulating the source (fig 4.4) is placed at each source coordinate. The figure 4.6 represents the top view of the acquisition scheme.

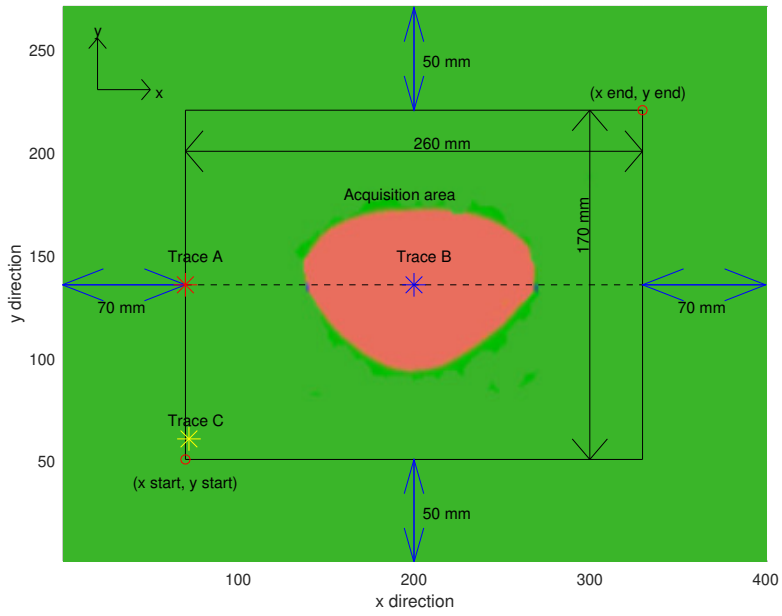

Figure 4.6. Top view of the WAVES model without the topmost layer, including the acquisition scheme of the zero offset data. Starting from the point (x start, y start) = (70 mm, 50 mm), ending at the point (x end, y end) = (330 mm, 220 mm). The dashed line represents the line chosen for this study, containing 260 sources and receivers. The red and blue asterisks represent the place where the receivers of traces A (x = 70mm, y = 135mm, z = 150mm) and B (x = 200mm, y = 135mm, z = 150mm) respectively are placed (see Figure 4.13 for the vertical view). The dimensions of the acquisition area are 260 mm and 170 mm in the x and y directions respectively. The yellow asterisk (trace C) corresponds to the approximated location of the trace that Solymosi has chosen to calibrate the region without crystal glass (salt dome). Modified from Personal Communication Favretto-Cristini [2020].

c) Spatial and temporal discretization.

To solve the equations of elastodynamics, we use fourth-order staggered grid finite differences (i.e the code UNISOLVER) and a same spatial step in all directions ($\Delta x = \Delta y = \Delta z$)[Graves, 1996]. To determine the spatial sampling interval we first evaluate the dispersion condition (equation 2.66), using the minimal S velocity value, corresponding to the resin A (1210 m/s). We then obtain that: $\Delta x = \Delta y = \Delta z = 0.0004m$.

To determine the temporal discretization, we apply the stability condition (equation 2.67) using the maximum P velocity (6441 m/s). We determine that a time step of $1.2\times10^{-8}s$ is adequate to fulfill the stability condition.

Because the original source data are sampled using a time step of $1\times10^{-7}s$, we interpolate them by applying a spline interpolation. Figure 4.7 shows a comparison between the original (Figure 4.5(a)) and interpolated source data, where we can see that the amplitudes are maintained. We also interpolated the real data, which were originally sampled with a time step of $5\times10^{-8}s$. We also show in figure 4.8 a comparison of the original and the interpolated data of the first receiver (located at $x = 70mm$, $y = 135mm$, $z = 150$mm), where the amplitudes are maintained.

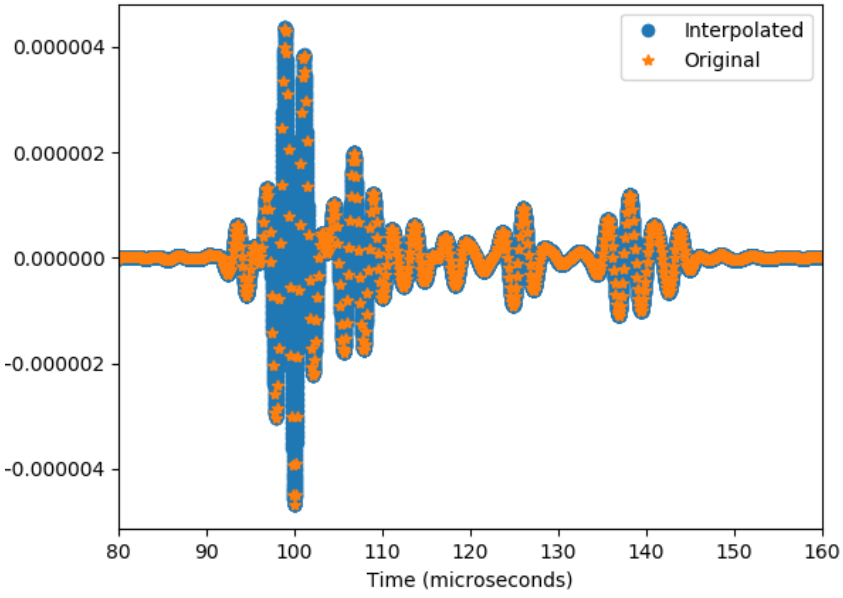

Figure 4.7. Comparison between the original source data (Figure 4.5(a)) and the interpolated source data for one of the transducer sources.

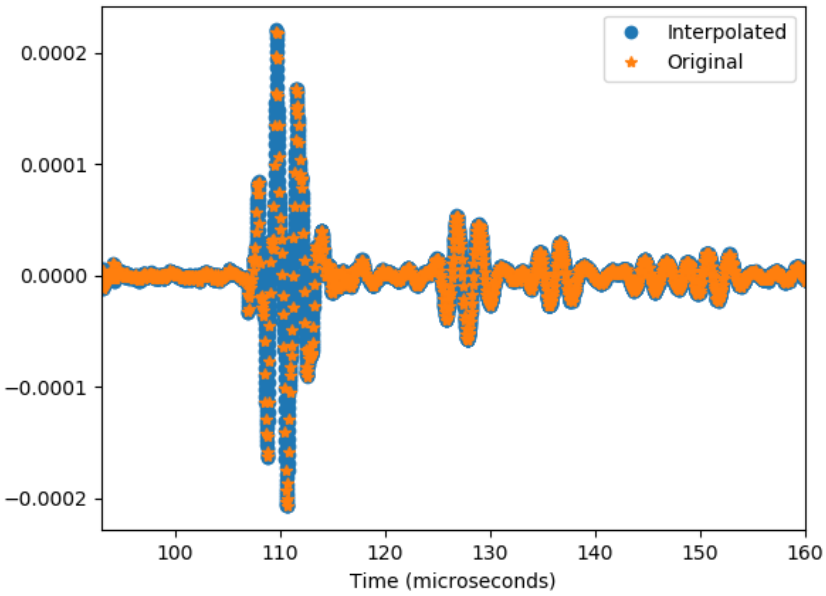

Figure 4.8. Comparison between the original data recorded by the receivers and the interpolated data for the first trace. Data are recorded at the first receiver (located at $x = 70mm$, $y = 135mm$, $z = 150mm$).

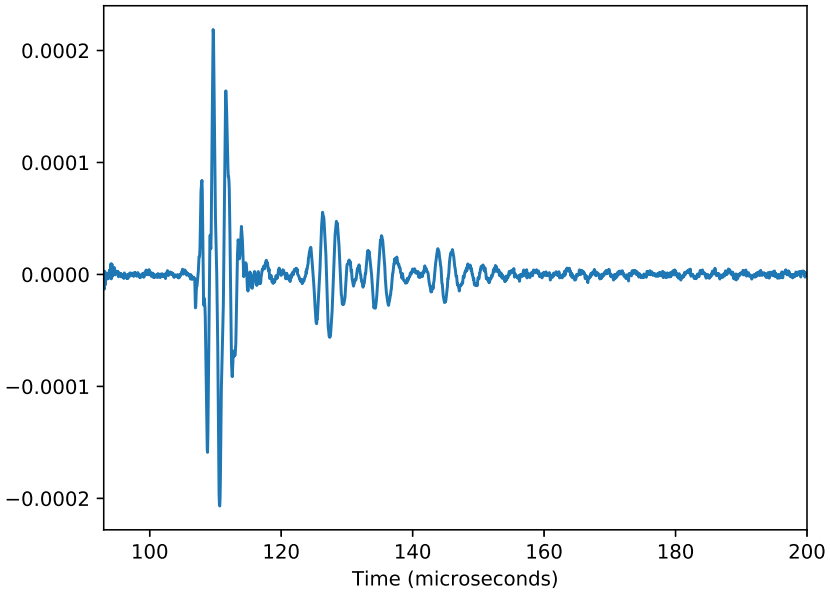

Figure 4.9. Raw data recorded at the first receiver after the interpolation in time (Figure 4.8).

d) Data filtering.

In figure 4.9, we present the interpolated data recorded at the first receiver, and in Figures 4.10 we present the frequency spectra of these data (Figure 4.10(a)) and of the filtered data (Figure 4.10(b)). We can observe that the data contain high frequency noise between 1000 and 2000 kHz and a peak of resonance around 1600 kHz. We apply a band-pass Butterworth filter between 250-650 kHz which is the same band-pass filter that was applied on the source. Therefore all time signals and spectra of the real data shown in the following figures (in the rest of the manuscript) correspond to the filtered real data with this band-pass filter. These data were used to solve the forward problem and to perform the seismic imaging. However, we invert low frequency signals by applying a 200 kHz low-pass filter over the source and the data because these frequency ranges are enough to describe the whole experimental model.

The figure 4.11 shows the filtered real data recorded by the receivers along the central line (red dashed line of figure 4.6).

The source was filtered in two stages: The first at LMA (with a band-pass filter between 250-650 kHz) and in a second stage we filter the source data using a Butterworth low-pass filter with a cutoff frequency, which is proportional to the sampling interval, thnaks to the Python code ScriptDataReading.py provided by the LMA. Figure 4.12 shows a comparison between these two stages: the original source (filtered at the LMA) and the source filtered in this work.

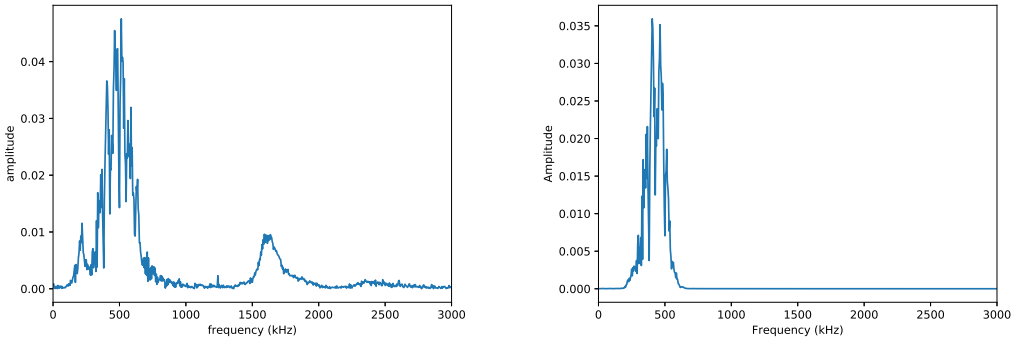

(a) (b)

Figure 4.10. Frequency spectrum of the raw and filtered data signals (figures (a) and (b) respectively) recorded at the first receiver. The raw spectrum contains high-frequency noise between 1500 and 2000 kHz. To filter the real data we apply a Butterworth band pass filter between 250-650 kHz that is the same band pass applied to filter the source. BY this mean we also remove a resonance peak at high frequency (greater than 1500 kHz).

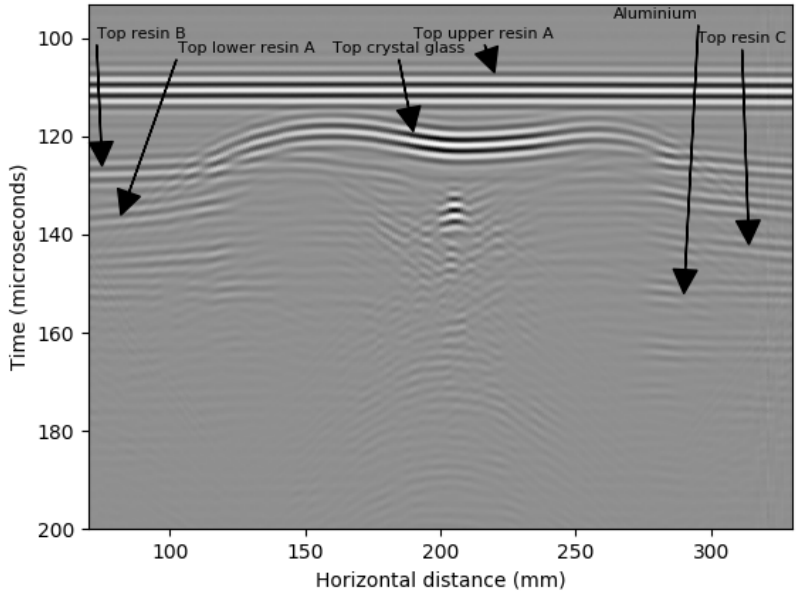

Figure 4.11. Real zero-offset data along the central longitudinal line (red dashed line in figure 4.6). We can only observe the events generated above the dome and the lateral layers. We can't see the events generated by the bottom and below the top of the dome.

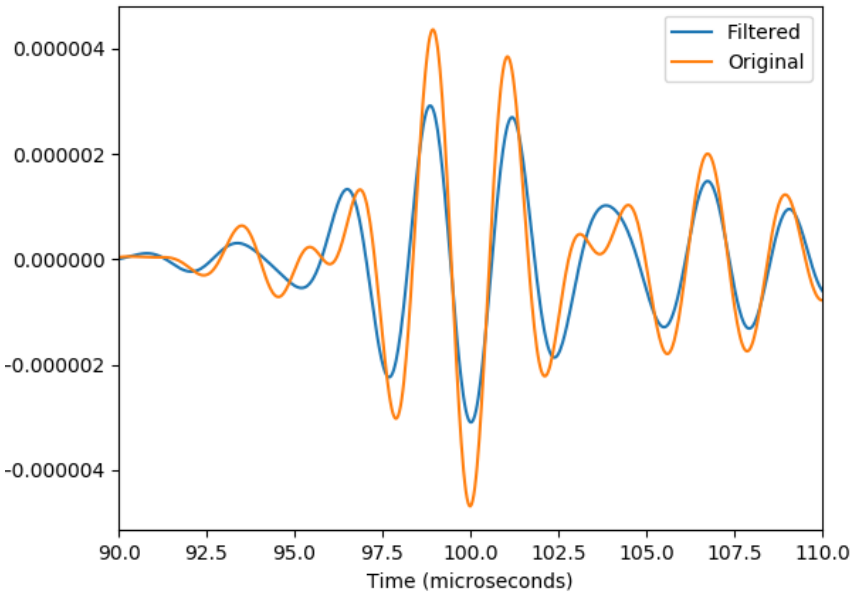

Figure 4.12. Comparison of the source filtered in a first stage with a band-pass filter at LMA (original) and the source filtered in this work with a low pass filter that is a percentage of the sampling frequency.

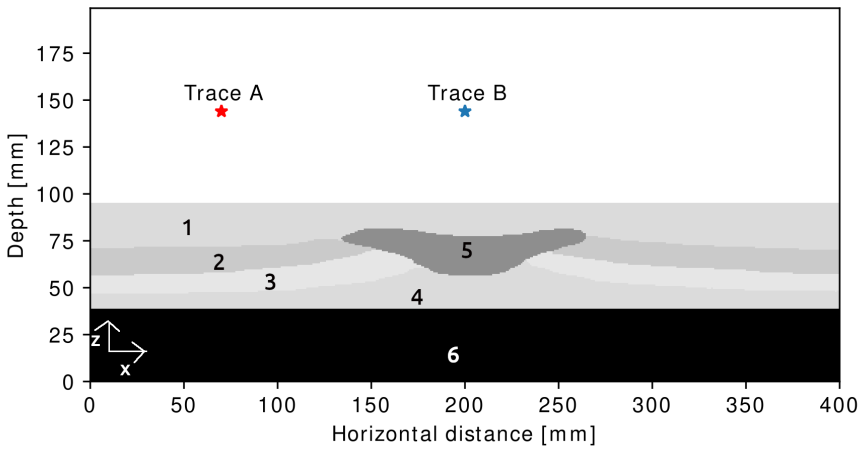

Figure 4.13. Vertical view of the WAVES model with the location of the two selected traces A and B to calibrate the model. The trace A is recorded at the red asterisk ($x = 70$mm, $y = 135$mm, $z = 150$mm). The trace B is recorded at the blue asterisk ($x = 200$mm, 135mm, $z = 150$mm). The numbers represent the material id. See the Figure 4.6 for the top view.

e) Calibration of the properties of the materials and implementation of the viscoelastic attenuation.

To calibrate the properties of the materials, we first calculate the forward problem using the measured materials expressed in Solymosi et al. [2020] (Table 4.1) with attenuation (viscoelastic) and without attenuation (elastic). We found that the fit between the real data and the data we have calculated using the measured properties from table 4.1 was not good, and therefore we had to perturb the materials until the fit was acceptable. In this purpose, we select the trace A, which is recorded at the left side of the model ($x = 70$mm, $y = 135$mm, $z = 150$mm), and the trace B, located above the salt dome ($x = 200$mm, $y = 135$mm $z = 150$mm). Figure 4.13 shows the location of the two traces in the longitudinal profile of the WAVES model. We compare the signals with and without attenuation (viscoelastic rheology) in the model properties.

In a first step, we calibrate the physical properties without attenuation. We follow an elastic rheology and we only perturb the material P velocities, and we find the values that produce a good fit in arrival times between real and synthetic data. Several tests (trial and error) have been done, and we can find the values of the calibrated materials of Solymosi et al. [2020] and our work in table 4.2 (for V_P parameters). We show in Figures 4.14 the results obtained for the trace A, where the comparison between the real and measured synthetic data is shown in Figure 4.14(a), and the comparison between the real and calibrated synthetic data is shown in Figure 4.14(b). In the same way, we present the results obtained for trace B in Figures 4.15.

The trace C that Solymosi uses to calibrate the region without crystal glass (salt dome) is different from the trace A that we use to calibrate the same region (see the Figure 4.6). The trace C was chosen quite far from the dome to be able to determine the properties of the layers that are almost horizontal and are less contaminated by diffracted waves coming from

the dome. While for the region with crystal glass (dome) we both use the same trace B.

Due to the fact that the measured signals at receivers are not sufficiently well reproduced by our numerical simulations when using a purely elastic rheology, we introduce now attenuation (viscoelastic rheology) in our simulations. We focus on the V_P, Q_P, and Q_S properties (keeping V_S unchanged) as in the Solymosi's methodology. We thus made the choice of adding attenuation by using Zener models (depicted in chapter 2) and we perturb the Q_P and Q_S attenuation factor parameters until the amplitude between predicted and observed data fits well (Table 4.3). We will discuss these results in the next subsection.

Material	**Number**	V_P Solymosi	V_P this work
Upper resin A	1	2549	2661
Resin B	2	3213	3250
Lower resin A	3	2560	2400
Resin C	4	3050	2900
Crystal glass	5	4325	4260
Aluminium	6	6491	6420

Table 4.2. Calibrated Vp values of the two dimensional work of Solymosi et al. [2020] (in blue) and our calibrated three dimensional V_p models of this present work(in red). Changes in the V_P values are generally lower than 1.5 % , but are between 5 and 6 % for lower resin A and resin B. The trace to calibrate the region without crystal glass (salt dome) is the trace A in this work and the trace C in Solymosi et al. [2020] (see Figure 4.6)

Material	**Number**	Q_p Solymosi	$Q_p$this work	Q_sSolymosi	$Q_s$this work
Upper resin A	1	123.8	309.5	88	88
Resin B	2	27.3	68.25	23	23
Lower resin A	3	41.7	208.5	30	150
Resin C	4	30	60	26	52
Crystal glass	5	∞	∞	∞	∞
Aluminium	6	∞	∞	∞	∞

Table 4.3. Calibrated Q_P and Q_S values of the two dimensional work of Solymosi et al. [2020] (in blue) and our calibrated three dimensional V_p models of this present work(in red). The trace to calibrate the region without crystal glass (salt dome) is the trace A in this work and the trace C in Solymosi et al. [2020] (see Figure 4.6)

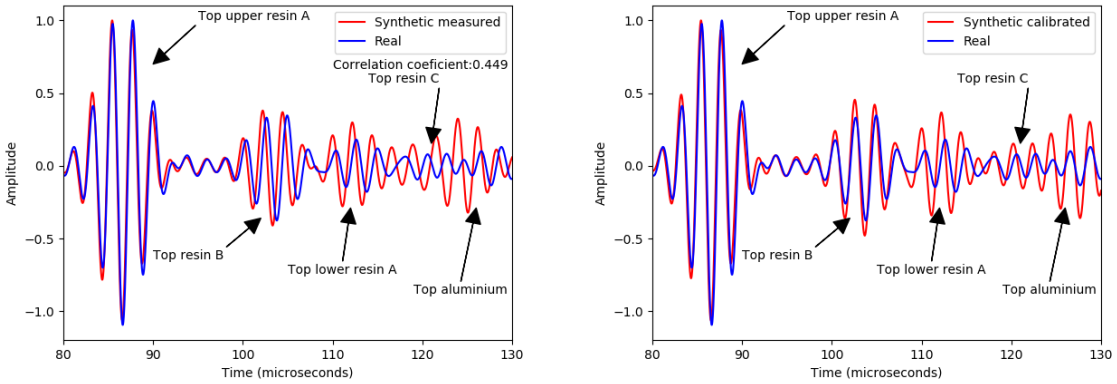

(a) 3D elastic, measured properties.

(b) 3D elastic calibrated properties.

Figure 4.14. At zero-offset in 3D without attenuation (purely elastic) : comparison of the synthetic and real data for trace A using the measured (figure (a)) and calibrated (figure(b)) properties of the different materials. All the data are filtered with a 250-650 kHz band-pass filter.

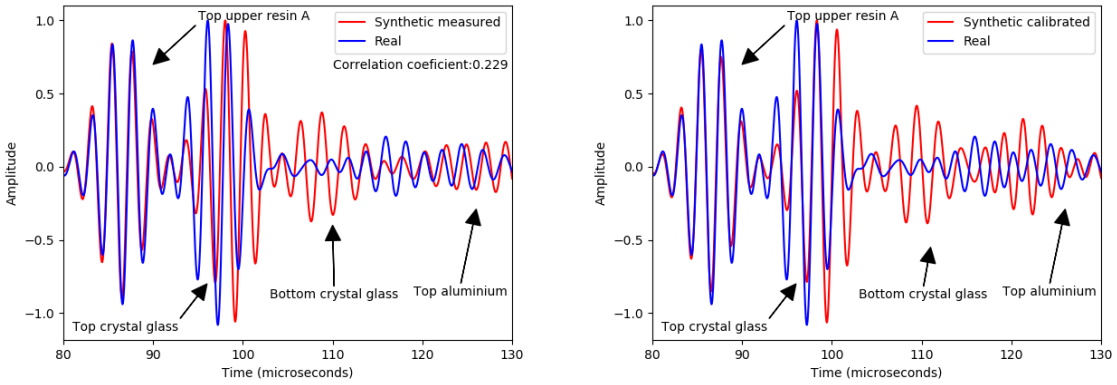

(a) 3D elastic, measured properties.

(b) 3D elastic, calibrated properties.

Figure 4.15. At zero-offset in 3D without attenuation (purely elastic): comparison of the synthetic and real data for trace B using the measured (figure (a)) and calibrated (figure(b)) properties of the different materials. All the data are filtered with a 250-650 kHz band-pass filter.

f) Implementation of viscoelasticity (zero-offset data) in 2D and 3D.

To analyze the attenuation effects, we implemented the 2D and 3D viscoelasticity equations.

-2D modelling issue with and without attenuation: In Figures 4.16 we show a comparison between the synthetic data calculated with attenuation (visco-elastic rheology) in 2D, and the synthetic data without attenuation (elastic rheology) in 2D, for traces A and B, using the measured quality factors Q_P and Q_S indicated in Table 4.1 (we don't perturb the quality factors here). We can observe that after the arrival of the top resin A (bathymetry), there is an attenuation effect in the data calculated with the viscoelastic equation. This is more noticeable in the figure 4.16(a), specially in the long term time periods.

It is not possible to inject in the two-dimensional simulation the same source used in the real acquisition because the coordinates of the 253 transducer sources are three-dimensional. Because of this the waveform is not similar in the two-dimensional data and in the real data. To compare, these data, we decided to compare their frequency spectra. In Figures 4.17 we can see the comparison of the spectra between the real zero-offset data and the two-dimensional synthetic zero-offset data (attenuated and non-attenuated) for trace A (Figure 4.17(a)) and trace B (Figure 4.17(b)). We can see a similarity in the frequency content in all the spectra, which is accentuated in the data of the trace B. This can be due to the fact that for trace B no attenuation (resin A, salt dome and metallic basement) or very low attenuation are present in the geological structures that are just beneath the source and the receiver B (located at the same place), while below trace A just resin A and metallic basement have low or no attenuation.

-3D viscoelastic modeling: Finally, following a Zener model viscoelastic rheology, we show in Figures 4.18 the comparison between 3D synthetic predicted data including viscoelastic attenuation, and the real data. For these results we perturbed the V_P parameters (table 4.2) and the quality factors Q_P and Q_S (table 4.3). We also compared the correlation coefficients that we obtained with those obtained by Solymosi et al. [2020]. We show these coefficients in table 4.4 and we can see very similar correlation coefficients. We observe a very good fit in the first trace (where the salt dome is not present). However in the central trace where the salt dome is present the experimental traces are not so well reproduced numerically. We also show in table 4.2 the original and calibrated properties of the P velocities obtained in Solymosi et al. [2020] and in this work, where our calibrated Vp velocities are similar than those obtained in Solymosi et al. [2020] although we use different traces to calibrate the region without crystal glass.

The viscoelasticity is associated with the intrinsic attenuation of the medium (and generally also with a velocity dispersion), and this attenuation is very difficult to determine because what is measured is an apparent attenuation (which is composed of the intrinsic attenuation of the medium and the decrease in signal amplitude caused by physical phenomena such as diffraction or geometric divergence). This apparent attenuation can be described from the Qp values obtained in this work and in Solymosi et al. [2020] (table 4.3). In Solymosi et al. [2020]

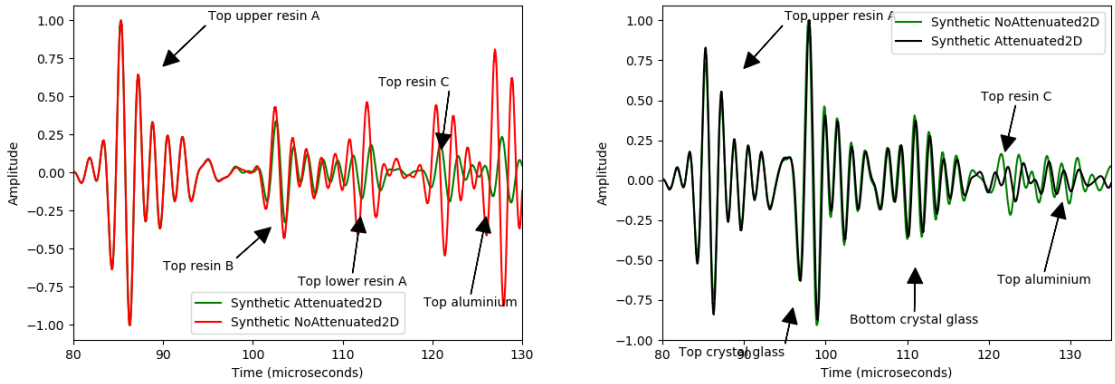

(a) 2D viscoelastic trace A.

(b) 2D viscoelastic trace B.

Figure 4.16. For the zero-offset data case in 2D: comparison between the synthetic 2D data with viscoelastic rheology (attenuation) and the synthetic 2D data with elastic rheology (no attenuation) for the traces A (Figure 4.16(a)) and B (Figure 4.16(b)). All the data are filtered with a 250-650 kHz band-pass filter.

they used trace C which is located in an area where the interfaces behave like a 2D layer-cake. On the other hand, our trace A is located in a region with slightly more curved geometry than Solymosi's trace C, because it is closer to the dome (see Figure 4.6). That is why the Qp values present an important difference between the two works (our work and Solymosi et al's work).

Correlation coefficient	Solymosi	This work
Trace A	0.94	0.96
Trace B	0.67	0.63

Table 4.4. Comparison between the correlation coefficients obtained by Solymosi et al. [2020] with SPECFEM and the correlation obtained in this work with 4-th order finite differences in space (UNISOLVER).

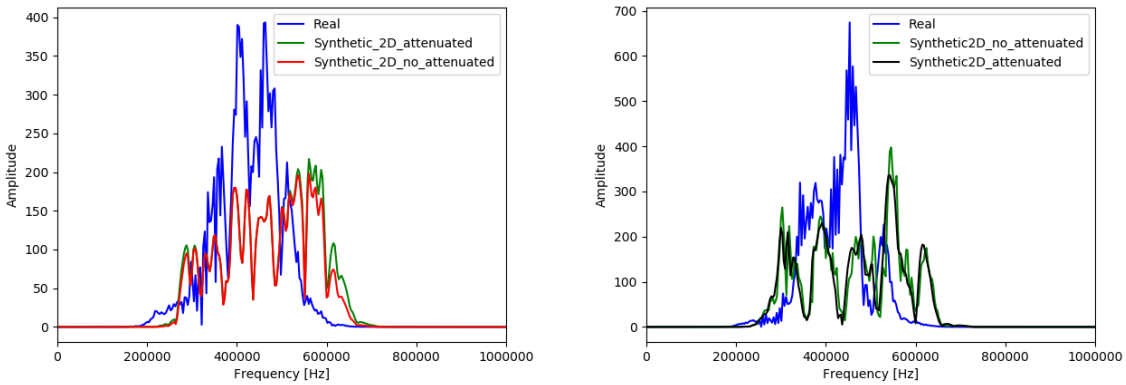

(a) 2D viscoelastic spectra trace A.

(b) 2D viscoelastic spectra trace B.

Figure 4.17. For the zero-offset data case in 2D: comparison between the amplitude spectra of the original (real data) and the amplitude spectra of the two-dimensional(2D) synthetic data with and without attenuation for trace A (Figure (a)) and trace B (Figure (b)). All the data are filtered with a 250-650 kHz band-pass filter.

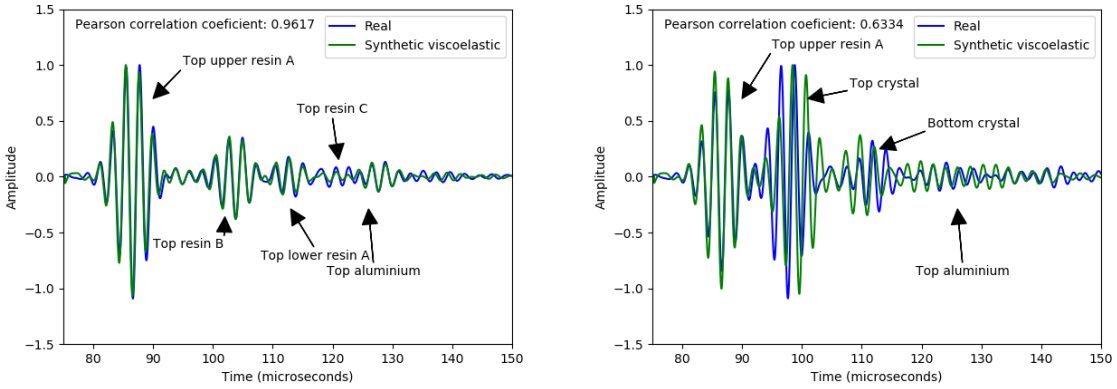

(a) 3D viscoelastic trace A

(b) 3D viscoelastic trace B

Figure 4.18. For the zero-offset data case in 3D with attenuation: comparison of the traces A (Figure 4.18(a)) and B (Figure 4.18(b) between the synthetic 3D data and the real data. All the data are filtered with a 250-650 band-pass kHz filter.

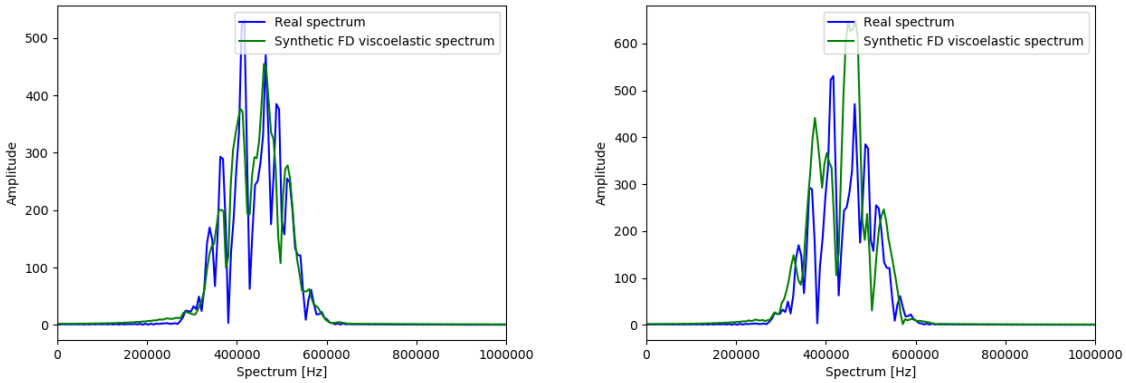

(a) 3D viscoelastic spectra trace A

(b) 3D viscoelastic spectra trace B

Figure 4.19. For the zero-offset data case in 3D with attenuation: comparison between the amplitude spectra of the original (real data) and the amplitude spectra of the three-dimensional synthetic data computed with a visco-elastic rheology (attenuation) for trace A (Figure (a)) and trace B (Figure (b)). All the data are filtered with a 250-650 kHz band-pass filter.

g) Zero offset kernels for elastic and viscoelastic rheologies.

In order to test the calibrated properties of the materials in the imaging process, we first calculate the sensitivity kernels using the zero offset data and the data computed with a smoothed background model : those kernels represent the high frequency perturbations around the background model that are also related to the data residuals defined by the difference between the real data and the background data. We show in Figures 4.20, 4.21 and 4.22 the principal interfaces of the WAVES model materials for the elastic kernels K_{Vp}, K_{Vs} and K_ρ preconditioned by the forward energy. We notice that we can see the correct location of almost all the interfaces (except the aluminium, which is not well defined). We also notice that in the kernel K_{Vs} there are some problems in the recovery of the low wavelengths. This is because the receivers only register the vertical component. To improve the kernel K_{Vs} it is necessary to register the vertical component and the two horizontal components. Furthermore, the nature of the zero-offset data does not allow to properly illuminate the acquisition area, that is why it is necessary to work with multi-offset data.

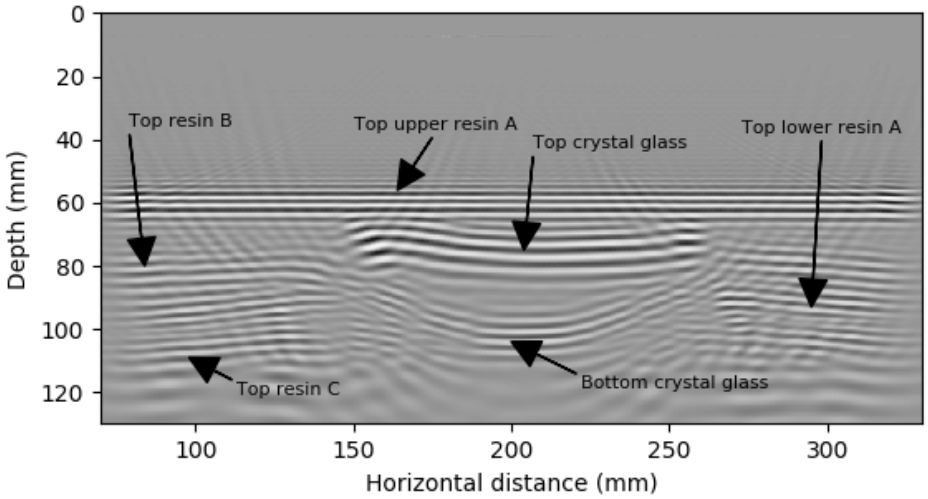

Figure 4.20. 3D elastic kernel K_{Vp} using the zero offset data and applying simultaneous sources.

In Figures 4.23, 4.24 and 4.25 we present the viscoelastic kernels K_{Vp}, K_{Vs} and K_ρ of the zero-offset data with simultaneous sources. We can see a much better definition of the high wavenumber interfaces (the top and even the bottom of the dome) compared to the elastic kernels shown in Figures 4.20, 4.21 and 4.22. We can then see the influence of implementing a viscoelastic rheology in the imaging condition process by increasing the correlation between the back-propagated and adjoint wavefields. The kernel K_{Vs} shows a better definition of the

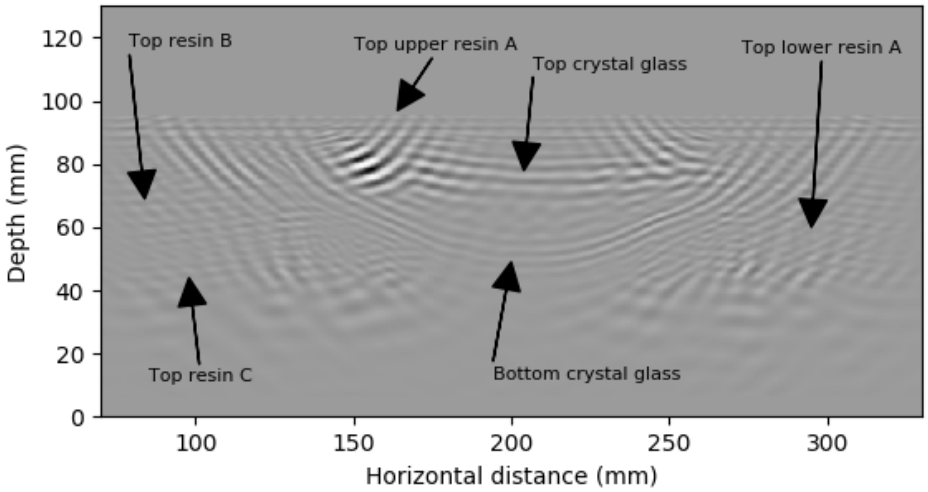

Figure 4.21. 3D elastic kernel K_{Vs} using the zero offset data and applying simultaneous sources.

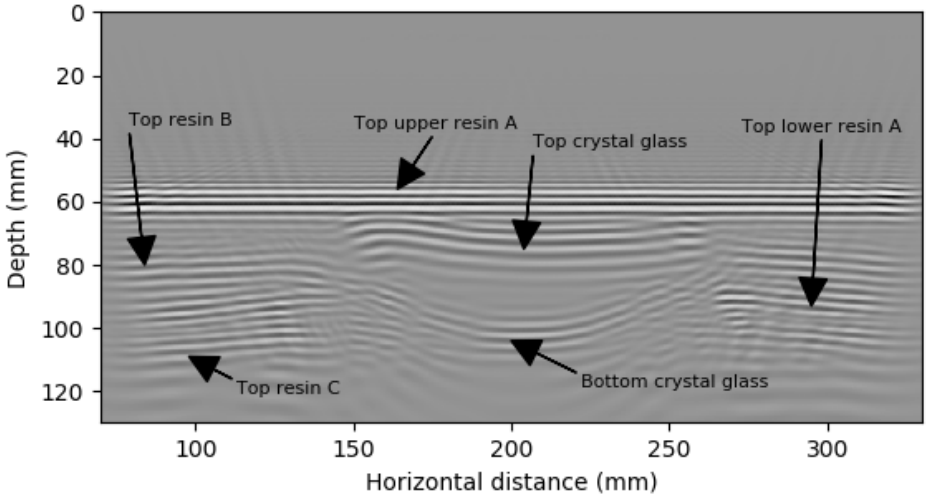

Figure 4.22. 3D elastic kernel K_{ρ} using the zero offset data and applying simultaneous sources.

borders of the dome when compared to purely elastic case. The K_{Vs} kernels should also be improved if three-component receivers were used.

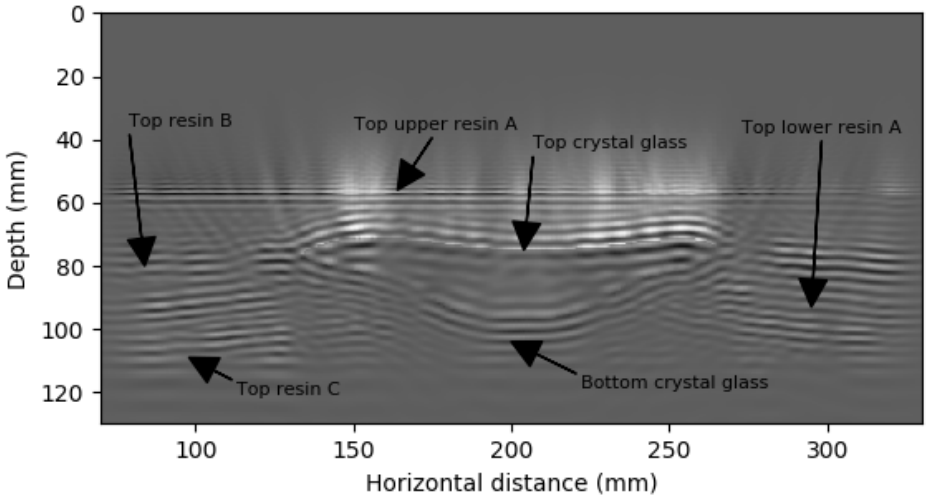

Figure 4.23. 3D viscoelastic kernel K_{Vp} using the zero offset data and applying simultaneous sources.

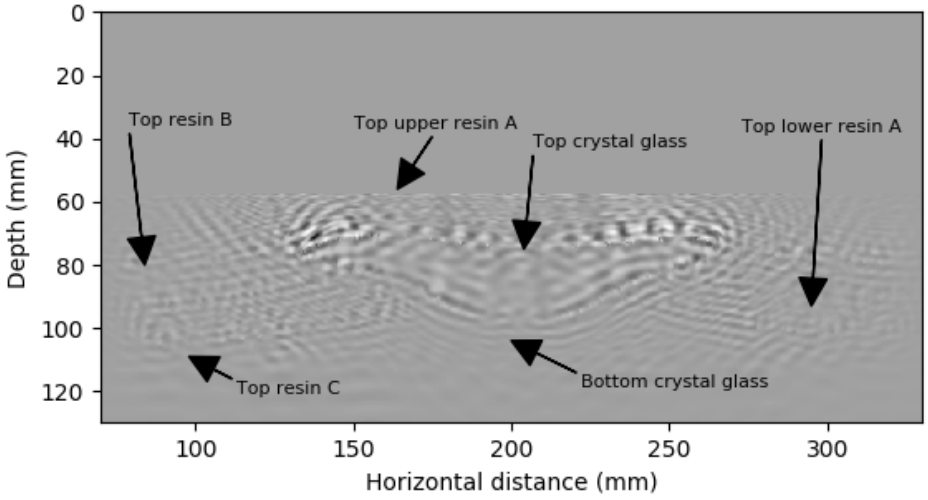

Figure 4.24. 3D viscoelastic kernel K_{Vs} using the zero offset data and applying simultaneous sources.

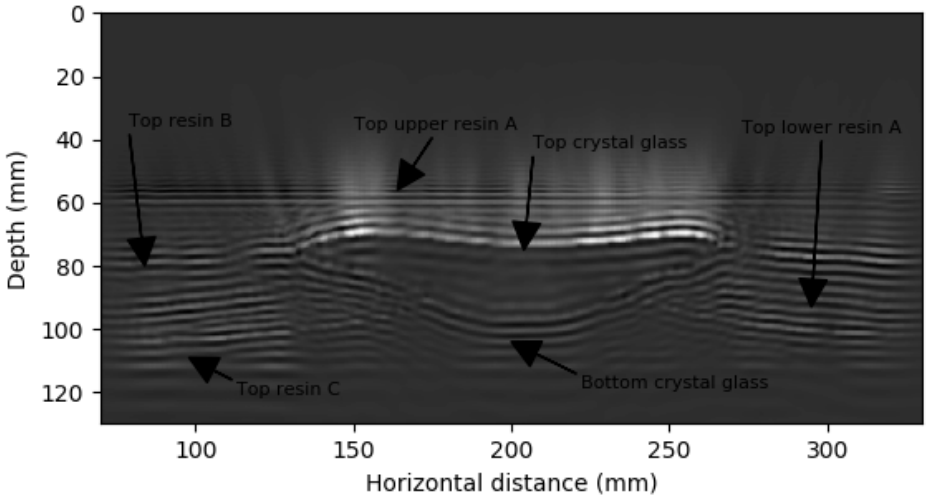

Figure 4.25. 3D viscoelastic kernel K_ρ using the zero offset data and applying simultaneous sources.

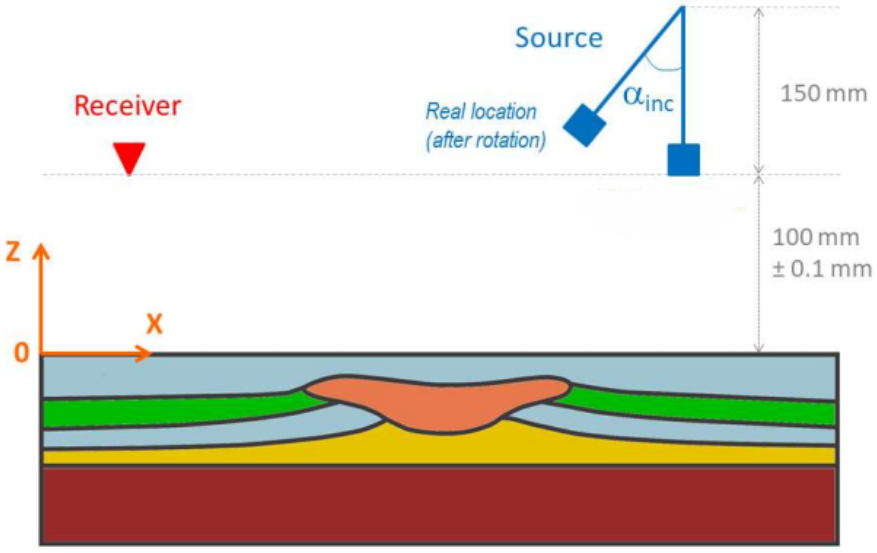

Figure 4.26. Acquisition scheme of the multi-offset data. The transducer (blue square) is inclined. The angle of inclination α takes the value of 19.7°, 20.1°, and 30°, which correspond to 3 different set of date. Taken from Personal Communication Favretto-Cristini [2020]

4.2.2 Configuration of multioffset experiment: Influence of viscoelastic modelling on the forward synthetic data.

As we have seen in the previous sections, the zero offset data is useful to calibrate the model properties. However, the detailed quality of the kernel images obtained using these data is not very good. This is why we resort to multi-offset data case, for which, due to the nature of the acquisition, the waves travel along more complex paths and can access to more complex regions (for instance close to the vertical borders of the dome and just below the dome), increasing the detail in the images. We aim here at seeing how well the viscoelastic properties defined at zero-offset can reproduce the multi-offset data and to know if it would help in the future (after this study) to perform seismic imaging and FWI using the multi-offset data. Generally they provide better images than simultaneous sources and zero-offset data.

In figure 4.26, we show the acquisition scheme used to obtain the multi-offset data. The receivers are located 100 mm above the bathymetry. In multi-offset data, the surveys have 3 different tilt angles (or incidence angles) of the source (19.7°, 25° and 30°) to illuminate different areas of the model as shown in Figure 4.26.

We choose the source with an inclination angle of 30° to have better illumination of the layers below the dome using reflected waves. The Figure 4.27 shows the location of the sources and the receivers used for viscoelasticity testing on multi-offset data. We selected one trace on the left of the model, and another trace just above the salt dome. All the traces shown here in 2D, with and without attenuation have been filtered using a 250-650 kHz band-pass filter.

We can see in Figures 4.28 and 4.29 the comparison between the original (real) data and the attenuated and non-attenuated 2D synthetic data recorded at receivers A and B respectively. We can see that the amplitudes of the real and synthetic data (attenuated and

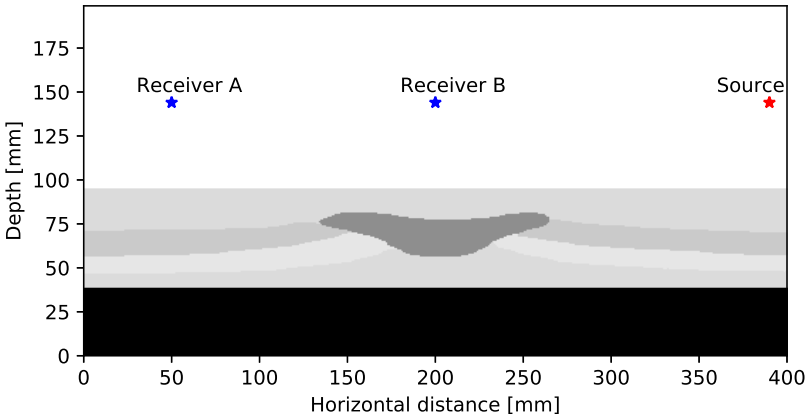

Figure 4.27. Multi-offset case : Location of the source (before the inclination of the transducer). We selected two traces: One is on the left side of the model (receiver A), and the other is on the salt dome (receiver B).

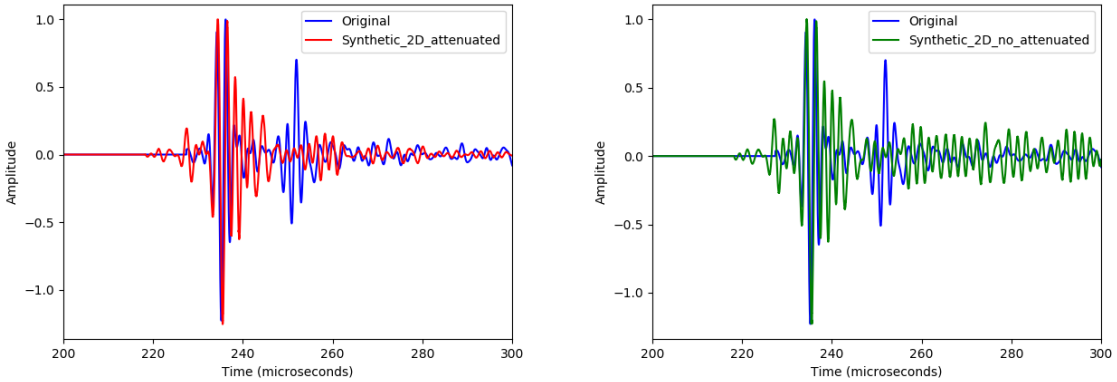

(a) 2D viscoelastic with attenuation.

(b) 2D viscoelastic without attenuation.

Figure 4.28. Multi-offset case : Figure (a) shows the comparison between the original (real) data and the 2D synthetic attenuated data recorded by receiver A. Figure (b) shows the comparison between the original (real) data and the synthetic non-attenuated data recorded by receiver A. All the data are filtered with a 250-650 kHz band-pass filter.

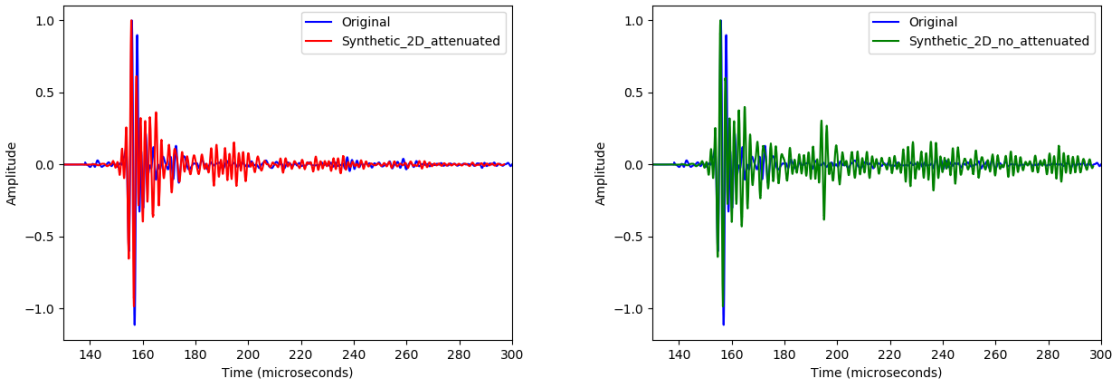

(a) 2D viscoelastic with attenuation.

(b) 2D viscoelastic without attenuation.

Figure 4.29. Multi-offset case : Figure (a) shows the comparison between the original (real) data and the 2D synthetic attenuated data recorded by receiver B. Figure (b) shows the comparison between the original (real) data and the synthetic non-attenuated data recorded by receiver B. All the data are filtered with a 250-650 kHz band-pass filter.

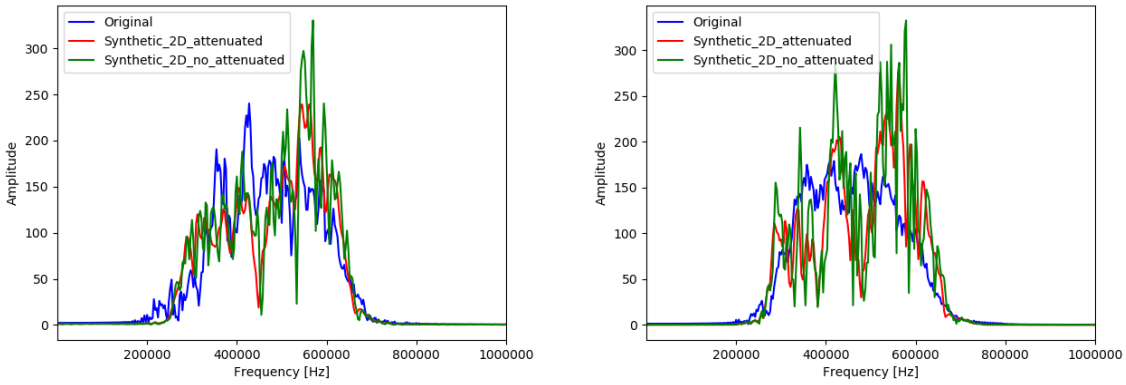

(a) Spectra receiver A

(b) Spectra receiver B

Figure 4.30. Comparison between the spectra of the original (experimental) data, the attenuated 2D synthetic data, and the non-attenuated 2D synthetic data for the traces recorded at receiver A (Figure (a)) and receiver B (Figure (b)). All the data are filtered with a 250-650 kHz band-pass filter.

non-attenuated data) fit well for the first arrival (bathymetry), because there is no attenuation in the water. For the later following arrivals, where the effect of the attenuation is present, there is generally agreement in amplitude between the real data and the attenuated data, unlike the non-attenuated data, which do not fit the amplitude of the real data in the late events.

In addition, the figures 4.30 show the comparison between the spectra of the original (real) data, the attenuated 2D synthetic data, and the non-attenuated 2D synthetic data for the traces recorded at receiver A (Figure 4.30(a)) and receiver B (4.30(b)). We can see that in general the spectra of all the data are in the same frequency range, although in terms of amplitude the spectrum of the real data fit better with the spectrum of the attenuated data.

4.3 Viscoelastic imaging results using FWI.

We perform now the FWI method in order to characterize the materials of the WAVES model but also to obtain the reflectivity images at each iteration (to compute search direction we must compute the reflectivity images, which are equivalent to the sensitivity kernels). Broadly speaking, we fix the density (ρ) and quality factors (Q_p and Q_s) and invert the impedances $Z_p = \rho V_p$ and $Z_s = \rho V_s$, due to the fact that seismic imaging and inversion are more sensitive to V_p and V_s seismic velocities.

4.3.1 Source encoding implementation.

We use the zero offset data to perform the FWI because we want to start the inversion process using the less complex data to obtain the first reflectivity images and new models, and then in the future we will try to make the inversion with the multi-offset data. In the zero-offset data we have 260 sources and receivers. Due to interference between the sources, which would cause crosstalk-attributed noise (source interferences), we decided to implement source encoding (Romero et al. [2000], Capdeville et al. [2005] Krebs et al. [2009],Schuster et al. [2011], Moghaddam et al. [2013], Castellanos et al. [2015], Rao and Wang [2017] among other authors). The objective of the source encoding technique is to decouple the sources to reduce the interference between them. By introducing a different and random delay in the sources of each shot gather, the interference between each source is reduced, making possible the simultaneous migration of different shot gathers.

We implemented source encoding by time statics for which we apply a random delay for each source. We set this random value to be between 0 and $3t_0$, where $t_0 = 1/f_0$ is the principal period of the source.

4.3.2 Inverse problem configuration.

Having implemented the source encoding technique, we designed the strategy to be followed to invert the WAVES model. According to Operto et al. [2013], it is convenient to use

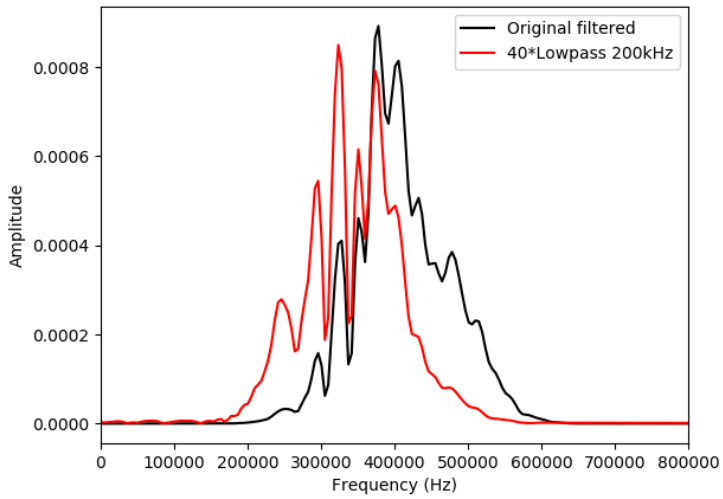

Figure 4.31. Spectra of the original band-pass filtered source and the low-pass filtered source.

a multifrequency inversion process, starting from lower frequency contents of the sources and data and incrementing them little by little until reaching the highest frequency contents. This allows to reduce the uncertainties by separating the different frequencies (i.e wavelengths) involved in the model. For low frequencies the largest wavelengths are solved and parts of the model are thus smooth. Then, by increasing the frequency content of the source slowly, the high frequency details of the model are appearing more and more step after step. We thus start here the inversion of the parameters with low frequencies. We decided to filter source and real data using a 3^{rd} order low-pass Butterworth filter of 200 kHz to image larger wavelengths. In figure 4.31 we can see the spectra of the initial source (filtered with a pass-band filter between 250-650 kHz) and the source filtered with a low-pass filter/LPF at 200 kHz. This second filtered source is used in the FWI process. The amplitude of the spectrum is very low which is the reason why we scale it in the figure 4.31 for comparative purposes. The dominant frequency increases from around 300 kHz (for the 200 kHz low-pass filtered source) to around 400 kHz (for the 250-650 kHz band-pass filtered original source).

The diagram in the figure 4.32 shows the steps we have followed specifically to invert the parameters of the WAVES model.

Having filtered the sources, we proceed to invert the impedances for each source, using the 200 kHz LPF filtered source. First, we set the background model as a smoothed model obtained by applying a spatial Gaussian filter with a standard deviation of 20 (m/s for velocity or kg/m^3 for density), in such a way that we ensure to have a sufficiently blurred background a priori model. Then, we compute the gradient $\nabla\chi$ of the data misfit function, and save the misfit of the background model $\chi(0)$. We compute the preconditioned search direction as:

$$Cg = \frac{-\nabla\chi}{\int_0^T \boldsymbol{u_x}^2 + \boldsymbol{u_y}^2 + \boldsymbol{u_z}^2 \mathrm{dt}}, \tag{4.1}$$

where $\boldsymbol{u_x}$, $\boldsymbol{u_y}$, and $\boldsymbol{u_z}$ represent the displacements in the x, y, and z directions. The denominator is also known as the forward kinetic energy in the system.

As we want the initial model perturbation to be sufficient but not too large to avoid possible too extreme increases of the global misfit function, we define the first step length as: $\alpha = max(abs(0.1\boldsymbol{m_0}/\boldsymbol{dk_0}))$. This allows a perturbation of the initial model not greater than 10% of the model. In this way we ensure to have : $max(abs(\alpha \boldsymbol{dk_0}/\boldsymbol{m_0})) \leq 0.1$, where $\boldsymbol{m_0}$ and $\boldsymbol{dk_0}$, represent the initial model and search direction respectively (as defined in section 2.3). After that, we iteratively update the background model as in equation 2.60 by computing the forward problem. We evaluate if the first Wolfe condition (misfit minimisation) is satisfied. If this is the case we save this step length and we compute the gradient for this updated model to obtain the next search direction **dk**. If the first Wolfe condition is not satisfied then we try with half the step length α and repeat until the first Wolfe condition is satisfied or until a maximum number of tests (here we take 10 different tests) has been reached, in which case we take the step length that produces the lowest misfit. Once we finish this step we have not only the new model m_1 but also the relative model perturbation $(m_1 - m_0)/m_0$ respect to the background m_0.

After this we pass to a second step by starting from the last model (i.e model 1 obtained in the first stage) taken as the new a priori model, and we compute the gradient and the search direction for the conjugate gradient method cycle (see equation 2.57). Then we update the model using a step length obtained as in the first stage ($\alpha = max(abs(0.1\mathbf{m}/\mathbf{dk}))$). After that, we compute the gradient several times and evaluate if the two Wolfe conditions (misfit and misfit curvature minimization) are satisfied. If this is the case we save this updated model, if not we try with half the step length until the two Wolfe conditions are satisfied or until a maximum number of tests has been reached in which case we take the step length that produces the minimum misfit. We repeat this stage 5 times and we obtain the second model m_2.

4.3.3 Results

In this subsection we present the models that resulted from the inversion of the zero offset data.

In Figures 4.33 we show the evolution of the P velocity model (from the background model to the model at iteration 2) with its respective relative error respect to the real model. The relative error e at each grid point is calculated as follows: $e = (\boldsymbol{r} - \boldsymbol{m})/r$, where $\boldsymbol{r}$ is the real model and $\boldsymbol{m}$ is the updated model.

The evolution of the misfit is shown in Table 4.5.

Model	Background	Model 1^{st} iter	Model 2^{nd} iter
Misfit	0.2092	0.2027	0.198

Table 4.5. Evolution of the misfit according to the different models. .

The background models (Figures 4.33(a) and 4.34(a) for the P and S velocities respec-

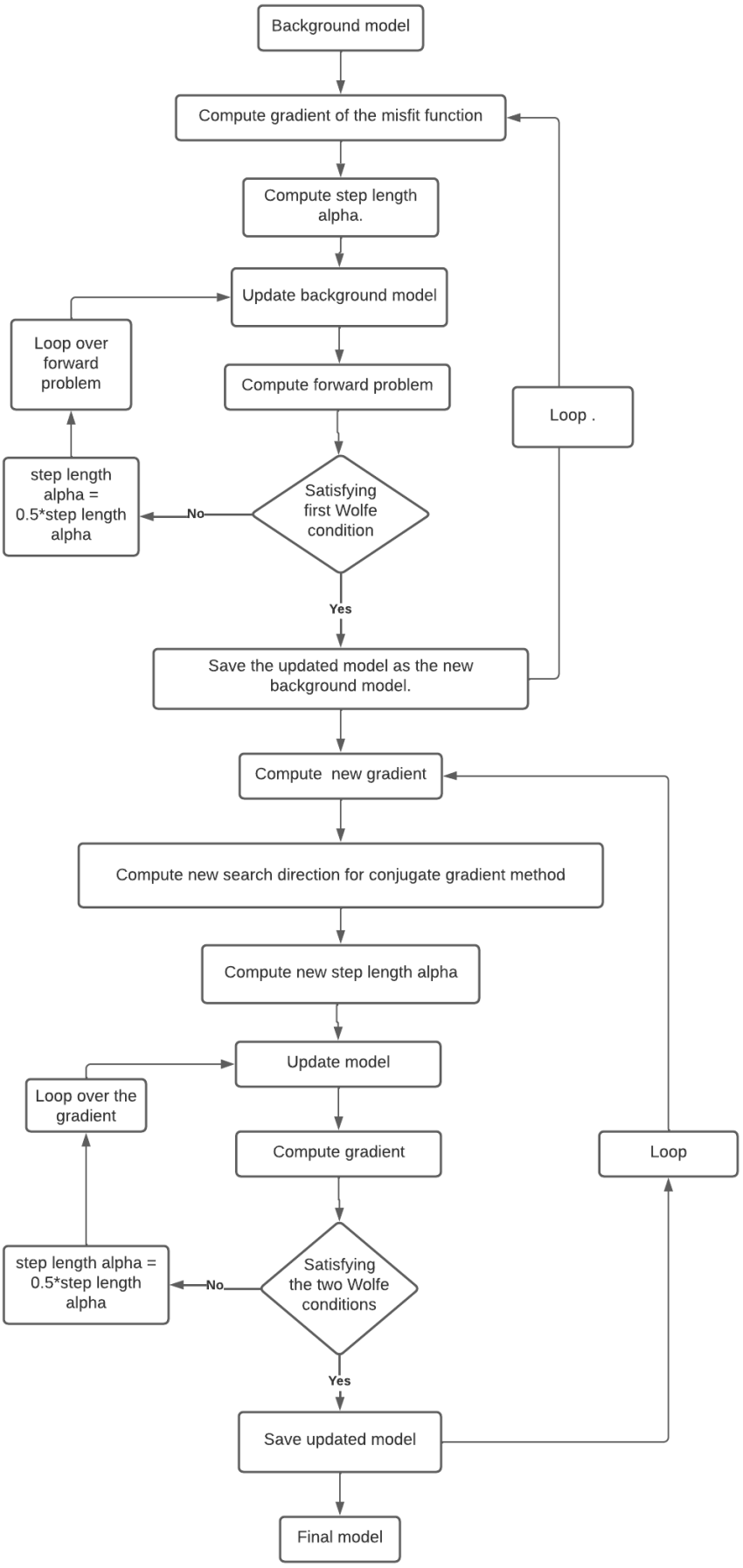

Figure 4.32. Stages followed to invert the WAVES model parameters. They are detailed in subsection 4.3.2.

tively) were obtained by applying a Gaussian filter with standard deviation of 20 m/s. We can observe an improvement in the interface boundaries of model 1. For example the limits of the salt domes are well defined and we can also see not only some of the limits of the adjacent layers of the dome but also the layers below the salt dome (the basement).

Referring to the images of the relative model perturbation respect to the background model, the Figure 4.35 shows that we have recovered the shape of the dome and also the interfaces under the dome (e.g. the basement). However, the V_s relative perturbation images images, (Figures 4.35b and 4.35d) show some clear artifacts on the sides of the dome (between 60 and 80 mm on the vertical axis). This is related to the fact that the receivers only record the vertical component. To obtain a better inversion of the V_s parameter it should be necessary to record all 3 components and place the receivers at the bottom of the water.

Figures 4.36 and 4.37 highlight the evolution of the misfit by evaluating the different step lengths α to obtain the model 1 and the model 2. To obtain the first model (model 1) we compute the forward problem 10 times with different models following a steepest-descent approach (Figure 4.36). We recall that we start by updating the model with a initial step length α and proceed with the next step length being half of the previous one until we reach a smaller misfit. We took the step length α that produces the best misfit (the third). We can also see that there is a tendency to stabilization in the last misfit calculations where the improvement is minimal. In other words, it is difficult to observe a strong improvement in the long term. This is due to the fact that a more optimized procedure like the non linear conjugate gradient algorithm along with the two Wolfe criteria verification must be used.

Therefore, to obtain the second (and better) model we use the nonlinear Conjugate Gradient approach, in which we compute the gradient 5 times with different step lengths (Figure 4.37), and we select the step length that produces the best misfit (the second step length α).

In both successive inversions (first steepest descent-like inversion for model 1 followed by the nonlinear CG inversion for model 2), the best misfit is obtained before the fifth step length of the nonlinear CG.

Figures 4.33 and 4.34 point out a qualitative improvement because the interfaces are progressively better defined. This fact is also verified quantitatively in table 4.5, where the misfit is reduced from the background to the model 2. However the same artifacts are observed for the models of velocity S (Figures 4.33b,d,f and 4.34b,d,f).

In the future for better convergence, more iterations should be required and also as in (Schuster et al. [2011], Feng and Schuster [2017], Rao and Wang [2017]), dynamic random delays and choices of source locations should be done on each new iteration to reduce even more the cross-talks and interferences between sources.

Code performance and CPU time

We have run our calculations on the Olympe machine at the CALMIP calculation center with Skylake Intel® processors. Using $\Delta x = \Delta y = \Delta z = 0.0004m$ we have 1000, 382 and 50

nodes in the directions x, y, and z respectively (we reduce the transversal direction z to reduce calculation time), and $\Delta t = 1.2 \times 10^{-8} s$ with 14000 time steps and 100 checkpointing frames.

With 250 processors we spend 13 minutes to compute the forward problem, and 23 minutes to compute the imaging condition (correlation of the back-propagated and adjoint wave-fields). This means that to compute the gradient of the misfit function we spend 36 minutes. To compute one iteration with the steepest descent method with 10 tests of the step α, we spend 166 minutes approximately, and to compute one iteration of the conjugate gradient method with 5 step α tests, we spend 216 minutes.

In order to optimize the calculation time, we should:

- Implement the parallelism in the other 2 directions.
- Make not only a global checkpointing but also a local checkpointing between two frames, which does not spend more memory than when using only the global checkpointing.
- Implement eighth-order finite differences in space and fourth-order finite differences in time to reduce the CPU time by a factor around 2.

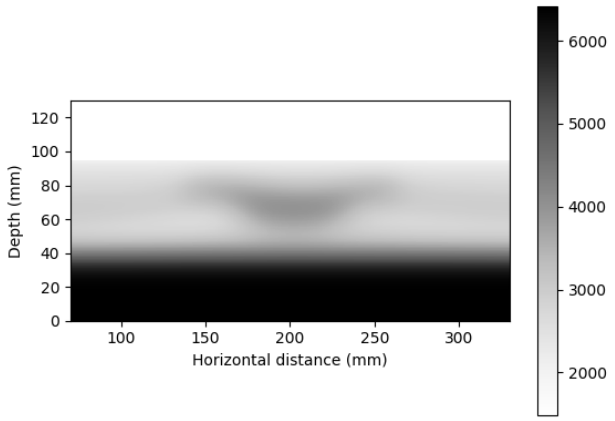

(a) Background P velocity model

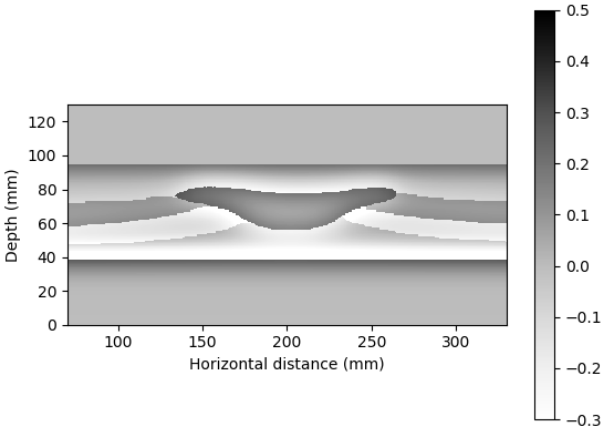

(b) Relative error of the background model.

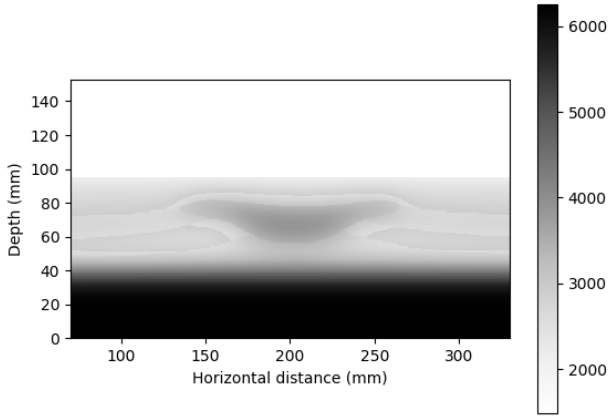

(c) V_p model 1 (after the first iteration)

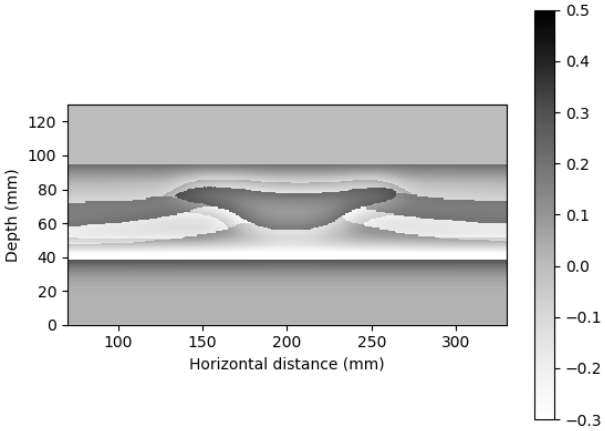

(d) Relative error of the V_p model 1

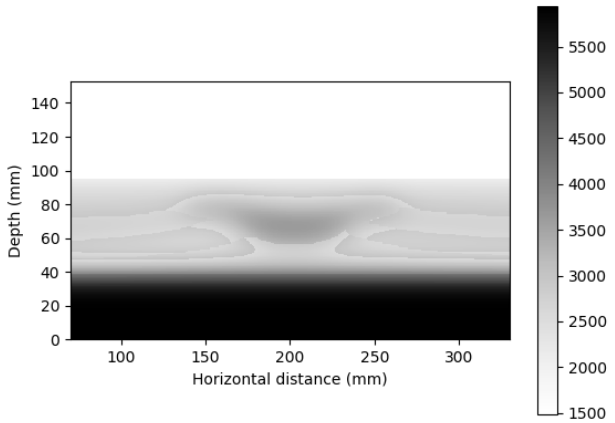

(e) V_p model 2 (after the second iteration)

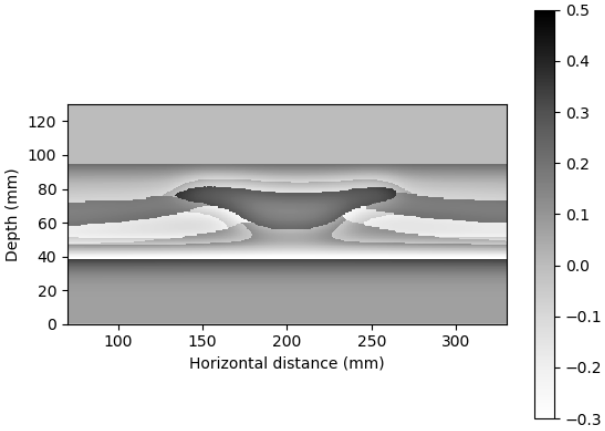

(f) Relative error of the V_p model 2

Figure 4.33. Evolution of the P velocity model and its relative error compared to the "true" V_p model using steepest descent-like inversion (model 1) followed by nonlinear CG inversion (model 2).

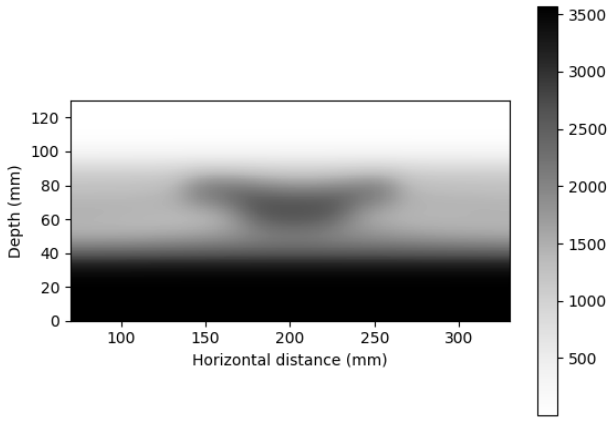

(a) Background S velocity model

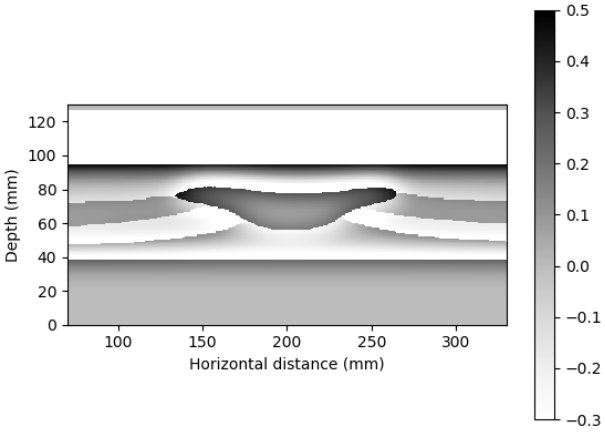

(b) Relative error of the background V_s model

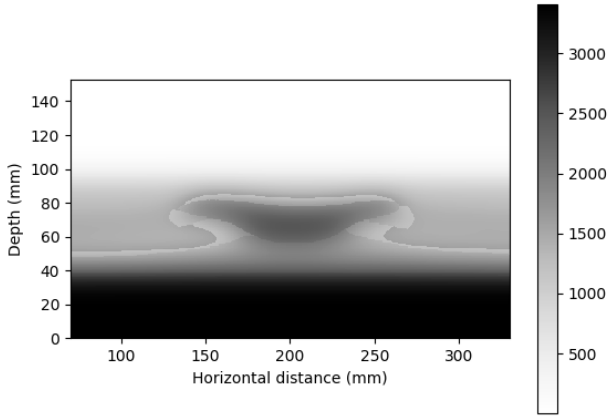

(c) V_s model 1 (after the first iteration)

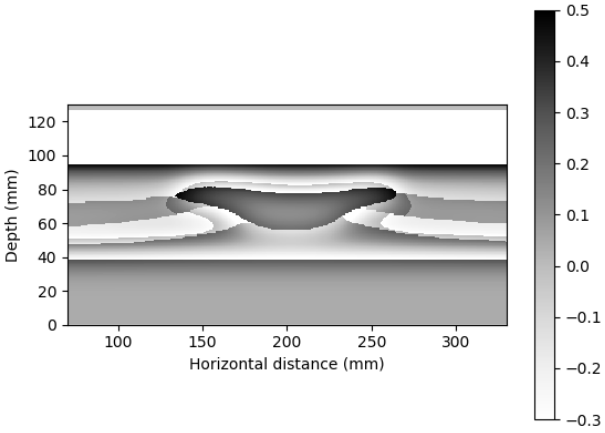

(d) Relative error of the V_s model 1

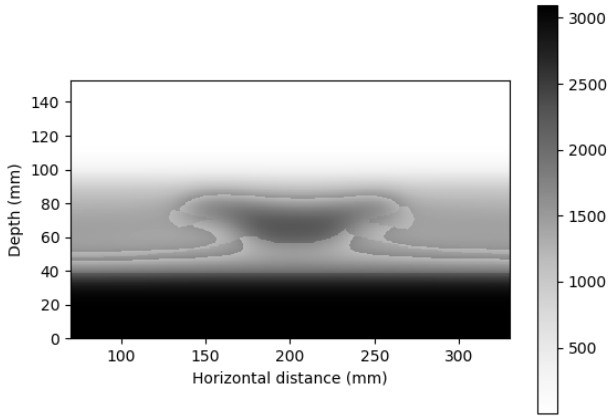

(e) V_s model 2 (after the second iteration)

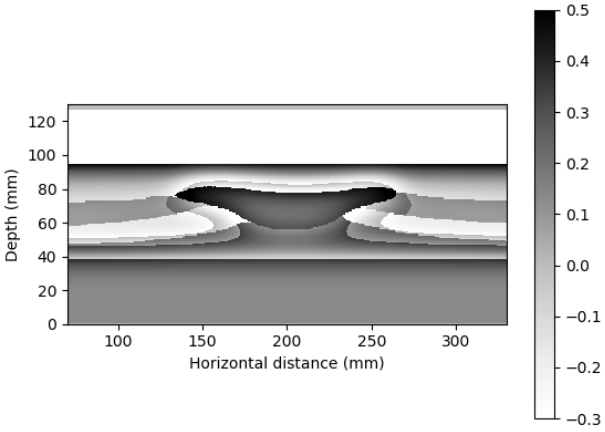

(f) Relative error of the V_s model 2

Figure 4.34. Evolution of the S velocity model and its relative error compared to the "true" V_s using steepest descent-like inversion (model 1) followed by nonlinear CG inversion (model 2).

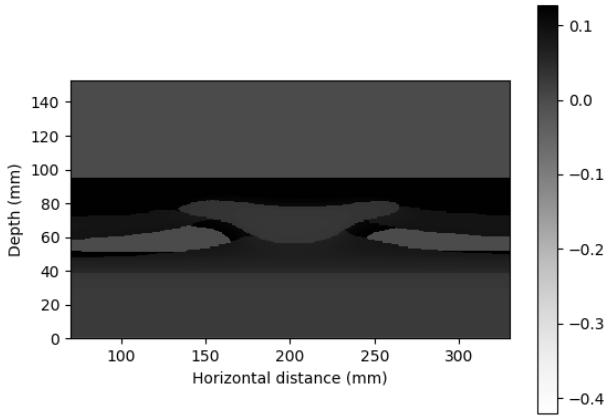

(a) Reflectivity of P-model 1

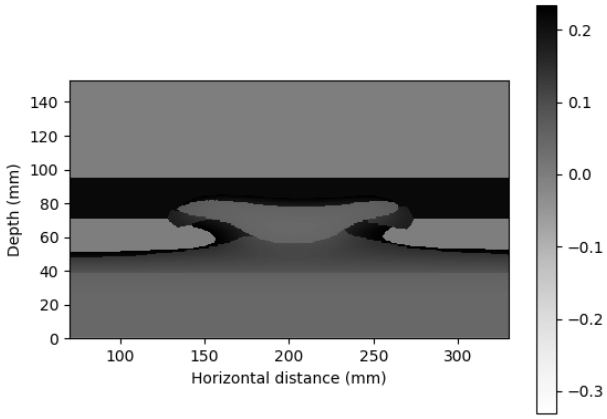

(b) Reflectivity of S-model 1

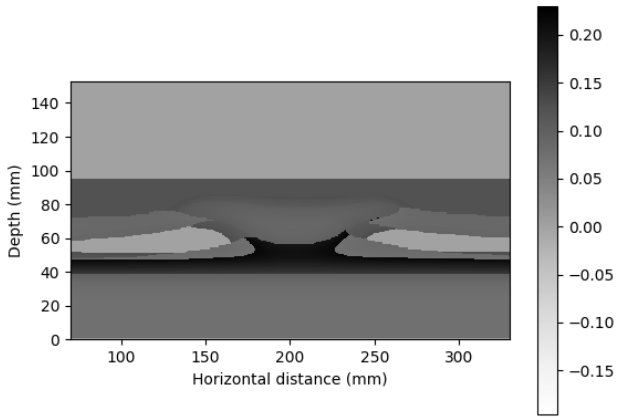

(c) Reflectivity of P-model 2

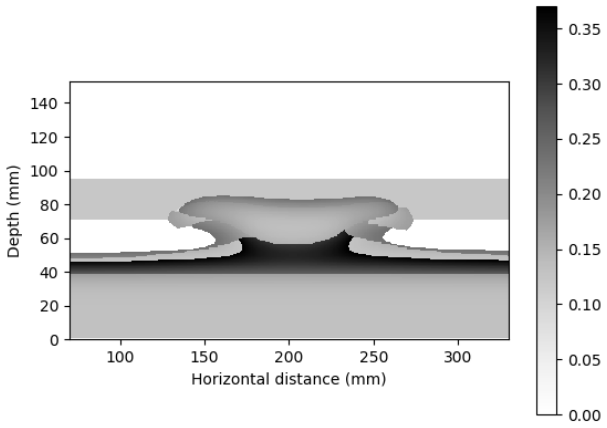

(d) Reflectivity of S-model 2

Figure 4.35. Evolution of the reflectivity for P and S velocities for model 1 (using steepest descent like method with first Wolfe criterion verification) and for model 2 (using nonlinear Conjugate Gradient with the two Wolfe criteria verification).

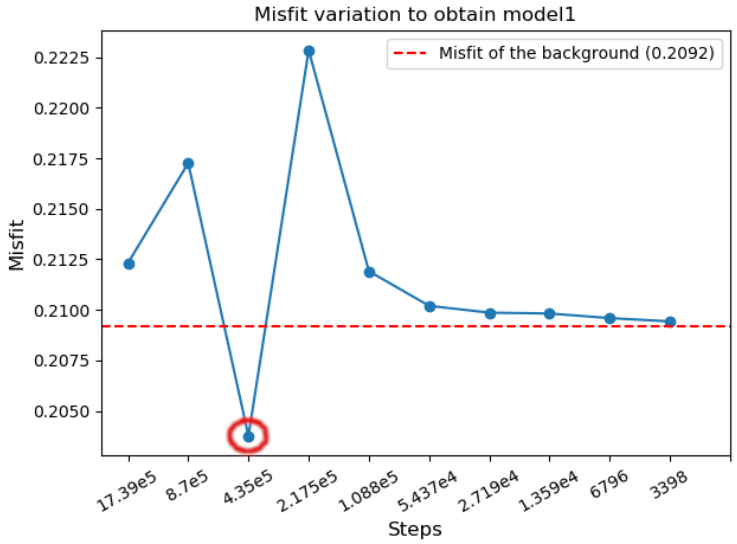

Figure 4.36. Misfit evolution for different step lengths before obtaining the best model 1. We use the step descent method (i.e the first Wolfe criterion verification) to obtain the model 1. We take the α value of 4.35×10^5 (third value) because it was the one which produced the best misfit (0.2037). The red dashed line corresponds to the data misfit respect to the initial background.

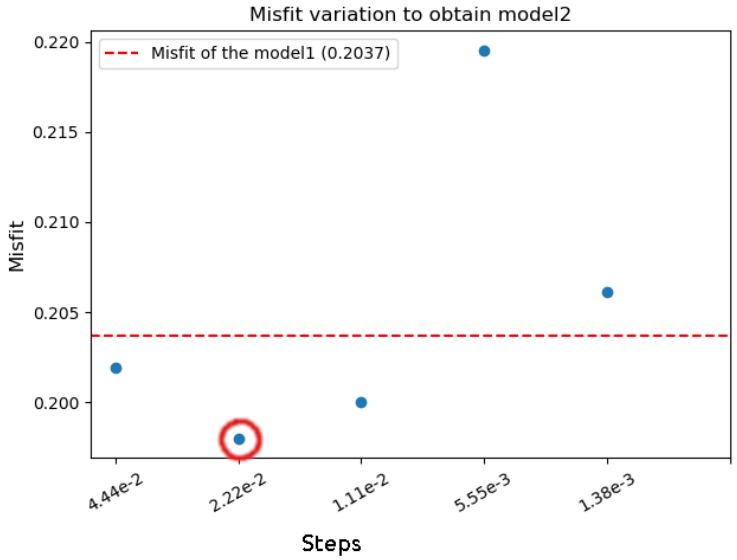

Figure 4.37. Misfit evolution for different step lengths before obtaining the best model 2 (model 1 is taken as the initial background). In this case, we use the nonlinear Conjugate Gradient method to obtain model 2 (i.e with the two Wolfe criteria verification). Among all these different α step lengths, we take the second value (2.22×10^{-2}), because it is the one that produces the best misfit (0.198).

4.4 Discussion

By the nature of the zero-offset data, they can be perfectly used to calibrate the physical properties of the model materials, because the seismic energy follows a vertical trajectory, making it easier to predict the seismic events that are recorded at the receivers. Also, by looking at the high quality image of the gather of the zero offset data (Figure 4.11), we have a better idea of the medium interfaces and properties. The zero offset data process is similar to the NMO correction used in classical seismic migration process, that is why the seismic events are at their "real position" in time. However, the seismic images (Figures 4.20, and 4.22) derived from the RTM method using the zero-offset data set suffer from a lack of detail (the high frequencies are not optimally highlighted). This is due to the fact that the waves only travel in one direction (vertical), which prevents the waves from hitting/illuminating the geological structures at different angles. For this reason it is always more convenient to implement and apply RTM methods to multi-offset data, because the different trajectories followed by the seismic waves enrich the information that a seismic image can provide. Despite these drawbacks, Figures 4.23-4.25 show the structure of the dome (top and bottom), and some of the layers under the dome. Besides, these models can be taken as a priori models at low computational cost for further data inversions using separated sources and muti-offset data.

Furthermore, it is very important to implement the viscoelasticity equations so that there is a better fit in amplitude between real and synthetic data (Figures 4.18, 4.28, and 4.29). This fact plays a crucial role in the RTM method at the time of calculating the imaging condition that consists in correlations between real and synthetic data. If both seismic wave phases (travel times) and signal amplitudes of synthetic and real data are similar, the correlations will be high and migrated images will give good reconstructions of the interfaces of the medium. However, if amplitudes are not fitting well enough between real and synthetic data, these correlations would be low and less accurate. In addition we can see that the amplitudes of the spectra of the attenuated data fit better with the amplitudes of the spectra of real data (Figures 4.17, 4.19, and 4.30). Despite not having all the components of the source, the V_s sensitivity kernel recovers the top and the base of the dome very well when we use a viscoelastic rheology. This emphasises the importance of using the right rheology to recover the structures better.

Comparing our RTM results with another recent work as Henke et al. [2020], the 3D joint inversion (seismic, gravity and magneto-telluric data) done by the authors give an image of the Wedehof salt dome in Northern Germany. This salt dome structure corresponds to a diapiric dome as the WAVES model. In their original seismic section, neither the top nor the base of the dome is visible. By integrating the information from the magneto-telluric data, a better definition of the top of the salt is retrieved. However, the base of the salt is still not very well visible. This indicates that it is still a challenge to image full salt domes structures even when using joint inversions to constrain salt dome interfaces and models. However, by using our methodology we are able to retrieve the full structure of the dome at least for this experimental case.

Analyzing the multi-offset RTM results of Solymosi et al. [2020] and our zero-offset RTM results, one can observe that in Solymosi's work the interfaces are well recovered (particularly when considering the impedance and compressibility modulus kernels). However, some artifacts are generated that are normally attributed to diving, head, and backscattered waves. In our work we also recovered the structure of the dome and the adjacent interfaces but almost no artifacts are observed, although this could be due to the nature of the zero-offset data in which fewer diving, head, and backscattered waves are generated.

In Li and Qu [2022] studies the salt domes seismic imaging with a viscoelastic rheology was done. The authors used synthetic data, 3 different methods (Gaussian-Beam migration (GBM), RTM and LSRTM), and a smoothed model as the a priori information. GBM fails to correctly recover the model interfaces (especially under the dome). However in RTM and LSRTM results, interfaces are well recovered. These results present a better definition of interfaces than those obtained in this work. However, in Li and Qu [2022] synthetic data were used and the smoothed a priori model is very close to the real model. Among other recent works we can find Aghamiry et al. [2021] in which they applied the FWI with Newton methods to invert the salt-synthetic models of SEG/EAGE, Marmousi and Valhala. Their results are very good, even though they started from a very smoothed initial model. They performed 70 iterations, which is possible mainly because the models they inverted are in 2D.

In Ren [2022] 2D synthetic data inversions are applied to Marmousi and BP models using acoustic FWI with a variant of the steepest-descent method that follows a linear-regression approach. He demonstrates that the convergence of his method is better than the L-BFGS method. One perspective of our work could be the integration of this methodology to reduce the number of inversion iterations, the computational cost due to the calculation of the gradient at each iteration, and also to provide much more accurate models without too much extra cost in terms of memory storage and computations.

We now discuss the reflectivity images computed as the relative model perturbation δ^i in each node for the $i-$th model obtained at the $i-$th inversion cycle:

$$\delta^i = (m_0 - m^i)/m_0, \tag{4.2}$$

where m_0 is the background and m^i is the current model (after iteration i = 1, 2 or n). We calculate the average av^i of the absolute value of each of the elements of the reflectivity images δ^i as:

$$av^i = (\sum^{N} |(m_0 - m^i)/m_0|)/N, \tag{4.3}$$

where N is the total number of elements, and we obtain for the velocity P values of 0.0223 and 0.0454 corresponding to the models of the first and second iteration respectively. While for the velocity S we obtain the values of 0.03 and 0.07. This is congruent because from one iteration to the next this perturbation should increase indicating a larger difference from the smoothed background model. The error between model 1 and the true model is 0.07 for V_p and 0.085 for

V_s. The difference in terms of error between V_p (weaker error) and V_s is due to the fact that we have not converged yet (more inversion iterations are needed) and that we only have the vertical component of the data and thus a less accurate V_s model.

To improve the reflectivity images of the Vp and Vs models we should add more iterations in the inversion process. We should also change randomly and automatically the time delays of the encoded sources or even the number of sources. Indeed, referring to the source-encoding issue, we can find in the literature that in order to efficiently reduce cross-talks it is necessary to perform a certain number of iterations, which depends on the total number of injected simulated sources. That is why in many cases only certain sources are randomly selected to reduce the number of iterations and different sources are injected at each new iteration until the total number of sources is covered (Schuster et al. [2011], Castellanos et al. [2015], Rao and Wang [2017]). In our case, despite having injected all the sources simultaneously, we only need two iterations to show and identify the main structures of the WAVES model due to the low complexity (large wavelengths) of the structures.

4.5 Conclusions

Regarding our inversion results, we have been able to invert the subsurface parameters for a three-dimensional model in a viscoelastic medium. For this purpose we use the time shift source encoding technique to reduce the generation of crosstalks. We used a search direction of the conjugate gradient method that is equivalent to the forward energy preconditioned gradient. The results are acceptable according to the difficulty of the problem. For example in the reflectivity images, we can see that the salt dome structure and adjacent sediments are well defined. However, the results for the S velocity model are not very good due to the nature of the data, where only the pressure component is recorded and inverted and thus only the compressional waves are better retrieved. In order to obtain better S velocity model, both components (vertical and horizontal) of the displacements or particle velocities should be recorded and inverted. Another point, the receivers should be located at the bottom of the bathymetry to capture both P and S waves coming from the structures below the bathymetry. It is also interesting to note that these results were obtained only using the low frequency source with a 200 kHz low-pass filter. This is due to the quite simple geometry (large wavelengths) of the model. So only using a low frequency source was sufficient.

The methodology we have implemented is complementary to the one used by Solymosi et al. [2020] and allows us to provide WAVES models and interfaces images, and also physical property estimates that can be used as prior models for further FWI of both zero-offset or multi-offset data with separated sources. We could now try to apply this methodology with data of more complex geometries. Other perspectives are to apply this methodology to multi-offset data to further highlight the structures. In addition we will improve the regularization term in the misfit function to penalize in a better way the spurious values of the model.

Another long-term perspective is to do an inversion using teleseismic waves (which is a

wave transmission approach) to increase the energy of the signal, because what is recorded is the refracted/transmitted wave. In addition, as these waves are incident on the structures from below, it would be possible to retrieve information of the structures from different travel paths than than those of a classical seismic survey.

Chapter 5

Conclusions and perspectives.

Conclusions

This work is divided into two case studies related to the seismic imaging of salt domes. The first case study consists of a geologic-two dimensional model containing a salt dome. It is a synthetic model that comes from a study that was done in the Gulf of Mexico. The second case study consists of the realistic experimental WAVES model developed by the LMA laboratory in Marseille (France). This model contains a salt dome, adjacent sediments and a basement. To simulate the physical properties of a real environment, glass, resins and aluminium were used respectively.

In both cases, we employed two adjoint-based methods to calculate the seismic images: The RTM and the iterative LS-RTM method. To solve the wave equation we used the 3D parallel Fortran 90 UNISOLVER code, which uses the fourth-order finite difference method, following the staggered grids approximation, employing CPML-type absorbing boundary conditions. In addition, in order to solve the viscoelastic wave equation, it was necessary to employ the checkpointing method at the time of calculating the image condition to take into account the physical phenomenon of seismic wave attenuation for high frequency sources as in the WAVES experiment (200-650 KHz frequency range). Also to speed up the computation time, we employed MPI parallelization.

The main objective of the first case study is to recover the boundaries of the salt dome structure and to appreciate the interfaces above and below the dome. For this purpose, we followed different strategies in the calculation of the sensitivity kernels:

- To reduce the effect of the free-surface multiples, we apply boundary conditions at the top of the computational domain (instead of free-surface conditions that are generally applied). These effects are studied in two-dimensional synthetic models.
- We normalize the kernel amplitude by the energy of the forward or the adjoint simulation. We also apply a depth-squared dependent gain (normalization) to the kernels to exhibit the interfaces much better at depth. These effects are studied in two-dimensional synthetic models.

- We apply different distribution configurations of sources and receivers: the classical distribution (sources and receivers at the surface), the OBC-like configuration (sources at the surface and receivers at the bathymetry), sources at the bathymetry and receivers at the surface, and finally both sources and receivers at the bathymetry. This comparison was made using the three-dimensional synthetic models.

- We use different parameterizations when calculating the kernels: i.e parametrizations like (ρ,λ), ($\ln\rho$,$\ln\lambda$)($\ln\rho$,$\ln\lambda$), ($\ln\rho$, $\ln V_p$), and ($\ln\rho$, $\ln Z_p$).

We learned that there is a moderate improvement in normalizing kernels using the forward energy than using the adjoint energy especially in the kernels related to the compressional seismic wave (kernels K_{Vp} and K_λ), while in the density kernels the difference is minimal. This could be related to the fact that compressional velocity kernels are more sensitive to the surface region of the models, which is the most energetic zone of the kernels.

Furthermore, among all the acquisition configurations we use, the one that produces the best results is when we inject the source into the sediments just beneath the bathymetry and the receivers are also located there (see Figure 3.22).

In addition, using the SNR, we studied the influence of some a priori models on the sensitivity kernels. We learned that:

- Compressional wave velocity related kernels (K_λ are more sensitive to the smallest wavelengths of the medium under study that are related to the shallow structures around the salt dome and close to the bathymetry , while the density kernels K_ρ are more sensitive to the highest wavelengths of the medium related to the deepest structures.

- SNRs of deep interfaces increase as we add more information on the a priori models for kernels K_ρ. However in kernels K_λ the opposite occurs (compressional kernel SNRs related to the shallowest interfaces and interfaces around the salt dome are more important).

The main objective in the second case (WAVES experiment) is to apply everything learned in the first case to real data. In addition, we analyze the effects of attenuation (Zener body models are used here) on the amplitude of the calculated data and more generally we compare the amplitudes and waveforms of calculated data (with and without attenuation) to those of the real data.

We can observe that in the figures of the calibrated properties (Figures 4.14(b) and 4.15(b)), the waveform coincides in time between the synthesized and original data. However, the amplitude does not coincide in the last arrivals because we do not consider attenuation in the model.

In the figures (4.28-4.30) related to the calculated two-dimensional WAVES model, we observe the effects of attenuation on the data, with a decreasing amplitude of the signals according to time and distance between the source and the receivers as is the case in the experimental data. Amplitudes are not exactly the same of course but similar attenuation

phenomena are observed in both experimental and calculated data, and the time arrivals are also very similar.

Furthermore, we can see how the amplitude spectra of the signals from real, 3D synthetic, and 2D synthetic data with and without attenuation are matching very well (Figures 4.17, 4.19, and 4.30).

In the kernels using the zero offset data (Figures 4.20 and 4.22), we can appreciate the location of the main structures of the WAVES model. There is not much resolution due to the nature of the data (offset zero). However, it is a good indication of what we might see with multi-offset data.

In the last chapter, referring to inversion results we can say that we applied a depth weigthing regularization as in Monteiller et al. [2015] to enhance the perturbations at depth. In addition, we have implemented the inversion of seismic data following a FWI approach of the LSRTM method. We have also been able to inject all the sources at the same time by following a source encoding type approach unlike Feng and Schuster [2017] where the sources are injected by segments. Finally, we have applied an impedance inversion of real seismic data in three dimensions in two steps: first we apply a steepest-descent stage and then we apply a conjugate gradient stage. The results are satisfactory given the difficulty of the problem.

Perspectives

For short-term perspectives we will extend the 2D implementation of the viscoelasticity equations into the 3D UniSolver code and subsequently calculate the kernels of the multi-offset data in the three-dimensional configuration. This will allow us to reproduce the experimental seismograms much better and to obtain much better sensitivity kernels and migration images with clearer interfaces. This is already being developped for WAVES experiment taken as a case study.

We can also try to improve the migration process by levels, following the idea of Marchenko's method [Jia et al., 2017; Wapenaar et al., 2014]. Indeed, we could first perform a classical migration to get an idea of the distribution of the interfaces, and then migrate iteratively depth level after depth level by following the boundaries of the interfaces using absorbing boundaries around the entire computational domain, so it is very likely that the internal and free-surface multiples will also be attenuated this way.

Subsequently, since we are able to compute 3D sensitivity kernels with or without attenuation, it will be possible now to use them for Full Waveform Inversion (FWI) in order to retrieve the properties of complex media in off-shore (elastic-solid coupling) and on-shore contexts. To improve the images drastically, we can imagine to apply the migration and FWI methodologies for 2D dense sensor arrays deployed at the free surface or at the bathymetry level, not only with active sources (at the surface or at the ocean bottom for OBC configurations) but also with teleseismic sources (earthquakes for instance). Indeed, with teleseismic waves, we could compute better migrated images at depth by illuminating the structures from below as

has been done with 1D or 2D dense sensor arrays configurations in different regions of the world for lithospheric imaging (MASE experiment in South-Mexico [Espindola-Carmona et al., 2021], PERUSE survey in Southern Peru, PYROPE and OROGEN surveys in the Pyrennees mountain chain between 2009-2018) or local imaging (MAUPASSACQ 2017/2018 experiment in southwest France). Teleseismic waves are now being implemented also inside UNISOLVER which part is accelerated using new generation processors.

Since active seismic surveys are less and less used those days due mainly to new environment government policies, seismic ambient noise tomography could also be an alternative to help in imaging the shallow structures in the upper crust and making the connection with deeper structures obtained with teleseismic inversion.

Finally, by combining active seismics, ambient noise tomography, teleseismic FWI, and by calculating the sensitivity kernels in presence of attenuation we could improve even further the geological structure seismic properties over a wide range of frequencies not only close to the surface but also at depth.

In addition we can apply an approach as in the Marchenko method, where we perform the inversion by segments in depth. In this way we believe that many of the internal multiples could be mitigated, and as a consequence the results could be improved. We can also try to invert the quality factors Q_P and Q_S in order to which we know always presents a challenge. We can also try to apply our same code to data containing all 3 components (that the S-wave is present), to evaluate if the S-wave velocity models can be improved.

Conclusions (en français)

Ce travail est divisé en deux études de cas relatives à l'imagerie sismique des dômes de sel. La première étude de cas consiste en un modèle géologique à deux dimensions contenant un dôme de sel. Il s'agit d'un modèle synthétique qui provient d'une étude réalisée dans le Golfe du Mexique. La deuxième étude de cas consiste en un modèle expérimental réaliste WAVES développé par le laboratoire LMA à Marseille (France). Ce modèle contient un dôme de sel, des sédiments adjacents et un socle. Pour simuler les propriétés physiques d'un environnement réel, du verre, des argiles et de l'aluminium ont été utilisés respectivement.

Dans les deux cas, nous avons utilisé la méthode RTM basée sur l'adjoint pour calculer les images sismiques. Pour résoudre l'équation d'onde, nous avons utilisé le code parallèle 3D Fortran 90 UNISOLVER, qui utilise la méthode des différences finies du quatrième ordre avec l'approximation des grilles en quinconce et en employant des conditions aux limites absorbantes de type CPML. En outre, afin de résoudre l'équation des ondes viscoélastiques, il était nécessaire d'employer la méthode de "Checkpointing" (i.e avec point de contrôle) au moment du calcul de la condition d'image pour prendre en compte le phénomène physique de l'atténuation des ondes sismiques pour les sources à haute fréquence comme dans l'expérience WAVES (gamme de fréquences de 100-650 KHz). Pour accélérer le temps de calcul, nous avons également utilisé la parallélisation MPI.

L'objectif principal de la première étude de cas est de retrouver les limites de la structure du dôme de sel et d'apprécier les interfaces au-dessus et au-dessous du dôme. Dans ce but, nous avons suivi différentes stratégies dans le calcul des noyaux de sensibilité:

- Pour réduire l'effet des multiples entre la surface libre et la bathymétrie, nous avons appliqué des conditions aux limites au sommet du domaine de calcul (au lieu des conditions de surface libre qui sont généralement appliquées). Ces effets sont étudiés dans des modèles synthétiques bidimensionnels.

- Nous avons normalisé l'amplitude des noyaux de sensitivité par l'énergie de la simulation directe ou de la simulation adjointe. Nous avons appliqué également aux noyaux un gain (normalisation) dépendant de la profondeur au carré afin de mieux faire ressortir les interfaces en profondeur. Ces effets sont étudiés dans des modèles synthétiques bidimensionnels.

- Nous avons appliqué différentes configurations de distribution des sources et des récepteurs: la distribution classique (sources et récepteurs à la surface), la configuration de type OBC (sources à la surface et récepteurs au niveau de la bathymétrie), les sources au niveau de la bathymétrie et les récepteurs en surface, et enfin les sources et les récepteurs au niveau de la bathymétrie. Cette comparaison a été faite en utilisant les modèles synthétiques tridimensionnels.

- Nous utilisons différentes paramétrisations pour calculer les noyaux:, c'est-à-dire des paramétrisations telles que (ρ,λ), ($\ln\rho$,$\ln\lambda$)($\ln\rho$,$\ln\lambda$), ($\ln\rho$, $\ln V_p$), et ($\ln\rho$, $\ln Z_p$).

Nous avons appris qu'il y a une amélioration modérée de la normalisation des noyaux en utilisant l'énergie directe plutôt que l'énergie adjointe, en particulier dans les noyaux liés à l'onde sismique de compression (noyaux K_{Vp} et K_λ), alors que dans les noyaux de densité, la différence est minime. Cela pourrait être lié au fait que les noyaux de vitesse de compression sont plus sensibles à la région de surface des modèles, qui est la zone la plus énergétique des noyaux.

De plus, parmi toutes les configurations d'acquisition que nous utilisons, celle qui donne les meilleurs résultats est celle où nous injectons la source dans les sédiments juste sous la bathymétrie et où les récepteurs sont également situés à cet endroit (voir Figure 3.22).

En outre, en utilisant le "SNR", nous avons étudié l'influence de certains modèles a priori sur les noyaux de sensibilité. Nous avons appris que:

- Les noyaux relatifs à la vitesse de l'onde de compression (K_λ) sont plus sensibles aux plus petites longueurs d'onde du milieu étudié qui sont liées aux structures peu profondes autour du dôme de sel et proches de la bathymétrie, alors que les noyaux de densité K_ρ sont plus sensibles aux plus grandes longueurs d'onde du milieu liées aux structures les plus profondes.

- Les "SNR" des interfaces profondes augmentent à mesure que nous ajoutons des informations sur les modèles a priori pour les noyaux K_ρ. Cependant, dans les noyaux K_λ, c'est le contraire qui se produit (les SNR des noyaux de compression liés aux interfaces les moins profondes et aux interfaces autour du dôme de sel sont plus importants).

L'objectif principal du deuxième cas (expérience WAVES) est d'appliquer tout ce qui a été appris dans le premier cas à des données réelles. En outre, nous avons analysé les effets de l'atténuation (des modèles de corps de Zener sont utilisés ici) sur l'amplitude des données calculées et, plus généralement, nous avons comparé les amplitudes et les formes d'onde des données calculées (avec et sans atténuation) à celles des données réelles.

Nous pouvons observer que dans les figures des propriétés calibrées (Figures 4.14(b) et 4.15(b)), la forme d'onde coïncide dans le temps entre les données synthétisées et les données originales. Cependant, l'amplitude ne coïncide pas dans les dernières arrivées car nous ne considérons pas l'atténuation dans le modèle.

Dans les figures (4.28-4.30) relatives au modèle WAVES bidimensionnel calculé, on observe les effets de l'atténuation sur les données, avec une amplitude décroissante des signaux en fonction du temps et de la distance entre la source et les récepteurs comme c'est le cas dans les données expérimentales. Les amplitudes ne sont pas exactement les mêmes bien sûr, mais des phénomènes d'atténuation similaires sont observés dans les données expérimentales et calculées, et les temps d'arrivée sont également très similaires.

De plus, nous pouvons voir que les spectres d'amplitude des signaux provenant de données réelles, synthétiques 3D et synthétiques 2D avec et sans atténuation se ressemblent très bien (Figures 4.17, 4.19, et 4.30).

Dans les noyaux utilisant les données à décalage nul/"zero offset" (Figures 4.20 et 4.22), nous pouvons apprécier l'emplacement des principales structures du modèle WAVES. Il n'y a pas beaucoup de résolution en raison de la nature des données (offset zéro). Cependant, c'est une bonne indication de ce que nous pourrions voir avec des données à décalage multiple.

Dans le dernier chapitre, en se référant aux résultats d'inversion, nous pouvons dire que nous avons appliqué une régularisation de pesage en profondeur comme dans Monteiller et al. [2015] pour améliorer les perturbations en profondeur. En outre, nous avons mis en œuvre l'inversion des données sismiques en suivant une approche FWI de la méthode LSRTM. Nous avons également pu injecter toutes les sources en même temps en suivant une approche de type encodage des sources contrairement à Feng and Schuster [2017] où les sources sont injectées par segments. Enfin, nous avons appliqué une inversion d'impédance de données sismiques réelles en trois dimensions en deux étapes : nous appliquons d'abord une étape de steepest-descent puis une étape de gradient conjugué. Les résultats sont satisfaisants compte tenu de la difficulté du problème.

Perspectives (en français)

Pour les perspectives à court terme, nous allons étendre l'implémentation 2D des équations de viscoélasticité dans le code 3D UniSolver et ensuite calculer les noyaux pour les données multi-offset dans la configuration tridimensionnelle. Cela nous permettra de reproduire beaucoup mieux les sismogrammes expérimentaux et d'obtenir de bien meilleurs noyaux de sensibilité et des images de migration avec des interfaces plus claires. Ceci est déjà en cours de développement pour l'expérience WAVES prise comme étude de cas.

Nous pouvons également essayer d'améliorer le processus de migration par niveaux, en suivant l'idée de la méthode de Marchenko [Jia et al., 2017; Wapenaar et al., 2014]. En effet, nous pourrions d'abord effectuer une migration classique pour avoir une idée de la distribution des interfaces, puis migrer itérativement niveau de profondeur après niveau de profondeur en suivant les limites des interfaces en utilisant des limites absorbantes autour de l'ensemble du domaine de calcul. Il est donc très probable que les multiples internes et de surface libre soient également atténués de cette manière.

Par la suite, puisque nous sommes capables de calculer des noyaux de sensibilité 3D avec ou sans atténuation, il sera désormais possible de les utiliser pour l'inversion de la forme d'onde complète (FWI) afin de récupérer les propriétés de milieux complexes dans des contextes off-shore (couplage élastique-solide) et on-shore. Pour améliorer drastiquement les images, on peut imaginer d'appliquer les méthodologies de migration et de FWI pour des réseaux de capteurs denses 2D déployés à la surface libre ou au niveau de la bathymétrie, non seulement avec des sources actives (à la surface ou au fond de l'océan pour les configurations OBC) mais aussi

avec des sources télésismiques (séismes par exemple). En effet, avec les ondes télésismiques, nous pourrions calculer de meilleures images migrées en profondeur en illuminant les structures par le bas, comme cela a été fait avec des configurations de réseaux de capteurs denses 1D ou 2D dans différentes régions du monde pour l'imagerie lithosphérique (expérience MASE dans le sud du Mexique [Espindola-Carmona et al., 2021], campagne sismique PERUSE dans le sud du Pérou, campagnes PYROPE et OROGEN dans la chaîne des Pyrénées entre 2009-2018) ou l'imagerie locale (expérience MAUPASSACQ 2017/2018 dans le sud-ouest de la France). Les ondes télésismiques sont maintenant mises en œuvre également dans UNISOLVER, dont une partie est accélérée par des processeurs de nouvelle génération.

Puisque les études sismiques actives sont de moins en moins utilisées de nos jours, principalement en raison des nouvelles politiques gouvernementales en matière d'environnement, la tomographie sismique du bruit ambiant pourrait également être une alternative pour aider à l'imagerie des structures peu profondes de la croûte supérieure et faire le lien avec les structures plus profondes obtenues par inversion télésismique.

Enfin, en combinant la sismique active, la tomographie du bruit ambiant, la FWI télésismique, et en calculant les noyaux de sensibilité en présence d'atténuation, nous pourrions améliorer encore plus les propriétés sismiques des structures géologiques sur une large gamme de fréquences, non seulement près de la surface mais aussi en profondeur.

En outre, nous pouvons appliquer une approche comme dans la méthode Marchenko, où nous effectuons l'inversion par segments en profondeur. De cette façon, nous pensons que de nombreux multiples internes pourraient être atténués et que les résultats pourraient être améliorés. Nous pouvons également essayer d'inverser les facteurs de qualité Q_P et Q_S dans l'ordre, ce qui, nous le savons, représente toujours un défi. Nous pouvons également essayer d'appliquer notre même code à des données contenant les 3 composantes (que l'onde S est présente), pour évaluer si les modèles de vitesse de l'onde S peuvent être améliorés.

Articles published by the author

Ortiz-Alemán, J.C., Abreu-Torres, J., Orozco-del-Castillo, M.G. et al. Pattern recognition applied to attenuation of multiples in subsalt Imaging. Pure Appl. Geophys. 176, 2411–2424 (2019). https://doi.org/10.1007/s00024-019-02135-1

J. Abreu-Torres, R. Martin, J.C Ortiz-Alemán, J. Darrozes, J. Urrutia-Fucugauchi. Salt tectonic using RTM imaging and sensitivity kernel wavelength analysis. Surveys in Geophysics (2022), 10.1007/s10712-021-09689-7

Appendix A

Principal subroutines of UniSolver

In the next lines I show the principal Unisolver subroutine in which I participate. This subroutine contains an external loop over the frames (checkpointing technique) and an internal loop over the stages in the RTM that we describe in the flowchart of Figure 1.15: Compute of the real data (forward problem over the true model, this stage is calculated in synthetic cases), compute of the predicted data (forward problem over the background model), and compute of the adjoint problem. The principal subroutines in which I made changes are:

- UniSolver.F90. Is the main program. In this code I add many variables and parameters, the big LSRTM loop, and the big loop over the separated sources kernels. We show a part of it in this appendix. This programs calls the subroutine SeismicSolver.F90

- SeismicSolver.F90. Is the subroutine that contains the iteration over the principal stages of the RTM method: Forward problem and adjoint problem. This subroutine also contains the iterations over the time. I add the calculation of the time delay (for the source encoding) and some modification related to the source and seismograms. This subroutine calls many subroutines contained in callCompute.F90

- callCompute.F90: This subroutine contains the communication between processors (I compute the communication for the 4th order finite differences scheme). The subroutine also contains the computation of the forward (callComputeForwardTime) and adjoint (callComputeCheckpointingAdjoint) problem. I modify some things of these two last subroutines related to seismograms and the source. This subroutine calls many important subroutines as: addSources.f90, computeVelocity.f90, computeStressSigma.f90, and computeKernels.f90

- addSources.f90: This subroutine calculates the temporal source function, or it reads this function from an external file. I add the options of injecting the source in the velocities (elastic), or in the stresses (acoustic). I also add the option to inject the source used in the WAVES project, which is simulated by a disk of 253 sources (transducer).

- computeVelocity.F90: This subroutine contains the calculation of the velocity fields in

each iteration. I add the calculation of the 4th order finite differences velocity fields for the forward and adjoint problem of the elastic wave equation.

- computeStressSigma.F90: This subroutine contains the calculation of the stress fields in each iteration. I add the calculation of the 4th order finite differences stress fields of the forward and adjoint problems for the elastic and viscoelastic wave equation.

- computeKernels.f90: This subroutine contains the computation of the sensitivity kernels, in which I upgrade to the 4th order the finite differences computation of the kernels. I also add the computation of the parametrizations (ρ, Z_P, Z_S), and the forward and adjoint energies.

The next lines are contained in the subroutine SeismicSolver.F90

```
subroutine seismic_solver_CPU(isour)
use simulation_parameters
use constant_parameters
use mpi_parameters
use simulation_variables
implicit none
integer :: irec, isour, flag_ker, ipass_inv, iter_inv
integer :: i,j,k,it, it_fr, it_sub, ipass, it1, it_temp, jend
kmin = 1
kmax = NZ_LOCAL
kmax = NZ_LOCAL - NPOINTS_PML
if(USE_PML_YMAX) then
   jmax = NY - NPOINTS_PML
else
   jmax = NY
endif
if(inversion)then
   ipass_begin = ipass_inv
end if
do ipass = ipass_begin, npass
   ! erase main arrays
   call resetMainSeismicArrays(ipass)
   ! Add inclusion at ipass 1
   if(add_inclusion .and. ipass == 1) then
      call computeInclusion()
      if(rank == rank_init) then
         call display_inclusion_information()
      endif
```

```
    endif
    ! Reset model for prior pass
    if(ipass == 2) then
       call reset_Lame_params()
       if(rank == rank_init) then
          call display_prior_information()
       endif
    endif
    !!Compute PML coefficients
    call compute_PML()
    !— beginning of time loop
    do it_fr = 1, NFRAMES
    !Save a frame
       if(ipass .eq. 2) then
          call save_frame(it_fr)
       endif
       if(ipass .eq. 3) then
          call ComputeCheckpointAdjoint(it_fr, ipass, isour, iter_inv)
       else
          call ComputeForwardTime(it_fr, ipass, isour)
       endif
    ! — end of loop over frames
    end do
end do
end subroutine
```

Appendix B

Separated sources case

This excerpt of the UniSolver program, contains the big loop over the sources to construct the sensitivity kernels of separated sources. These lines are found in the main program UniSolver.F90:

```
elseif (SOURCE_TYPE == 2) then
   kernel_rho_sepa(:,:,:) = ZERO
   kernelp_rho_sepa(:,:,:) = ZERO
   kernel_vp_sepa(:,:,:) = ZERO
   kernel_vs_sepa(:,:,:) = ZERO
   kernel_mu_sepa(:,:,:) = ZERO
   kernel_lambda_sepa(:,:,:) = ZERO
   do isour = 1, NSOURCE
      if (rank == rank_init)then
         print*, 'source =', isour
      end if
      call seismic_solver_cpu(isour)
      kernelp_rho_sepa(:,:,:) = kernelp_rho_sepa(:,:,:) + kernelp_rho(:,:,:)
      kernel_vp_sepa(:,:,:) = kernel_vp_sepa(:,:,:) + kernel_vp(:,:,:)
      kernel_vs_sepa(:,:,:) = kernel_vs_sepa(:,:,:) + kernel_vs(:,:,:)
      kernel_rho_sepa(:,:,:) = kernel_rho_sepa(:,:,:) + kernel_rho(:,:,:)
      kernel_lambda_sepa(:,:,:) = kernel_lambda_sepa(:,:,:) + kernel_lambda(:,:,:)
      kernel_mu_sepa(:,:,:) = kernel_mu_sepa(:,:,:) + kernel_mu(:,:,:)
      sisvx(:,:) = ZERO
      sisvy(:,:) = ZERO
      sisvz(:,:) = ZERO
      sis_sigmaxx(:, :) = ZERO
      sis_sigmayy(:, :) = ZERO
      sis_sigmazz(:, :) = ZERO
   end do
```

end if

Appendix C

Fourth-order and visco-elastic implementation

In this appendix I present a part of the Unisolver code where I implemented the fourth-order finite differences schema and the visco-elastic computation of the relaxation mechanisms. These lines are found in the subroutine computeStressSigma.f90.

```
do k = k2begin, NZ_LOCAL
        kglobal = k + offset_k
        do j = 2, NY
           do i = 1, NX - 1
              value_dvx_dx = (27.d0*vx_i(i+1, j, k) - 27.d0*vx_i(i ,j, k) -vx_i(i+2, j, k) +
              vx_i(i-1 ,j ,k)) * ONE_OVER_DELTAX/24.d0


              value_dvy_dy = (27.d0*vy_i(i, j, k) - 27.d0*vy_i(i, j-1, k) -vy_i(i, j+1, k)
              + vy_i(i, j-2, k)) * ONE_OVER_DELTAY/24.d0


              value_dvz_dz = (27.d0*vz_i(i, j, k) - 27.d0*vz_i(i, j, k-1) -vz_i(i, j, k+1)
              + vz_i(i, j, k-2)) * ONE_OVER_DELTAZ/24.d0


              memory_dvx_dx(i, j, k) = b_x_half(i) * memory_dvx_dx(i, j, k) + a_x_half(i)
              * value_dvx_dx


              memory_dvy_dy(i, j, k) = b_y(j) * memory_dvy_dy(i, j, k) + a_y(j)
              * value_dvy_dy
```

```
        memory_dvz_dz(i, j, k) = b_z(kglobal) * memory_dvz_dz(i, j, k) + a_z(kglobal)
        * value_dvz_dz
        value_dvx_dx = value_dvx_dx / K_x_half(i) + memory_dvx_dx(i, j, k)
        value_dvy_dy = value_dvy_dy / K_y(j) + memory_dvy_dy(i, j, k)
        value_dvz_dz = value_dvz_dz / K_z(kglobal) + memory_dvz_dz(i, j, k)
        div = value_dvx_dx + value_dvy_dy + value_dvz_dz


        !Evolution e1
        sum_e1 = ZERO
        do i_sls = 1, N_SLS
           tauinv = -inv_tau_sigma_nu1_grd(i,j,k,i_sls)
           Un = e1(i,j,k,i_sls)
           Sn = div * phi_nu1_grd(i,j,k,i_sls)
           tauinvUn = tauinv * Un
           Unp1 = (Un + deltat*(Sn+0.5d0*tauinvUn))/(1.d0-deltat*0.5d0*tauinv)
           e1(i,j,k,i_sls) = Unp1
           sum_e1 = sum_e1 + e1(i,j,k,i_sls)
        end do


        !Evolution e11
        sum_e11 = ZERO
        do i_sls = 1, N_SLS
           tauinv = -inv_tau_sigma_nu2_grd(i,j,k,i_sls)
           Un = e11(i,j,k,i_sls)
           Sn = (value_dvx_dx - div/3) * phi_nu2_grd(i,j,k,i_sls)
           tauinvUn = tauinv * Un
           Unp1 = (Un + deltat*(Sn+0.5d0*tauinvUn))/(1.d0-deltat*0.5d0*tauinv)
           e11(i,j,k,i_sls) = Unp1
           sum_e11 = sum_e11 + e11(i,j,k,i_sls)
        end do
     end do
  end do
end do
```

Appendix D

Finite elements method.

Variational form of the wave equation.

In a general way the finite elements method consist in discretizing a domain in several sub-domains in which the wave equation is approximated by its variational form (see Lysmer and Drake [1972], Reddy [2010], Zienkiewicz et al. [2005]). Each sub-domain is called a finite element and the intersections between them are the nodes. One of the characteristics of the discretization in the finite elements method is that the elements do not have to be the same: that is why they can be adapted to very complex domains. In figure D.1, we can see an example of a discretization used in the finite elements method.

To express in a general way the variational form of the wave equation, we start from equations 2.32, which for a bounded domain Ω are rewritten as follows:

$$\begin{aligned} \nabla \cdot \boldsymbol{\tau} + \boldsymbol{f} &= \rho \boldsymbol{a} \text{ in } \Omega, \\ \boldsymbol{\tau} \cdot \overrightarrow{n} &= \boldsymbol{T}^d \text{ on } \partial\Omega, \end{aligned} \tag{D.1}$$

where $\boldsymbol{\tau}$ is the stress tensor, $\boldsymbol{a}$, is the acceleration vector, $\boldsymbol{f}$ is the external force field, $\overrightarrow{n}$ is the vector normal to the surface, and $\boldsymbol{T}_d$ is the vector force of the surface. The free surface conditions must be satisfied as follows:

$$\boldsymbol{\tau} \cdot \overrightarrow{n} = 0 \text{ on } \Gamma_s, \tag{D.2}$$

where Γ_s is the free surface.

Integrating the conservation equation of the momentum using any displacement (or velocity) test vector $\hat{\boldsymbol{u}}$, we obtain:

$$\int_\Omega \nabla \cdot \boldsymbol{\tau} \hat{\boldsymbol{u}} \mathrm{d}\Omega + \int_\Omega \boldsymbol{f} \hat{\boldsymbol{u}} \mathrm{d}\Omega = \int_\Omega \rho \boldsymbol{a} \hat{\boldsymbol{u}} \mathrm{d}\Omega \tag{D.3}$$

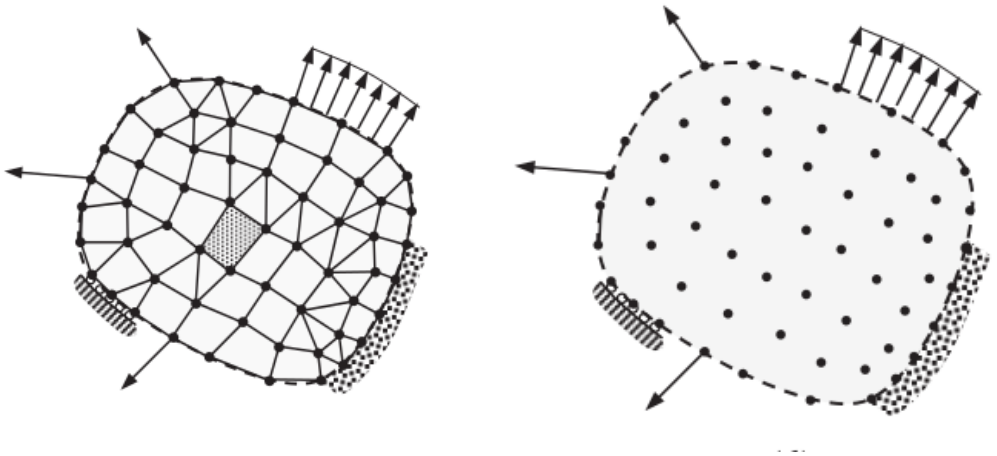

(a) (b)

Figure D.1. Discretization of domain for the finite elements method. (a)Representation of the discretization of a domain by a collection of triangles and quadrilateral elements. (b)Representation of the discretization of a domain by a collection of nodes. Both figures taken from Reddy [2010].

Integrating by parts the first term we have:

$$-\int_{\Omega} \boldsymbol{\tau} : \boldsymbol{\epsilon}(\hat{\boldsymbol{u}})\mathrm{d}\Omega + \int_{\Omega} \boldsymbol{f}\hat{\boldsymbol{u}}\mathrm{d}\Omega + \int_{\partial\Omega} \boldsymbol{T^d}\hat{\boldsymbol{u}}\mathrm{d}\partial\Omega + \int_{\Gamma_s} \boldsymbol{\tau}\cdot\overrightarrow{n}\hat{\boldsymbol{u}}\mathrm{d}\Gamma_s = \int_{\Omega} \rho\boldsymbol{a}\hat{\boldsymbol{u}}\mathrm{d}\Omega, \tag{D.4}$$

where $\boldsymbol{\epsilon}(\hat{\boldsymbol{u}})$ is the strain tensor of the test vector $\hat{\boldsymbol{u}}$, and the operator ":" denotes the contracted product of two tensors.

In the particular case of an isotropic medium, the relation between stresses and strains is given by the Hooke law as follows:

$$\boldsymbol{\tau} = \boldsymbol{C} : \boldsymbol{\epsilon}, \tag{D.5}$$

where $\boldsymbol{C}$ represents the fourth order elastic tensor. We can write the variational form of the problem by substituting D.5 in D.4 for any displacement $\hat{\boldsymbol{u}} \in \mathcal{S}$ as follows:

$$\begin{aligned} -\int_{\Omega} \boldsymbol{\epsilon}(\boldsymbol{u}) : \boldsymbol{C} : \boldsymbol{\epsilon}(\hat{\boldsymbol{u}})\mathrm{d}\Omega + \int_{\Omega} \boldsymbol{f}\hat{\boldsymbol{u}}\mathrm{d}\Omega + \int_{\partial\Omega} \boldsymbol{T^d}\hat{\boldsymbol{u}}\mathrm{d}\partial\Omega \\ + \int_{\Gamma_s} \boldsymbol{\tau}\cdot\overrightarrow{n}\hat{\boldsymbol{u}}\mathrm{d}\Gamma_s - \int_{\Omega} \rho\frac{\partial^2\boldsymbol{u}}{\partial t^2}\hat{\boldsymbol{u}}\mathrm{d}\Omega = 0, \end{aligned} \tag{D.6}$$

where $\mathcal{S}$ is the set of displacements with the following initial conditions:

$$\begin{aligned} \boldsymbol{u}(\boldsymbol{x}, 0) &= \boldsymbol{u_0} \\ \boldsymbol{v}(\boldsymbol{x}, 0) &= \boldsymbol{v_0}, \end{aligned} \tag{D.7}$$

with $\boldsymbol{v}$ being the velocity vector.

We will now briefly discuss the solution of the spectral element methods, which are a

variant of the finite element methods. These methods were proposed in the 1980s for fluid mechanics application [Patera, 1984]. In these methods the order of the Lagrange interpolation polynomials are generally high [Casarotti et al., 2008; Faccioli et al., 1997; Komatitsch and Vilotte, 1998]. The solution consists in approximating the solution of the variational wave equation using polynomial functions of the Legendre type, and using quadratic numeric rules over the Gauss-Lobatto-Legendre points.

According to Komatitsch et al. [2009], equation D.6 is solved in hexahedral mesh to better adapt to geological discontinuities. The unknown wavefields is expressed in terms of Lagrange polynomials on Gauss-Lobatto-Legendre integration points, which will result in a diagonal matrix. We can express the equation D.6 in matrix form as follows:

$$M\ddot{d} + Kd = F, \tag{D.8}$$

where d is the displacement vector, M is the diagonal matrix, k is the stiffness matrix, F is the source term, the double dot over d denotes the second derivative with respect to time.

a) Spatial discretization of the spectral element methods.

To numerically solve equation D.6, the computational domain Ω is divided into a number of non-overlaping elements Ω_e, $e = 1, ..., n_e$, with n_e being the total number of elements (see Figure D.2.

According to Komatitsch and Tromp [1999], each hexahedral element Ω_e can be mapped to a reference cube within which the points are defined by the vector $\boldsymbol{\xi} = (\xi, \eta, \zeta)$, where $-1 \leq \xi \leq 1$, $-1 \leq \eta \leq 1$, $-1 \leq \zeta \leq 1$. The mapping between the hexahedral elements of Ω_e and the reference cube are given by:

$$\boldsymbol{x}(\boldsymbol{\xi}) = \sum_{a=1}^{n_a} N_a(\boldsymbol{\xi})\boldsymbol{x}_a, \tag{D.9}$$

where $\boldsymbol{x}_a$ are the control nodes in which each element volume is defined, n_a is the number of control nodes and $N_a(\boldsymbol{\xi})$ are the shape functions. We can see in Figure D.3 a 2D transformation between the Gauss-Lobatto-Legendre collocation points and a transformed element Ω_e.

The infinitesimal volume $dx\ dy\ dz$ within a given element Ω_e is related by an element of volume $d\xi\ d\eta\ d\zeta$ of the reference cube by:

$$dx\ dy\ dz = J_e\ d\xi\ d\eta\ d\zeta, \tag{D.10}$$

where J_e is the Jacobian of the transformation defined by:

$$J_e = \frac{\partial(x, y, x)}{\partial(\xi, \eta, \zeta)} \tag{D.11}$$

In the calculation of the Jacobian J_e, we need to know the partial derivative $\partial\boldsymbol{x}/\partial\boldsymbol{\xi}$, obtained

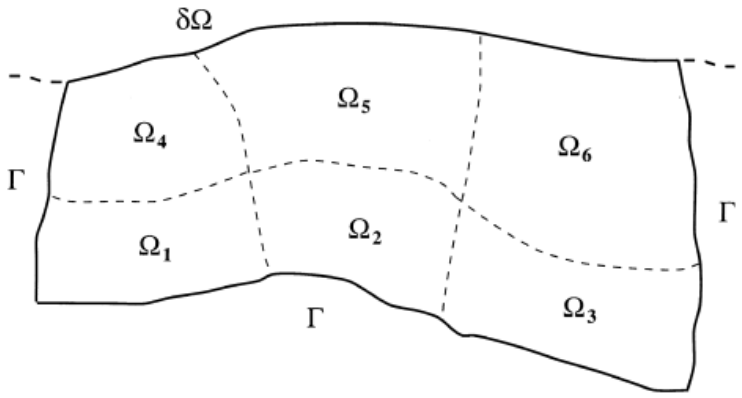

Figure D.2. Example of a discretization in the Finite Element method. Note that the elements are not necessarily equal. Therefore, they could adapt to the edges of the model. Taken from Komatitsch and Tromp [1999].

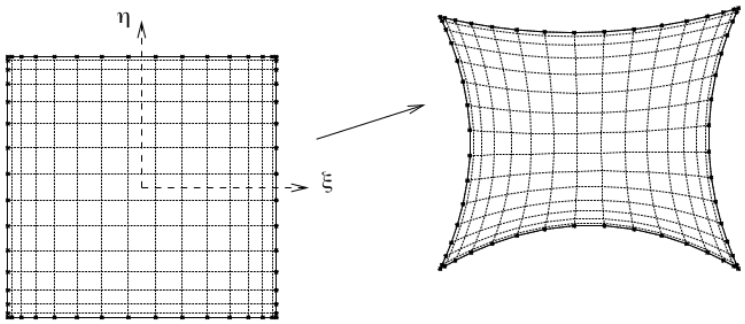

Figure D.3. Example of a 2D Gauss-Lobatto-Legendre grid in the reference domain. Taken from Komatitsch [1997].

by:

$$\frac{\partial \boldsymbol{x}}{\partial \boldsymbol{\xi}} = \sum_{a=1}^{n_a} \frac{\partial N_a}{\partial \boldsymbol{\xi}} \boldsymbol{x}_a \tag{D.12}$$

The partial derivatives of the shape functions are determined analytically from the Lagrange polynomials and their derivatives. The elements of the domain must be constructed in such a way that the Jacobian J_e never vanishes, which poses great constraints on the mesh generation.

b) Other methods based on the weak form.

In addition to the finite ans spectral element methods, we can also find the following methods that are based on the weak formulation of the wave equation:

- Galerkin discontinuous method: This method uses very varied approach spaces. It is different from the finite element method which uses Galerkin-type approach, in which the base and interpolation functions are identical. For more information, we refer to Dumbser and Käser [2006], and de la Puente et al. [2007].

- Boundary element method: This method is used for the study of site effects. This method

is based on the theory of boundary integral equations. This theory is based on the principle of equivalence of surfaces, where only the boundary of the computational domain is discretized. For more information see Bonnet [1999] and Dangla et al. [2005].

Appendix E

Other results from chapter 3

In this appendix we decided to place some results that were present in chapter 3. These results are linked to the a priori models that were previously M2 and M3, and are now called MA1 and MA2 in this appendix. These models contain information from the dome (MA1) and from the dome and surrounding interfaces (MA2) respectively. The reason we moved these results to this appendix is because the MA1 and MA2 models present information from the dome and surrounding interfaces, and by applying the residual between the observed and synthesized data as an adjoint source, some of the interfaces that appear as information in the a priori model would not appear in the sensitivity kernels. In these results we inject the observed data as an adjoint source to be able to observe all the interfaces that compose the models.

E.1 Sensitivity kernels for the a priori model MA1, injecting simultaneous sources.

After setting the values of the salt dome parameters (Figures E.1(a) and E.1(b)), we present in Figures E.2 the logarithm kernels $K_{\ln\lambda}$, $K_{\ln\rho}$, K_{lnVp}, $K''_{ln\rho}$, and K_{lnZp}, for the parametrizations $(\ln\rho, \ln\lambda)$, $(\ln\rho, \ln V_p)$, $(\ln\rho, \ln Z_p)$

We can see a considerable improvement at the deep interface 9, which corresponds to the basement, with respect to Figures 3.10. We can also appreciate the upper interface 3, 6 and the salt dome (which was set in the a priori model). We can see that all kernels (i.e with the different log-parametrizations) give almost the same information.

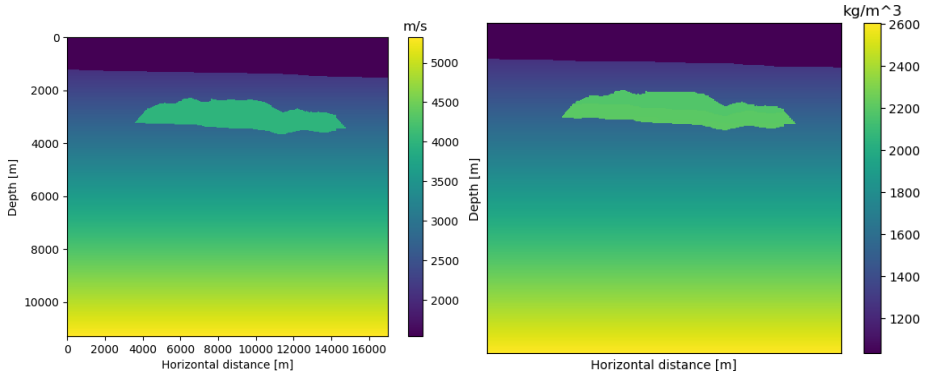

(a) P velocity model MA1 (b) Density model MA1

(c) P velocity MA2 (d) Density model MA2

Figure E.1. Figures a and b represent the a priori models "MA1" used after the first migration, where we interpreted the presence of a salt dome and its boundaries. In Figures c and d, we set the geology around the salt dome where we can see some ambiguities between velocity and density models (a priori model "MA2").

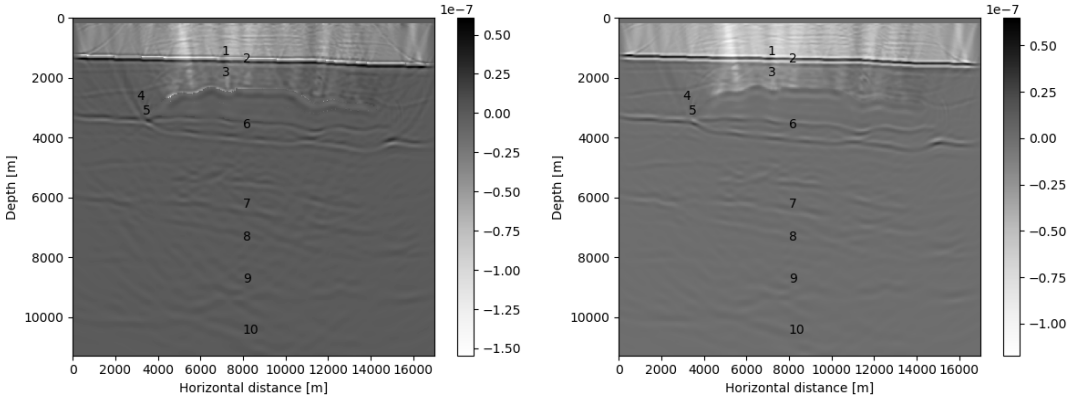

(a) Kernel $K_{\ln\lambda}$.

(b) Kernel $K_{\ln\rho}$.

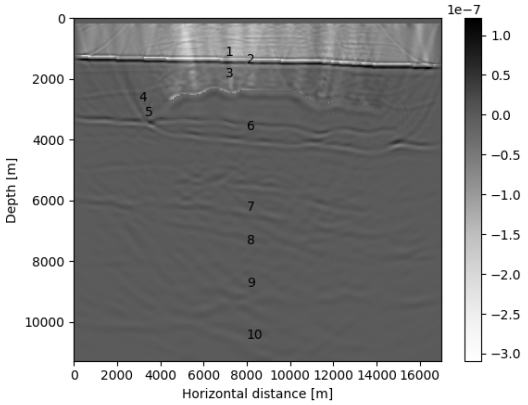

(c) Kernel $K_{\ln Vp}$.

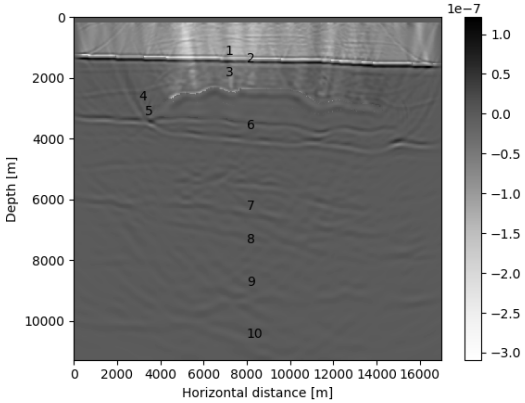

(d) Kernel $K_{\ln Zp}$.

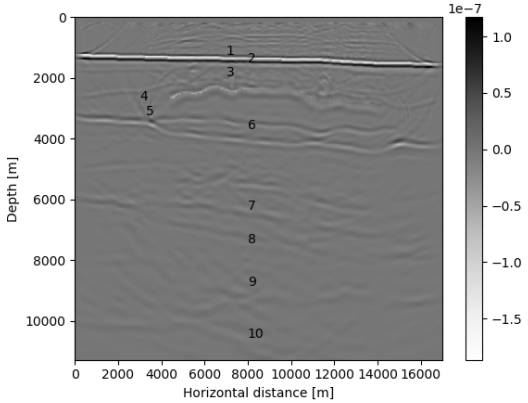

(e) Kernel $K''_{\ln\rho}$.

Figure E.2. Kernels computed using the prior model MA1, applying the case 2 with $\boldsymbol{f^{\dagger}}$=$\boldsymbol{d_{obs}}$.. Figures (a,b): Kernels $K_{\ln\lambda}$ and $K_{\ln\rho}$ for the parametrization ($\ln\rho$, $\ln\lambda$). Figure (c): kernel $K_{\ln V_p}$ for the parametrization ($\ln\rho, \ln V_p$. And figures (d,e): kernels $K''_{\ln\rho}$ and $K_{\ln Z_p}$ for the parametrization ($\ln\rho$, $\ln Z_p$). To compute the image we used absorbing boundary conditions at the top of the computational domain. The simultaneous sources are injected below the surface.

E.2 Sensitivity kernels for the a priori model MA1, injecting separated sources.

In Figures E.3 we now show the kernels using the a priori model defined by a depth-gradient function and setting the values of the salt dome (figures E.1(a) and E.1(b)), we injected 50 separated sources as in the previous section. We applied the same gain as in the previous section.

We can appreciate that artifacts close to the upper surface attributed to in-between source interferences are eliminated. A consequence of this fact is that the interfaces are seen more clearly: the interface 3, the salt dome, the interfaces 6 (below the base of the salt dome), 9 and 10 (the basement). However, there exist some ambiguities in the depth of some interfaces.

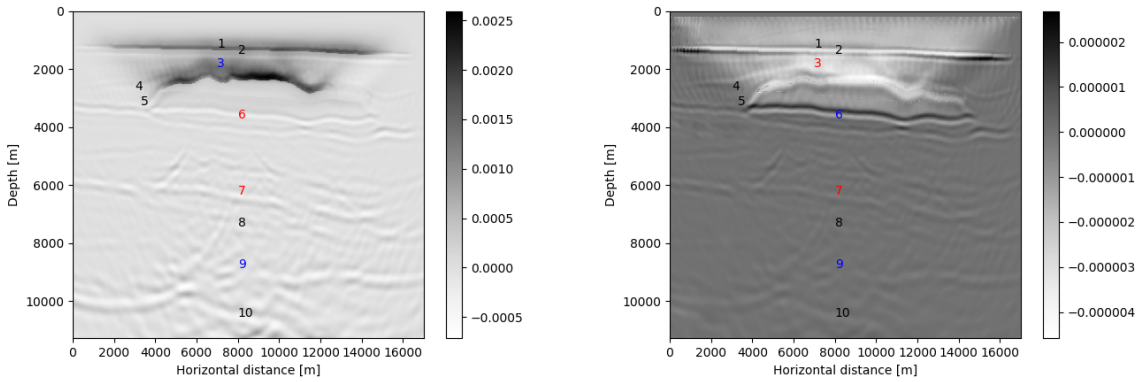

(a) Kernel K_ρ. (b) Kernel K_λ.

Figure E.3. Kernels K_λ and K_ρ using the model M2 as the a priori model (Figures E.1(a) and E.1(b)), applying the case 2 with $f^\dagger = d_{obs}$. These kernels were obtained using 50 separated sources. To compute the image we used absorbing boundary conditions at the top of the computational domain. The sources and receivers are located below the surface.

E.3 Sensitivity kernels for the a priori model MA2, injecting separated sources.

In Figures E.4 we show the separated-sources kernels using the a priori models after setting the geology around the salt dome (figures E.1(c) and E.1(d)). We can see good definition of the upper interfaces (3, 5, 6, and the salt dome). Furthermore, we can moderately see the deeper interfaces 7 and 9. However, physical noise attributed to internal multiples is still present below the salt dome and the basement (interface 9).

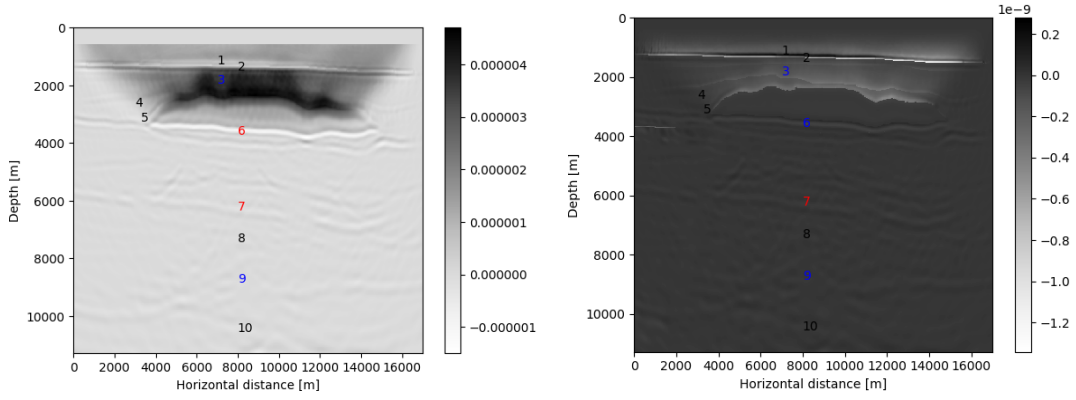

(a) Kernel K_ρ. (b) Kernel K_λ.

Figure E.4. Kernels K_λ and K_ρ using the model MA2 as the a priori model (Figures E.1(c) and E.1(d)), applying the case 2 with $f^\dagger = d_{obs}$. These kernels were obtained injecting 50 separated sources. To compute the image we used absorbing boundary conditions at the top of the computational domain. The sources and receivers are located below the surface.

Appendix F

F.1 Case 3: Sensitivity kernels using absorbing-boundary conditions to compute the forward and adjoint problems. The observed data were computed using also absorbing-boundary conditions.

In this subsection of the appendix, the adjoint source is injected as the residual between the observed and synthetic data ($f^{\dagger} = d_{obs} - d_{syn}$). In Figures F.1 and F.2 we show the kernels K_ρ and K_λ calculated with the models M1 and M2 as the a priori models, using the computational domain shown in Figure 3.6(b). The observed data were computed using the computational domain of Figure 3.6(b) (free-surface multiples are attenuated). The imaging conditions used to compute the kernels is described in equations 3.36. We observe that only the bathymetry is well retrieved. This fact could be attributed to the imaging condition 3.36, which consists in a difference between two similar terms, and a large part of the signal attributed to the interfaces may be cancelled.

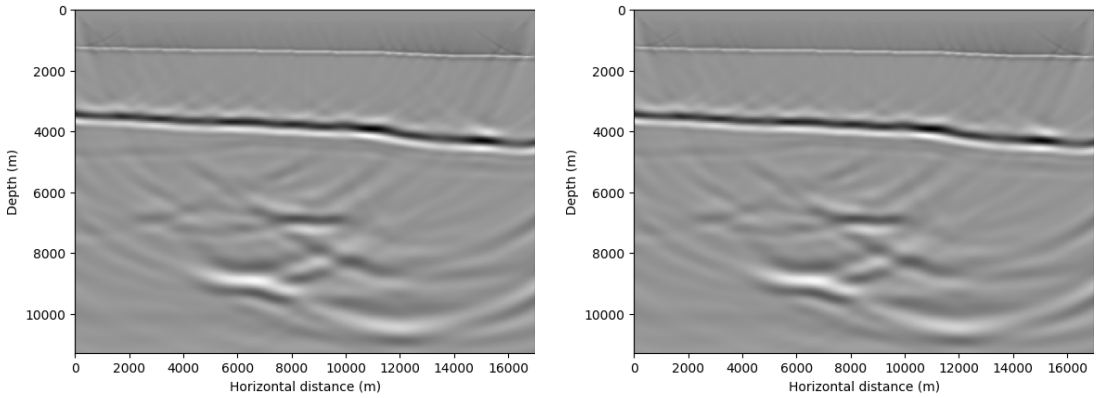

(a) Kernel K_ρ.

(b) Kernel K_λ.

Figure F.1. Kernels K_λ and K_ρ using absorbing-boundary conditions to compute the forward and adjoint problems using the model M1 as the a priori model, applying the case 3 with $f^{\dagger}=d_{cal}-d_{obs}$. The observed data are computed using absorbing-boundary conditions at the top of the computational domain (free-surface multiples are attenuated). The sources and receivers are located at the top of the water.

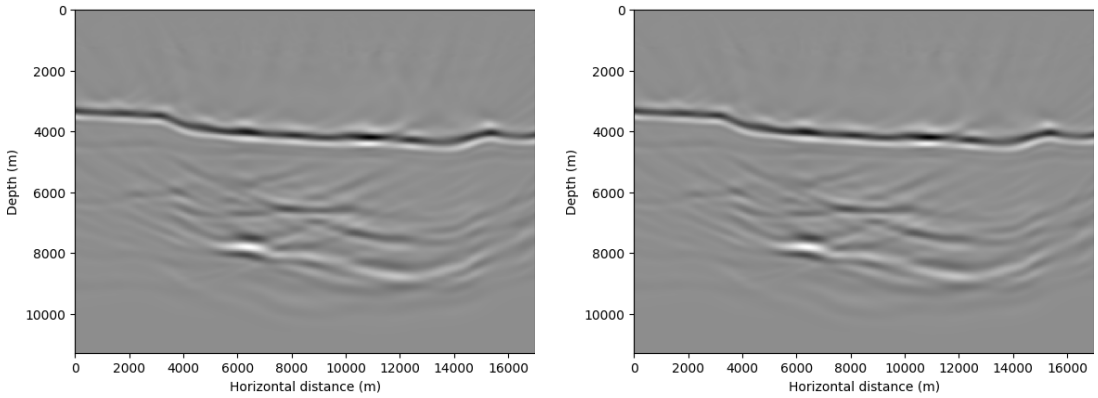

(a) Kernel K_ρ.

(b) Kernel K_λ.

Figure F.2. Kernels K_λ and K_ρ using absorbing-boundary conditions to compute the forward and adjoint problems using the model M2 as the a priori model, applying the case 3 with $f^\dagger = d_{cal} - d_{obs}$. The observed data are computed using absorbing-boundary conditions at the top of the computational domain (free-surface multiples are attenuated). The sources and receivers are located at the top of the water.

Bibliography

Aghamiry, H., Gholami, A., and Operto, S. (2021). Full waveform inversion by proximal newton method using adaptive regularization. Geophysical Journal International, 224(1):169–180.

Alford, R., Kelly, K., and Boore, D. M. (1974). Accuracy of finite-difference modeling of the acoustic wave equation. Geophysics, 39(6):834–842.

Asnaashari, A., Brossier, R., Garambois, S., Audebert, F., Thore, P., and Virieux, J. (2013). Regularized seismic full waveform inversion with prior model information. Geophysics, 78(2):R25–R36.

Baysal, E., Kosloff, D. D., and Sherwood, J. W. (1983). Reverse time migration. Geophysics, 48(11):1514–1524.

Behura, J. and Forghani, F. (2012). A practical approach to prediction of internal multiples and ghosts. In SEG Technical Program Expanded Abstracts 2012, pages 1–5. Society of Exploration Geophysicists.

Belenitskaya, G. (2016). Salt tectonics at the margins of young oceans. Geotectonics, 50(3):244–256.

Berkhout, A. and Verschuur, D. (2006). Imaging of multiple reflections. Geophysics, 71(4):SI209–SI220.

Bevc, D. (1997). Imaging complex structures with semirecursive kirchhoff migration. Geophysics, 62(2):577–588.

Blanc, E., Komatitsch, D., Chaljub, E., Lombard, B., and Xie, Z. (2016). Highly accurate stability-preserving optimization of the zener viscoelastic model, with application to wave propagation in the presence of strong attenuation. Geophysical Supplements to the Monthly Notices of the Royal Astronomical Society, 205(1):427–439.

Bonnet, M. (1999). Boundary integral equation methods for solids and fluids. Meccanica, 34(4):301–302.

Buehnemann, J., Henke, C. H., Mueller, C., Krieger, M. H., Zerilli, A., and Strack, K. M. (2002). Bringing complex salt structures into focus—a novel integrated approach. In SEG Technical Program Expanded Abstracts 2002, pages 446–449. Society of Exploration Geophysicists.

Cao, J., Brossier, R., and Metivier, L. (2021). 3d fluid-solid coupled full-waveform inversion for ocean-bottom seismic data. In First International Meeting for Applied Geoscience & Energy, pages 832–836. Society of Exploration Geophysicists.

Capdeville, Y., Gung, Y., and Romanowicz, B. (2005). Towards global earth tomography using the spectral element method: a technique based on source stacking. Geophysical Journal International, 162(2):541–554.

Carcione, J. M. (1993). Seismic modeling in viscoelastic media. Geophysics, 58(1):110–120.

Carcione, J. M. (2007). Wave fields in real media: Wave propagation in anisotropic, anelastic, porous and electromagnetic media. Elsevier.

Casarotti, E., Stupazzini, M., Lee, S. J., Komatitsch, D., Piersanti, A., and Tromp, J. (2008). Cubit and seismic wave propagation based upon the spectral-element method: An advanced unstructured mesher for complex 3d geological media. In Proceedings of the 16th international meshing roundtable, pages 579–597. Springer.

Castellanos, C., Métivier, L., Operto, S., Brossier, R., and Virieux, J. (2015). Fast full waveform inversion with source encoding and second-order optimization methods. Geophysical Journal International, 200(2):720–744.

Chang, W.-F. and McMechan, G. A. (1986). Reverse-time migration of offset vertical seismic profiling data using the excitation-time imaging condition. Geophysics, 51(1):67–84.

Chattopadhyay, S. and McMechan, G. A. (2008). Imaging conditions for prestack reverse-time migration. Geophysics, 73(3):S81–S89.

Claerbout, J. F. (1971). Toward a unified theory of reflector mapping. Geophysics, 36(3):467–481.

Claerbout, J. F., Green, C., and Green, I. (1985). Imaging the earth's interior, volume 6. Blackwell scientific publications Oxford.

Cooper, J. K., Lawton, D. C., and Margrave, G. F. (2010). The wedge model revisited: A physical modeling experiment. Geophysics, 75(2):T15–T21.

Dai, W., Boonyasiriwat, C., and Schuster, G. T. (2010). 3d multi-source least-squares reverse time migration. In SEG Technical Program Expanded Abstracts 2010, pages 3120–3124. Society of Exploration Geophysicists.

Dai, W., Fowler, P., and Schuster, G. T. (2012). Multi-source least-squares reverse time migration. Geophysical Prospecting, 60(4-Simultaneous Source Methods for Seismic Data):681–695.

Dai, W. and Schuster, G. (2013a). Reverse time migration of prism waves for salt flank delineation: 83rd annual international meeting, seg, expanded abstracts, 3861–3865. Abstract.

Dai, W. and Schuster, G. T. (2013b). Plane-wave least-squares reverse-time migration. Geophysics, 78(4):S165–S177.

Dai, W., Xu, Z., and Coates, R. (2015). Least-squares reverse-time migration for visco-acoustic media. In 2015 SEG Annual Meeting. OnePetro.

Dangla, P., Semblat, J.-F., Xiao, H., and Delépine, N. (2005). A simple and efficient regularization method for 3d bem: application to frequency-domain elastodynamics. Bulletin of the Seismological Society of America, 95(5):1916–1927.

de la Puente, J., Käser, M., Dumbser, M., and Igel, H. (2007). An arbitrary high-order discontinuous galerkin method for elastic waves on unstructured meshes-iv. anisotropy. Geophysical Journal International, 169(3):1210–1228.

Deeks, J. and Lumley, D. (2015). Prism waves in seafloor canyons and their effects on seismic imagingprism waves in seafloor canyons. Geophysics, 80(6):S213–S222.

Dellmour, R., Stueland, E., Lindstrom, S., Tari, G., and Purkis, S. (2016). The håpet dome in the norwegian barents sea, structural evolution and morphometry of salt basins. In 78th EAGE Conference and Exhibition 2016, volume 2016, pages 1–5. European Association of Geoscientists & Engineers.

Dix, C. H. (1955). Seismic velocities from surface measurements. Geophysics, 20(1):68–86.

Dong, S., Cai, J., Guo, M., Suh, S., Zhang, Z., Wang, B., and Li, e. Z. (2012). Least-squares reverse time migration: Towards true amplitude imaging and improving the resolution. In SEG technical program expanded abstracts 2012, pages 1–5. Society of Exploration Geophysicists.

Douma, H., Yingst, D., Vasconcelos, I., and Tromp, J. (2010). On the connection between artifact filtering in reverse-time migration and adjoint tomography. Geophysics, 75(6):S219–S223.

Dumbser, M. and Käser, M. (2006). An arbitrary high-order discontinuous galerkin method for elastic waves on unstructured meshes—ii. the three-dimensional isotropic case. Geophysical Journal International, 167(1):319–336.

Durrani, T. and Bisset, D. (1984). The radon transform and its properties. Geophysics, 49(8):1180–1187.

Dutta, G. and Schuster, G. T. (2014). Attenuation compensation for least-squares reverse time migration using the viscoacoustic-wave equation. Geophysics, 79(6):S251–S262.

Eby, J. B. and Clark, R. P. (1935). Relation of geophysics to salt-dome structures. AAPG Bulletin, 19(3):356–377.

Ekanem, A., Wei, J., Li, X.-Y., Chapman, M., and Main, I. (2013). P-wave attenuation anisotropy in fractured media: A seismic physical modelling study. Geophysical Prospecting, 61:420–433.

Escalona, A. and Mann, P. (2006). An overview of the petroleum system of maracaibo basin. AAPG bulletin, 90(4):657–678.

Espindola-Carmona, A., Peter, D., and Ortiz-Aleman, C. (2021). Crustal and upper-mantle structure below central and southern mexico. Journal of Geophysical Research: Solid Earth, 126(6):e2020JB020906.

Faccioli, E., Maggio, F., Paolucci, R., and Quarteroni, A. (1997). 2d and 3d elastic wave propagation by a pseudo-spectral domain decomposition method. Journal of seismology, 1(3):237–251.

Favretto-Cristini, N. (2020). Datasets for the validation of numerical methods and input data for imaging methods – description of the experimental set-up and data acquisition for zero-offset and offset configurations. cnrs-lma report on waves lab experiments, 25 pages. Personal Communication.

Feng, Z. and Schuster, G. T. (2017). Elastic least-squares reverse time migration. Geophysics, 82(2):S143–S157.

Foster, D. J. and Mosher, C. C. (1992). Suppression of multiple reflections using the radon transform. Geophysics, 57(3):386–395.

Gedney, S. D. (1998). The Perfectly Matched Layer absorbing medium. In Taflove, A., editor, Advances in Computational Electrodynamics: the Finite-Difference Time-Domain method, chapter 5, pages 263–343. Artech House, Boston, USA.

Gholami, A. (2017). Deconvolutive radon transform. Geophysics, 82(2):V117–V125.

Graves, R. W. (1996). Simulating seismic wave propagation in 3D elastic media using staggered-grid finite differences. Bull. Seismol. Soc. Am., 86(4):1091–1106.

Griewank, A. and Walther, A. (2000). Algorithm 799: revolve: an implementation of checkpointing for the reverse or adjoint mode of computational differentiation. ACM Transactions on Mathematical Software (TOMS), 26(1):19–45.

Guo, P., Guan, H., and McMechan, G. A. (2020). Data-and model-domain up/down wave separation for reverse-time migration with free-surface multiples. Geophysical Journal International, 223(1):77–93.

Guo, P. and McMechan, G. A. (2018). Compensating q effects in viscoelastic media by adjoint-based least-squares reverse time migration. Geophysics, 83(2):S151–S172.

Guo, P. and McMechan, G. A. (2020). Up/down image separation in elastic reverse time migration. Pure and Applied Geophysics, 177:4811–4828.

Hagedoorn, J. G. (1954). A process of seismic reflection interpretation. Geophysical prospecting, 2(2):85–127.

Hale, D., Hill, N., and Stefani, J. (1992). Imaging salt with turning seismic waves: Geophysics.

Henke, C. H., Krieger, M. H., Strack, K., and Zerilli, A. (2020). Subsalt imaging in northern germany using multiphysics (magnetotellurics, gravity, and seismic). Interpretation, 8(4):SQ15–SQ24.

Hermans, T., Vandenbohede, A., Lebbe, L., Martin, R., Kemna, A., Beaujean, J., and Nguyen, F. (2012). Imaging artificial salt water infiltration using electrical resistivity tomography constrained by geostatistical data. Journal of Hydrology, 438:168–180.

Hokstad, K. (2000). Multicomponent kirchhoff migration. Geophysics, 65(3):861–873.

Hudec, M. R. and Jackson, M. P. (2006). Advance of allochthonous salt sheets in passive margins and orogens. AAPG bulletin, 90(10):1535–1564.

Hudec, M. R. and Jackson, M. P. (2007). Terra infirma: Understanding salt tectonics. Earth-Science Reviews, 82(1-2):1–28.

Jahani, S., Callot, J.-P., de Lamotte, D. F., Letouzey, J., and Leturmy, P. (2007). The salt diapirs of the eastern fars province (zagros, iran): A brief outline of their past and present. In Thrust belts and foreland basins, pages 289–308. Springer.

Jahani, S., Hassanpour, J., Mohammadi-Firouz, S., Letouzey, J., de Lamotte, D. F., Alavi, S. A., and Soleimany, B. (2017). Salt tectonics and tear faulting in the central part of the zagros fold-thrust belt, iran. Marine and Petroleum Geology, 86:426–446.

Jakubowicz, H. (1998). Wave equation prediction and removal of interbed multiples. In SEG Technical Program Expanded Abstracts 1998, pages 1527–1530. Society of Exploration Geophysicists.

Janna, F., Le-Hussain, F., et al. (2020). Effectiveness of modified co2 injection at improving oil recovery and co2 storage—review and simulations. Energy Reports, 6:1922–1941.

Jia, B., Tsau, J.-S., and Barati, R. (2019). A review of the current progress of co2 injection eor and carbon storage in shale oil reservoirs. Fuel, 236:404–427.

Jia, X., Guitton, A., Singh, S., and Snieder, R. (2017). Subsalt marchenko imaging: a gulf of mexico example. In SEG Technical Program Expanded Abstracts 2017, pages 5588–5592. Society of Exploration Geophysicists.

Jones, I. F. (2012). Tutorial: Incorporating near-surface velocity anomalies in pre-stack depth migration models. First Break, 30(3).

Jones, I. F. and Davison, I. (2014a). Seismic imaging in and around salt bodies. Interpretation, 2(4):SL1–SL20.

Jones, I. F. and Davison, I. (2014b). Seismic imaging in and around salt bodies. Interpretation, 2(4):SL1–SL20.

Karnkowski, P. H. and Czapowski, G. (2007). Underground hydrocarbons storages in poland: actual investments and prospects. Przegląd Geologiczny, 55(12/1):1068–1074.

Kelly, K. R., Ward, R. W., Treitel, S., and Alford, R. M. (1976). Synthetic seismograms: A finite-difference approach. Geophysics, 41(1):2–27.

Komatitsch, D. (1997). Méthodes spectrales et éléments spectraux pour l'équation de l'élastodynamique 2D et 3D en milieu hétérogène. PhD thesis.

Komatitsch, D. and Martin, R. (2007). An unsplit convolutional perfectly matched layer improved at grazing incidence for the seismic wave equation. Geophysics, 72(5):SM155–SM167.

Komatitsch, D., Michéa, D., and Erlebacher, G. (2009). Porting a high-order finite-element earthquake modeling application to nvidia graphics cards using cuda. Journal of Parallel and Distributed Computing, 69(5):451–460.

Komatitsch, D. and Tromp, J. (1999). Introduction to the spectral element method for three-dimensional seismic wave propagation. Geophysical journal international, 139(3):806–822.

Komatitsch, D. and Vilotte, J.-P. (1998). The spectral element method: an efficient tool to simulate the seismic response of 2d and 3d geological structures. Bulletin of the seismological society of America, 88(2):368–392.

Komatitsch, D., Xie, Z., Bozdağ, E., Sales de Andrade, E., Peter, D., Liu, Q., and Tromp, J. (2016). Anelastic sensitivity kernels with parsimonious storage for adjoint tomography and full waveform inversion. Geophysical Journal International, 206(3):1467–1478.

Krebs, J. R., Anderson, J. E., Hinkley, D., Neelamani, R., Lee, S., Baumstein, A., and Lacasse, M.-D. (2009). Fast full-wavefield seismic inversion using encoded sources. Geophysics, 74(6):WCC177–WCC188.

Krzywiec, P. (2004). Triassic evolution of the kłodawa salt structure: basement-controlled salt tectonics within the mid-polish trough (central poland). Geological Quarterly, 48(2):123–134.

Kudin, K. N., Kryvohuz, M., Kuehl, H., Selim, M. F., Butler, W. H., Theriot, C., and Yin, A. (2018). Prism waves for imaging steep geologic features and sediment terminations against salt flanks: Examples from the gulf of mexico. The Leading Edge, 37(3):223–229.

Lailly, P. and Bednar, J. (1983). The seismic inverse problem as a sequence of before stack migrations.

Lailly, P. and Santosa, F. (1984). Migration methods: partial but efficient solutions to the seismic inverse problem. Inverse problems of acoustic and elastic waves, 51:1387–1403.

Li, Z.-C. and Qu, Y.-M. (2022). Research progress on seismic imaging technology. Petroleum Science, 19(1):128–146.

Liro, L. M. (1992). Distribution of shallow salt structures, lower slope of the northern gulf of mexico, usa. Marine and petroleum geology, 9(4):433–451.

Liu, B., Yang, S., Ren, Y., Xu, X., Jiang, P., and Chen, Y. (2021). Deep-learning seismic full-waveform inversion for realistic structural modelsdl seismic fwi. Geophysics, 86(1):R31–R44.

Liu, H.-P., Anderson, D. L., and Kanamori, H. (1976). Velocity dispersion due to anelasticity; implications for seismology and mantle composition. Geophysical Journal International, 47(1):41–58.

Liu, Q. and Tromp, J. (2006). Finite-frequency kernels based on adjoint methods. Bulletin of the Seismological Society of America, 96(6):2383–2397.

Liu, Y., Chang, X., Jin, D., He, R., Sun, H., and Zheng, Y. (2011). Reverse time migration of multiples for subsalt imaging. Geophysics, 76(5):WB209–WB216.

Liu, Y., Hu, H., Xie, X.-B., Zheng, Y., and Li, P. (2015). Reverse time migration of internal multiples for subsalt imaging. Geophysics, 80(5):S175–S185.

Loewenthal, D., Lu, L., Roberson, R., and Sherwood, J. (1976). The wave equation applied to migration. Geophysical Prospecting, 24(2):380–399.

Lombard, B. and Matignon, D. (2016). Diffusive approximation of a time-fractional burger's equation in nonlinear acoustics. SIAM Journal on Applied Mathematics, 76(5):1765–1791.

Lysmer, J. and Drake, L. A. (1972). A finite element method for seismology. Methods in computational physics, 11:181–216.

Madariaga, R. (1976). Dynamics of an expanding circular fault. Bulletin of the Seismological Society of America, 66(3):639–666.

Malcolm, A. E., De Hoop, M. V., and Ursin, B. (2011). Recursive imaging with multiply scattered waves using partial image regularization: A north sea case study. Geophysics, 76(2):B33–B42.

Martin, R., Chevrot, S., Komatitsch, D., Seoane, L., Spangenberg, H., Wang, Y., Dufréchou, G., Bonvalot, S., and Bruinsma, S. (2017). A high-order 3-d spectral-element method for the forward modelling and inversion of gravimetric data—application to the western pyrenees. Geophysical Journal International, 209(1):406–424.

Martin, R. and Komatitsch, D. (2009). An unsplit convolutional perfectly matched layer technique improved at grazing incidence for the viscoelastic wave equation. Geophysical Journal International, 179(1):333–344.

Martin, R., Komatitsch, D., Blitz, C., and Le Goff, N. (2008). Simulation of seismic wave propagation in an asteroid based upon an unstructured MPI spectral-element method: blocking and non-blocking communication strategies. Lecture Notes in Computer Science, 5336:350–363.

Martin, R., Monteiller, V., Komatitsch, D., Perrouty, S., Jessell, M., Bonvalot, S., and Lindsay, M. (2013). Gravity inversion using wavelet-based compression on parallel hybrid cpu/gpu systems: application to southwest ghana. Geophysical Journal International, 195(3):1594–1619.

Martin, R., Ogarko, V., Komatitsch, D., and Jessell, M. (2018). Parallel three-dimensional electrical capacitance data imaging using a nonlinear inversion algorithm and lp norm-based model regularization. Measurement, 128:428–445.

Marton, L. G., Tari, G. C., and Lehmann, C. T. (2000). Evolution of the angolan passive margin, west africa, with emphasis on post-salt structural styles. Geophysical Monograph-American Geophysical Union, 115:129–150.

McCann, D., Comas, A., Martin, G., McGrail, A., and Leveille, J. (2012). Seismic data processing empowers interpretation: A new methodology serves to mesh processing and interpretation. Hart's E&P.

McMechan, G. A. (1983). Migration by extrapolation of time-dependent boundary values. Geophysical prospecting, 31(3):413–420.

Métivier, L., Brossier, R., Operto, S., and Virieux, J. (2015). Acoustic multi-parameter fwi for the reconstruction of p-wave velocity, density and attenuation: Preconditioned truncated newton approach. In SEG Technical Program Expanded Abstracts 2015, pages 1198–1203. Society of Exploration Geophysicists.

Métivier, L., Brossier, R., Operto, S., and Virieux, J. (2017). Full waveform inversion and the truncated newton method. SIAM review, 59(1):153–195.

Métivier, L., Brossier, R., Virieux, J., and Operto, S. (2013). Full waveform inversion and the truncated newton method. SIAM Journal on Scientific Computing, 35(2):B401–B437.

Moczo, P. and Kristek, J. (2005). On the rheological models used for time-domain methods of seismic wave propagation. Geophysical Research Letters, 32(1).

Moczo, P., Kristek, J., and Halada, L. (2000). 3d fourth-order staggered-grid finite-difference schemes: Stability and grid dispersion. Bulletin of the Seismological Society of America, 90(3):587–603.

Moghaddam, P. P., Keers, H., Herrmann, F. J., and Mulder, W. A. (2013). A new optimization approach for source-encoding full-waveform inversion. Geophysics, 78(3):R125–R132.

Monteiller, V., Chevrot, S., Komatitsch, D., and Wang, Y. (2015). Three-dimensional full waveform inversion of short-period teleseismic wavefields based upon the sem–dsm hybrid method. Geophysical Journal International, 202(2):811–827.

Mora, P. (1987). Nonlinear two-dimensional elastic inversion of multioffset seismic data. Geophysics, 52(9):1211–1228.

Nocedal, J. and Wright, S. (2006). Numerical optimization. Springer Science & Business Media.

Operto, S., Gholami, Y., Prieux, V., Ribodetti, A., Brossier, R., Metivier, L., and Virieux, J. (2013). A guided tour of multiparameter full-waveform inversion with multicomponent data: From theory to practice. The leading edge, 32(9):1040–1054.

Ortiz-Alemán, J., Abreu-Torres, J., Orozco-del Castillo, M., and Hernández-Gómez, J. (2019). Pattern recognition applied to attenuation of multiples in subsalt imaging. Pure and Applied Geophysics, 176(6):2411–2424.

Pan, W., Innanen, K. A., and Liao, W. (2017). Accelerating hessian-free gauss-newton full-waveform inversion via l-bfgs preconditioned conjugate-gradient algorithm. Geophysics, 82(2):R49–R64.

Patera, A. T. (1984). A spectral element method for fluid dynamics: Laminar flow in a channel expansion. Journal of Computational Physics, 54(3):468–488.

Pilcher, R. S., Kilsdonk, B., and Trude, J. (2011). Primary basins and their boundaries in the deep-water northern gulf of mexico: Origin, trap types, and petroleum system implications. AAPG bulletin, 95(2):219–240.

Plessix, R.-E. (2006). A review of the adjoint-state method for computing the gradient of a functional with geophysical applications. Geophysical Journal International, 167(2):495–503.

Postma, G. (1955). Wave propagation in a stratified medium. Geophysics, 20(4):780–806.

Pratt, R., Song, Z.-M., Williamson, P., and Warner, M. (1996). Two-dimensional velocity models from wide-angle seismic data by wavefield inversion. Geophysical Journal International, 124(2):323–340.

Rao, Y. and Wang, Y. (2017). Seismic waveform tomography with shot-encoding using a restarted l-bfgs algorithm. Scientific Reports, 7(1):1–9.

Ratcliff, D. W., Gray, S. H., and Whitmore Jr, N. (1992). Seismic imaging of salt structures in the gulf of mexico. The Leading Edge, 11(4):15–31.

Reddy, J. (2010). An introduction to the finite element method, volume 1221. McGraw-Hill New York.

Reed, J. (1994). Probable cretaceous-to-recent rifting in the gulf of mexico basin an answer to callovian salt deformation and distribution problems? part 1. Journal of Petroleum Geology, 17(4):429–444.

Ren, Q. (2022). Seismic acoustic full waveform inversion based on the steepest descent method and simple linear regression analysis. Journal of Applied Geophysics, page 104686.

Ren, Y., Xu, X., Yang, S., Nie, L., and Chen, Y. (2020). A physics-based neural-network way to perform seismic full waveform inversion. IEEE Access, 8:112266–112277.

Ren, Z., Liu, Y., and Sen, M. K. (2017). Least-squares reverse time migration in elastic media. Geophysical Journal International, 208(2):1103–1125.

Robertsson, J., Blanch, J., and Gupta, H. (2011). Encyclopedia of solid earth geophysics.

Robinson, E. A. and Enders, A. (1983). Migration of geophysical data. Springer.

Roden, J. A. and Gedney, S. D. (2000). Convolutional pml (cpml): An efficient fdtd implementation of the cfs-pml for arbitrary media. Microwave and optical technology letters, 27(5):334–338.

Romero, L. A., Ghiglia, D. C., Ober, C. C., and Morton, S. A. (2000). Phase encoding of shot records in prestack migration. Geophysics, 65(2):426–436.

Sacchi, M. D. and Ulrych, T. J. (1995). High-resolution velocity gathers and offset space reconstruction. Geophysics, 60(4):1169–1177.

Schneider, W. A. (1978). Integral formulation for migration in two and three dimensions. Geophysics, 43(1):49–76.

Schuster, G. T. (2011). Seismic Imaging, Overview, pages 1121–1134. Springer Netherlands, Dordrecht.

Schuster, G. T., Wang, X., Huang, Y., Dai, W., and Boonyasiriwat, C. (2011). Theory of multisource crosstalk reduction by phase-encoded statics. Geophysical Journal International, 184(3):1289–1303.

Shen, X., Ahmed, I., Brenders, A., Dellinger, J., Etgen, J., and Michell, S. (2017). Salt model building at atlantis with full-waveform inversion. In SEG Technical Program Expanded Abstracts 2017, pages 1507–1511. Society of Exploration Geophysicists.

Sheriff, R. E. (2002). Encyclopedic dictionary of applied geophysics. Society of exploration geophysicists.

Soleimani, M., Aghajani, H., and Heydari-Nejad, S. (2018). Salt dome boundary detection in seismic image via resolution enhancement by the improved nfg method. Acta Geodaetica et Geophysica, 53(3):463–478.

Solymosi, B. (2018). A two-way approach to adapt small-scale laboratory experiments and corresponding numerical simulations of offshore seismic surveys. PhD thesis, Aix-Marseille Université, Marseille, France.

Solymosi, B., Favretto-Cristini, N., Monteiller, V., Cristini, P., Ursin, B., and Komatitsch, D. (2020). Seismic surveying and imaging at the laboratory scale: A framework to cross-validate experiments and simulations for a salt-body environment. Geophysics, 85(3):T123–T139.

Solymosi, B., Favretto-Cristini, N., Monteiller, V., Komatitsch, D., Cristini, P., Arntsen, B., and Ursin, B. (2018). How to adapt numerical simulation of wave propagation and ultrasonic laboratory experiments to be comparable—a case study for a complex topographic modelcomparison of synthetic and laboratory data. Geophysics, 83(4):T195–T207.

Stanton, A. and Sacchi, M. D. (2014). Least squares migration of converted wave seismic data. CSEG Recorder, 39(10):48–52.

Stewart, R. R., Dyaur, N., Omoboya, B., De Figueiredo, J., Willis, M., and Sil, S. (2013). Physical modeling of anisotropic domains: Ultrasonic imaging of laser-etched fractures in glass. Geophysics, 78(1):D11–D19.

Sun, J., Niu, Z., Innanen, K. A., Li, J., and Trad, D. O. (2020). A theory-guided deep-learning formulation and optimization of seismic waveform inversion. Geophysics, 85(2):R87–R99.

Talbot, C. and Alavi, M. (1996). The past of a future syntaxis across the zagros. Geological Society, London, Special Publications, 100(1):89–109.

Talbot, C. J. and Jackson, M. P. (1987). Salt tectonics. Scientific American, 257(2):70–79.

Tang, Y. and Lee, S. (2010). Preconditioning full waveform inversion with phase-encoded hessian. In 2010 SEG Annual Meeting. OnePetro.

Tarantola, A. (1984). Inversion of seismic reflection data in the acoustic approximation. Geophysics, 49(8):1259–1266.

Tarantola, A. and Valette, B. (1982). Generalized nonlinear inverse problems solved using the least squares criterion. Reviews of Geophysics, 20(2):219–232.

Tari, G., Molnar, J., and Ashton, P. (2003). Examples of salt tectonics from west africa: a comparative approach. Geological Society, London, Special Publications, 207(1):85–104.

Tarkowski, R. and Czapowski, G. (2018). Salt domes in poland–potential sites for hydrogen storage in caverns. international journal of hydrogen energy, 43(46):21414–21427.

Telford, W. M., Telford, W., Geldart, L., and Sheriff, R. E. (1990). Applied geophysics. Cambridge university press.

Tromp, J., Tape, C., and Liu, Q. (2005). Seismic tomography, adjoint methods, time reversal and banana-doughnut kernels. Geophysical Journal International, 160(1):195–216.

Vdovina, T., Bansal, R., Baumstein, A., Tang, Y., and Yang, D. (2015). Multistage full wavefield inversion process that generates a multiple free data set. US Patent 20160238722A1.

Verschuur, D. and Berkhout, A. (1992). Surface-related multiple elimination: practical aspects. In SEG Technical Program Expanded Abstracts 1992, pages 1100–1103. Society of Exploration Geophysicists.

Virieux, J. (1986). P-sv wave propagation in heterogeneous media: Velocity-stress finite-difference method. Geophysics, 51(4):889–901.

Virieux, J. and Operto, S. (2009). An overview of full-waveform inversion in exploration geophysics. Geophysics, 74(6):WCC1–WCC26.

Wang, P., Gomes, A., Zhang, Z., and Wang, M. (2016). Least-squares rtm: Reality and possibilities for subsalt imaging. In SEG Technical Program Expanded Abstracts 2016, pages 4204–4209. Society of Exploration Geophysicists.

Wang, P., Zhang, Z., Mei, J., Lin, F., and Huang, R. (2019). Full-waveform inversion for salt: A coming of age. The Leading Edge, 38(3):204–213.

Wang, Y., Chang, X., and Hu, H. (2013). Simultaneous reverse time migration of primaries and free-surface related multiples without multiple prediction. Geophysics, 79(1):S1–S9.

Wang, Y., Zheng, Y., Xue, Q., Chang, X., Fei, T. W., and Luo, Y. (2017). Reverse time migration of multiples: Reducing migration artifacts using the wavefield decomposition imaging condition. Geophysics, 82(4):S307–S314.

Wang, Y., Zhou, H., Chen, H., and Chen, Y. (2018). Adaptive stabilization for q-compensated reverse time migration. Geophysics, 83(1):S15–S32.

Wapenaar, K., Thorbecke, J., Van Der Neut, J., Broggini, F., Slob, E., and Snieder, R. (2014). Marchenko imaging. Geophysics, 79(3):WA39–WA57.

Warren, J. (1989). Evaporite-hydrocarbon association: The importance of salt structures.

Weglein, A. B., Gasparotto, F. A., Carvalho, P. M., and Stolt, R. H. (1997). An inverse-scattering series method for attenuating multiples in seismic reflection data. Geophysics, 62(6):1975–1989.

Weibull, W. W. and Arntsen, B. (2014). Reverse-time demigration using the extended-imaging condition. Geophysics, 79(3):WA97–WA105.

Whitmore, N. D. (1983). Iterative depth migration by backward time propagation. In SEG Technical Program Expanded Abstracts 1983, pages 382–385. Society of Exploration Geophysicists.

Wong, M., Ronen, S., and Biondi, B. (2011). Least-squares reverse time migration/inversion for ocean bottom data: A case study. In 2011 SEG Annual Meeting. OnePetro.

Wu, S., Bally, A. W., and Cramez, C. (1990). Allochthonous salt, structure and stratigraphy of the north-eastern gulf of mexico. part ii: Structure. Marine and Petroleum Geology, 7(4):334–370.

Xu, C., Di, B., and Wei, J. (2016). A physical modeling study of seismic features of karst cave reservoirs in the tarim basin, china. Geophysics, 81(1):B31–B41.

Xu, S., Wang, D., Chen, F., Zhang, Y., and Lambare, G. (2012). Full waveform inversion for reflected seismic data. In 74th EAGE Conference and Exhibition incorporating EUROPEC 2012, pages cp–293. European Association of Geoscientists & Engineers.

Yang, P., Brossier, R., Métivier, L., and Virieux, J. (2016). Wavefield reconstruction in attenuating media: A checkpointing-assisted reverse-forward simulation method. Geophysics, 81(6):R349–R362.

Yang, P., Gao, J., and Wang, B. (2015a). A graphics processing unit implementation of time-domain full-waveform inversiongpu implementation of fwi. Geophysics, 80(3):F31–F39.

Yang, Y. (2021). Anderson acceleration for seismic inversion. Geophysics, 86(1):R99–R108.

Yang, Z., Hembd, J., Chen, H., and Yang, J. (2015b). Reverse time migration of multiples: Applications and challenges. The Leading Edge, 34(7):780–786.

Yee, K. (1966). Numerical solution of initial boundary value problems involving maxwell's equations in isotropic media. IEEE Transactions on antennas and propagation, 14(3):302–307.

Yilmaz, Ö. (2001). Seismic data analysis: Processing, inversion, and interpretation of seismic data. Society of exploration geophysicists.

Yu, W., Lashgari, H. R., Wu, K., and Sepehrnoori, K. (2015). Co2 injection for enhanced oil recovery in bakken tight oil reservoirs. Fuel, 159:354–363.

Zhang, D. and Schuster, G. T. (2013). Least-squares reverse time migration of multiples. Geophysics, 79(1):S11–S21.

Zhang, D. and Schuster, G. T. (2014). Least-squares reverse time migration of multiples. Geophysics, 79(1):S11–S21.

Zhang, W., Gao, J., Cheng, Y., Li, Z., Jiang, X., and Zhu, J. (2022). Deep-learning for accelerating prestack correlative least-squares reverse time migration. Journal of Applied Geophysics, 200:104645.

Zhang, W. and Shi, Y. (2019). Imaging conditions for elastic reverse time migration. Geophysics, 84(2):S95–S111.

Zhang, Y., Duan, L., and Xie, Y. (2015). A stable and practical implementation of least-squares reverse time migration. Geophysics, 80(1):V23–V31.

Zhu, H., Bozdağ, E., Duffy, T. S., and Tromp, J. (2013). Seismic attenuation beneath europe and the north atlantic: Implications for water in the mantle. Earth and Planetary Science Letters, 381:1 – 11.

Zhu, H. and Tromp, J. (2013). Mapping tectonic deformation in the crust and upper mantle beneath europe and the north atlantic ocean. Science, 341(6148):871–875.

Zienkiewicz, O. C., Taylor, R. L., and Zhu, J. Z. (2005). The finite element method: its basis and fundamentals. Elsevier.